NORTHWESTERN UNIVERSITY

Synthetic and Analytical Techniques to Break Symmetry and Control Structure in Crystals Engineered with DNA

A DISSERTATION

SUBMITTED TO THE GRADUATE SCHOOL

IN PARTIAL FULFILLMENT OF THE REQUIREMENTS

for the degree

DOCTOR OF PHILOSOPHY

Field of Chemical and Biological Engineering

By

Christine Rose Laramy

EVANSTON, ILLINOIS

December 2018

ABSTRACT

When attached to another species (e.g. a nanoparticle), the sequence specificity of DNA can be repurposed to program interactions between such entities and to direct their formation into ordered structures. The research presented in this thesis aims to push the boundaries of structures that can be made via this approach. Specifically, it focuses on the development of syntheses for exotic low-symmetry nanoparticles that can be used as building blocks, the development of new analytical tools that enable high-throughput structural analysis of such building blocks, and the introduction of post-synthetic modifications to tune structure. Chapter 1 describes the state-of-the field and presents several *Lessons* learned over the past two decades that guide the use of DNA for crystal engineering. Chapter 2 presents a strategy to algorithmically characterize the structure of a nanoparticle population with individual particle resolution. In particular, image analysis software was developed for measuring quantitative structural values for >7 anisotropic particle shapes from electron microscopy images. This tool is extremely useful for nanomaterials characterization and provides important structural insight, and thus it was made freely available online. Chapters 3 and 4 explore the origins of symmetry breaking in nanoparticle syntheses. Specifically, these chapters identify a previously unexplained nanoparticle-catalyzed nucleation mechanism and detail a platform-type approach for synthesizing a number of low symmetry nanoparticles. Chapter 5 explores the DNA-mediated crystallization of particles from Chapter 4 and identifies a unique series of phase transitions. This chapter identifies a novel symmetry breaking event in the DNA shell that enables the formation of an unexpected low symmetry lattice. Chapter 6 describes how the intrinsic properties of DNA can induce significant structural changes in response to specific stimuli which enable one to tune crystal properties (e.g. optoelectronic). These advances dramatically progress the ability to rationally design complex colloidal crystals for diverse applications ranging from metamaterials to catalysis to therapeutics.

Thesis Advisor: Professor Chad A. Mirkin

ACKNOWLEDGEMENTS

To my advisor and committee: I am grateful for your lessons, encouragement, and challenges to grow. In particular, thank you to my advisor, Prof. Chad Mirkin, for posing difficult questions and believing that I could answer them. I am grateful to have had the opportunity to learn from you and the exceptional team of researchers that you have brought together. Thank you to Prof. Michael Jewett for convincing me to pursue my degree at Northwestern and for championing me during my graduate career. Thank you to Profs. George Schatz and Monica Olvera de la Cruz for serving on my committee and for being exceptional collaborators. Our conversations always challenged me to think about a scientific question from a different perspective. Thank you to Prof. Julius Lucks for joining my committee and providing feedback on my research projects.

To my mentor: Thank you to Marla Persky for developing me professionally over the last two years. I am grateful that you took a chance on me as a mentee during my second year of graduate school and have continued to give your time to see me grow. Thank you counting me as "one of your own."

To my INVO mentors and friends: Thank you to Dr. Dimitra Georganopoulou for encouraging me to pursue an internship with INVO. I am grateful to have learned about technology transfer under your mentorship. Thank you to Dr. Sonia Kim for creating the Practicum program and for hiring me as an intern. It was an invaluable learning experience. Thank you to John Haugen and Dr. Sarah Kamper for your career and IP advice.

To my Skills and Careers in Science Writing professors: Thank you to Profs. Patti Wolter and Donna Leff for training me to weave a scientific story. You taught me to break down complex ideas into bits like rungs on a ladder, so that readers are able to reach the next rung from the

previous. Perhaps more importantly, you showed me the importance of making science accessible, relatable, and interesting to broad audiences. This is a core value that I will carry with me throughout my career.

To my Northwestern collaborators and friends (Prof. Keith Brown, Dr. Matt O'Brien, Dr. Lam-Kiu Fong, Prof. Jarad Mason, Dr. Byeongdu Lee, Dr. Martin Girard, Hector Lopez-Rios, Prof. Matt Jones, Dr. Devleena Samanta, Dr. Michael Ashley, Dr. Jeff Brodin, Kacper Skakuj, Andrea D'Aquino, Dr. Lisa Cole, Dr. Kevin Metcalf, Oliver Hayes, Janet McMillan, Melissa Puga, and Peter Winegar): I owe a lot of thanks to each of you, but I will try to be brief. Thank you to Keith and Matt who first taught me how to approach a problem as a scientist. Your enthusiasm for science and learning was infectious. Thank you to Lam-Kiu, Jarad, Kacper, Devleena, and Mike for being strong collaborators and even better friends. Thank you to Hector and Martin for your tireless efforts as collaborators on our project, for teaching me how to think like a theorist, and for brightening my day with our sometimes >2 hours meetings. Thank you to Andrea and Lisa for making graduate school fun, whether at the bench, a lab party, or on the volleyball court. Thank you to Lam-Kiu and Kevin for eating your way through Chicago with me and Matt. Thank you to my mentees, Melissa and Peter, for your excitement and ideas. I look forward to seeing you grow as scientists and develop creative answers to questions that no one had thought to ask before.

To my mom, Judy Stuckman: Thank you for instilling in me a sense of confidence and direction. You taught me to persist, even when the task at hand seemed overwhelming, because you believed that I could do it. You taught me this lesson over many years: by helping me to practice spelling the challenge word on my first grade spelling test ("echolocation"); by gluing construction paper onto a trifold board for my second grade platypus project; by reassuring me

that one low score in the fourth grade did not mean that I was bad at math; by making sure that I always completed my homework, even if it meant driving me in early for extra help in high school; and by doing all of this as a single, working parent. I would not have made it to or through graduate school without your continual support – thank you.

To my sister, Michelle Stockton: Thank you for being a supportive and encouraging younger sister. You have always believed in me in a way that motivates me to live up to your expectations.

To my college roommates and friends: Thank you to Madison Estes, Rachel Sawyers, and Julia Goodwin (Eaddy) who put up with my late nights studying, always knew how to keep me going (most often cookies from Tiff's Treats or queso from Kirby Lane, thankfully both were open 24 hours), and who have continued to cheer me on at each step of my graduate school journey. I am grateful for the last decade of our lifelong friendships. Thank you to Alex Atalis for being my study partner in our undergraduate BME program, for always indulging my love of popcorn, and for support during some of our most challenging obstacles in life and in graduate school. Thank you to Megan McKinney for being the best listener I know. There is not a problem that you cannot solve, and I am grateful to count you as my former Spirit Haunt partner and as lasting a friend.

To woman's best friend: Thank you to my energetic dog, Charlotte, who keeps me playful and makes sure that I do not take myself too seriously.

To my partner and best friend: Thank you to Dr. Matt O'Brien who has been a more complete partner than I ever imagined that I would find. You first ignited my curiosity for science as a mentor and then taught me to what it means to live life with someone as a boyfriend, fiancé, and, soon, husband. I am grateful for your support, guidance, love, patience, and encouragement.

You ensure that I always have faith in myself and continue to grow. Thank you for the rare chance to share so much with one person.

My PhD was not earned in isolation. I am grateful to everyone who played a role.

- Christine

September 2018

This dissertation is dedicated to the family and friends that inspired and encouraged me throughout this journey.

TABLE OF CONTENTS

LIST OF FIGURES

LIST OF TABLES

SECTION ONE – DEFINING A GENETIC CODE FOR CRYSTAL ENGINEERING

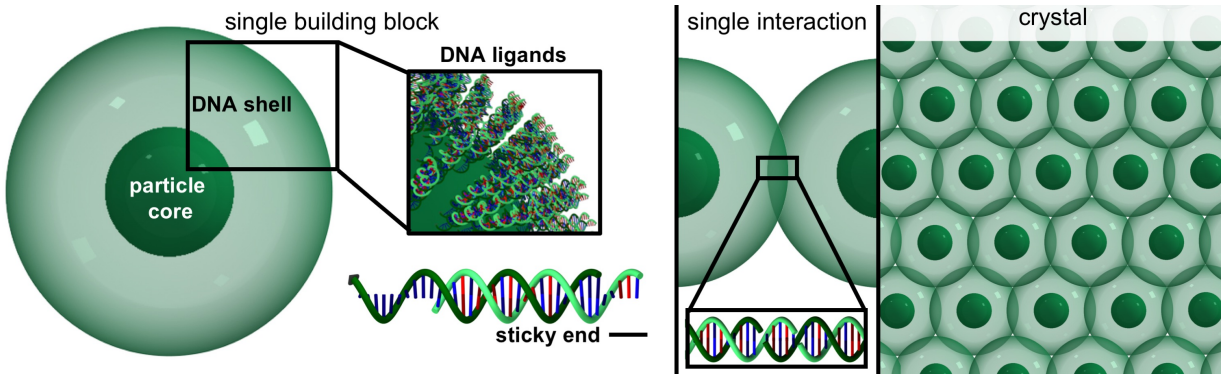

1 CHAPTER ONE: CRYSTAL ENGINEERING WITH DNA

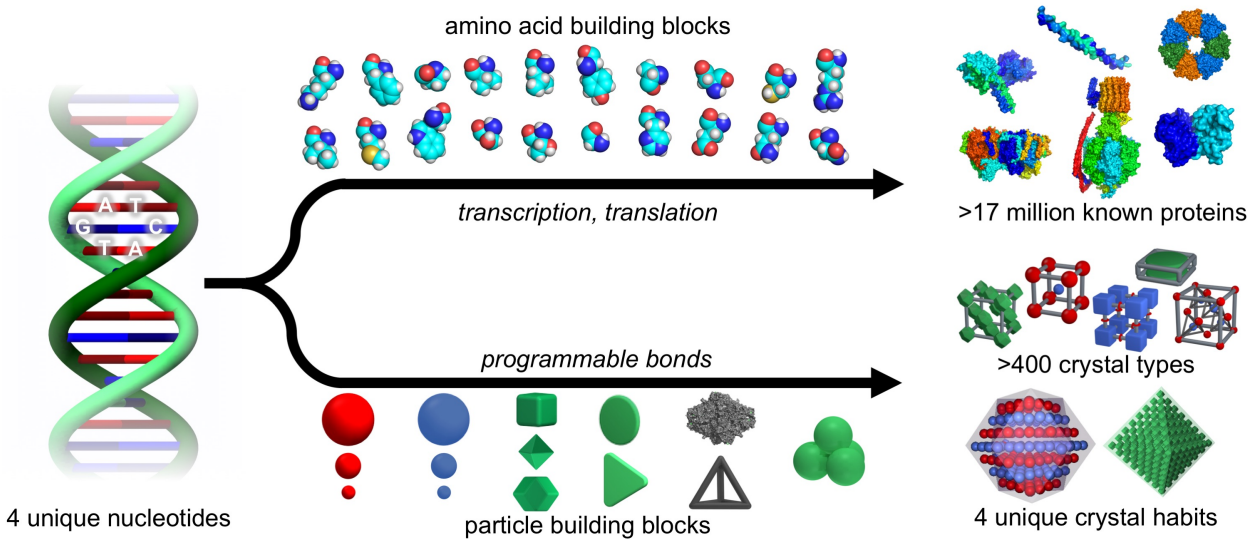

Material in this chapter is based upon submitted work:

C.R. Laramy, M.N. O'Brien, C.A. Mirkin. *Under Review* (at *Nature Reviews Materials*)

1.1 Introduction

Biological processes build complex, functional materials from a molecular blueprint for life – the biopolymer deoxyribonucleic acid (DNA). DNA directs material synthesis with encoded messages written in the sequence of four fundamental units called nucleotides (adenine, guanine, cytosine, and thymine) and a small number of post-translational modifications.[31] Cellular machinery translates these sequences into custom materials (proteins) using a pool of twenty amino acids.[31] Despite this limited set of building blocks, cells utilize the specificity and flexibility of the genetic code to produce millions of unique proteins.

The transmission and communication of DNA's code relies on specific "Watson-Crick" base-pairing interactions: each nucleotide, or base, preferentially binds to one other nucleotide, adenine (A) to thymine (T) and guanine (G) to cytosine (C).[32, 33] The decryption of these interactions and, later, of DNA's central role in the synthesis of biological materials, transformed DNA from an enigmatic carrier of hereditary information into an elegantly designed biopolymer. The establishment of a defined structure laid the foundation for how to read and make nucleic acids. Decades of subsequent research progressed DNA sequencing and synthesis technologies from thought-provoking concepts to routine bench top instrumentation.[34] These tools enabled unprecedented insight into and command over DNA's biological function, which revolutionized drug discovery and modern medicine. Unintentionally, the removal of the barriers to entry also enabled DNA to be used outside of its biological function and repurposed as a synthetic material (Figure 1).[2, 3, 35-39]

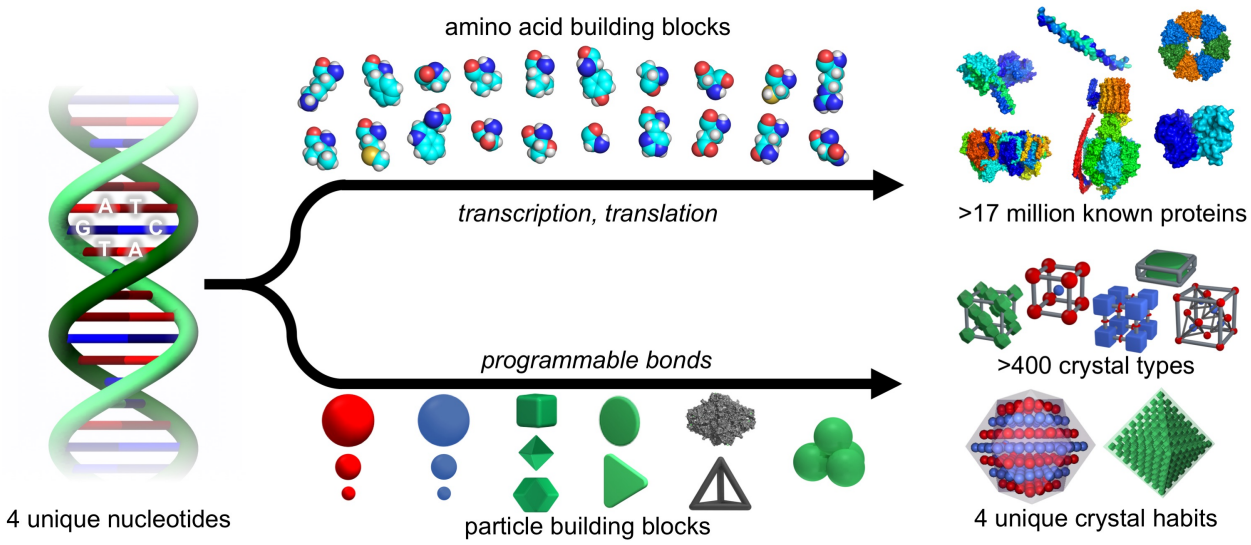

Figure 1. Comparison of biological material design with DNA and crystal engineering with DNA. Crystal engineering with DNA affords a high degree of control over material structure and the incorporation of a library of materials with tunable size, shape, composition, and functionality.

DNA molecules could now be designed with an arbitrary sequence, programmed base by base. Within the sequence for each DNA molecule, instructions could be encoded to interact in a predictable, highly specific manner with other DNA molecules. If connected to other species (*e.g.* small molecules, biomolecules, or nanomaterials), DNA could similarly function to connect arbitrary species together into larger structures. Local and directional interactions between species, repeated over and over, could lead to the assembly of extended, macroscopic materials comprised of structural elements in pre-specified, precise arrangements. This vision forms the foundation for the "genetic code" for crystal engineering, where new classes of functional materials can be rationally and systematically programmed with DNA to push far beyond what has been structurally possible with naturally occurring crystalline materials or those made by more conventional crystal engineering strategies. This approach uniquely enables the deliberate control of building block composition, size, and shape; lattice symmetry and dimensions; and even crystal habit.

In general, the implementation of DNA for designer materials has followed two distinct strategies, which have resulted in materials that are, in essence, only separated by a preposition: materials composed *of* DNA and materials composed *with* DNA. The first strategy initiated the field of structural DNA nanotechnology, which relies on entirely DNA-based structural elements. With this technique, intentionally placed base-pair interactions bend or fold DNA strands into well-defined two- and three-dimensional structures. Through judicious design of DNA sequence, distinct regions within a strand can be complementary to two or more other strands in order to create rigid "branch points," a process analogous to reciprocal exchange of strands in biological systems.[40-43] A major subset of this field, DNA origami, derives its name from the ability to create arbitrary, complex structures by folding a single, long "template" DNA strand.[44] A series of short "staple" DNA strands hold the folds of this template strand in place through complementary interactions in key regions.[44-46] Importantly, the persistence length of DNA and thickness of the DNA double helix define the precision of these techniques, which allows for the construction of micron-scale materials with nanoscale structural features. Several recent reviews have highlighted the advances in the field of structural DNA nanotechnology, where the resultant nucleic acid materials are predominantly amorphous or polycrystalline.[42, 46] This perspective will focus on the second strategy which produced the field of crystal engineering with DNA.

Crystal engineering with DNA marries biological programmability with an expanded toolbox of organic and inorganic structures: micro- to nanoscale particles with varied composition, size, and shape (Figure 1). Similar to structural DNA nanotechnology, this strategy relies on Watson-Crick base pairs to direct the assembly of structural elements. However, instead of exploiting branch points or "staple" strands to impart rigidity, particles act as templates to impart

directionality to DNA attached to their surface at high loading (*i.e.* DNA ligands forced to stand upright).[47] The sequence of these DNA ligands drives specific interactions between particles, which, in principle, allows for angstrom-level spatial control. An over two-decade journey through careful design of DNA sequence, particle structure, and external stimuli has defined a "genetic code" for crystal engineering resulting in exquisite architectures. These architectures, including the prototypical "spherical nucleic acid" (SNA) design, have also significantly advanced fields outside of the crystal engineering, including medical and biological diagnostics and therapeutics.[48] The aim of this perspective is to highlight the critical advances that enabled the present level of structural control, and to inspire researchers to envision how this "genetic code" for crystal engineering can be applied to their area of expertise.

1.2 Defining the "Genetic Code" for Crystal Engineering

The vision for this field was established in the mid-1990s, when our group showed that DNA could be chemically interfaced with gold nanoparticles, and complementary DNA interactions could be used to reversibly organize them into periodic materials.[36] In the years since the development of this original "building block," the SNA, the lessons learned have been distilled into design rules, underpinned by the programmability of DNA as a ligand. The following concepts and *Lessons* define this "genetic code" for crystal engineering. Around the same time, researchers also demonstrated that DNA can act as a specific labelling ligand to direct the formation of short-range, finite structures (*i.e.* clusters of 2-10 particles). These concepts, which do not involve crystal engineering, are beyond the scope of this perspective, and the authors direct readers to two excellent reviews in this area.[43, 49]

In this Perspective, a "building block" is defined by two components: a micro- to nano-sized particle core and a dense shell of DNA strands (described more broadly as ligands) attached to the particle's surface (Figure 2). A region of each surface-attached strand is then hybridized to a region on a complementary strand in a manner that leaves unpaired bases at the DNA terminus furthest from the particle surface. The hybridized region(s) imparts rigidity to each DNA molecule, while the single-stranded region acts as a "sticky end" – a term borrowed from the molecular biology community to describe the single-stranded overhang regions of DNA which result from cuts made by restriction enzymes.[50] In molecular biology, these sticky ends serve as recognition sequences to chemically link particular DNA fragments together for gene editing.[51] In the field of crystal engineering with DNA, the sticky ends drive sequence-specific interactions between building blocks.

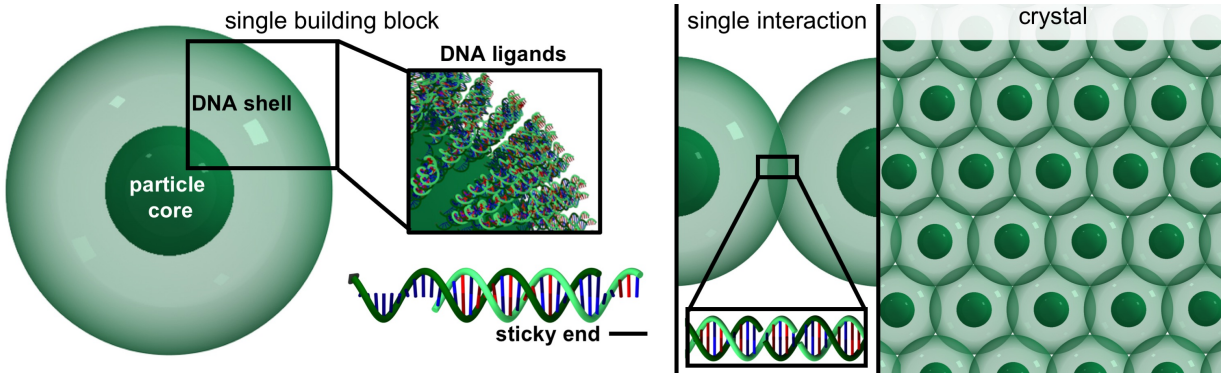

Figure 2. The "genetic" code for crystal engineering arranges building blocks into predictable positions based on the sequence of the sticky ends and the arrangement of the DNA shell.

The sticky end sequence determines the specific interactions (or lack thereof) with nearby building blocks and the DNA arrangement on the particle surface modulates the accessibility of sticky ends between adjacent building blocks. Locally, building block connections that allow for the most thermodynamically favorable interactions (*i.e.* most often the greatest number of sticky end hybridization events) form and persist. Macroscopically, these connections drive building blocks to assemble into materials which, with appropriate design and external conditions, can

exhibit a high degree of order (Figure 2). In these "superlattices," order is defined analogously to crystalline atomic systems where a fundamental, repeat unit (*i.e.* unit cell) maintains translational symmetry over a long-range.[52] Several local and global techniques exist to probe the degree of order in these systems, including optical and electron microscopy and x-ray scattering, respectively.[52, 53]

The following four *Lessons* detail the use of these building blocks through a series of foundational lessons related to the DNA design; the role of the particle core will be addressed in the next section. These lessons include the design of a relatively short sticky end to allow for rapid particle reorganization, precise control of temperature and chemical environment to guide the crystallization pathway, elucidation of the implications of ligand density in multivalent systems, and the importance of DNA ligand flexibility. The result is a march from early, relatively low order aggregates to highly faceted, single crystals composed of millions of precisely positioned building blocks. Several models have been developed to understand the phenomenon described in the following *Lessons*. For a detailed discussion of these models, we direct readers to a number of important reviews.[54-57]

1.2.1 Lesson 1: Weak, collective interactions between building blocks are key to enable their reorganization into crystalline structures.

DNA-mediated particle assembly occurs in solution, through each building block sampling its local environment to find stable interactions. Kinetic barriers can arrest this sampling and prevent the formation of thermodynamically favored structures.[58, 59] If the kinetically trapped states are not uniform, long-range order may be difficult to achieve. One strategy to overcome kinetic barriers is through the incorporation of weak, collective interactions.[55, 59-63]

A "weak," but favorable interaction requires an interaction potential between building blocks slightly greater than k_BT.[56, 64, 65] Since interactions primarily result from enthalpically favorable hydrogen bonding and base stacking between Watson-Crick base pairs, sticky end design (both sequence and length) modulates this interaction potential. Initial DNA designs leveraged nearest-neighbor models that describe the stability of DNA duplex formation free in solution to predict the "melting" temperature (T_m) - the temperature at which half of the DNA strands exist in a hybridized state and half exist as single strands.[66, 67] Based on these models, one might hypothesize that in order to drive specific, favorable interactions, the sticky end T_m must be slightly greater than room temperature, which typically requires eight to sixteen base pairs depending on the sequence. However, the earliest building blocks assembled with such sticky end designs resulted in materials with limited long-range order.[36, 68]

The reason for this limited order was that the collective interactions of sticky ends between building blocks arrested their rearrangement. In other words, the collective interactions of building blocks prevented individual sticky ends from hybridizing and de-hybridizing on short time scales relative to the time required for the diffusion of interacting components.[69-71] This was supported by melting experiments, which showed a substantially greater T_m for DNA-assembled building blocks relative to the T_m of the same double-stranded DNA free in solution (sometimes greater than 10 °C).[72-74] Later experiments validated this conclusion by using shorter sticky ends (4-7 bases).[3] Despite nearest-neighbor model predictions that, as free DNA duplexes, these shorter sticky end sequences should remain predominantly single stranded as low as 0 °C, building blocks assembled in a sequence-specific fashion into highly crystalline materials. As a result of weak, collective interactions and the thermal strategies described in *Lesson 2*, DNA emerged as a ligand

capable of driving not only periodic aggregation, but *crystallization* processes for single and multi-component systems.[2, 3]

1.2.2 Lesson 2: The programmable properties of the building blocks allow one to use thermal control to modulate DNA hybridization and enable building blocks to dynamically sample their environment.

Crystallization processes in atomic and nanoscale systems have long benefitted from thermal treatments, often described as annealing, in order to achieve long range order.[75] By definition, thermal treatments temporally change the energy input to the assembly or crystallization environment (*i.e.* k_BT).[75, 76] Thus, similar to *Lesson 1,* this lesson relates to the production of "weak" interactions (as defined relative to k_BT). Elevated temperatures can be used to modulate the interaction potential between building blocks because DNA has a sequence-specific thermal response: de-hybridization (or "melting").[67, 71, 72, 76-79] The first successful approach to overcome the challenge of "strong" interactions described in *Lesson 1* was to heat building blocks to a temperature just below the T_m, determined by both the sticky end sequence (*Lesson 1*) and the electrostatic environment (discussed in *Lessons 3* and *5*), during assembly. This annealing treatment increased the frequency of dehybridization events, decreased the effective rate constant (k_{on}/k_{off}), and allowed for greater particle rearrangement within a pre-formed aggregate. Indeed, in contrast to earlier systems, annealed building blocks with shorter sticky ends resulted in the first highly crystalline materials.[2, 3]

An alternative approach, commonly used to increase crystal grain size in bulk metals and semiconductors, is to begin above the T_m, and slowly cool. Taken to its extreme limit, an ideal "slow" cooling procedure allows species to achieve thermodynamic equilibrium at each

infinitesimal temperature increment.[1] In the context of crystal engineering with DNA, this slow cooling can be achieved when individual sticky end interactions remain dynamic, but the total number of interactions between building blocks approaches a constant or equilibrium state. Put another way, each building block is given sufficient time to sample its environment and find its thermodynamically preferred configuration. Initiation of crystallization from a "melted" state (*i.e.* free building blocks) helps to eliminate kinetic traps and grain boundaries that frequently occur in the initial disordered aggregates that typically form at ambient conditions. The effects of these traps were evident in annealed systems, which frequently yielded polycrystalline materials with micron-sized grains.[2, 3, 9, 24] Identical systems cooled from a temperature above the system's T_m at a sufficiently slow rate (0.01 °C/minute) form single crystals with habits predicted from the lattice symmetry.[1] The transition from polycrystalline assemblies to faceted, single crystals is a critical advance since it dramatically expands the use of such materials as functional components within single crystal device architectures such as microcavities[80, 81] and photonic crystals[82] (vide infra Functional Consequences of Crystal Engineering with DNA).

1.2.3 Lesson 3: High DNA surface density orients sticky ends into configurations that facilitate collective interactions.

Lesson 1 intuitively suggests that higher DNA ligand densities are beneficial for the formation of ordered assemblies – the probability of a given sticky end hybridization event increases and the greater number of bonds collectively strengthens the connection between building blocks. A second benefit arises from the effect of ligand density on ligand orientation. In general, when ligands are packed onto a substrate with sufficient density, adjacent ligands can

interact and induce collective configurational changes. To minimize unfavorable steric or electrostatic interactions with their neighbors, ligands can adopt an extended configuration with decreased configurational entropy (termed the "polymer brush effect").[83-85] In the systems described here, the polymer brush effect with highly charged DNA ligands results in the projection of sticky ends away from the particle core into a configuration that facilitates hybridization events.[85, 86] The effects of high DNA density – favorable DNA orientation and multivalent interactions – can be qualitatively explored via DNA melting experiments, where early work with nanoparticle building blocks revealed that increased DNA density raised the T_m and dramatically narrowed the breadth of the transition.[72, 87]

To load DNA onto particle surfaces, the existing surface ligands or functional groups must be exchanged or reacted with DNA, while maintaining sufficient ligand coverage throughout functionalization to preserve colloidal stability and particle structure.[55] If DNA is added without further treatment, even in an extreme excess of DNA relative to available surface sites, its polyanionic nature prevents a high loading density. Therefore, the negative charge of DNA ligands must be partially screened, typically through the slow addition of salt that balances reduced repulsion between neighboring ligands and surface-charge mediated colloidal stability.[88] This experimental technique is useful for both nanoparticle and microparticle systems, but achieving comparable densities in microparticle systems requires additional considerations.

In microparticle systems, early DNA assembly work was similarly plagued by frustrated aggregates or materials with short-range order.[89] The limited order present in these systems was attributed to synthetic challenges that restricted the motion of particles upon initial hybridization (*i.e.* "hit and stick" models).[90] Drawing on *Lessons 1* and *2*, researchers hypothesized that the

limited order may originate from the DNA design, which could be addressed with weaker sticky ends or thermal treatments. Indeed, several studies revealed that these strategies do improve short-range order, but not to the same degree as in analogous systems with nanoparticle cores.[89, 91] Puzzlingly, the sticky end designs required for assembly still remained much longer (11 bases).[92] A key insight that led to successful DNA-mediated crystallization of microparticle-based building blocks was that the melting transition was often broader than in nanoparticle-based systems. This insight was ultimately connected to *Lesson 3* and addressed by pioneering work from the Pine group in 2015.[93]

To understand the challenge, it is helpful to review three size-dependent differences with DNA functionalization and its relation to crystallization. First, the surface roughness of microparticles can be on the order of the DNA length, which creates an inconsistent configuration of DNA ligands on the surface, and thus an inhomogeneous surface potential. In contrast, nanoparticle cores typically possess atomically-defined facets or surface roughness at the sub-nanometer scale. Second, microparticle functionalization historically utilized bulky biotin-streptavidin interactions, which led to low DNA densities[94] compared to nanoparticle systems (1.5-5 nm mean distance between the center of DNA duplexes).[88] Last, if all particle surfaces could be made smooth, the large radius of curvature (relative to the DNA length) for microparticles, forces the full length of each DNA to be in close proximity to adjacent ligands.[88] In contrast, the radius of curvature and DNA length are comparable for nanoparticles, which allows DNA to splay and explore more volume near their termini, thereby reducing the extent of repulsion between neighboring ligands.

Pine's group overcame these challenges through a clever synthetic scheme, which included revised particle syntheses that resulted in smoother surfaces and the use of azide-alkyne click chemistry that attached DNA ligands via a less bulky linking moiety.[94] As a result, they achieved DNA densities more comparable to nanoparticle systems (1 strand/27 nm^2 with a mean distance of 5.2 nm between the center of DNA duplexes).[93, 94] These modifications enabled weaker sticky end designs (4-8 bases) to be used[93] and yielded the first highly ordered, crystalline materials comprised of microparticles with sharp melting transitions. The similarities between nano- and microparticle systems here highlight the universality of crystal engineering with DNA across diverse length scales and core compositions.

1.2.4 Lesson 4: Modest DNA flexibility can increase the free volume accessible to sticky ends and facilitate more hybridization events between building blocks.

The earliest building blocks incorporated a design that, upon assembly, resulted in a rigid, entirely double-stranded DNA connection. In addition to the changes described in *Lessons 1* and *2*, later designs began to incorporate a region of high flexibility to improve order.[2, 3] Subsequent systematic studies of ligand design revealed that even modest increases in DNA ligand flexibility dramatically increase the accessible free volume of DNA sticky ends and improve their ability to explore their environment. [24, 54, 69, 95] This enables DNA ligands to sample hybridization interactions with a greater number of DNA ligands on adjacent particles. Importantly, modulation of DNA flexibility can be used to overcome heterogeneity in nanoparticle size and shape, and thereby increase the design space over which building blocks can crystallize – a point illustrated by the successful crystallization of building blocks with microparticle cores and fully single-stranded DNA ligands.[24, 56, 93]

However, there are limits to the benefits of DNA ligand flexibility, especially as the particle core approaches the nanoscale. When the ligand becomes too flexible relative to the particle core size, order decreases and eventually crystallization behavior may deviate from the predicted Watson-Crick base-pairing interactions.[24, 96] This unexpected behavior can be attributed to the random coiling behavior of highly flexible ligands, analogous to flexible polymer systems. In order to illustrate the effect of DNA ligand flexibility in these systems it is useful to consider a quantitative measure of flexibility – persistence length. The persistence length is defined as the length over which a polymer acts as a rigid rod.[97] In the case of DNA, hybridization to its complementary strand dramatically changes the characteristic persistence length: 1 nm for single-stranded DNA[98] and 50 nm for double-stranded DNA.[99] Although single-stranded DNA anchored to the surface of a densely functionalized particle would certainly be more oriented than the persistence length implies (as a result of the polymer brush effect described above[83]), its flexibility would still allow for random coiling. Furthermore, the effects of this random coiling become more pronounced further from the surface, toward the sticky end, which can limit sticky end access for hybridization events.[52, 85, 100] Random coiling behavior also reduces the energetic favorability of sticky end hybridization through the introduction of a configurational entropy cost.[54, 92] Thus, the incorporation of a limited double-stranded region in the DNA ligand promotes greater ligand orientation and, therefore, improves the accessibility of sticky ends for hybridization events.

1.3 Crystal Symmetry and Habit Engineering with DNA

Researchers have utilized the "genetic code" for crystal engineering to realize superlattices with a high degree of order. In this section, we discuss how the arrangement and sequence of DNA

on the particle core can be controlled to access dozens of unique symmetries and multiple crystal habits (Figures 3 and 4). Each lesson in this section explores a distinct strategy to modify the symmetry of how particles interact and the resultant implications for the formation of defined, macroscopic structures. Early work focused on how to tune chemical complementarity with spherical particle cores, given the accessibility of this particle shape and the ease of DNA modification. As syntheses for anisotropic particles improved in uniformity and yield, this opened up a library of new building blocks, whose shape could be used to break the radial symmetry of spherical cores and introduce directional interactions. Selective functionalization of the aforementioned cores, or new cores with chemically-distinct binding sites, can be used to localize interactions to specific sites or regions of a particle. Surfaces encoded with DNA can be used as a template that further prescribes crystallization behavior and enables control of crystal position and orientation. Together, these four lessons enable symmetry and habit engineering with DNA.

1.3.1 Lesson 5: Crystal symmetry and habit are controlled by the competition between maximization of hybridization events and minimization of repulsion between building blocks.

Self-assembly, the spontaneous and reversible ordering of disordered components in a system, requires a balance between competing repulsive and attractive interactions.[65, 101] *Lesson 1* teaches that DNA-mediated assembly introduces an attractive enthalpic interaction through the hybridization of complementary sticky ends. As building blocks dynamically sample their environment, the most thermodynamically favorable position and orientation is most often the one that allows for the maximization of these hybridization events.[9, 102, 103] This hypothesis, first put forth by the Complementary Contact Model (CCM)[9] and, later, by several subsequent models,[76,

[102-106] enables prediction of the most stable crystal symmetry that a particular building block can adopt upon crystallization. Specifically, the CCM describes how the sticky end sequence, size, and molar ratio between building blocks, and the relative number of sticky ends per building block (often referred to as the "linker ratio") may all modulate sticky end availability, and thus impact crystal symmetry (Figure 3a).[9] The CCM predicts the most stable structure as the one that maximizes complementary interactions, thereby allowing for crystal symmetry design rules based upon simple geometric arguments.

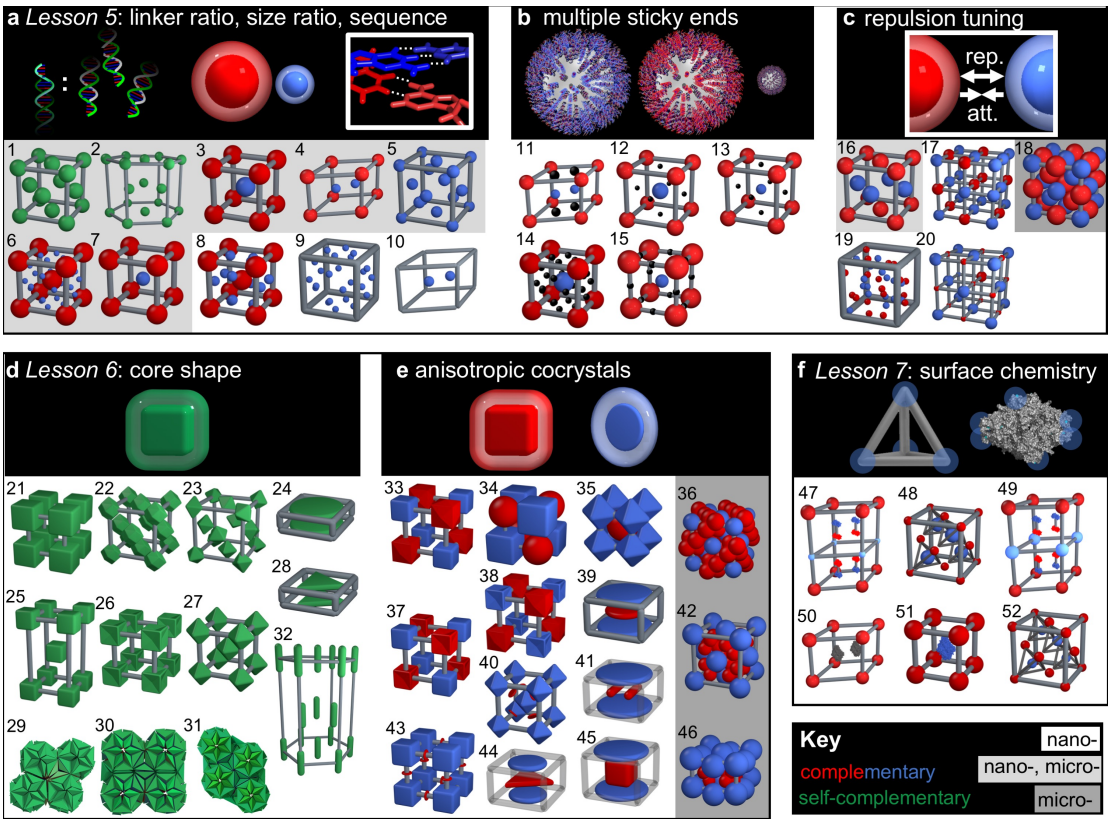

Figure 3. Crystal engineering with DNA allows access to over 50 unique symmetries by modulation of: a the linker ratio, size ratio, sticky end sequence, b number of sticky ends, and c repulsion between building blocks (Lesson 5); d & e the core shape (Lesson 6); and f the core surface chemistry (Lesson 7). Key: Green particles indicate self-complementary sticky ends. Dark red particles have sticky ends complementary to dark blue particle and, in **f**, light red particles have sticky ends complimentary to light blue particles. White and grey shadings indicate the size of building block which has accessed a particular symmetry. Transparent unit cells in (41), (44), and (45) indicate plastic crystals where the red particles have in-plane rotational freedom. Numbers 1-52 indicate unique crystal symmetries: face-centered cubic (1)[2, 3], hexagonal close-packed (2)[9], body-centered cubic (3)[2, 3], AB_2 (4)[9], NaTl (5)[14], Cs_6C_{60} (6)[9], CsCl (7)[9], Cr_3Si (8)[9], lattice X (9)[17], graphite-like (10)[17], AB_4 (11)[18], face perovskite (12)[18], A_2B_3 (13)[18], ABC_{12} (14)[18], edge perovskite (15)[18], NaTl (16)[19], simple cubic (17)[9], CuAu (18)[20], Th_3P_4 (19)[21], NaCl (20)[9], simple cubic with cubes (21)[8], face-centered cubic with rhombic dodecahedra (22)[22], plastic face-centered cubic with octahedra (23)[2, 8], 1D lattice with disks (24)[9, 23], body-centered tetragonal with cubes (25)[8, 24], simple cubic with concave cubes (26)[25], body-centered cubic with octahedra (27)[22], 1D lattice with triangular prisms (28)[22], clathrate II with trigonal bipyramids (29)[26], clathrate I with trigonal bipyramids (30)[26], clathrate IV with trigonal bipyramids (31)[26], simple cubic co-crystal with cubes and convex cubes (33)[25], simple cubic co-crystal with cubes and spheres (34)[27], body-centered cubic co-crystal with octahedron and spheres (35)[27], $MgCl_2$ co-crystal with spheres and tetrahedral sphere clusters (36)[10], simple cubic co-crystal with cubes and concave cubes (37)[25], simple cubic co-crystal with concave and convex cubes (38)[25], 1D co-crystal with two differently sized disks (39)[23], body-centered cubic co-crystal with disks in interstitial spaces between octahedra (40)[25], 1D co-crystal with alternating disks and rods (41)[23], AB_8 co-crystal with spheres and tetrahedral clusters (42)[10], simple cubic co-crystals with disks in interstitial spaces between cubes (43)[25], 1D co-crystal with disks and triangular prisms (44)[23], 1D co-crystal with disks and cubes (45)[25], AB_4 co-crystal with spheres and tetrahedral clusters (46)[10], hexagonal layered structure with Janus protein particles (47)[28], zinc blende with DNA origami cages (48)[15], hexagonal layered structure with Janus protein particles (49)[28], AB_2-like structure with proteins (50)[29], body-centered cubic-like structure with proteins (51)[30], and diamond with DNA origami cages (52)[15].

Experimental work with micro- and nanoparticle cores validates many of the predictions made by the CCM and other models. Single component systems with self-complementary sticky ends crystallize into close-packed, face-centered cubic (FCC) arrangements, similar to entropy-driven systems.[2, 3, 93, 107] In multicomponent systems, two or more types of building blocks may be designed with sticky end sequences complementary to *other* building blocks, but not to *like* building blocks.[2, 3, 93] To understand this concept, first consider the consequences of this design for systems with a nanoparticle core. In the simplest case, two similar types of building blocks (size ratio = 1, linker ratio = 1), but with complementary sticky ends, crystallize with a body-centered cubic (BCC) symmetry.[2, 3, 9, 93] This phase exists over a gradient of sizes and linker ratios before transitioning to lower symmetries at extreme differences between particles. For example, for a fixed size ratio of 0.6, an increase in the linker ratio from 0.1 to 1 to 2.5 will result in a transition from CsCl-like (similar to BCC but with a size ratio less than one) to AB_2 (isostructural with AlB_2, a hexagonal lattice where the dimensions $a = b \neq c$) to AB_3 (isostructural with Cr_3Si) symmetries.[9] Similarly, for a fixed linker ratio of 2.5, if the size ratio is further decreased from 0.6 to 0.3, the Cr_3Si lattice transitions to an AB_6 symmetry (isostructural with Cs_6C_{60}).[9]

One may expect deviations in behavior as the sizes of the particle cores increase from the nano- to microscale. However, similar size ratios lead to analogous symmetry outcomes across both length scales, which suggests a packing efficiency explanation. Building blocks with microparticle cores predictably transition from CsCl-like to AB_2 and AB_6 lattices as the size ratio decreases from 1 to 0.3.[93] However, relative sticky end coverage (*i.e.* linker ratio), does not enable the same degree of symmetry engineering for larger building blocks.[20, 93] To understand this difference, it is helpful to consider how the building block radius of curvature impacts the number

of oligonucleotides engaged in each interparticle interaction. For a nanoparticle, there are a smaller absolute number of oligonucleotides per particle and fewer involved in each collective DNA bond (relative to a microparticle). As a result, changes in the number of linkers represent a more significant fraction of the total interaction and would be expected to have a greater impact on crystallization kinetics and thermodynamics. Furthermore, because the display and conformation of individual oligonucleotides are influenced by the underlying particle core, the smaller radius of curvature leads to more dramatic changes in sticky end availability.

Importantly, for both micro- and nanoparticle cores, while purely entropy-driven assembly may favor phase segregation between dissimilar components, crystal engineering with DNA *specifies* their interaction.[108-110] The specificity of this system has enabled two-component systems of highly symmetric, spherical building blocks to access nearly a dozen unique crystal symmetries with predictable phase boundaries based on size and linker ratios alone.[9, 93] With synthetic strategies to crosslink DNA ligands at the particle surface and subsequently remove the particle core, additional symmetries may be accessed.[17]

Crystal engineering with DNA need not be limited to two-component systems: a single building block may be designed with multiple distinct sticky ends to engage in unique, simultaneous interactions (Figure 3b).[9, 111] For example, a two-component "parent" lattice can "host" a third "daughter" building block at predictable positions as long as the DNA shell is of the appropriate size to accommodate intercalation.[18] This strategy enables access to several superlattices with complex binary and ternary symmetries, some of which do not have natural analogs (no mineral equivalent).[18]

Crystallization behavior can be further tuned by exploiting the molecular properties of DNA as a polyanionic polymer (Figure 3c). These characteristics introduce enthalpically- and entropically-driven repulsive forces between DNA ligands on a single particle, which can cause deviations from the CCM predictions. Enthalpic repulsion arises from the unfavorable electrostatic interaction between the negatively charged phosphate backbone of adjacent DNA ligands. The effects of this type of repulsion may be modulated through DNA length, building block radius of curvature, and the introduction of screening species (*e.g.* salts). Entropic repulsion results from excluded volume effects, which reflect the ligand's configurational entropy. *Lessons 3* and *4* of the first section teach that this configurational entropy may be reduced through an increase in DNA functionalization density or a reduction in DNA length or flexibility.

The intentional tuning of repulsion between DNA ligands results in interesting consequences for symmetry engineering, particularly at the phase boundaries between the above-mentioned symmetries.[106, 107] For example, two-component nanoparticle systems can deviate from the expected CsCl-type symmetry to form a Th_3P_4 symmetry. This example highlights that lower symmetry structures may be accessed if predominantly repulsive DNA ligand interactions are used to increase separation between *like* building blocks.[19, 21, 111-113] Conversely, the repulsion between *like* building blocks may be reduced through the introduction of a second sticky end which creates an enthalpically favorable interaction. This design has been shown to lead to higher fill-fraction structures like AuCu (analogous to an FCC lattice), NaCl and, intriguingly, NaTl, a symmetry that contains two interpenetrating diamond lattices.[9, 14, 19, 20, 111] The surprising formation of the NaTl lattice in both nanoparticle and microparticle systems, where models predict a CsCl-type lattice should form, emphasizes the necessity to explicitly consider DNA as a polyanionic ligand.[14, 19] For

a more quantitative discussion of these repulsive interactions, we refer readers to a recently developed model.[113]

The ability to control the crystal symmetry enables the possibility to engineer macroscopic structural features, such as crystal habit. In classical atomic crystallization, the Gibbs-Curie-Wulff theorem teaches that equilibrium crystals will be bound by their lowest surface energy facets.[114] Facet surface energy, as approximated by a broken-bond model, will be inversely proportional to the density of constituent atoms within a facet plane.[115] Thus, symmetry will dictate the densest packed plane, and in turn, crystal habit (Figure 4). These lessons from atomic crystallization translate to DNA-mediated particle crystallization and have been used to experimentally realize well-defined habits. For two-component, spherical nanoparticle systems with a size ratio of ~1 and a body-centered cubic (BCC) symmetry, the densest packed family of planes is the {110} (Figure 4a). Indeed, slow cooling of these systems (as described in Section 1, *Lesson 2*) results in a rhombic dodecahedron crystal habit - a structure fully enclosed by {110} facets.

Despite access to more than a dozen unique crystal symmetries, spherical building blocks have yet to be used to access many, unique crystal habits. This limitation has been attributed to the high rotational symmetry of spherical building blocks.[1, 6] Without directional interactions to constrain particle orientation and create significant differences in surface energy between crystalline planes, there is insufficient preference to form a single crystal habit. For example, single-component, face-centered cubic systems produce a mixture of habits and twin plane defects, as is observed in atomic systems of the same symmetry.[1] Alternatively, these limitations may be experimental in nature, attributable to imperfect building blocks, which leads to defect formation

and a loss of long-range translational symmetry, or insufficiently controlled crystallization conditions, which introduces fluctuations greater than the surface energy differences.

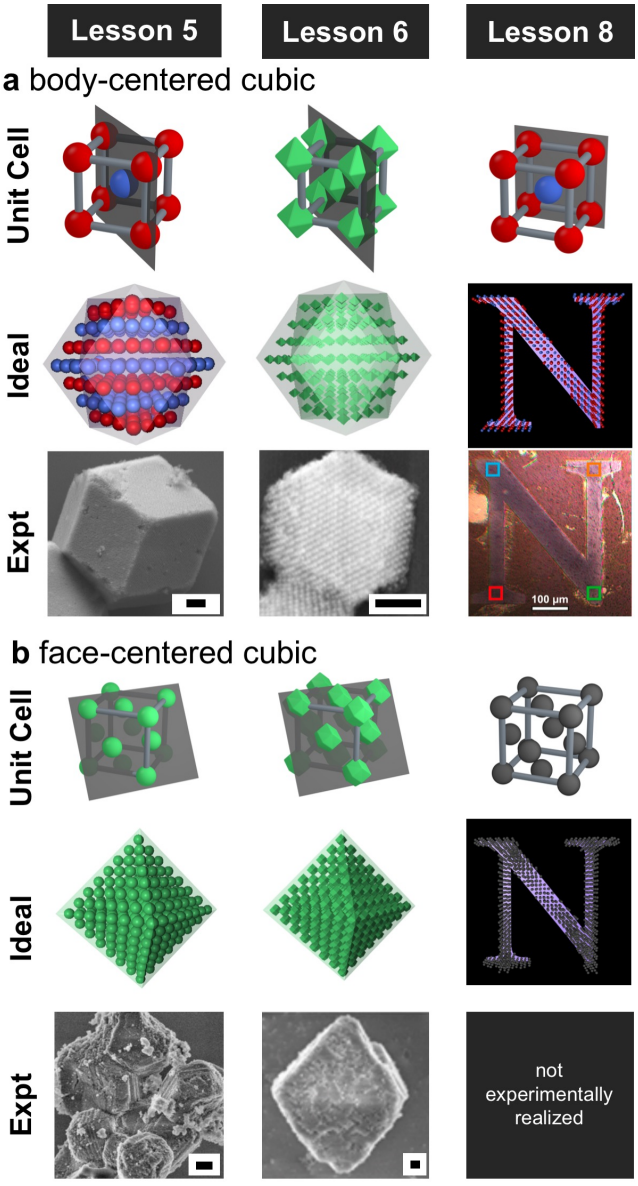

Figure 4. Each Lesson reveals a set of strategies for symmetry engineering that can produce several distinct crystal habits. **a** Spherical building blocks with complementary sticky ends[1] and octahedral building blocks with self-complementary sticky ends[6] access a body-centered cubic symmetry and, as a result, a rhombic dodecahedron crystal habit bound by {110} facets indicated in the unit cell. Heterogeneous nucleation onto a lithographically-defined pattern of an arbitrary shape (e.g. "N") comprised of a lattice of DNA-functionalized posts (e.g. designed to match the {100} plane indicated in the unit cell) can be used to grow a superlattice of the same symmetry into a pre-defined pattern.[11] **b** Spherical[1] and rhombic dodecahedral[6] building blocks with self-complementary DNA access a face-centered cubic symmetry. Experimentally, this symmetry results in crystals bound by {111} planes (indicated in the unit cells) which ideally lead to an octahedron crystal habit. For the case of spherical building blocks, single crystal growth is prevented by the formation of twinned planes and defects. An FCC symmetry has not yet been realized on a lithographically-defined surface. Images reprinted with permission of reference [1].

One approach to overcome these limitations and realize lower symmetry single crystals with spherical building blocks proposes three key design principles: 1) crystallization into a non-cubic unit cell; 2) strong preference for a single structure (to minimize defect formation); and 3) sufficient differences in facet growth rates to manifest in a well-defined habit. Non-cubic unit cells can possess families of planes where the constituent planes are not energetically equivalent. Since planes of the same family have symmetry with respect to each other, differences in growth rates may manifest and produce a kinetically-favored crystal habit. Recent efforts that satisfy these principles show that a two-component system with AB_2 symmetry yields an anisotropic crystal habit due to a barrier to nucleation on one facet within a family of planes. Despite the equilibrium preference for crystals bound by the lowest surface energy planes, this system produces a hexagonal prism-shaped crystal habit where the rectangular faces are bound by the highest surface energy facet ($(10\bar{1}0)$) due to a large barrier to nucleation onto this surface, thus favoring growth along a single direction. The next lesson explores another strategy that enables access to additional crystal habits: the use of polyhedral, anisotropic particle cores.

1.3.2 Lesson 6: Particle core shape introduces collective, directional interactions between building blocks, analogous to the defined coordination geometry of a metal-ligand complex.

Lesson 3 teaches that the dense functionalization of DNA onto a particle can induce collective DNA orientation relative to the particle surface due to the polymer brush effect (Figure 5a).[116] When the atomically flat facets of polyhedral anisotropic particle cores are densely functionalized, this introduces collective, directional DNA orientations along each facet. Each

facet is thus capable of forming a collective DNA "bond," analogous to coordination geometry in atomic systems.[22, 27, 116, 117] Based on this concept, a cube should be able to form six potential directional bonds, one along each of its six facets, analogous to a transition metal with an octahedral coordination environment. Upon crystallization, these collective DNA interactions should drive the formation of a simple cubic symmetry, where each cube orients to align its square facets with its neighbors, since this configuration maximizes the number of DNA interactions (Figure 3d).[22, 25, 27] Experiments show that interactions along crystallographically-defined facets are thermodynamically and kinetically favored due to the greater number of DNA interactions that can form, the high local concentration of DNA sticky ends available, and the potentially reduced conformational stresses associated with interactions between flat surfaces relative to interactions between curved surfaces.[22, 25, 116] As the symmetry of the particle core decreases, this valency and bond directionality allows for more complex interactions, which simulations predict to result in more exotic symmetries.[118]

Experimental realization of valency-based approaches to control crystal symmetry rely upon the availability of suitable chemical syntheses. Particles must be made with sufficient uniformity in size and shape (including faceting, corner truncation, and corner rounding), as to minimize defects that inhibit crystal formation.[7, 52, 116] This stringent requirement necessitated advances in particle synthesis to expand the library of building blocks that can be used.[12, 119-124] These successes provide a glimpse of what may be possible with new, lower symmetry cores. For example, a trigonal bipyramid nanoparticle core is similar to a cube in the number of equivalent facets (six) and thus the number of predicted directional interactions. However, these interactions occur at different angles. This difference leads to a significant loss of symmetry operators and

drives the formation of a set of complex clathrate structures with more than twenty building blocks in a single unit cell.[26] Alternatively, low symmetry microparticle building blocks can be made from the controlled association of four spherical microparticles into a tetrahedral cluster core. This unique cluster can be crystallized with complementary spherical building blocks into a $MgCu_2$ superlattice, which contains interpenetrating diamond and pyrochlore lattices.[10, 26]

If the particle core possesses more than one type of structurally-defined region on its surface (*e.g.* exposed surface facet, area of curvature), the resultant directional interactions can compete. If a similar DNA density could be achieved in each region, one would hypothesize that the larger surface area regions would dictate crystallization behavior. Indeed, for effectively "two-dimensional" plate-like particles (*e.g.* triangular prisms, circular disks), the larger surface area interactions drive the formation of one-dimensional lattices.[22, 23, 116] Interestingly, due to the large disparity in interaction strength between the face and side interactions, minimal order is seen between one-dimensional lattices. One would hypothesize that if synthetic advances enabled independent control over each dimension for a triangular prism building block, the relative strength of these interactions could be tuned to enable graphite-like structures, with hexagonal symmetry within planes driven by side interactions and one-dimensional, lamellar symmetry between planes driven by face interactions.

The ability to use core shape to dictate symmetry requires a consideration of DNA design. As the DNA flexibility increases (*e.g.* through an increase in length), the free volume available for ligands to explore increases, and their collective orientation decreases (*Lesson 4*). The length of DNA ligands relative to the characteristic length of the particle thus forms the basis for a "zone of anisotropy," where the anisotropy of the underlying particle core drives the crystallization

behavior. Experiments show that outside of this zone of anisotropy, when the length of DNA greatly exceeds that of the particle core dimensions, anisotropic building blocks can lose their "valency".[8] In this phase space, superlattices retain positional order, but relinquish particle orientational order such that self-complementary building blocks assemble into a FCC symmetry regardless of core particle shape.[8] Interestingly, phases with intermediate symmetry may exist within this transition, dictated by an interplay between the directional interactions described in this *Lesson* and the DNA repulsion interactions described in *Lesson 5*. For example, as the length of DNA increases for cube building blocks, the six-fold symmetry of the cube is broken to form a body-centered tetragonal lattice, where face-to-face overlap is preserved in one plane and broken in another. This finding highlights the importance of exploring structures at the boundary of existing phase diagrams.

The specificity of DNA-based interactions introduces a chemical complementarity that favors the co-crystallization of specified building blocks (Figure 3e) instead of phase separation or alloy formation. Whether two sets of anisotropic building blocks will co-crystallize into an ordered structure depends on their structural complementarity to each other, including the dimensional similarity and the packing efficiency of their interacting facets.[25, 27] The stringent chemical and structural complementarity requirements for co-crystallization are difficult to experimentally realize via other assembly approaches, and thus a DNA-based approach is uniquely positioned to probe this design space and construct novel co-crystals. To understand this concept, first consider the interaction of two types of similarly sized cubes with systematically controlled surface concavity or convexity. For building blocks with a high degree of structural complementarity, such as a concave cube and convex cube, the "lock and key" nature of their

interactions results in highly ordered crystals with a lower defect density and larger grain size compared to building blocks with a low degree of structural complementarity, such as a cube and convex cube. However, these structures only require consideration of a single type of interaction between particles (*e.g.* the concave and convex features of the cubes).

If instead, a building block with two types of interactions (*e.g.* a disk) is co-crystallized with a building block only capable of one type of interaction (*e.g.* a cube), an interesting phase behavior occurs. Disks impose two strong directional interactions 180° from each other along their circular facets and a weaker interaction along the cylindrical side walls.[22, 116] The ratio of the disk and cube dimensions can modulate whether certain interactions are possible to form unusual structures. If the disk diameter (D) is larger than the cube edge length (L), 1D structures are favored since only two disks may interact with each cube at opposite facets. In these structures, the positional orientation of the cube does not carry through to subsequent layers. If D is smaller than L, the resulting symmetry is analogous to a simple cubic symmetry with respect to the cube building blocks, but with disks intercalated between and parallel to each face-to-face interaction.[25] An analogous relationship has been shown for octahedron-disk co-crystals, where a BCC lattice of octahedra with intercalated disks forms when $D < L$.[25] Building on this work, co-crystals formed from disks and rods similarly show a 1D lattice of alternating rods and disks, but with an interesting deviation. Despite the lack of chemically complementary interactions, two rods assemble side-by-side in each layer. This side-by-side orientation enables both rods to hybridize along their full lengths to the disks above and below, and importantly, imparts greater rigidity between layers than a single particle would, to enable 1D lattice formation.[23]

Directional interactions imparted by anisotropic building blocks enable control of macroscopic crystal habit (Figure 4a and 4b). The thermodynamic preference for face-to-face interactions, and the associated energetic penalty for rotational deviations, can lead to greater surface energy differences between competing crystallographic planes (as compared to analogous spherical systems). These greater energetic differences can minimize defect formation due to competition between structures and thus lead to well-defined habits. To illustrate this concept, building blocks with a rhombic dodecahedron core crystallize with a FCC symmetry, with a {111} closest-packed plane, and form single crystals with an octahedral habit, bound by {111} facets (Figure 4b). Interestingly, this symmetry did not result in uniform crystal habits for spherical building blocks due to competition between hexagonal close-packed (HCP) and FCC lattices, similar to the analogous atomic systems, and the formation of twinning defects.[6] This approach has also been used with other nanoparticle core shapes: octahedron building blocks crystallize with BCC symmetry, with a {110}-closest packed plane, and form a rhombic dodecahedron crystal habit, bound by {110} facets similar to BCC spherical systems (Figure 4a); and cube building blocks crystallize with simple cubic symmetry, with a {100}-closest packed plane, and form a cube crystal habit, bound by {100} facets. To expand the number of crystal habits that can be accessed via this valency-based approach requires syntheses that produce highly uniform, low symmetry particle cores and, if necessary, chemistries that enable these cores to be densely functionalized with DNA.[118]

1.3.3 Lesson 7: Chemical anisotropy on the particle surface enables building blocks to engage in unique, spatially separated interactions.

While building blocks with anisotropic cores break symmetry by the physical localization and orientation of DNA, an intriguing alternative is to chemically localize DNA in specific areas (Figure 5b). Strategies to produce chemically anisotropic building blocks typically follow one of two approaches: those that act at the particle surface and those that act at the DNA shell surface. Early approaches to develop chemical anisotropy relied on small-scale techniques, such as lithography and partial steric blocking of surfaces.[125] This section will focus on more recent solution-phase syntheses that can result in the higher throughputs necessary for the assembly of building blocks into large, 3D materials as opposed to discrete clusters.

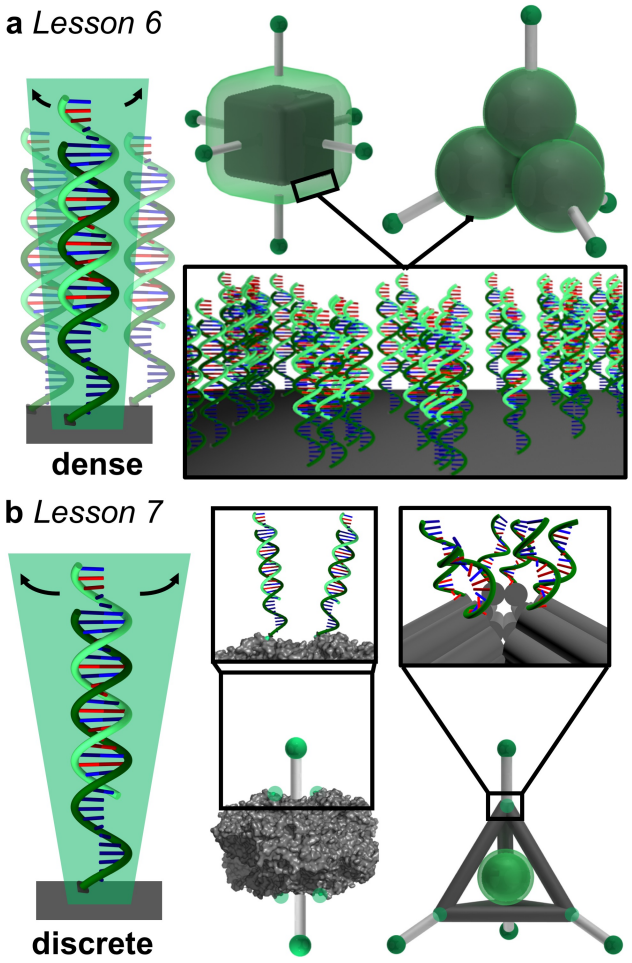

Figure 5. Building block anisotropy can be achieved with collective or discrete DNA interactions. a Dense functionalization of nano- and microparticle surfaces leads to anisotropy through collective orientation of DNA ligands relative to the particle surface, induced by steric and electrostatic interactions with neighboring ligands. Cube[8] and tetrahedral cluster[10] cores exemplify this strategy. **b** Discrete functionalization leads to anisotropy through localization of individual DNA ligands in precise locations on the particle surface. A protein[13] and DNA origami cage[15] both act as molecularly pure cores, where specific sites may be modified with DNA ligands. The lack of adjacent strands allows for each DNA ligand to access a greater free volume. Protein renderings created using The PyMOL Molecular Graphics System, Version 1.8 Schrödinger, LLC.[16]

Particles with chemically anisotropic surfaces, sometimes referred to as "patchy particles," can have highly symmetric particle cores, but asymmetric surface chemistries.[126] Controlled synthesis of patchy particles with tunable patch size and number emerged from the microparticle community due to the availability of chemistries which direct the formation of microparticle

clusters with 2-7 particles in regular, predictable arrangements.[123, 127] Subsequently, these clusters may be encapsulated by overgrowth with different amounts of another polymer precursor to expose regions of the underlying clusters with tunable surface area on the particle surface.[123, 126, 127] DNA can then be modified to possess unique anchoring moieties that preferentially react with the functional groups present at particular surface sites. Through this approach, one can generate asymmetrically functionalized "patchy particles" comprised of one or more unique DNA sequences, dependent on the number of orthogonal surface chemistries.[127, 128] To date, the assembly of these types of building blocks has resulted in discrete clusters, but simulations suggest that the potential remains for their crystallization into unique, long-range structures, including non-close packed symmetries such as the diamond lattice.[127-133]

At the nanoscale, access to uniform, synthetic patchy particles remains a challenge for inorganic cores, despite recent high-throughput strategies for the synthesis of multicomponent nanoparticles.[134-137] One strategy to overcome this challenge, and a major future direction of this field, is the development of molecularly pure particle cores with chemically discrete surface sites, produced via chemical methods (*e.g.* fullerenes)[138] or via biological systems (*e.g.* proteins).[30] For proteins, the amino acid sequence and tertiary structure dictate the location and surface accessibility of reactive functional groups. With the appropriate DNA modifications, these exposed surface sites can react to precisely place DNA (Figure 5b). The position of these surface sites may be deliberately modified through common biotechnology strategies that alter the sequence of amino acids, such as site-specific mutagenesis. This approach has enabled two distinct DNA ligands to be attached at specific surface locations, which has enabled a unique strategy to control crystal symmetry (Figure 3f).[13, 29, 139] When isotropically functionalized with a single type

of DNA ligand, protein-core building blocks typically crystallize with predictable symmetries analogous to spherical building blocks.[14, 30] However, when the DNA is restricted to a limited number of asymmetrically distributed surface sites, this breaks the symmetry of the building block and results in hexagonal lattices.[29]

If separate proteins functionalized with distinct sticky ends could be connected, one can imagine building blocks with multiple, discrete, and chemically distinct sites. Since proteins may contain two orthogonal types of functionalization sites based on their surface residues, one approach is to attach two types of DNA ligands with different sequences to the protein surface. One ligand forms a bond between two proteins and the other ligands provide sticky ends for crystallization. This approach yields a Janus-type particle where each half of the building block contains different, spatially restricted sticky end sequences. When crystallized with spherical building blocks these broken symmetry particles direct the formation of a hexagonal structure where the nature of each layer (*e.g.* core size, composition, etc.) and the distance between layers can be independently tuned (Figure 3f).[28]

Symmetry breaking at the DNA shell surface relies on the ability to tune the specificity and strength of interactions with Watson-Crick base pairing. One possibility is to use a "lift off" approach to transfer assembly instructions to particular regions of the building block, either to the particle core or the DNA shell. This requires the design of DNA "linker" strands that have a weaker interaction with the DNA shell of one building block relative to another.[140-144] If pre-hybridized to the building block with a weaker interaction, the thermal preference for DNA strands to engage in the greatest number of hydrogen bonding events allows the transfer of strands from the shell with the weaker interaction to the shell with the stronger interaction at the place of contact. Similarly,

instead of a Watson-Crick induced thermal preference, the DNA strands may have a reactive moiety which covalently interacts with the particle core at the point of contact in order to favor transfer.[143, 145] To date these approaches have resulted in the localization of sticky ends to a single discrete region which precludes the formation of extended crystalline structures. However, if extended to multiple, discrete sites, nanoscale building blocks with inorganic cores may be able to access lower symmetry structures.

An alternative approach to DNA shell modification pioneered by Gang *et al*. borrows from the structural DNA nanotechnology community and builds a DNA cage around a building block (Figure 5b). The result is another molecularly pure structure where discrete sticky ends may be placed at arbitrarily designed points on the DNA cage.[15, 43, 146, 147] The cage can hold the building block in place through a second set of single stranded regions which are complementary to the sticky ends of the building block. Importantly, these structures have provided access to a number of different crystal symmetries using spherical particle cores, including a low packing-fraction symmetry, the diamond lattice, and other close-packed structures (Figure 3f). Diamond lattices have been challenging to realize via assembly strategies that utilize isotropic building blocks due to their stringent requirement for highly-oriented tetrahedral interactions and the number of energetically similar symmetries that compete with its formation. A truncated tetrahedron-shaped DNA origami framework satisfied these requirements through the placement of DNA ligands at tetrahedral sites and, more subtly, through control over the degree of truncation.[15] For particular degrees of truncation relative to the size of the complementary building block, an energetic barrier prevents the formation of other similar phases due to higher rotational entropy for the DNA frameworks in the cubic diamond symmetry. This approach enables perfection out of imperfection:

the inherent inhomogeneities of the particles can be overcome through encapsulation in DNA frameworks to enable the building blocks to behave as if they were molecularly pure. Alternatively, the frameworks need not contain a particle core and may act instead as a molecularly pure linker between building blocks.[146] In principle, this strategy may be applied to achieve a number of other synthetically challenging symmetries that require stringent bond directionality for length scales over which double-stranded DNA is sufficiently rigid to impart directionality (*i.e.* up to the persistence length of double-stranded DNA or bundles of double-stranded DNA).[148, 149]

Although chemically anisotropic building blocks have yet to result in well-defined crystal habits, their ability to access new and lower symmetries may enable access to unique habits not attainable via other approaches. However, the challenge remains to engineer these systems with the requisite uniformity, low defect density, lack of competing symmetries, and preference for particular surface facets to realize a uniform crystal habit. Molecularly pure building blocks, such as proteins and DNA frameworks, represent a promising avenue to overcome these challenges.

1.3.4 Lesson 8: Templates can be used to impose spatial restrictions on the orientation and location of DNA hybridization events

Structural information can be encoded onto a template in the form of molecular or nanomaterial species and used to direct growth. In the context of colloidal crystallization with DNA, templated structural information is most often encoded onto substrates via top-down patterning approaches or onto molecular frameworks via structural DNA nanotechnology. These templates can then be used to define specific locations for particles to connect in order to form one-, two-, and three-dimensional extended lattices. Based on the spacing, symmetry, and shape

of these templated binding sites, this approach can be used to program crystallographic parameters of the lattice and orient the resulting crystals with respect to particular facets.

Early efforts in this space explored the possibility of assembly on uniformly DNA-functionalized substrates.[150-152] Two primary challenges prevented the realization of crystalline lattices: heterogeneous nucleation onto substrates occurred at multiple spots across the large surface area, which limited the grain size, and the strength of interactions between building blocks and between building blocks and the surface (analogous to early solution-phase assemblies). Lithography and top-down printing techniques provided a means to confine building blocks to specific locations through spatially-defined surface functionalization or transfer of building blocks from a patterned surface.[150, 153-156] Through exposure to alternating layers of building blocks with complementary DNA, assemblies could then be grown in a layer-by-layer fashion on these templates. With the incorporation of thermal strategies to increase order, borrowed from solution-phase assemblies (*Lesson 2*), crystals could be formed on substrates, but remained polycrystalline with domain sizes on the order of microns.[157, 158] Unfortunately, not all lessons could be effectively translated, such as the slow cooling procedure from high to low temperature through the T_m. Due to the favorability of particle-particle interactions over particle-surface interactions, attempted crystallization via slow cooling in the presence of a surface preferentially occurs via homogeneous nucleation in solution, rather than via heterogeneous nucleation onto a substrate. If a pre-formed assembly is thermally treated via slow cooling, delamination from the surface occurs.

A key advance in the improvement of order drew from observations in the atomic layer deposition field: lattice mismatch between the first monolayer and the substrate propagated into subsequent layers to inhibit single crystal growth.[159] Epitaxial growth, in contrast, favored the

formation of ordered crystals with few or no grain boundaries. To achieve analogous epitaxial growth, one must program the location of DNA strands on the surface into a pattern that matches a crystallographic plane of the intended lattice with precise lattice parameters. Recent efforts successfully incorporated lithographically patterned patches of DNA that directly match the expected interparticle spacing for their building block system.[160] In principle, this approach can use the symmetry, spacing, and shape of the templated sites to program lattice symmetry, crystallographic plane, lattice parameters, lattice dimensionality, and particle orientation within the lattice. The result is the ability to assemble at least ten layers of building blocks into single crystalline lattices up to nearly 1 cm^2 in area. Interestingly, this also opens up the possibility to define an arbitrary crystal habit, as defined by the surface pattern.[11] Consequently, this approach can effectively decouple the crystal symmetry from the crystal habit, and thereby provide access to habits, some realized and some hypothesized, not achievable via solution-based approaches. Furthermore, each crystal habit formed via this approach can have a precisely-defined number of particles (as compared to the heterogeneity present in homogeneously nucleated crystals) and a regular orientation with respect to a surface (as compared to the random orientation of solution-suspended lattices).

Templates can also be used to spatially localize building blocks into crystalline arrangements without the use of interparticle interactions. Two primary strategies provide this control: lithographically-defined pores and sheets of DNA formed from DNA structural nanotechnology, both of which may present sticky ends at regularly spaced intervals greater than the size of the building block.[161-164] The interaction of a single building block with either surface at pre-defined

locations produces 2D and 3D crystals arranged into any symmetry and spacing that may be patterned.

Lithography can be used to define a template with regularly spaced pores that may be selectively functionalized with DNA.[163-165] The confinement of particle assembly within pores, affords two additional levels of control: pore shape can create a preference for building block orientation and pore thickness can facilitate the vertical growth of multiple layers of building blocks with complementary sticky ends. Unlike solution-based crystallization, or the previously described surface assembly strategies that require structurally and chemically complementary building blocks, template-confined assembly enables arbitrary building blocks to be added in each layer. However, the incorporation of anisotropic cores and the removal of in-plane interparticle interactions requires additional considerations for DNA sticky end design. Due to the pre-orientation of DNA ligands on flat facets (*Lesson 6*), sticky ends attached to anisotropic cores are more likely to engage in non-specific, non-canonical Watson-Crick base pairing.[166] Further, confined assemblies lack the increased thermal stability afforded by hybridization within an extended lattice, and can suffer from surface delamination as each new layer is introduced.[11] Recent work addressed both of these challenges through the use of Locked Nucleic Acids (LNAs) in the sticky ends.[164] In this context, LNAs simultaneously increase the thermal preference for Watson-Crick interactions and the T_m for each interaction. The result of this design is the ability to controllably arrange up to three different shapes of particles into regularly-arranged 1D lattices in high yield.[164] Thus, template-confined assembly enables independent control over both the in-plane spacing (determined by the lithographically patterned template) and the out-of-plane spacing

(determined by the DNA shell) in crystals comprised of oriented particles with arbitrary size, composition, and shape on a surface.

In place of lithography, one can construct a template entirely comprised of complementary DNA strands which may arrange into tiles, sheets, and/or 3D structures. Although in recent years the resolution of lithographic techniques has approached tens of nanometers or, in some cases, even several nanometers, the use of DNA templates, in principle, enables the placement of building blocks with greater precision – on the order of a few nanometers.[167] To successfully form such scaffolds requires sequence design with a significant energetic preference for the formation of a single template structure and sufficient rigidity to control particle position.[38, 43] These considerations initially led to the design of DNA "tiles" comprised of double crossover (DX) motifs in which one strand has, for example, an eight-base region of complementarity with two different strands in two different regions to produce a crossover formation with four double-stranded segments.[43] This design requires minimization of the complementarity between regions outsides of the DX motif (*e.g.* stretches of less than five bases). These tiles may be subsequently linked via additional DNA hybridization to form an extended, periodic 1D or 2D template that can display short single-stranded DNA overhangs in regular locations.[43, 168] Overhanging sequences may subsequently hybridize to and localize building blocks to produce 1D or 2D lattices with symmetry and interparticle spacing dictated by the template.[161] Since tiles may be designed to contain different overhang sequences, DNA-based templates can guide the crystallization of multiple, unique building blocks.[162, 169]

When structural DNA nanotechnology units remain discrete they can act as templates for 3D crystals. This requires the display of DNA overhangs in multiple directions. In one approach, tiles

similar to those described above can be designed to present DNA overhangs on both sides of the tile to direct the formation of an alternating 1D lattice of building blocks and tiles.[170] One implementation of this strategy led to the formation of helical, chiral crystals comprised of nanorods oriented 45° with respect to adjacent rods.[170]

Subsequent advances in structural DNA nanotechnology, including the specific placement of flexible regions and the development of DNA origami, led to the formation of 3D DNA-based frameworks.[35, 43, 171-173] The resultant symmetry in these structures is governed by the shape of the scaffold and the location of DNA overhangs. In one iteration of this design, the scaffold may form an extended rod comprised of multiple triangular prism frameworks connected by overhangs on the top and bottom triangular faces.[168] An orthogonal set of overhangs binds to nanoparticle building blocks to localize particles within the hollow core of the framework.[168] Conversely, particles may attach to the outside of a 3D template. The combination of scaffolds formed from bundles of DNA and stochiometric control over scaffold to building block ratio reveals a strategy to access 1D arrangements of building blocks with left or right chirality and tunable periodicity dictated by the scaffold which runs through the center of the helix.[174]

Both lithographically-defined templates and templates constructed from structural DNA nanotechnology afford new opportunities to impart crystallization information in order to create low symmetry structures and ones comprised of diverse building blocks. Structural DNA nanotechnology templates access high resolution regimes limited almost exclusively by the size of the building block, but still face challenges in terms of the formation of desired template structures relative to unintended or misfolded assemblies. Lithographically-defined templates continue to

improve in terms of resolution and offer the ability to orient lattices with respect to a surface, a feature that will be particularly important in the next section.

1.3.5 Future Outlook: Pushing the boundaries of structures that can be made

Crystal engineering with DNA represents a powerful tool to discretize assembly instructions onto each building block in the form of bond directionality, valency, and specificity.[175] Unlike conventional crystal engineering strategies, the programmable nature of DNA demystifies the crystallization process, which can be distilled into teachable *Lessons*. These *Lessons* enable one to imagine a desired structure, to rationally predict the building block that will drive its formation, and to deliberately make the intended crystal. This paradigm can widely apply across building blocks with different particle core compositions, and effectively decouple material identity from structure – a grand challenge of materials by design. However, of the greater than 50 unique lattices realized with DNA, the majority have a cubic unit cell with high volume fraction and symmetry. In order to push the boundaries of accessible structures, researchers must devise strategies to impart building blocks with more complex assembly instructions.

Lesson 6 teaches that the building block core can modulate bond valency and directionality. As an extension of this *Lesson*, simulations predict that the densest packing of more anisotropic particle cores results in lower symmetry crystals than their more isotropic counterparts.[118] Experimental realization of these predicted structures, however, is limited by the availability of syntheses for highly anisotropic particles, with sufficient uniformity and yield, and the associated strategies to functionalize them with DNA. One potential strategy to further break symmetry is to explore syntheses for non-conventional materials with lower crystallographic symmetries, controllable defect structures, or ligands which enable the persistence of high energy facets.[134, 176-

[180] Alternatively, available anisotropic nanoparticles can be used as "precursors" in a multi-step synthesis that selectively removes or adds material onto particular facets or features.[181, 182] Both approaches would expand the library of available building blocks and enable a more complex interplay of DNA "bonds" to be encoded on each particle core.

Lesson 7 points to several strategies to define chemically discrete regions, including protein cores and DNA frameworks. If each of these regions could be tuned independently to present unique, specific interactions at precise locations, this would enable further complexity to be encoded into the building block. In the case of proteins, the location of amino acids with chemically addressable functional groups determines the location of DNA ligands. With multiple, distinct surface-exposed amino acids and corresponding orthogonal chemistries for DNA functionalization, protein cores could display DNA ligands with different sticky ends (discrete specificity) at spatially defined locations. To date, this approach has resulted in protein cores with multiple, spatially discrete functional sites, up to two of which can be chemically unique.[28, 29, 183] Techniques like site-specific mutagenesis and the advent of platforms that enable the introduction of non-standard amino acids could enable greater control over which amino acids a protein displays on its surface and push toward a greater number of unique sequences per protein (*i.e.* more complex crystallization instructions).[184] Similarly, DNA frameworks can introduce multiple distinct sticky ends at specified locations through careful design of the constituent framework DNA. Current experimental results show that DNA tile or framework building blocks can encode up to four chemically distinct sites.[147] In principle, it should be possible to incorporate more unique sticky ends and predictably generate a single structural outcome relative to several partially-folded

or incorrect possibilities.[185] The challenge remains to produce such complete DNA frameworks in sufficiently high yield, given the need for a unique DNA design for each new structure.[186]

The ultimate goal of crystal engineering with DNA is to encode the precise location of each building block within and at the bounds of a structure, and ultimately to combine discrete structures together into even larger architectures. Realization of this vision requires the community to combine and push beyond the lessons discussed above and to control an ever more complex set of assembly instructions. Complexity will likely originate at the individual building block level, through the incorporation of multiple, unique sequences arranged on unique cores (as described above), and through the interaction of many sets of building blocks, each carrying its own encoded instructions. To balance this sophisticated interplay and drive toward a controlled end state will likely require the development of predictive tools and simulations that can accurately capture experimental inputs and specify the necessary design criteria. The *Lessons* elucidated over the last three decades provide the foundation that guides this vision and may one day make it a reality.

1.4 Functional Consequences of Crystal Engineering with DNA

The preceding sections of this *Perspective* describe *how* to encode for the structure of a colloidal crystal using DNA. In this concluding section, we will focus on the functional consequences of this structural control, and begin to answer *why* these structures may be of use.[187] In the context of this paper, functional refers to a material with an ability to actively respond to external stimuli. A response may include a physical change in structure or the interaction with and subsequent change of an input stimulus (*e.g.* electromagnetic radiation). This section is not intended to be a comprehensive review of colloidal crystal functionality, as this has been described

elsewhere.[65, 188-193] Instead, the goal is to highlight advances in the understanding and control of functional responses in colloidal crystals engineered with DNA and to point to future opportunities accessible via this approach.

1.4.1 Functional Behavior Driven by DNA

While DNA has been described throughout this *Perspective* as a ligand with a temperature-responsive, encoded sticky end, it has the potential to respond to a more complex set of chemical and biological cues, which can induce structural changes that impact its functional behavior. In principle, the appropriate stimuli could transform DNA from a static to an *active* structure-directing ligand capable of modifying colloidal crystals *on demand*. An ideal stimulus would trigger a rapid, stable, reversible, and controllable structural response while maintaining order in the colloidal crystal.

In solution, chemical stimuli can directly interact with DNA (*e.g.* hybridization, intercalation) or indirectly influence DNA through modification of the medium (*e.g.* change in pH or dielectric constant).[111, 194-198] In response, DNA can undergo conformational changes, such as the formation of predictable folded structures (*e.g.* hairpins, i-motifs) due to intramolecular hybridization, extension or compression of the duplex, or non-specific (*e.g.* electrostatic) intramolecular or intermolecular interactions. When applied to DNA as part of a colloidal crystal, these stimuli can effect hierarchical structural responses, as a conformational change in the DNA on each individual building block can propagate throughout a crystal.[187] In principle, this can lead to changes in the lattice parameter, lattice symmetry, or particle orientation within the lattice.

One of the most useful chemical stimuli has been other nucleic acids, which are able to penetrate through a crystal to hybridize with single-stranded regions not engaged in hybridization or to displace strands with lower complementary.[111, 194, 196, 199] In particular, DNA can be designed to engage in intramolecular hybridization and the formation of a double helix that ends in an unpaired loop. This folded conformation can be located in a region that lies either within or outside of the sticky end region on a ligand. When located outside of the sticky end region, the ligand can be unfolded through addition of a short DNA complementary to the unpaired loop, to drive a local change in DNA length and macroscopic change in the lattice parameter.[194, 196, 199] Conversely, when the hairpin lies within the sticky end region, it can be used to prevent or enable interparticle interactions.[200] For example, a single building block can be grafted with two different DNA sequences, each with their own hairpin-containing sticky end that can drive the formation of a distinct crystal symmetry. Chemical stimuli (*e.g.* DNA sequences complementary to the hairpin loop) can thus be selectively added to unfold one specific set of sticky ends to modulate the building block specificity and, ultimately, the overall crystal symmetry.[196] Remarkably, lattice parameter changes are rapid (*i.e.* occur on the order of a few minutes), and both lattice parameter and symmetry changes are reversible over several cycles.

Changes in the external environment around the DNA (*e.g.* pH, solvent, counterions) can similarly affect structural changes. I-motifs are folded conformations that result from the intramolecular interaction of a long, cytosine-rich single-stranded region of DNA under acidic conditions.[201] The programmed location of this structure in DNA ligands can modulate the lattice parameter or symmetry of a crystal, similar to the hairpin motifs discussed above, in response to changes in pH.[198] Alternatively, a change in the solvent dielectric constant can enable ions in solution to more

effectively screen the negative charge of DNA's phosphate backbone and thereby induce both single and double-stranded DNA to precipitate, a common molecular biology purification strategy.[202, 203] When applied to colloidal crystals engineered with DNA through addition of a high percentage of ethanol (*i.e.* lowered dielectric constant), a rapid, significant contraction (up to 75% decrease in unit cell volume) can occur.[197] Interestingly, this contraction occurs *on demand* (*i.e*. in less than five minutes), crystals retain their symmetry and habit in the condensed state, and the lattice returns to its original spacing upon removal of ethanol. The significant spatial and temporal structural control afforded by these methods allows crystals engineered with DNA to demonstrate distinct properties in response to stimuli, a few examples of which will be discussed in *Section 2*.

1.4.2 Functional Behavior Driven by Particle Core

The multiple levels of structural control required to build a colloidal crystal (*e.g.* building block, lattice, crystal habit) enable hierarchical functionality to be encoded. Each level can be encoded with its own structural and functional information. The structure and function at each higher level originates from interactions at lower levels, which may simply yield a sum function or potentially yield emergent properties. In this section, several examples will be given at each scale to demonstrate the breadth of possibilities available.

Building Blocks

Each building block carries function encoded by the shape, size, and composition of its core and the sequence and arrangement of the nucleic acids. Much of the foundational efforts to develop the field of crystal engineering with DNA, which underpin the above *Lessons,* relied

on particle cores of gold, due to the command of chemical syntheses to control shape and size, and the accessibility of surface chemistries to attach DNA. These *Lessons* provide the foundations to understand structural control, and in principle, should apply to any materials of comparable size and shape, granted they can be similarly functionalized with DNA. Indeed, researchers have been able to demonstrate comparable colloidal crystals with building blocks of at least 27 different core compositions, which include inorganic and organic materials as diverse as metal-organic frameworks (MOFs) and proteins.[17, 30, 36, 94, 138, 139, 204-208] Compositional changes enable researchers to encode building blocks with the unique optoelectronic, catalytic, magnetic, or storage properties of these materials relative to their corresponding bulk counterparts.[189] The modified or confined electronic structures of metallic and semiconducting materials enables the control of light-matter interactions.[192, 209, 210] The increased surface area-to-volume ratio of catalytic materials provides more surface sites to facilitate chemical reactions and the potential to impart reaction selectivity.[211-214] Magnetic particles can orient in response to a magnetic field to alter particle orientation and perform work.[215, 216] Hollow particles can carry cargo, such as therapeutically-relevant molecules or enzymes.[206, 217]

While this diversity of cores demonstrates the versatility of functionalities that can, in principle, be imparted to a building block, not all functions directly translate from discrete nanoparticle to building block. For example, the attachment of DNA to the surface may restrict access to surface sites for catalysis or inhibit the release of cargo.[30, 218] Consequently, researchers must systematically confirm the persistence or modification of target properties at each step to ensure they manifest in the finished product.

Lattices

Building blocks interact at the particle core and nucleic acid shell levels to create new properties not found in the individual building blocks, controlled by their arrangement within a structure. The key interaction parameters to these properties are the distance, symmetry, and orientation between adjacent building blocks, and most interactions are localized to nearest neighbors. To illustrate the potential types of interactions and consequences, two examples will be described, based on optical coupling or spatial proximity for catalysis.

For the majority of colloidal crystals made to date, comprised of building blocks with spherical metallic particle cores, light interacts via the electric-field induced, collective oscillation of their conduction electrons; a phenomenon known as a localized surface plasmon resonance (LSPR). When assembled into a colloidal crystal, the collective optical response can often be well-described solely based on the volume fraction of the particle core within the crystal.[219, 220] At high volume fractions (*i.e.* interparticle spacings ranging from about 0.1 to 2.5 times the particle diameter), the collective oscillations of individual particle cores can interact to produce a coupled mode, often with enhanced electric fields between the particles.[23, 24, 209, 221] Despite these localized interactions between particles, order and symmetry (not factored into volume fraction other than how they change the average distance between particles), do not significantly impact the collective optical response. Order plays a greater role in multi-component systems with unique particle core compositions. If randomly alloyed, the volume fraction of each component would similarly drive a summative optical response,[222] however, the confinement of each composition within discrete layers or at specific positions can produce emergent optical responses that arise from the ordering of the layers (*i.e.* the composition of particles in the first layer encountered by the electromagnetic

wave significantly impacts material response) or non-sum coupling between distinct particles or surfaces.[81, 163, 164, 222, 223]

Highly anisotropic metallic particle cores enable greater control of light-matter interactions due to the unique plasmonic modes they can support and the more complex architectures that can be built.[23, 164, 224] For example, one-dimensional lattices comprised of "two-dimensional" building blocks, such as circular disks or triangular prisms, represent broken symmetry structures that would be difficult if not impossible to construct via other techniques. By nature of their order and orientation, the individual nanoparticles couple in a textbook fashion according to plasmon hybridization theory (analogous to molecular orbital theory for plasmons) to access optical modes that would be conventionally "dark" or unobserved in other colloidal crystal systems.[23] These modes can be systematically tuned in their wavelength and strength based on the DNA length and particle size, and more complex coupled modes can be introduced by using two differently shaped or sized particle cores. Such behavior forms the foundation for potential solution-based metamaterials, which could lead to exotic optical phenomena, such as negative refraction or electromagnetically induced transparency.

The ability to precisely position nanoscale components can similarly benefit the catalysis field, where a powerful, emerging design strategy for multi-step reactions is tandem catalysis. Tandem catalysis pairs catalysts with complementary functions (*e.g.* the product from one reaction acts as the reactant for a second reaction) and thus the particular arrangement can drive advances in reaction yield and selectivity.[225-227] Initial efforts have already revealed that colloidal crystals engineered with DNA-assembled spherical gold nanoparticles can act as catalysts upon transfer to a solid state matrix and subsequent removal of DNA ligands.[218] In principle, the structural control

afforded by crystal engineering with DNA could facilitate tandem catalysis for inorganic (*e.g.* Au/Pd nanoparticle systems) or organic catalysis (*e.g.* enzymes) alike. For example, DNA ligands can arrange and orient proteins with respect to one another.[13, 139] If enzymatic proteins were similarly modified with DNA and crystallized, these building blocks could form a cascade where the active site of one would be oriented to face that of the next enzyme for efficient multi-step syntheses. Realization of this cascade would require researchers to explore the fundamental relationship between enzyme spacing and catalytic efficiency. At long distances between enzymes, the products of one enzyme may diffuse away before they can act as reactants for the next enzyme and, at short distances, steric hindrance may prevent access of reactants to active sites or release of products from active sites.

Crystal Habits

Lessons 5 and *6* teach that the lattice symmetry determines mesoscale structure (crystal habit and size).[224] Control over crystals at this length scale affords access to functionality that originates from the interplay of emergent mesoscale properties with interactions occurring at the lattice and building block levels. One illustrative example of crystal habit-based functionality is the ability to manipulate light through the emergence of photonic modes. Such photonic modes emerge when colloidal crystals form defined structures that approach the wavelength of light.[219] Photonic modes can be coupled with the constituent optical modes to tune the absorption, scattering, and/or reflective properties of the colloidal crystal over a broad spectrum.[219, 224] These colloidal crystals can alter the direction of propagating light waves or display orientation-dependent optical properties that arise from differences in plasmonic coupling along different

lattice vectors.[81, 219] These directionally dependent properties can be enhanced with the use of anisotropic building blocks, due to further shape-dependent differences in coupling.[224, 228, 229]

In principle, these properties lay the foundation for individual crystals to function as optical devices, such as lasers that permit the transmission of a narrow spectrum of light or waveguides that change the direction of incident light. The typical size of these crystals and their constituent components makes them attractive for optical computing, a field that has historically been limited by the challenges associated with control of material structure at the nanoscale and the ability to create regular 3D crystals.[230] Colloidal crystal engineering with DNA offers distinct advantages in both areas and could open the possibility of optical computing with crystals strategically arranged to create logic gates that could aid in data storage or transmission.

SECTION TWO – ANALYTICAL DETERMINATION OF NANOMATERIAL STRUCTURE

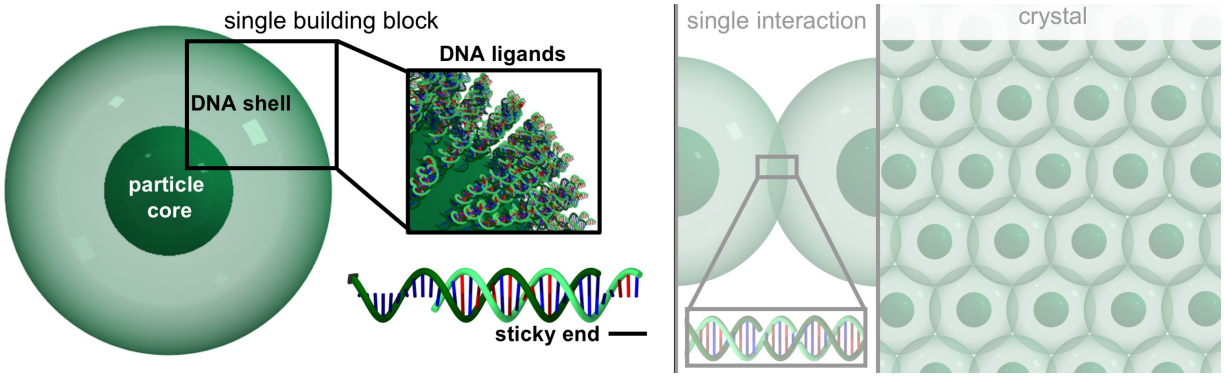

2 CHAPTER TWO: HIGH-THROUGHPUT, ALGORITHMIC DETERMINATION OF NANOPARTICLE STRUCTURE FROM ELECTRON MICROSCOPY IMAGES

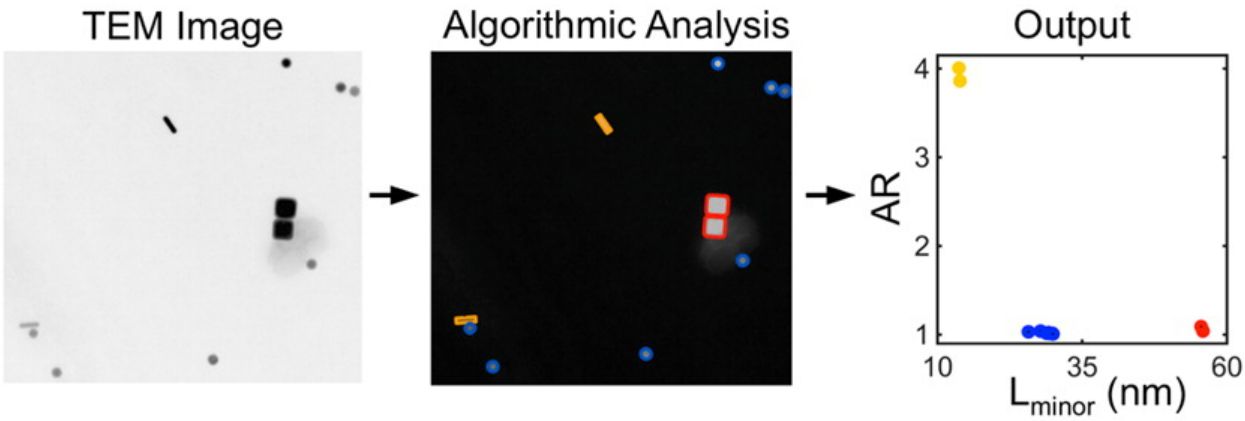

Material in this chapter is based upon published work:

C.R. Laramy,* K.A. Brown,* M.N. O'Brien, C.A. Mirkin. *ACS Nano.* **2015**, *9*, 12488-12495.

2.1 Abstract

Electron microscopy (EM) represents the most powerful tool to directly characterize the structure of individual nanoparticles. Accurate descriptions of nanoparticle populations with EM, however, are currently limited by the lack of tools to quantitatively analyze populations in a high-throughput manner. Herein, we report a computational method to algorithmically analyze EM images that allows for the first automated structural quantification of heterogeneous nanostructure populations, with species that differ in both size and shape. This allows one to accurately describe nanoscale structure at the bulk level, analogous to ensemble measurements with individual particle resolution. With our described EM protocol and our inclusion of freely available code for our algorithmic analysis (see Methods section below), we aim to standardize EM characterization of nanostructure populations to increase reproducibility, objectivity, and throughput in measurements. We believe this work will have significant implications in diverse research areas involving nanomaterials, including, but not limited to, fundamental studies of structural control in nanoparticle synthesis, nanomaterial-based therapeutics and diagnostics, optoelectronics, and catalysis.

2.2 Background

Analytical molecular characterization techniques can provide atomic level structures of chemical species, and given the ensemble nature of these measurements, can be used to quantitatively evaluate molecular purity. Nanoparticle species, on the other hand, are challenging to control and characterize in an analogous fashion, because nanoparticles are composed of a large and variable number of atoms.[231-234] As a consequence, ensemble measurements of nanoparticle

populations with techniques such as small angle X-ray scattering (SAXS) or UV-Vis spectroscopy can often capture an average size or shape, but cannot quantitatively describe the distribution of sizes or shapes without many restrictive assumptions.[235-242] Use of ensemble techniques for structural determination is therefore limited to qualitative evaluations of independently characterized homogeneous populations.

In contrast to ensemble measurements, electron microscopy (EM) can be used to directly measure the structure of individual nanoparticles, including size, shape, and defects.[12, 179, 243-249] However, EM is intrinsically a sampling technique, and therefore accurate characterization of nanoparticle populations is limited by low throughput analysis and a lack of systematic methods to quantify structural uniformity. For example, if one wanted to compute the yield of a nanoparticle synthesis with two products within a precision of ±1%, as many as 2,500 nanoparticles would have to be counted. Recent computational methods have begun to address these limitations through the automated identification of classes of nanoparticle shapes or the determination of a single structural parameter (*e.g.* size) for limited cases of homogeneous nanoparticle populations.[12, 250-255] However, these methods lack the structural detail and shape specificity required to characterize a nanoparticle population in a way that correlates with ensemble measurements.

2.3 Results and Discussion

Herein, we describe a high-throughput, quantitative, structurally specific computational analysis of EM images that allows us to relate a small sample (relative to the total number of particles) to the global properties of heterogeneous populations. This methodology represents a significant advance in nanoparticle characterization that allows one to systematically study and quantitatively evaluate multiple classes of nanoparticle reactions, including structural

transformations and multi-shape syntheses. When this structural evaluation is combined with complementary global measurement techniques, it further allows for one to rapidly elucidate difficult to measure physical properties, such as optical extinction coefficients. By presenting a protocol for this methodology, and making the software freely available, we aim to establish a standard characterization process that can be duplicated in any lab (Figure 1).

Currently, structural analysis of nanoparticle populations with EM presents a significant number of challenges, which result in inconsistent characterization and limited validity of quantitative comparison between samples. To address these limitations, we defined a series of best practices for sample preparation and image acquisition, and more importantly, developed an algorithmic method to determine nanoparticle structure (Figure 6, Figure 10, Figure 11, Figure 12, Figure 13). In particular, samples for EM analysis were prepared from dilute particle solutions and quickly dried to prevent size- and shape-segregation effects.[62, 256] Images were collected from at least 10 unique regions of the EM grid at low-magnification to further reduce these effects and to eliminate bias associated with what portion of the particle population is analyzed. Algorithmic determination of nanoparticle shape and size, described in greater detail below, eliminates bias and irreproducibility associated with user defined measurements (*e.g.* what is the edge of a nanoparticle, see Figure 14 for a comparison of user structural measurement to automated structural measurement) and allows for a richer, higher throughput analysis of nanoparticle structure (*e.g.* perimeter, area, aspect ratio, and circularity for a circularly-shaped object, as opposed to a single diameter).

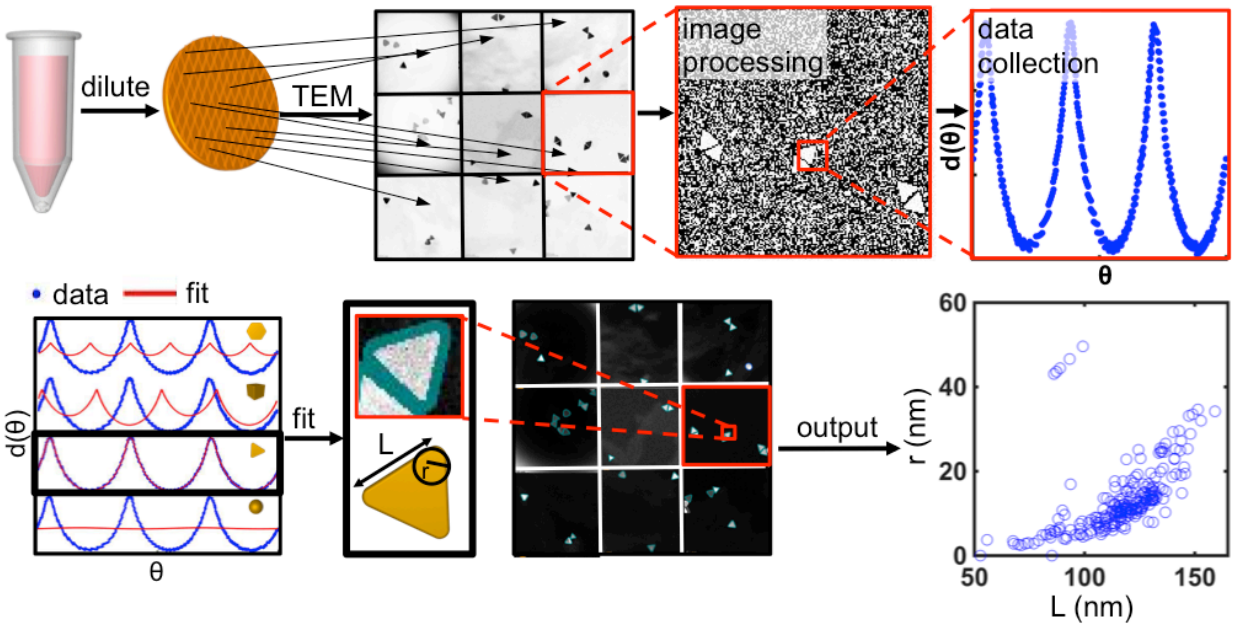

Figure 6. Overview of the process for quantitative EM analysis including EM methods and computational processing. In particular, the most appropriate EM data collection requires dilute sample preparation and acquisition of images at diverse grid locations. Computationally, the program first processes raw EM images, extracts angular distance data, d(θ), from individual particles, performs a shape fit and repeats the process iteratively for multiple images to produce population statistics.

To algorithmically determine nanoparticle structure, we utilized the diverse tools for image processing developed in the computer science and machine vision communities[257-260] to build on our previously reported method for determining the geometry of homogeneous nanoparticle populations.[12] In particular, a software script was written to algorithmically determine the size and shape of each particle through a procedure in which the distance from the edge of the particle to its center as a function of angle, d(θ), is used as a shape-specific signature. Since ideal values of d(θ) can be found analytically for a given shape, we hypothesized that fitting the measured d(θ) to ideal curves for various shapes would provide the structural specificity required to define a nanoparticle population (Figure 6). In order to encompass a diverse set of nanoparticles, we have explored four primitive shapes for exact fitting: ellipses, rectangles, triangles, and hexagons. These primitive shapes represent the two-dimensional projection of several three-dimensional

morphologies including rods, spheres, cubes, triangular prisms, disks, and rhombic dodecahedra. Thus, the algorithm proceeds by fitting $d(\theta)$ to functions that correspond to each of these shapes using a non-linear least squares approach, and the best fit is selected as the match. This analysis therefore requires images of non-overlapping particles with consistent orientations, such that the two-dimensional projection of each individual particle can be fit to one of the available primitive shapes. Importantly, using functions that define these shapes exactly allows us to directly determine parameters of interest including major and minor edge lengths, L_{minor} and L_{major}, aspect ratios (AR; $AR=L_{major}/L_{minor}$), and radius of curvature, r. Through this degree of structural specificity, we hypothesize that EM images can be used to quantitatively characterize structural evolution in nanoparticle reactions, at both an individual particle and global population scale.

To demonstrate the capabilities of our algorithm, we considered two classes of nanoparticle reactions: ones in which nanoparticle shape transformations occur and ones that yield multiple unique nanoparticle shapes. In the first reaction class, we characterize the change in structural uniformity of a population of similarly shaped particles by a standard uniformity metric, the coefficient of variation (CV), for particle area and perimeter. To gain a deeper structural understanding of the shape transformation, we also algorithmically measured the average sharpness of the corner features of a given class of particles. In the second reaction class, we demonstrate the high throughput nature of our analysis to characterize the relative yield of multiple unique nanoparticle shapes. In combination, the study of both reaction classes allows for evaluation of algorithmic EM analysis in understanding global particle populations from a structural level.

2.3.1 Reaction Class I: Changes in the Cross-Sectional Shape, Size, and Uniformity of Similarly Shaped Nanoparticles.

In order to test the structural sensitivity of our algorithmic EM analysis, we performed a series of experiments to better understand our recently reported method for the shape transformation of Au triangular prisms into Au circular disks via oxidative dissolution.[261] This shape transformation is an ideal case study to quantitatively analyze structure, as it represents a single class of nanoparticles changing primarily in their cross-sectional shape. In our previous work, we proposed that the reaction selectively proceeded at triangular prism sites with the lowest metal coordination number, and in this way, a population of triangular prisms with varying degrees of truncation can be driven, through a self-limiting reaction, to a uniform population of circular disks (Figure 7a, Figure 15).[12, 261] However, this proposed mechanism was based on qualitative analysis of EM images before and after the reaction, rather than a quantitative analysis of the population over time. Therefore, we hypothesized that a detailed kinetic investigation of shape transformation could be used to determine valuable information about the selectivity of the reaction for particular nanoparticle features, the reaction chemistry, and the relevant time scales over which each stage of the transformation occurs.

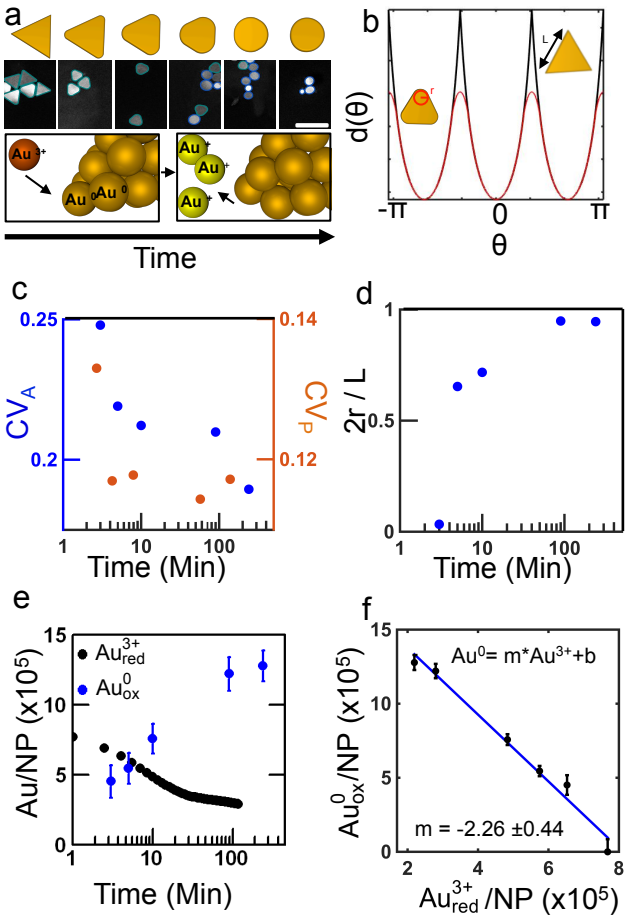

Figure 7. Algorithmic analysis of a nanoparticle shape transformation reaction, shown here as the oxidative dissolution of gold triangular prisms to circular disks. a The shape transformation from triangular prisms to circular disks proceeds through a conproportionation reaction upon addition of a Au(III) salt, wherein surface atoms are oxidized in a tip-selective fashion. Scale bar represents 200 nm. **b** Precise shape and size for each nanoparticle is determined from a fit of the angular distance data, d(θ), versus angle, θ. Data for triangular prisms with sharp (black) and rounded (red) corners is plotted here to show how corner rounding affects d(θ). **c** Structural uniformity of nanoparticles in this reaction can be evaluated by the coefficient of variation (CV = standard deviation/mean) of the cross-sectional area (A) and perimeter (P). **d** Degree of corner rounding normalized by the particle size. **e** The oxidation of the nanoparticles (Au^0) and reduction of the (Au^{3+} species) can be monitored independently with EM and UV-Vis, respectively, to quantify reaction stoichiometry. **f** Data in e replotted to show that the ratio of oxidized to reduced species agrees with the expected chemistry. Error bars in **d-f** represent the standard deviation of three trials.

To more closely investigate the nature of this transformation, we imaged samples from this reaction with EM at various time points and analyzed the images with our custom algorithm. For this reaction, we determined the shape, cross-sectional area (A), perimeter (P), L_{minor}, L_{major}, and r for several hundred particles for multiple time points, where A and P are direct outputs of image analysis and L_{minor}, L_{major}, and r are determined through fitting d(θ) (Figure 7b). We define r as the

radius of the inscribed circle that defines the corner of the shape. In this way, a maximally rounded shape approaches a circle with radius equal to $L_{minor}/2$, such that the term $2r/L_{minor}$ should asymptote to unity. The parameter $2r/L_{minor}$ therefore provides insight into the extent of structural transformation from triangular prisms to circular disks.

Analysis of the dispersity in A and P over time indicates that this transformation results in a considerable homogenization of particle size, and that most of this homogenization occurs within the first 10 minutes of the reaction (Figure 7c). Significantly, analysis of $2r/L_{minor}$ as a function of time suggests that the increased uniformity in A and P is a result of triangular prism oxidation occurring rapidly at the tips of the structure. The reaction proceeds such that >60% of the rounding occurs similarly within 10 minutes of oxidizing agent addition (Figure 7d). The rapid nature of this initial transformation likely comes from the lower metal coordination number of the atoms at the tips of the triangular prism. Accordingly, rounding then slows as the difference in metal coordination number between the tips and edges decreases and as expected, $2r/L_{minor}$ approaches one as the reaction proceeds toward circular disks. When combined with the analysis of A and P above, these results suggest that oxidative dissolution improves uniformity largely by removing differences in corner rounding and truncation associated with the initial triangular prisms.

To further confirm the chemical reaction underlying this shape transformation, we compared EM measurements of gold content per nanoparticle with *in situ* bulk spectroscopic measurements. In particular, we would expect the redox stoichiometry of the reaction to be:

$$Au^{3+} + 2Au^{0} \leftrightharpoons 3Au^{+}$$

where each Au^{3+} species oxidizes, and therefore liberates, two gold atoms from a nanoparticle, and results in three Au^{+} species.[262] Spectroscopically, the Au^{3+} species in this reaction contains a

characteristic absorption peak at 271 nm that shifts to 314 nm upon reduction. Comparison of the decrease in absorbance of the Au^{3+} species to the decrease in the number of gold atoms per nanoparticle, as calculated from our analysis of EM images, confirms the expected stoichiometry (Figure 7e). This can be seen in Figure 7f which shows a slope of ~2 Au^0/Au^{3+}. By combining two complementary approaches to reaction monitoring – analysis of particle size and shape, and a joint structural-spectroscopic analysis – this work highlights the ability of our algorithmic method to quantify both structural and chemical information about nanoparticle-based reactions.

2.3.2 Reaction Class II: Quantification of Reaction Shape Yield

Beyond reactions involving a single class of nanoparticles, we hypothesized that our algorithmic EM analysis could be similarly applied to heterogeneous nanoparticle populations composed of multiple unique shapes, given that each shape could be differentiated. Computationally, differentiation between nanoparticle classes occurs via a fitting decision process that independently considers the number of edges, L_{minor}, $L_{major,}$ AR, and r (Figure 8a). The periodicity of $d(\theta)$ is dictated by the symmetry of the nanoparticle, which is directly related to the number of edges of a given nanoparticle cross section. For example, $d(\theta)$ for a triangular prism has a periodicity of three while $d(\theta)$ for a cube has a periodicity of four. In addition to fitting the periodicity of $d(\theta)$, the algorithm also evaluates AR and r (Figure 8b) to further differentiate shape.

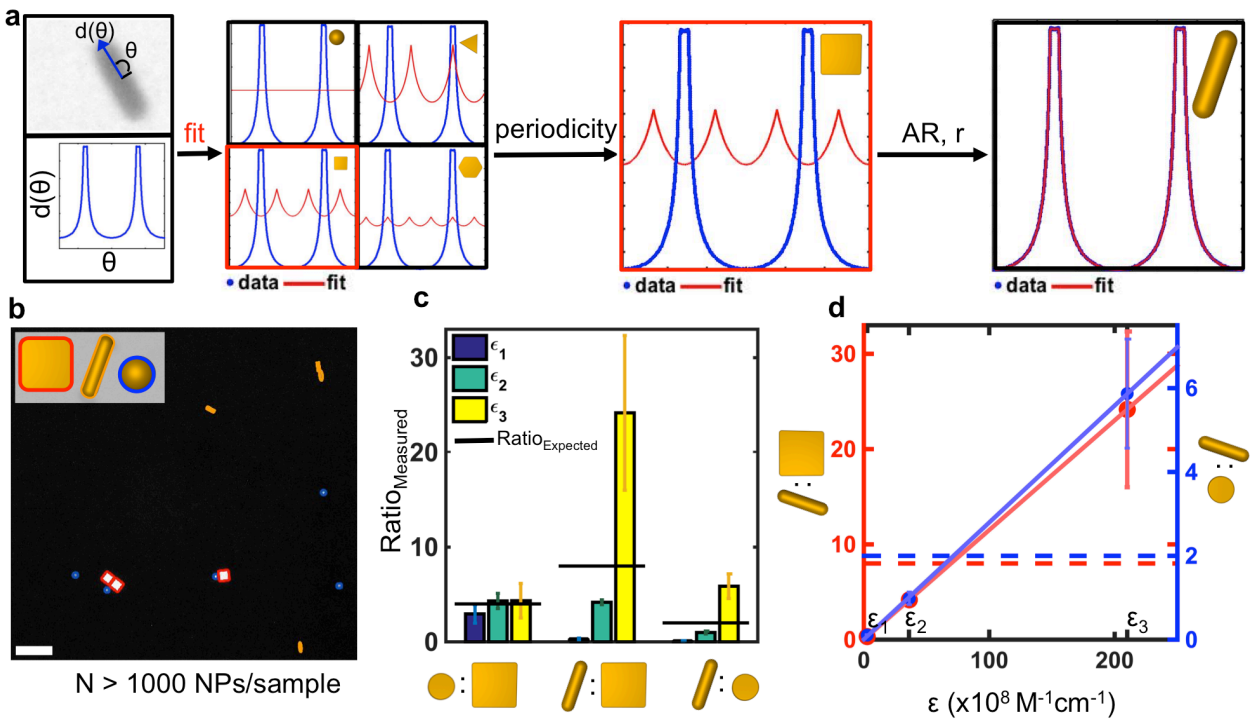

Figure 8. Algorithmic determination of particle shape and the resulting quantification of shape yield and evaluation of global physical properties. a Computational analysis determines the perimeter of each particle shape and the associated d(θ) data. The algorithm fits d(θ) based on several parameters including the periodicity of d(θ), the aspect ratio (AR) and corner rounding (r) of the particle's cross sectional area, shown here for the case of a rod. Although the algorithm calculates each metric simultaneously, the schematic separates periodicity fitting from AR and r fitting for clarity. **b** EM image overlaid with the fit determined for each particle. The image contains multiple nanostructure shapes, with color indicating the shape classification and the border indicating the calculated fit. Scale bar represents 200 nm. **c** Analysis of several thousand nanoparticles led to the calculation of the measured ratio between rods and two internal standards (spheres and cubes) for evaluation of multiple reported rod extinction coefficient values. $\varepsilon_1 = 2.7 \times 10^8$ $M^{-1}cm^{-1}$ (Nanopartz, Inc.), $\varepsilon_2 = 3.6 \times 10^9$ $M^{-1}cm^{-1}$ (El Sayed), and $\varepsilon_3 = 2.1 \times 10^{10}$ $M^{-1}cm^{-1}$ (Nanoseedz). The black line represents the expected ratio of shapes based on the use of UV-Vis measurements and the extinction coefficient. In this way, the accuracy of the extinction coefficient can be understood by comparison to the expected ratio. Error bars indicate the standard deviation of three trials for each experiment. **d** Data in c replotted to show the deviation of rod ratios from expected ratio of shapes for both internal standards vs. extinction coefficient. Dashed lines indicate the expected ratios. Solid lines indicate a linear fit of the data. Error bars indicate the standard deviation of three trials for each experiment.

We additionally hypothesized that our analysis could be used to quantify the relative abundance of different nanoparticle species, given appropriate sample preparation and image collection protocols. To test the ability of our algorithm to quantitatively analyze heterogeneous populations, we prepared a solution of Au spheres and Au cubes at equal concentrations, as determined via UV-Vis measurements (Figure 9, Figure 16, Table 1). Each sample was prepared

in triplicate. Importantly, EM analysis confirmed equal amounts of cubes and spheres within the error of the measurement, as expected (Figure 17, Figure 18).

With the capability to quantify the relative abundance of different nanoparticle populations, as well as structural information, we further hypothesized that algorithmic EM analysis could be used to study multi-shape nanoparticle syntheses[120, 232, 263-265] and to evaluate physical properties. One particularly useful physical property to quantify is the optical extinction coefficient (ε) of a nanoparticle species, which allows one to calculate nanoparticle concentration from spectroscopic measurements. Traditionally, accurate determination of ε requires time-intensive, precise analytical measurement of atomic content, nanoscale structure, and optical response.[12, 266-268] For example, there are several conflicting ε values for Au rods[267, 269, 270,271] - among the most widely studied inorganic nanostructures[265] - which limits the reliable measurement of concentration in self-assembly, biomedical, and sensing applications.

With this automated approach, we hypothesized that ε could be determined directly from EM measurements. To determine ε for Au rods (specifically, rods with an average diameter of 10 nm and an aspect ratio of 3.5), we intentionally prepared a heterogeneous population of Au nanoparticles with several shapes (cubes, spheres, and rods). Cubes and spheres were used as an internal standard for each experimental condition, and the rod concentration was set relative to these given each reported extinction coefficient in a 1:4:8 ratio, respectively. Specifically, we evaluated three reported values of rod extinction coefficients, spanning three orders of magnitude. Each sample was then prepared for EM in triplicate, and imaged such that nearly 10^4 particles were analyzed in the study (Figure 18). Importantly, we find that the computationally calculated ratios of cubes to spheres (1:4) matches with our predicted ratios in each experiment (Figure 8c), and

that the rod ratios differ by factors consistent with their ε values. To evaluate the best ε from these experiments, we compared the measured ratios for each ε to both internal standards (Figure 8d). Based on these results, we find that the values published by El-Sayed and coworkers extinction coefficient determination agrees best, within a factor of 2 of our results.[267] Together, this study demonstrates the power of this analysis to determine reaction yields, stoichiometry (relative abundance), and with the appropriate standards, even physical properties.

2.4 Conclusion

The high-throughput, structurally specific, algorithmic EM analysis presented here introduces a powerful and extremely useful method for the measurement of nanoparticle structure. This analysis expands the complexity of nanoparticle populations that can be identified and quantified with computational EM analysis, and opens a channel in the previously described "nanomaterial characterization bottleneck."[231] We envision this approach as a major step toward standardized structural analysis that will facilitate direct comparison across the nanomaterial community, in a manner analogous to analytical molecular chemistry techniques. While a collection of four shapes was used here, analogous procedures could be developed from this work to process additional shapes with different symmetries. In particular, this analysis should enable an objective, high-throughput screening and optimization of currently known nanostructure synthesis protocols, and will facilitate the exploration and identification of novel nanostructures. While this analysis focused on Au nanoparticles, the protocols described herein are suitable for analyzing any particle that can be imaged with high resolution, including semiconductor (e.g. CdSe, CdS, PbSe), oxide (e.g. CuO_2, Fe_2O_3, ZnO_2), metal (e.g. Pt, Pd, Ag), and organic nanoparticles that can be synthesized

with different shapes. Quantitative analysis should additionally hold implications to any application that relies on structurally specific properties of nanomaterials, with particular relevance to biomedicine, sensing, optoelectronics, and self-assembly.[25, 62, 117, 236, 272-275]

2.5 Experimental Methods and Supplementary Materials

2.5.1 Materials

The following chemicals were purchased and used as received. Cetyltrimethylammonium bromide (CTAB, >99%) and cetylpyridinium chloride monohydrate (CPC) were purchased from bioWorld. Sodium borohydrate ($NaBH_4$, >99%), tetrachloroaurate trihydrate ($HAuCl_4$, >99%), L-ascorbic acid (AA, >99%), silver nitrate ($AgNO_3$, >99%), potassium bromide (KBr, >99%), and sodium chloride (NaCl, >99%) were purchased from Sigma-Aldrich. Thiolated oligoethyleneglycol (OEG) was purchased from ProChimia. Bis-(*p*-sulfonatophenyl)phenylphosphine dehydrate potassium salt (BSPP, >97%) was purchased from Strem Chemical.

2.5.2 Nanoparticle synthesis

The reaction converting triangular prisms to circular disks was performed according to O'Brien et al.[261] Triangular prisms were synthesized according to Jones et al. and purified by a centrifugation process according to Young et al.[266, 276] Rods were synthesized as reported by Nikoobakht and El-Sayed.[277] Spheres were synthesized through an iterative oxidation and reduction process reported by O'Brien et al. and acted as the seeds for the synthesis of cubes.[12]

Before use in both the relative abundance study and the extinction coefficient study, we characterized the structure of spheres, cubes and rods in order to accurately determine an extinction coefficient based on reported values.[12,278] Figure 9 shows representative EM images, UV-Vis extinction spectra, and population statistics from our automated analysis of EM images. Table S1 lists the extinction coefficients chosen for each particle species. UV-Vis

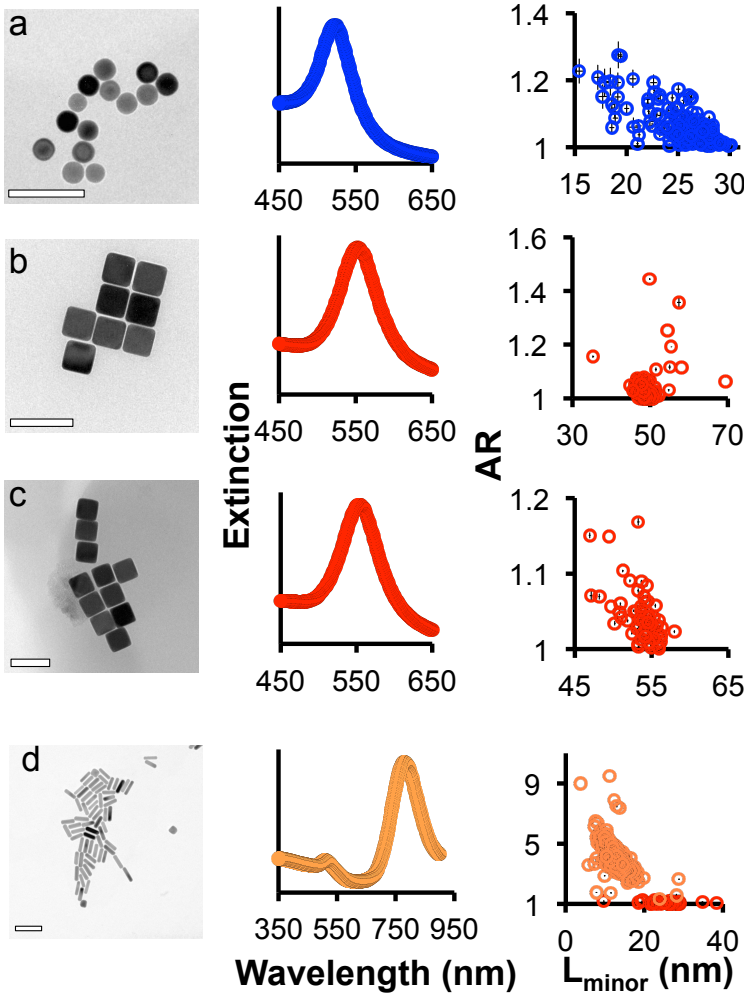

Figure 9. Structural characterization of particle species for both the relative abundance and rod extinction coefficient studies by UV-Vis spectroscopy and algorithmic EM image analysis. Color scheme is consistent with Figure 8b for distinguishing sphere vs. cube vs. rod data. Each row shows a representative EM image, UV-Vis spectroscopy measurement, and algorithmic EM image analysis for a particle species. All scale bars represent 100 nm. **a** Characterization of spheres for both the relative abundance study and the rod extinction coefficient study, **b** Characterization of cubes for the relative abundance study, **c** Characterization of cubes for the rod extinction coefficient study, **d** Characterization of rods for the rod extinction coefficient study. Red data points are consistent with the color scheme and indicate cube impurities from rod synthesis.

spectroscopy measurements for each colloidal solution were collected with a Cary 5000 spectrophotometer. All samples were imaged using a Hitachi 8100 TEM at 200kV. Images were collected at greater than 10 unique locations on the sample grid.

Table 1. The concentration of nanoparticle species were determined using UV-Vis spectroscopy and ε. This table lists ε for the species used in this study.

Species	**ε ($M^{-1}cm^{-1}$)**
Sphere[279]	4.0×10^{9}
Cube[12]	1.0×10^{11}

2.5.3 Summary of Algorithmic Analysis Software

BeanCounter.m is the main script responsible for analyzing EM images. Users can pass images into this script through a graphical user interface (GUI) and the script will output a single excel sheet containing particle statistics. If the user selects an entire directory for analysis, BeanCounter.m will aggregate each individual excel sheet into a single excel document. Users can specify the output location of these excel files using the GUI. The excel sheet contains: minor edge length, minor edge length error, aspect ratio, aspect ratio error, corner rounding, corner rounding error, goodness of fit, area, perimeter, and the shape classification or identifier. All errors are determined by the confidence interval of the fit. The shape identifier is a number that corresponds to a particular shape (i.e. 1: rod, 2: circle, 3: triangle, 4: square, 6: hexagon). The GUI has additional options for specifying output images and processing parameters. The following discussion describes additional sample preparation considerations and processing parameters in greater detail.

2.5.4 Image Acquisition for Algorithmic Analysis

To realize accurate algorithmic nanoparticle detection and analysis, several considerations must be taken during sample preparation and EM image collection.

First, the MATLAB Image Analysis Toolbox is used to initially process images and extract nanoparticle perimeter data. Included in the toolbox is an edge detection function that identifies edges as a gradient between adjacent pixels. When a region is fully contained by edge pixels it is considered a closed object. The custom algorithm analyzes only closed objects as particles. Therefore, the full edge of the nanoparticle must be visible (i.e. not overlapping or fused with adjacent particles) in images. In this way, images with overlapping or fused particles can lead to the analysis of multiple particles as a single particle or prevent particles from being identified as a closed shape (Figure 10). This methodology leads to two primary requirements in the sample preparation and image acquisition process:

1. Only shapes that do not overlap in EM images can be analyzed. For example, octahedron nanoparticles most frequently dry in an orientation with a facet parallel to the substrate. When packed closely, this leads to an overlap of adjacent particles, such that there is no visible border between particles, and therefore this analysis would not work for this particular sample. Another example would be if closely packed cube nanoparticles were imaged at a non-normal angle to their facet, such that particles appeared to overlap in EM images. In this case, the sample can simply be rotated to an angle where the gaps between particles become visible.
2. Samples must not be fused in a manner that distorts the original nanoparticle shape. Fusion or aggregation, as described here, frequently occurs as a result of sample preparation and

can result in two or more distinct particles forming a single shape that is recognized by the analysis. Ideally, this problem can be avoided through proper sample preparation. However, if this cannot be avoided, and the resultant fused nanoparticle shape is not properly fit as one of the primitive shapes selected for analysis, the fused particle can be excluded in the analysis. Alternatively, users can correlate the image analyzed with the associated data file and remove any outliers.

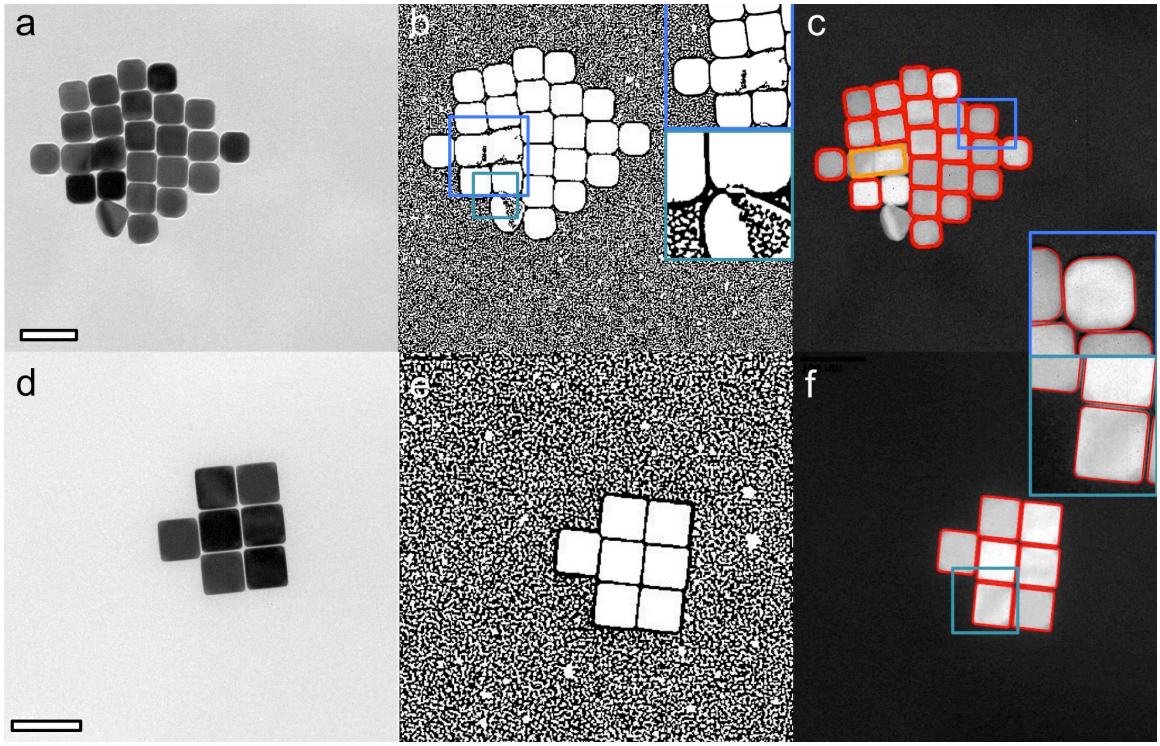

Figure 10. Image processing and analysis steps for an EM image with overlapping and fused particles in comparison to an EM image with fully separate particles. Scale bars represent 100 nm. **a** Original TEM image with overlapping and fused particles. **b** MATLAB edge detection output for **a**. Dark blue inset shows fused particles; light blue inset shows overlapping particles. **c** Fitting analysis output for **a**, where fused and overlapping particles are not recognized as cubes (cube recognition denoted by red border). **d** Original TEM image with fully separate particles. **e** Matlab edge detection output for **d**, **f** Analysis output for **e**, where light blue inset shows a zoomed in image of fully separated particles.

Second, the magnification and resolution of the image influences the image processing and the speed of processing. MATLAB's edge detection output may identify closed objects that

are not nanoparticles as a result of background noise. These closed objects can be removed from processing by setting thresholds for: the size of closed shapes (in pixels), the solidity of closed shapes, and the average pixel intensity of closed shapes (from the original image).

1. Thresholding the size of closed objects for positive nanoparticle identification can remove background noise (such as the noise in Figure 10b and e). More than either of the two additional thresholding steps, size thresholding increases the processing speed of the algorithm. Determining a reasonable number of pixels for area thresholding before processing large amounts of data can save considerable time. Magnification and resolution both influence the number of pixels defining a single nanoparticle by changing the total area the particle takes up within a frame as well as the pixel density within the particle.
2. Thresholding by the average pixel intensity of the closed shape in the original image and solidity removes larger background noise closed objects. These thresholds can become particularly significant for low magnification images.
3. Solidity is the ratio of the area of the closed shape divided by the convex area of the closed shape (with a value ranging from 0 to 1). The convex area of an object is the area of the smallest convex polygon (*i.e.* a polygon with all interior angles less than 180 degrees) that contains all points on the perimeter of the object. Figure 11a below shows a particle with a solidity near 1. Conversely, Figure 11b shows a background object with low solidity.

Together, these three parameters increase speed and improve algorithm accuracy by eliminating non-nanoparticle objects from further processing. (Area, average intensity and solidity thresholds can be modified within the BeanCounter.m file just after image processing steps)

Third, the accuracy of the output of this analysis is limited by the pixilation of the source image. While this may not be significant in the determination of the overall particle size, it may limit the degree to which their corner radius can be computed. As such, the upper bound of this systematic pixilation error is estimated to be equal to the width of a single pixel in EM. Due to this restriction, there is a tradeoff between throughput, resolution, and processing speed that requires optimization depending on experimental conditions. For example, the yield quantification studies described here required a significantly high throughput analysis enabled by lower magnification imaging (i.e. ~8,000×). In order to compensate for lower magnification, image resolution was increased (i.e. 2048×2048 pixels) such that the error was ≤ 0.85 nm.

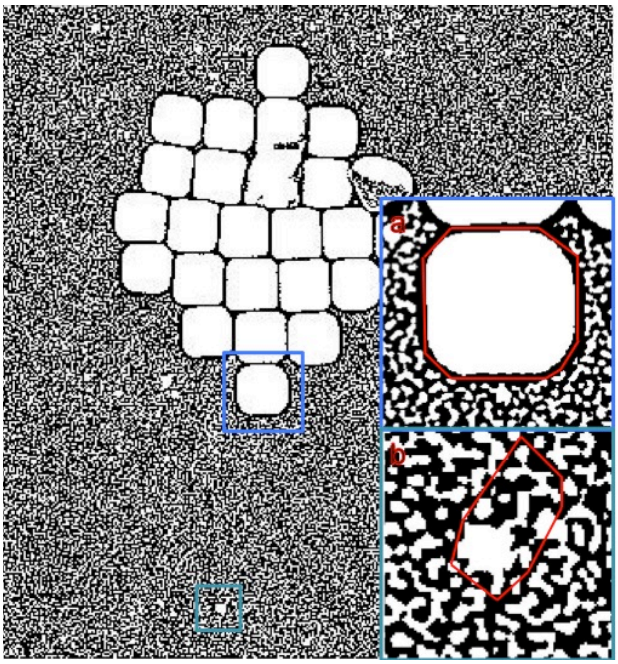

Figure 11. Illustration of convex area determination for solidity calculation. a convex area is near object area (solidity ~ 1), **b** convex area is greater than object area (solidity <<1)

2.5.5 Code architecture

Once the user inputs "AnalysisGUI" into the MATLAB command window, a GUI appears as shown in Figure 12. From this window the user can select either an image or a directory of images to analyze and a location to save resulting output statistics, along with several other processing parameters including:

- *Aspect ratio thresh:* This value defines the aspect ratio threshold for classifying a circle or square as a rod. The default setting is 1.3.
- *Pixel conversion factor*: This value converts between pixels and physical units. Many image processing software programs have measurement tools available that allow measurement of the pixel length of image scale bars. This value should go here in the format length/pixel.
- *Select shapes to fit*: These boxes indicate which 2D shapes the program should attempt to fit particles. All may be selected.
- *Select outputs:* "Fit Overlay" outputs images such as Figure 10c and Figure 10f for each image. "Minor vs. AR" outputs a plot of minor axis length vs. aspect ratio for all nanoparticles within a single image. "Minor vs. Rounding" produces a similar plot but with corner rounding (r) instead of aspect ratio. "Image Processing" outputs a figure with three images including the original image, an edge detection image, and an image with the closed objects from edge detection filled in (Figure 10b and Figure 10e). Lastly, "Percent of Shapes" outputs a figure with a bar graph representing the percent of each shape fit in the image.

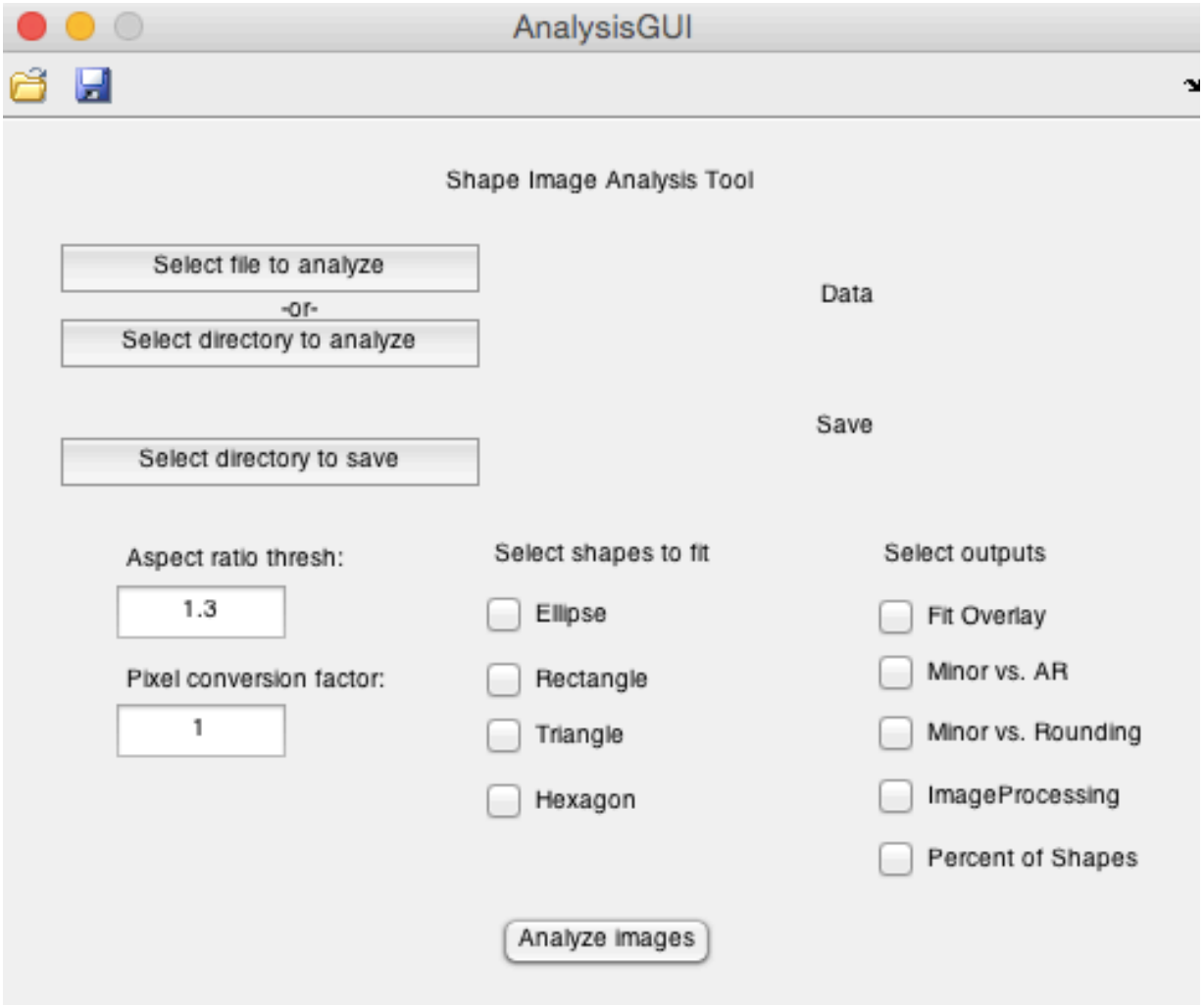

Figure 12. GUI for user input of EM image, output save location, additional processing parameters, and optional output figures.

Once the user clicks "Analyze Images" the specified EM image or first image in the specified directory is loaded into BeanCounter.m. A series of image processing and analysis steps, pictorially represented by Figure 13, follow. These include:

- *MATLAB Image Analysis Toolbox image processing.* First, BeanCounter.m processes the image and creates a list of pixel coordinates corresponding to the perimeter and centroid of

each positively identified particle (filtered by area, intensity and solidity thresholds described previously). The centroid is the coordinate within a closed shape defined as the average of all coordinates (*i.e.* the center of mass).

- *Calculation of d(θ).* BeanCounter.m iterates through the perimeter coordinates of the first particle creating d(θ) and θ, a list of the distance and angle between the centroid and the perimeter coordinate.
- *Determination of shape and structural parameters.* BeanCounter.m passes d(θ) and θ to GetFormics.m which calculates seeds, or starting points, for structural fitting parameters (L_{major}, L_{minor}, r, etc.) based on known geometric relationships (*i.e.* for a circle d(θ) is equal to the radius and therefore ½ of L_{minor}). This accelerates nonlinear least squares fitting which requires starting points for fit parameter values. GetFormics.m calculates different seeds for each of four custom functions (MirkEllipse.m, MirkTriangle.m, MirkSquare.m, and MirkHex.m), which together define our library of primitive shapes (circle, triangle, rectangle, and hexagon). GetFormics.m then utilizes native MATLAB fitting tools in the curve fitting toolbox to compute fits to each shape using the associated seeds and d(θ). The fit with the highest goodness of fit (determined through a nonlinear least squares method) is selected as the best fit. The GetFormics subroutine then returns the best fit to BeanCounter.m.
- *Additional structural considerations.* BeanCounter.m iterates through each particle collecting fit parameters returned from GetFormics.m. Fit values are converted from pixels to a real space length distance and a final evaluation of which shape to classify each particle is performed. While most particle shapes are determined by the fit shape returned by

GetFormics.m, BeanCounter.m reclassifies some particles as rods by comparing the aspect ratio of fit parameters returned for circle and square fits against the user set aspect ratio threshold. Additionally, BeanCounter.m will reclassify highly rounded shapes as circles (i.e. as r approaches a fractional value of L, this threshold can be modified in BeanCounter.m).

- *Data output.* Lastly, BeanCounter.m aggregates final particle statistics and outputs a single excel file for each EM image. If a whole directory is selected, an excel sheet containing the total statistics for each image in the directory is output. An example output can be seen in Figure 13. In addition to an excel sheet containing all population statistics, a second excel sheet is produced that contains the total nanoparticle shape yield within the analyzed population.

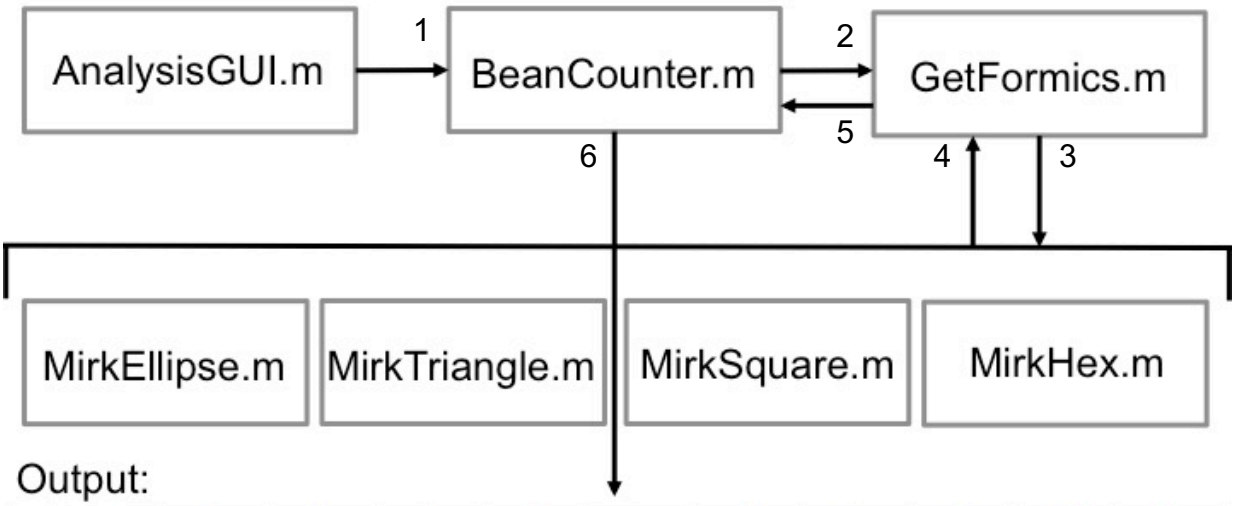

	A	B	C	D	E	F	G	H	I	J	K
1	Minor (nm)	Minor error (	AR	AR error	Rounding (nr	Rounding err	Rsq	GOF Rsq	Area (nm2)	Perimeter	Shape Identi
2	67.9784	0.059969	1.0207	0.00128	5.7335	0.0011808	0.9892	0.9892	4626	260.21	4
3	67.4554	0.064844	1.0458	0.0014275	6.1032	0.0012861	0.98733	0.98733	4666	260.764	4
4	67.2885	0.060011	1.0565	0.0013319	5.3788	0.0011661	0.98944	0.98944	4696	263.187	4
5	68.6068	0.058776	1.0045	0.0012146	4.4791	0.0010931	0.99037	0.99037	4645	262.815	4
6	67.6364	0.065247	1.0447	0.0014364	7.7549	0.0013634	0.98699	0.98699	4663	258.341	4
7	69.4591	0.059435	1.0126	0.0012215	5.6258	0.001126	0.99008	0.99008	4793	264.957	4
8	69.0072	0.060081	1.0257	0.0012679	6.048	0.0011707	0.98947	0.98947	4788	264.494	4

Figure 13. EM image processing and analysis architecture and example output, numbers indicate processing order.

2.5.6 Image processing and analysis

TEM images were directly processed in our custom MATLAB script that combines image processing and analysis steps. Image inputs were selected using a custom developed graphical user interface (GUI). This package is available free of charge via the internet on the Matlab File

Exchange (under "High-Throughput, Algorithmic Determination of Nanoparticle Structure from Electron Microscopy Images") as well as the Mirkin Group website.

2.5.7 Evaluation of Algorithm Measurement Accuracy

In order to evaluate the accuracy of our algorithmic image analysis software we compared the data from the algorithm with data calculated manually using a measurement tool common in image editing software (specifically, the "Measurement" tool in Adobe Photoshop). Two authors separately measured L_{minor} and L_{major} (and thus calculated an AR) from EM images for ~150 cubes. Figure 14 shows both manual calculations as well as the computational output. The computational data shows strong agreement with both sets of manual data.

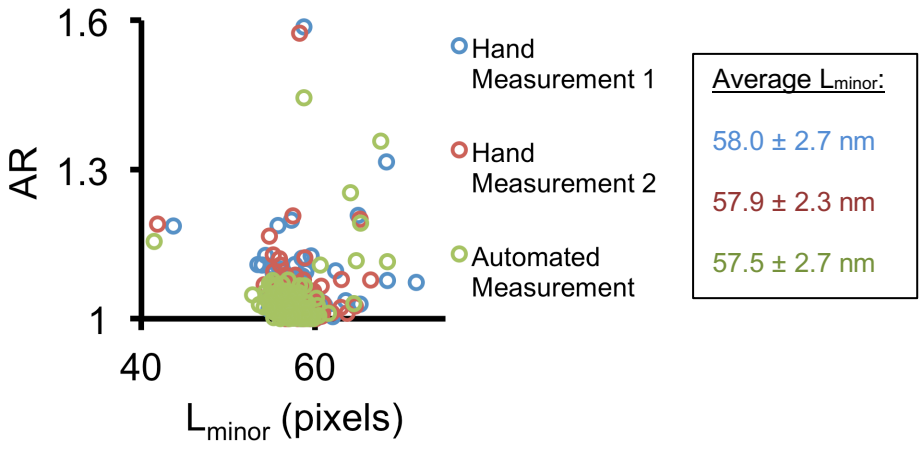

Figure 14. A comparison of computationally measured particle structure vs. manual measurements using Adobe Photoshop.

2.5.8 Triangular prism and circular disk transmission electron microscopy (TEM) sample preparation

For each time point, an aliquot of 1 mL of as synthesized particles[279] was removed from a reaction mixture (20 mL total volume) and placed in a 1.5 mL Eppendorf centrifuge tube. Immediately upon removal, the reaction was stopped by bringing the solution to 50 μM BSPP, previously shown to strongly passivate the surface of Au nanoparticles.[280] 50 μL of the stopped reaction mixture was then diluted with nanopure water to 1 mL in a 1.5 mL Eppendorf centrifuge tube and centrifuged for 11 minutes at 12,300 rcf to remove excess surfactant for imaging. The supernatant was then removed and the particles resuspended in 200 μL of nanopure water. 9 μL of the resuspended solution was drop-cast on a copper TEM grid. 1 μL of OEG solution (created by diluting 1 μL of OEG in 1 mL of nanopure water) was thoroughly mixed with the solution on the grid to protect the particles from additional oxidation during drying. The grid was placed in a vacuum desiccator until dry and imaged within 24 hours using TEM. Each time point was prepared in triplicate. Figure 15 below shows representative EM images at each time point during triangular prism dissolution.

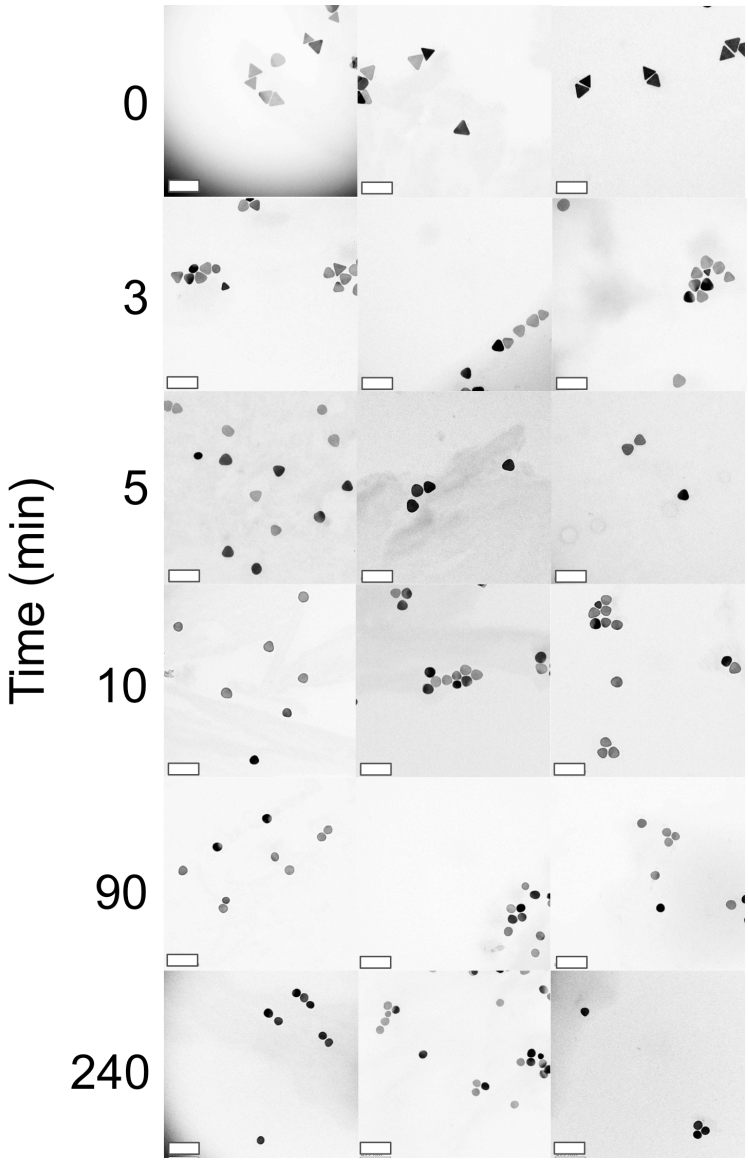

Figure 15. Three representative EM Images for each time point during prism dissolution. Scale bars represent 200 nm.

2.5.9 Reaction shape yield supplementary experiments, sample preparation, and image collection

For each condition, three 1 mL samples were prepared composed of cubes, spheres, and rods at 10, 40, and 80 pM, respectively. The solutions were then centrifuged at 5283 rcf for 12

minutes to remove excess surfactant, the supernatant was removed, and the particles were resuspended in nanopure water. 9 μL of the colloid solution was drop cast on a copper TEM grid and immediately wicked away using VWR grade 413, qualtitative filter paper (batch #FC005127) to reduce evaporative drying effects. This process was repeated 10 times. The copper grids were imaged immediately following this process. Each of the three sample conditions was prepared in triplicate drawing from the same colloid solution batch.

Concentrated stock solutions of cubes and spheres (in 50 mM CTAB) were each measured with UV-Vis following dilution with water, and concentrations were determined using Table S1. A 750 μL solution was then prepared containing cubes and spheres at 40 pM, diluted with water. This solution was then centrifuged to remove CTAB (5283 rcf, 11min) and particles were re-suspended in 750 μL of nanopure water. Next, 9 μL of the nanoparticle solution was drop cast on a copper TEM grid and immediately wicked away using filter paper to reduce evaporative drying effects. This drop casting and wicking process was repeated 10 times. Grids were prepared in triplicate using the same solution and preparation procedure. The copper grids were imaged immediately following sample preparation. Representative images for each of the three samples are shown below in Figure 16. Analysis of these samples by EM shows that spheres and cubes were found in a 1:1 ratio within experimental error (Figure 17).

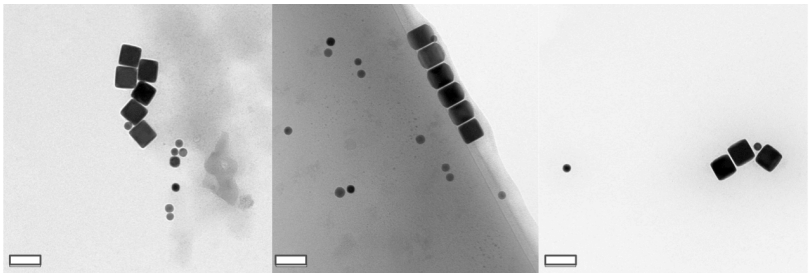

Figure 16. Representative EM images for the relative abundance study. Scale bars represent 100 nm.

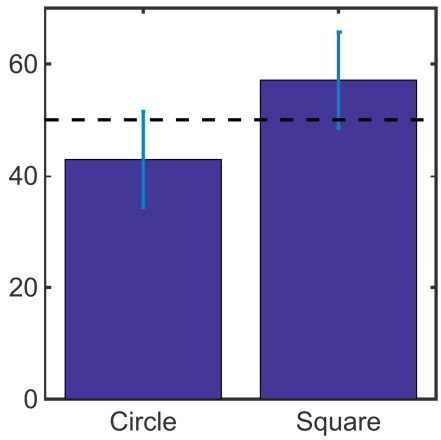

Figure 17. Relative amounts of Spheres (Circle) and Cubes (Square) calculated with automated analysis from EM images. The dashed line indicates 50% (the expected relative amount of both spheres and cubes). Error bars represent the standard deviation of three samples.

Figure 18 below shows representative EM images for each of the three experimental conditions investigated in Figure 8. In each of these conditions, a different ε was used to calculate the concentration of rods and to set an expected ratio of cube:sphere:rod of 1:4:8, respectively. Exact ε values and their sources are listed in the caption of Figure 8.

Using the nanoparticle density and magnifications described above, we find an average of 40 nanoparticles per frame. As the image does not need to be magnified, focused, or contrast-adjusted between frames, we find that imaging the 25 frames needed to accumulate ~1000 nanoparticles took ~30 minutes after the initial focusing process. Computational image analysis of these 25 images requires less than 10 minutes. In total the process of analyzing a sample requires less than one hour.

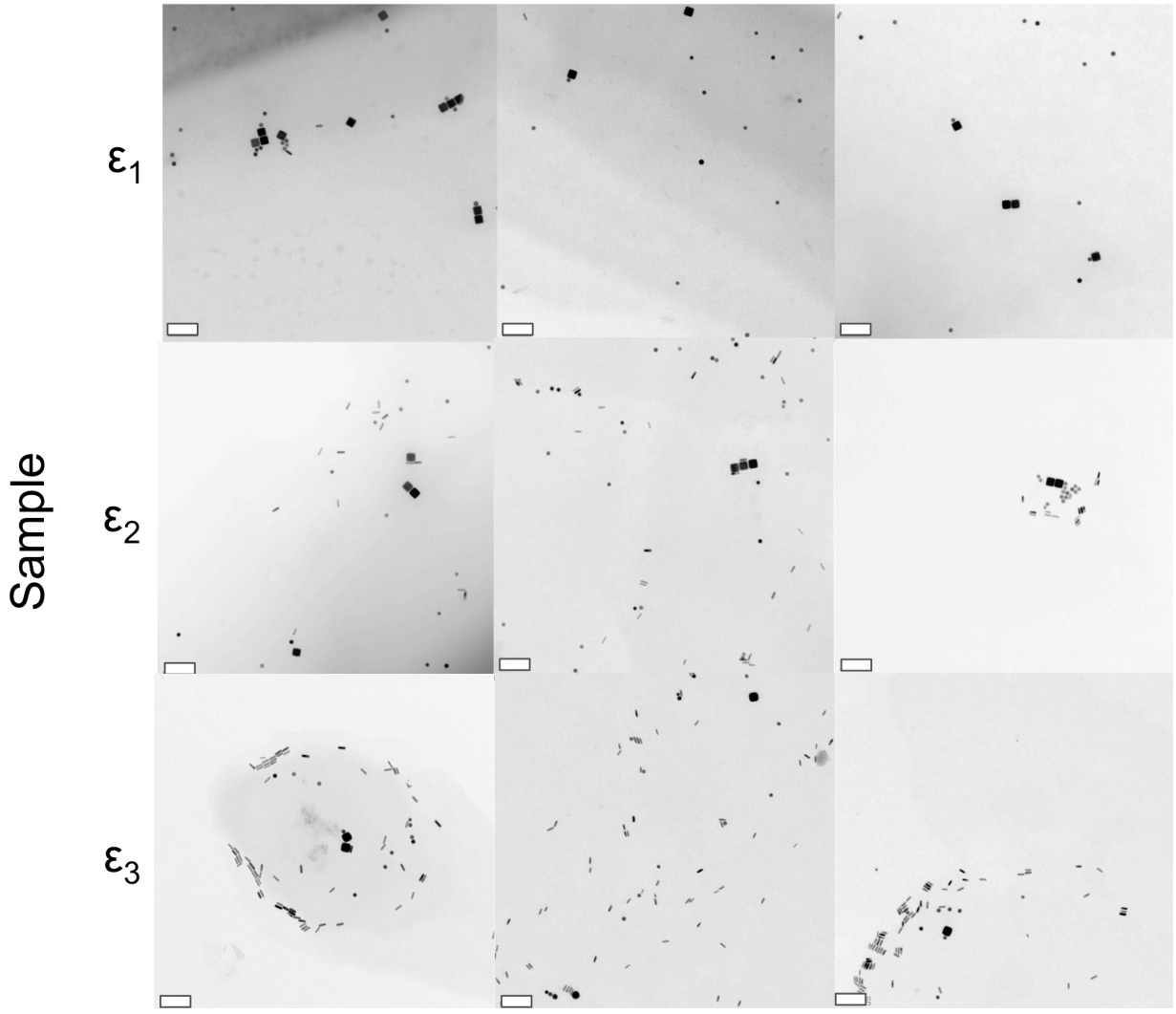

Figure 18. Representative EM images from each of the three experimental conditions investigated in Figure 8. Scale bars represent 200 nm.

SECTION TWO – BREAKING SYMMETRY IN NANOCRYSTALS

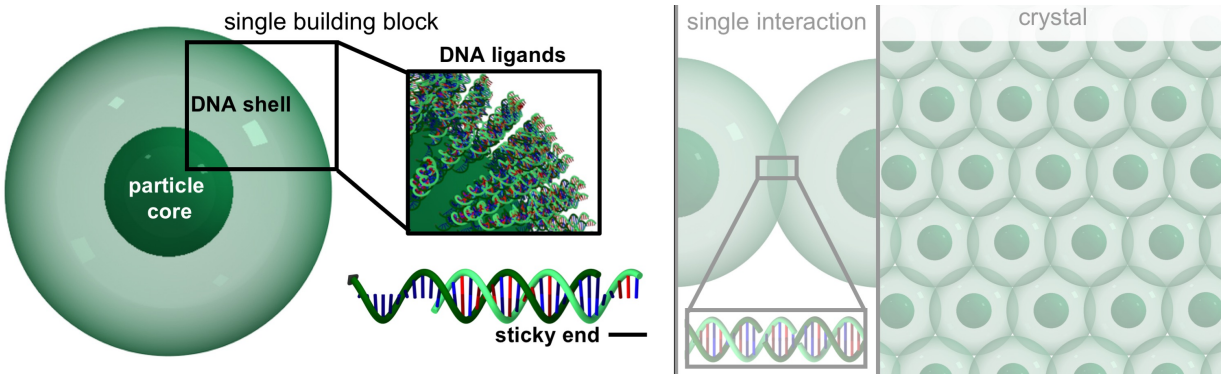

3 CHAPTER THREE: UNDERSTANDING NANOPARTICLE-MEDIATED NUCLEATION PATHWAYS OF ANISOTROPIC NANOPARTICLES

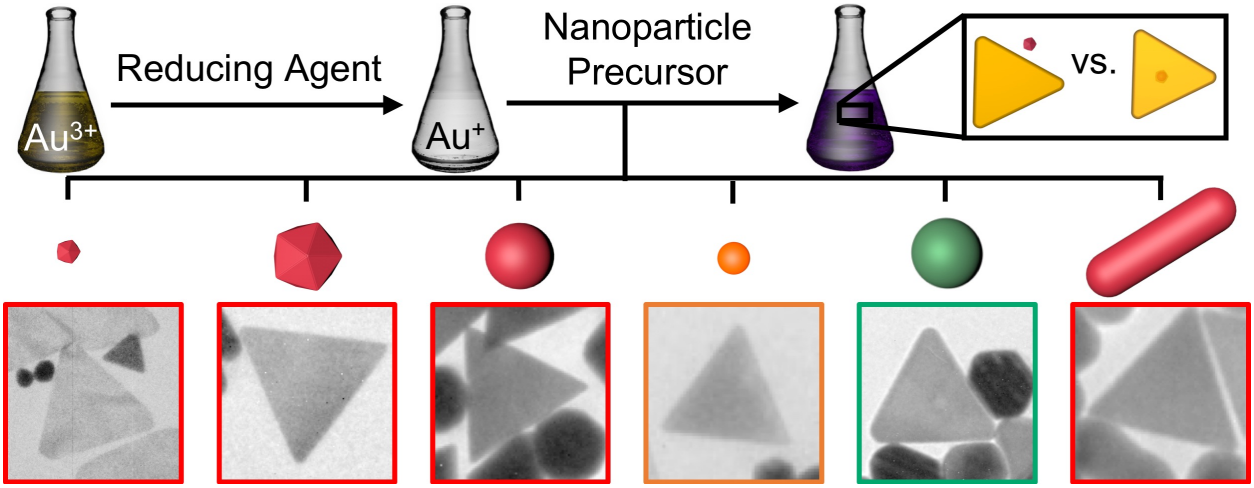

Material in this chapter is based upon published work:

C.R. Laramy,* L.K. Fong,* M. R. Jones, M.N. O'Brien, G.C. Schatz, C. A. Mirkin. *Chemical Physics Letters* **2017**, *683*, 389-392.

3.1 Abstract

Several seed-mediated syntheses of low symmetry anisotropic nanoparticles yield broad product distributions with multiple defect structures. This observation challenges the role of the nanoparticle precursor as a seed for certain syntheses and suggests the possibility of alternate nucleation pathways. Herein, we report a method to probe the role of the nanoparticle precursor in anisotropic nanoparticle nucleation with compositional and structural "labels" to track their fate. We use the synthesis of gold triangular nanoprisms (Au TPs) as a model system. We propose a mechanism in which, rather than acting as a template, the nanoparticle precursor catalyzes homogenous nucleation of Au TPs.

3.2 Background

The "seed-mediated" approach to nanoparticle synthesis has enabled reproducible control of nanoparticle structure and dramatic improvements in nanoparticle uniformity over earlier synthetic techniques.[4, 12, 232, 234, 265, 281] In this approach, pre-formed nanoparticle "seeds" are added to a solution of atomic precursors in the presence of a molecular reducing agent, as a means to spatiotemporally separate particle nucleation (*i.e.* seed formation) from growth. The underlying hypothesis of this approach centers on the use of nanoparticle precursors that act as static structural templates for heterogeneous nucleation. This hypothesis is supported by experiments that show a strong relationship between the size, shape, and defect structure of seeds and products.[12, 232, 264, 265, 282-284]

However, even with highly uniform seed populations, certain "seed-mediated" syntheses remain limited by product distributions with multiple defect structures suggesting that, in some cases, the nanoparticle precursors may "mediate" nanoparticle growth in a reaction-dependent,

rather than universal manner.[285-287] The synthesis of gold triangular prisms (Au TPs) poses an interesting example of this phenomenon (Figure 19).[266, 288] While many Au TP syntheses make use of nanoparticle precursors, it is unclear what role these precursors play.[244, 266, 289, 290] One possibility is that they act as structural templates (i.e. seeds) for heterogeneous nucleation. Two primary pieces of evidence have been used to support this hypothesis: 1) addition of particle precursors initiates the growth of Au TPs and 2) the size of the Au TPs can be tailored through careful changes in the relative concentrations of particle and Au ion precursors.[288] An alternative, and more intriguing, possibility for the role of the precursor is suggested by several striking differences that exist in the synthesis of Au TPs relative to other seed-mediated syntheses. The products of this reaction differ in their defect structure: Au TPs have a planar-twinned defect structure parallel to their {111}-triangular cross-section,[244] while other products possess a multiply-twinned defect structure (decahedra and icosahedra).[291] Further, there are many syntheses with diverse reducing agents, capping ligands, shape-directing additives, nanoparticle precursor defect structures, or no nanoparticle precursors at all that produce Au TPs as products.[292-295] This suggests that arguments for crystal facet blocking and "seed" defect structure being responsible for anisotropic particle growth may not fully explain the growth of Au TPs.[244, 264, 281, 289, 296-300] Additionally, recent work has shown that multiple chemical equilibria can compete at a particle surface beyond the simple reduction of additional material.[232, 301] Therefore, we hypothesize that nanoparticle precursors play a more intricate chemical role beyond simply templating growth in the nucleation of Au TPs.

Herein, using the synthesis of Au TPs as a model system, we systematically explore the role of the nanoparticle precursors as a function of their composition, crystal symmetry and shape.[266]

In each experiment, the Au TP synthesis "growth solution" remains constant while nanoparticle precursor morphologies, defect structures, and compositions are deliberately varied to track the fate of the nanoparticle. Importantly, we find that in many cases the nanoparticle precursor does mediate the synthesis of Au TPs, but it does not act as a template for Au TP growth (*i.e.* reside inside of the final nanoparticle). Instead, Au TPs are the result of homogeneous nucleation favored by the presence of and proximity to catalytic nanoparticle precursors in the system. While nanoparticle precursors often act as seeds, their role as catalysts can, in some cases, be as important or even more important than their role as templates.

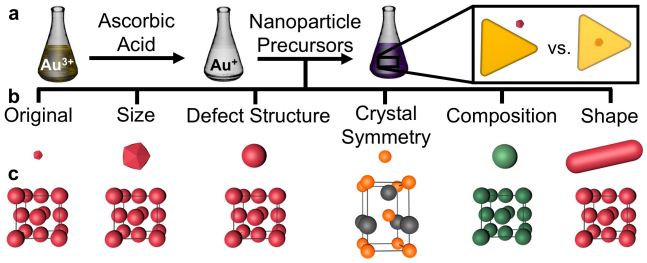

Figure 19. The nucleation pathway of Au TPs can be probed by the systematic substitution of different nanoparticle precursors under identical reaction conditions. a) Schematic shows graphical representation of synthesis conditions. b) Nanoparticle precursors with deliberately varied size, defect structure (single crystalline), crystal symmetry (wurtzite), composition (Pd), and shape (aspect ratio > 1) with respect to the original particle precursors. c) Unit cells for each particle precursor in b). Note: atoms are drawn smaller relative to their unit cell for clarity.

3.3 Results and Discussion

3.3.1 Using particle precursor lattice structure to probe nucleation of Au TPs

One implication of the current understanding of seed-mediated synthesis is that the defect structure of the initial seeds determines the potential reaction products. In the case of the Au TPs, this implication suggests that some population of nanoparticle precursors must have a planar twinned defect structure in order to template planar twinned products.[120] To directly test this understanding in the Au TP synthesis, the original nanoparticle precursors[266] - a heterogeneous

mixture of particles that vary in size and defect structure – were substituted for uniform, well-characterized particles (Figure 22). The size and shape of all particle precursor populations were rigorously characterized using software that enables quantitative analysis of electron microscopy (EM) images of ~10^3 particles per sample.[7]

The products from Au TP syntheses performed with multiply-twinned and single-crystalline particle precursors were first directly compared. To minimize the effect of high mobility of surface atoms in small nanoparticles (~5 nm), large (~20 nm) Au particles were used (Figure 20).[302, 303] Interestingly, substitution of small particle precursors for large multiply-twinned or single-crystalline particles both produced Au TPs (Figure 20, Figure 23). This experiment suggests that particle precursor defect structure does not dictate the formation of Au TPs. Further, atomic force microscopy (AFM) of Au TPs grown from multiply-twinned Au particles reveals that Au TPs are smaller than the initial particle precursors (Figure 24-Figure 26). These results suggest that Au TPs may not be templated by heterogeneous nucleation onto "seeds", but instead result from homogeneous nucleation and subsequent growth.

3.3.2 Particle precursor composition enables one to track its fate

In order to directly test the hypothesis that Au TPs form as a product of homogeneous nucleation, the original gold nanoparticle precursor was substituted with a particle that would make heterogeneous nucleation and subsequent epitaxial growth of gold onto its surface energetically unfavorable. Wurtzite CdSe@ZnS quantum dots (QDs) were chosen as a substitute (Figure 27), as they have a large symmetry and lattice mismatch compared to FCC gold.[304] Although there have been reports of epitaxial growth of FCC metals onto transition metal chalcogenide nanocrystals[305,

[306], such a large lattice mismatch makes epitaxy unlikely under the mild, aqueous conditions of the Au TP synthesis. Interestingly, with wurtzite QD precursors, this synthesis produced Au TPs in yields comparable to those using the original Au particles, 29% (Figure 20, Figure 23). EM reveals circular holes and concave features on the Au TPs as well as pseudo-spherical impurity products (Figure 20, Figure 28, Figure 29). In addition, we observed the presence of small particles of low contrast relative to the Au TPs; EDX analysis of these particles indicates the presence of Cd (Figure 20, Figure 28). As expected, Au was found in the Au TPs as well as the pseudo-spherical impurity products, but no Cd was identified. These data support the hypothesis that Au TPs are products of a homogeneous nucleation growth pathway.

With strong evidence in support of the homogeneous nucleation of Au TPs, a compositionally distinct precursor closely mimicking the original Au TP synthesis was next used to track the fate of the particle precursor.[307] In particular, a large Pd particle was chosen, because Pd has a similar crystal structure to Au, and the particle can be easily identified in Z-contrast TEM images (Figure 20, Figure 30, Figure 31).[4] Interestingly, the Au TPs synthesized with Pd particle precursors had circular and concave edge features similar to those synthesized with QDs (Figure 20). SEM images revealed that these features were holes and EDX identified that in most cases Pd was absent from these holes (Figure 20, Figure 31, Figure 32). Conversely, while little Pd was found in Au TPs, Pd formed the core of most pseudo-spherical impurity products.

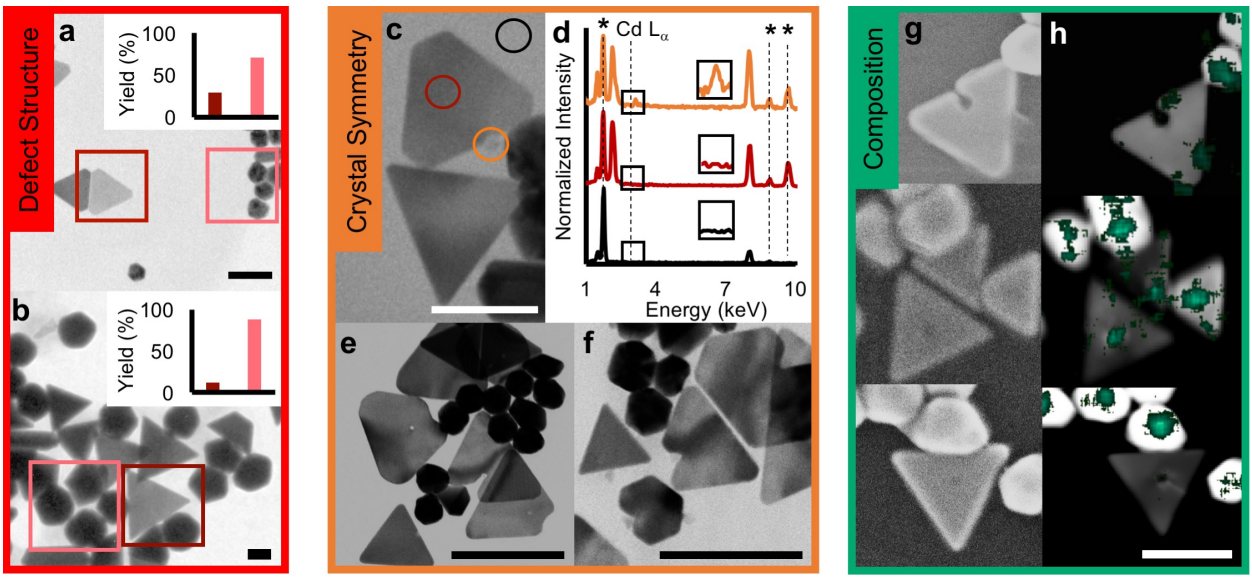

Figure 20. Au TP synthesis with multiply twinned Au (17 ± 1.6 nm), single-crystalline Au (26 ± 1.6 nm), CdSe@ZnS (5.7 ± 1.5 nm) and Pd particles (22.7 ± 3.9 nm). Syntheses with all particles produce Au TPs. Scale bars represent 100nm. a) Synthesis with multiply-twinned Au particles yield 29% Au TPs. b) Synthesis with single-crystalline Au particles yield 12% Au TPs. d) EDX analysis of Au TPs synthesized with QD particles over selected regions in c) indicated by colored circles. Colors correspond to plot. e,f) Representative EM images of Au TPs synthesized with QD particles showing holes, concave features, and low contrast particles. g) Representative SEM images of Au TPs synthesized with Pd particles. h) EDX maps of images on left. Green indicates Pd L signal.

3.3.3 Development of a mechanism for Au TP nucleation

The presence of hole features and the absence of Pd and Cd in the AuTPs suggest a similar nanoparticle-mediated homogeneous nucleation pathway for both the Pd and QD nanoparticle precursors (Figure 21). In particular, we propose that Au TPs form in proximity to nanoparticle precursors. This hypothesis is supported by closer inspection of the hole sizes found in the Au TPs, which were of similar size to the particle precursors (Figure 29, Figure 33, Figure 34). Since homogeneous nucleation of Au particle products requires the reduction of an aqueous Au species, nucleation of Au TPs near the surface of Pd and QD particles suggests that nanoparticle precursors can function as catalysts for nucleation through either the direct channeling of an electron to Au^{+} or the stabilization of small molecule reducing agents (ascorbate/ascorbyl radical) which promotes reduction of Au^{+} (Figure 21, path **1**). Additionally, the presence of Pd at the core of impurity

particles implies that the nanoparticle precursors may also induce heterogeneous nucleation, in agreement with seed-mediated particle synthesis literature (Figure 21, path **2**).[308-310] In both paths **1** and **2**, ascorbic acid is identified as the predominant electron source based on reaction stoichiometry, the amount of electrons required for the reduction of gold, and the final pH of the reaction (Table 2). Lastly, in this synthesis, it is evident that a nanoparticle precursor must also be present in order for nucleation to occur (Figure 35). Interestingly, while a variety of nanoparticle precursor compositions have been shown to catalyze this reaction, there are exceptions. For example, ~20 nm TiO_2 precursors did not catalyze the nucleation of Au TPs (Figure 35-Figure 38). This suggests that the interactions between the particle precursor and the molecular species in solution, such as ascorbic acid, are significant and that the presence of a nanoscale surface alone is not sufficient for catalysis. Cumulatively, these data suggest that the same nanoparticle precursor population may be both structurally (Figure 21, path **2**) and catalytically (Figure 21, path **1**) relevant for product nucleation.

In order to test the proposed mechanism for a gold particle precursor system, we hypothesized that the growth of Au TPs could be prevented or promoted by varying reaction conditions to favor either heterogeneous or homogeneous nucleation, respectively. Homogeneous nucleation was favored by providing fewer sites for heterogeneous nucleation (e.g. reduce particle precursors or "seed" concentration) or by increasing the pH of the reaction (e.g. increase strength of reducing agent).[311] Here, particle precursor shape was used as a probe. Under high concentrations of Au single-crystalline rod precursors (aspect ratio = 3.6 ± 0.7) and low pH (pH = 3.4) conditions, heterogeneous nucleation is favored and, in support of the proposed mechanism, Au TPs were not observed as products (Figure 39). However, as the Au rod concentration

decreased or the pH increased, Au TPs appeared as products. Further, many impurity products with an aspect ratio greater than one were observed, in support of path **2** (Figure 21). These observations suggest that Au TP nucleation likely occurs by the same nanoparticle-catalyzed mechanism with gold particle precursors (Figure 21).

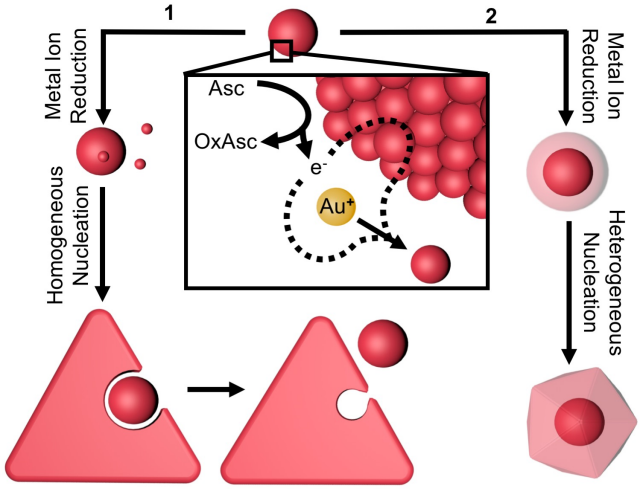

Figure 21. Proposed mechanism for alternate role of the nanoparticle precursors. Path **1**: The precursor stabilizes the reducing species (Asc: ascorbate or ascorbyl radical, OxAsc: ascorbyl radical or dehydroascorbic acid) such that it can donate electrons to reduce Au^{+} to Au^{0} and produce Au nuclei. Path **2**: The precursor acts as a template for metal reduction and subsequent growth of pseudospherical impurity particles (e.g. acts as a seed).

3.4 Conclusion

Cumulatively, this work points toward an alternative role by which nanoparticle precursors can mediate particle synthesis. With respect to the Au TP synthesis, the ability to produce the same structure (Au TPs) from nanoparticle precursors of diverse size, defect structure, and composition strongly suggests a similar underlying homogeneous nucleation mechanism catalyzed by nanoparticle precursors. More broadly, this work highlights the fact that the role of nanoparticle precursors is reaction dependent. For example, a catalytic role of precursors may explain the

distribution of product defect structures associated with some classes of "seed-mediated" syntheses, which often include shape-directing additives (e.g. Ag^+, I^-). This observation suggests that shape-directing additives in the growth solution may not only direct the product morphology, but also the product nucleation pathway. Furthermore, these results are consistent with the large body of, often high-yielding, "seedless" syntheses for certain classes of anisotropic nanoparticles, which rely on controlled homogeneous nucleation. Looking forward, improved experimental understanding of early homogeneous nucleation time points (*e.g. in situ* techniques) would build on this investigation and shed light on the structure of the nuclei as well as the nature of symmetry breaking. Ultimately, while improving the uniformity of the seed often leads to improved uniformity in products, the chemical environment and nature of the particle precursor also play significant, and in some cases dominant, roles in dictating both the uniformity and shape of the resultant products.

3.5 Experimental Details and Supplementary Materials

3.5.1 Materials

The following chemicals were purchased and used as received. Cetyltrimethylammonium bromide (CTAB, >99%) was purchased from bioWorld. Sodium borohydrate ($NaBH_4$, >99%), tetrachloroaurate trihydrate ($HAuCl_4$, >99%), L-ascorbic acid (AA, >99%), silver nitrate ($AgNO_3$, >99%), sodium hydroxide (NaOH, powder, 97%), Titanium(IV) Oxide 21nm particles (powder, >99.5%) and sodium chloride (NaCl, >99%) were purchased from Sigma-Aldrich. Multiply-twinned Au particles and CdSe@ZnS particles were purchased from Ted Pella and Invitrogen, respectively. Thiolated oligoethyleneglycol (OEG) was purchased from ProChimia.

3.5.2 Au TP Growth Solution

Au TP were synthesized according to a literature procedure with modifications.[266] Briefly, 9 mL of 50 mM cetyltrimethylammonium bromide (CTAB) was brought to 50 μM sodium iodide. To this 250 μL of 0.01M chloroauric acid, 50 μL of 0.1M fresh sodium hydroxide and 50 μL of 0.1M fresh ascorbic acid was added. This was defined as the growth solution for each experimental condition. Next this solution was brought to a set concentration of nanoparticle precursor. Concentrations ranged from 5 to 500 pM for the synthesis of Au TP with Au multiply-twinned, Au single-crystalline, QD, and Pd single crystalline particles. For TiO_2 particle experiments, concentrations ranged from 1 to 1000 pM. For low particle concentration experiments with Au single-crystalline spheres and rods, concentrations ranged from 0.1 pM to 1 pM. All glassware was rinsed with aqua regia prior to use.

3.5.3 Nanoparticle precursor concentration determination

Au particle concentration was determined through a UV-Vis spectroscopy measurement in combination with the Beer-Lambert Law. An extinction coefficient was calculated based on particle size, shape and composition. For spherical particles the extinction coefficient can be calculated analytically based on Mie Theory. In order to determine the size of the particles, algorithmic analysis of EM images of at least 100 nanoparticles was performed.[7] ICP-MS was used to determine the concentration of Pd particles. QD particle concentrations were given by the manufacturer. A known mass of TiO_2 particles were first suspended in 50 mM CTAB to produce a concentrated stock solution for subsequent experiments

3.5.4 Nanoparticle synthesis

Single crystalline, Au spherical particles [12] and Au rods[267] were synthesized according to literature protocol.

Single-crystalline Pd cubes were synthesized according to a literature protocol.[4] Immediately post-synthesis of ~22 nm Pd cubes, particles were centrifuged (30 minutes, 15,000 rpm) and resuspended in 50mM CTAB twice. 0.5 mL aliquots of particles were exposed to a range of aqua regia dilutions (2,000 to 20,000x dilution) at 85°C for one hour. After, one-hour test batches were evaluated with EM to determine which produced the most uniform, spherical Pd particles. The full batch was subsequently exposed to the same dissolution conditions to produce a uniform batch of single-crystalline spherical Pd particles. All glassware was rinsed with aqua regia prior to use.

3.5.5 Characterization techniques

The resulting particle products from the above syntheses were characterized by EM (Hitachi H8100 200keV, Hitachi HD-2300 200keV), UV-Vis spectroscopy (Agilent Cary 5000), AFM (Bruker Dimension Icon), selected area electron diffraction (SAED) and energy-dispersive x-ray (EDX) spectroscopy.

3.5.6 EM sample preparation

Typically, an aliquot of sample (Au TP products or particle precursors) was diluted to 1.5 mL with nanopure water in a 1.5 mL Eppendorf centrifuge tube, centrifuged (10 minutes at 10,000 rpm for Au TP products, 20 minutes at 15,000 rpm for particle precursors unless otherwise noted),

and resuspened in nanopure water to approximately four times the volume of the original aliquot. 1 μL of a dilute solution (1 μL in 1 mL) of OEG was added to 9 μL of the above diluted particle solution to a final volume of 10 μL. This volume was deposited on a copper TEM grid. For EDX studies OEG was omitted.

3.5.7 pH measurement

All pH measurements were carried out using a Mettler Toledo FiveEasy pH meter. The meter was washed three times with nanopure water before each measurement.

3.5.8 Characterization of nanoparticle precursors

EM and UV-Vis Spectroscopy represent powerful techniques for characterizing nanoparticle structure. In particular, when paired with algorithmic analysis techniques, EM can provide population level statistics about particle structure, analogous to global techniques like UV-Vis spectroscopy.[7] All particles used as precursors for each Au TP synthesis were characterized using algorithmic analysis of EM images as well as with UV-Vis Spectroscopy (Figure 22).

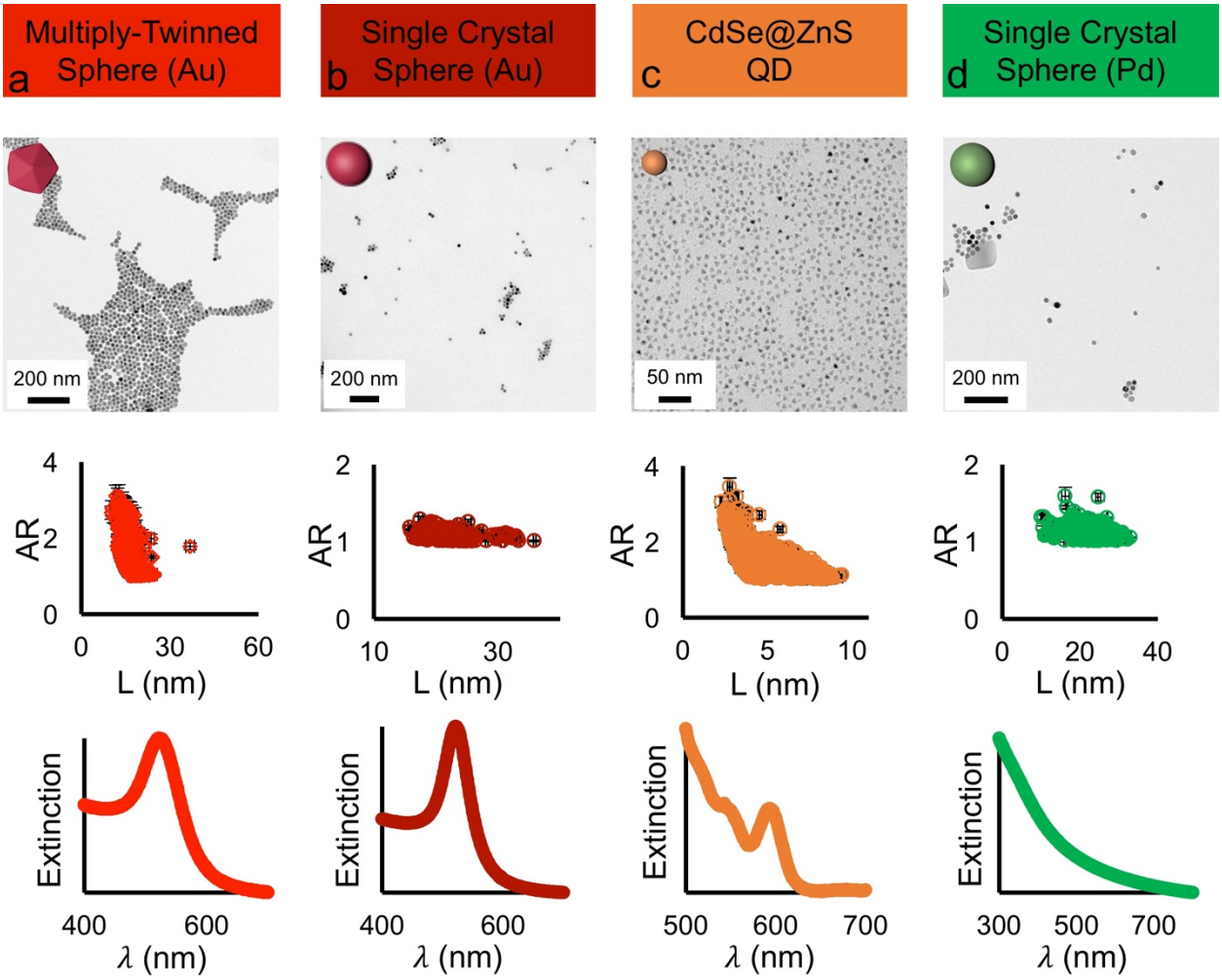

Figure 22. EM and UV-Vis Spectroscopy enable characterization of particles for use as precursors in Au TP growth. (Top) Representative EM image of particles. (Middle) Algorithmic analysis of EM images to determine particle diameter (L) and aspect ratio (AR). (Bottom) UV-Vis spectroscopy of particles. a) Multiply-twinned Au particles purchased from Ted Pella. Middle plot shows algorithmic analysis of EM images of 1,667 particles (d = 16.3 ± 1.8 nm).[7] b) Single crystalline Au spheres synthesized by the O'Brien et al. method.[12] Middle plot shows algorithmic analysis of EM images of 364 particles (d = 22.5 ± 3.0 nm). c) CdSe@ZnS particles purchased from Invitrogen. Middle plot shows algorithmic analysis of EM images of 1,997 particles (5.7 ± 1.5 nm). d) Single crystalline Pd spheres synthesized by a modified version of the Niu et al. method.[4] Middle plot shows algorithmic analysis of 657 particles (d = 22.7 ± 3.9 nm).

3.5.9 Selected area electron diffraction of Au TP

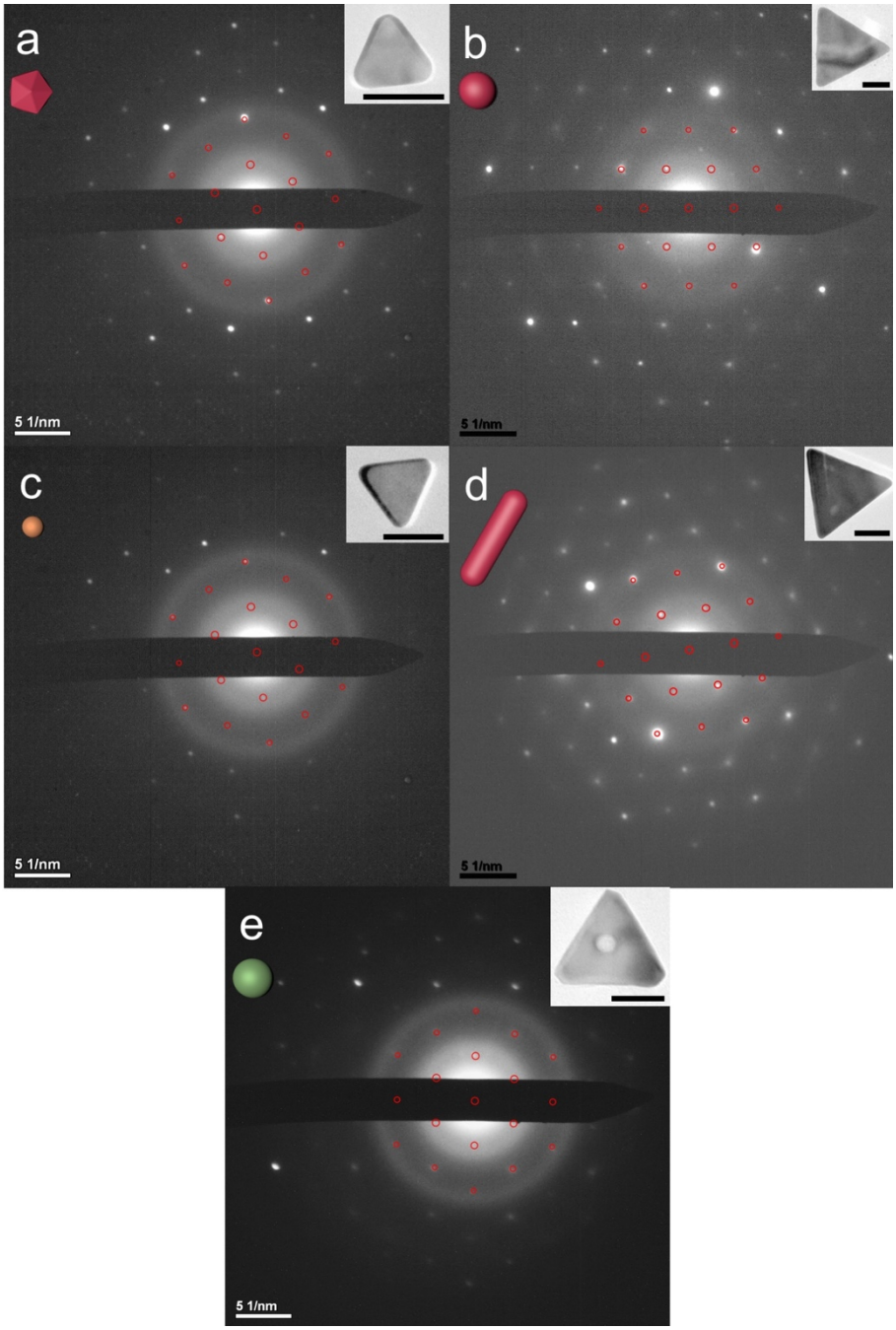

Figure 23. Selected area electron diffraction of Au TP grown with a) multiply-twinned Au NP precursors, b) single crystalline Au NP precursors, c) CdSe@ZnS NP precursors, d) single crystalline Au rod NP precursors, e) single-crystalline Pd sphere NP precursors. Insets show Au TP. Scale bars represent 50nm. Simulated patterns for {111}-Au plane are overlaid in red. The d-spacing for each sample (0.243nm, 0.248nm, 0.252nm, 0.240nm follows the expected value for {111}-Au plane (0.236nm).

3.5.10 Atomic force microscopy (AFM) of Au TP

AFM and EM are complimentary techniques for probing particle structure. In order to accurately calculate Au TP thickness from AFM measurements, the thickness of the surfactant bilayer (e.g. CTAB) must be taken into account. First, the combined thickness of Au TP and the surfactant bilayer can be determined from AFM for a standard sample (Figure S3, 12.1 nm). Next, the thickness of the Au TP alone from the same sample can be determined from EM measurements (Figure S4). This requires Au TP to be driven to assemble on their thin edge dimension using high concentrations and slow drying conditions (Figure S4, 7.9 ± 1.5 nm). Subtraction of the EM

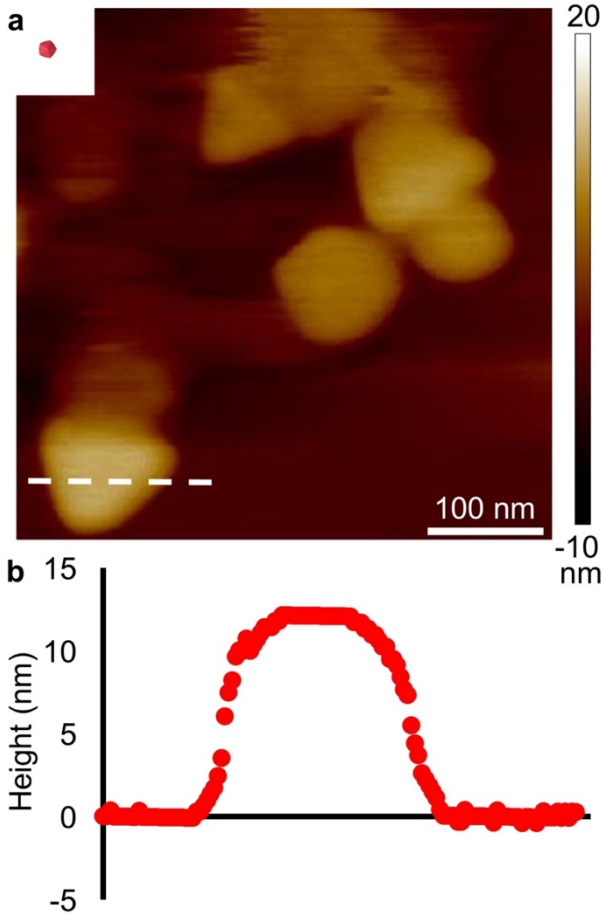

Figure 24. AFM analysis of Au TP grown from original, small multiply-twinned Au particles (3.1 ± 0.9 nm) shows Au TP and CTAB bilayer have a combined height of 12.1 nm. a Height map of Au TPs and pseudospherical impurity products. b Height at every point along the dashed line in a.

thickness from the AFM thickness reveals the thickness of the CTAB bilayer (2.1 nm per bilayer, two bilayers per Au TP). This measurement of the CTAB layer enables AFM alone to be used to calculate Au TP thickness for additional samples. AFM measurement of Au TP grown with large, multiply-twinned particles (16.3 ± 1.8 nm) reveal the height (or thickness of thin edge dimension) of Au TP in combination with a thin CTAB bilayer. Subtraction of the CTAB bilayer reveals a thickness of 11.4 nm. Interestingly, this is thicker than the value calculated for Au TP grown from small, multiply-twinned NP precursors but is still smaller than particles added as "seeds."

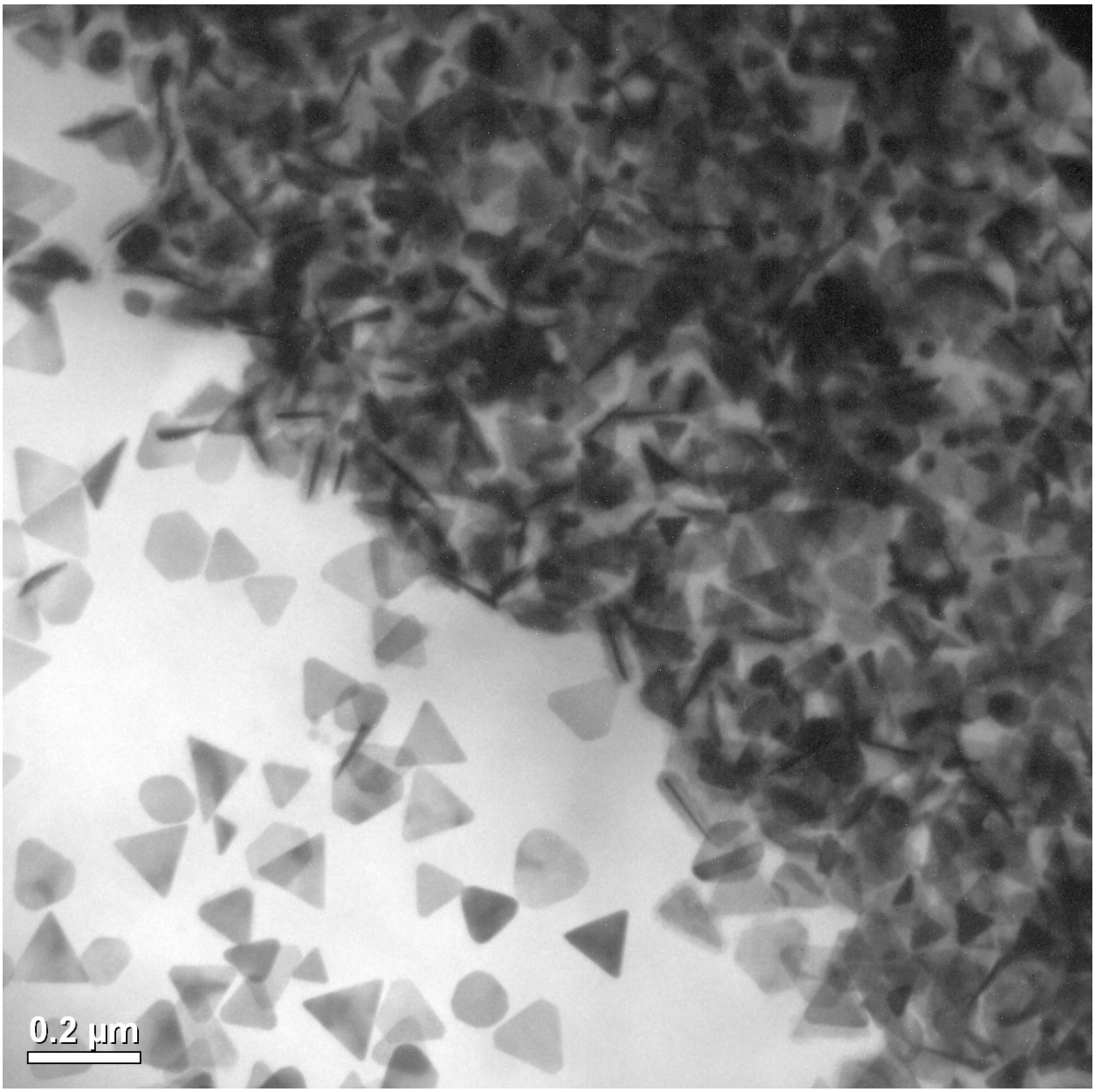

Figure 25. Representative EM image of Au TP grown from original, small multiply-twinned particles (3.1 ± 0.9 nm) assembling on their edge face. Analysis of 93 Au TP reveals that Au TP are 7.9 ± 1.5 nm along their thin edge dimension. Red arrows indicate examples of Au TP assembled on their edge.

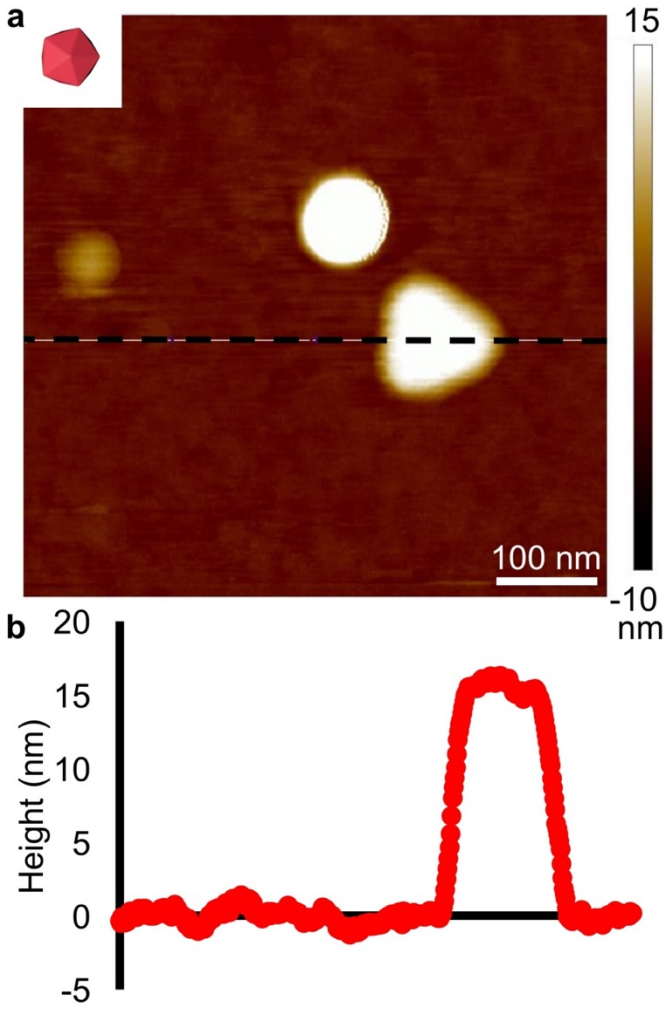

Figure 26. AFM analysis of Au TP grown from large multiply-twinned Au particles (d = 16.3 ± 1.8 nm) shows Au TP and CTAB bilayer have a combined height of 15.6 nm. a Height map of Au TP and pseudospherical impurity product. b Height at every point along dashed line in a.

3.5.11 X-ray diffraction of QD particles

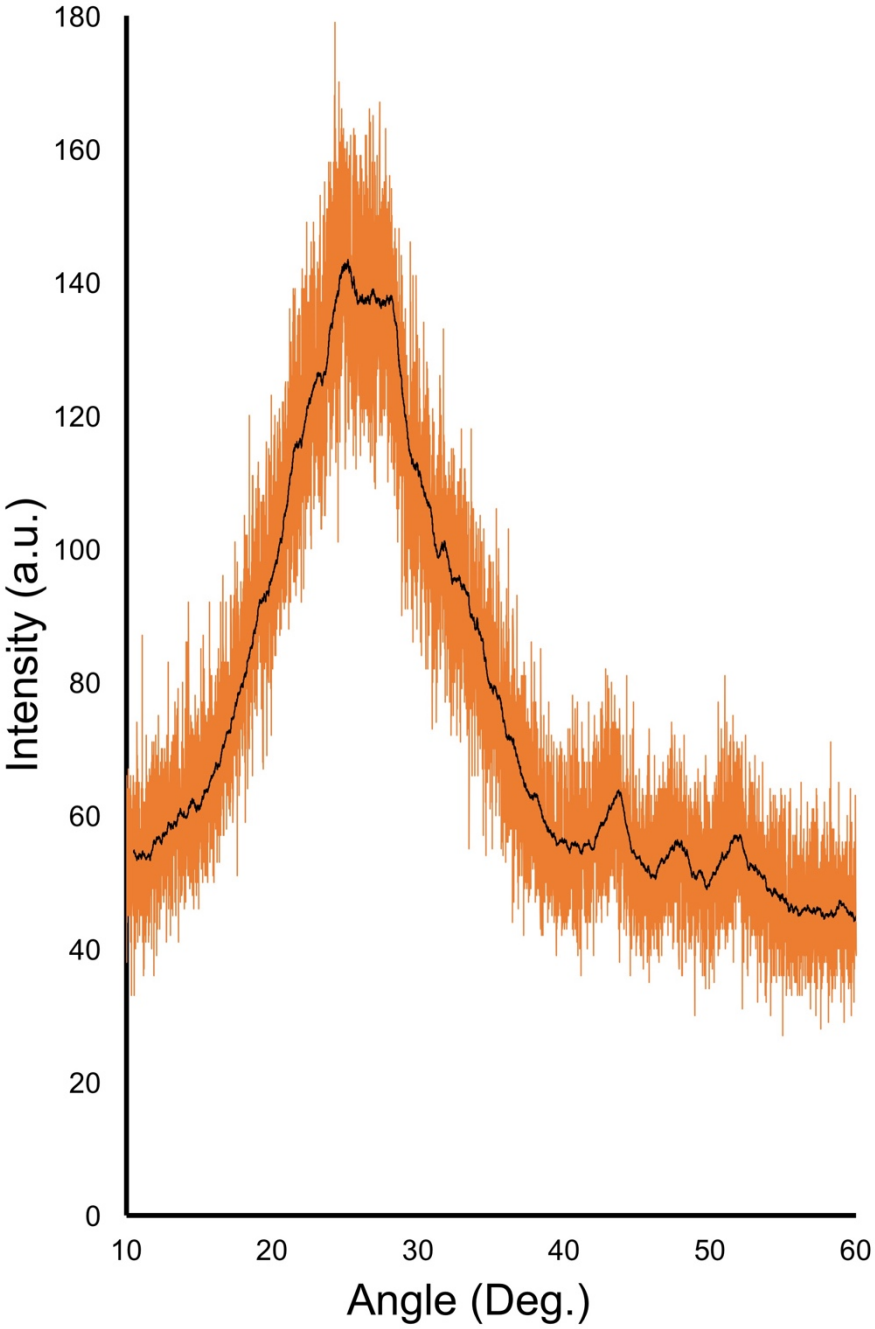

Figure 27. X-Ray diffraction (XRD) enables characterization of CdSe@ZnS particles. Orange trace represents raw data collected at 1.54 Å at a scan rate of 0.006 degrees/measurement. Black trace represents a moving average of the raw data, effectively down sampling to a scan rate of 0.5 degrees/measurement.

Figure 27 shows XRD data consistent with a small CdSe@ZnS core shell particle with a wurtzite crystal symmetry.[304] The broadness of the peaks may be explained by the small size of the particles and the large size distribution.

Lattice mismatch is calculated by the following equation:

$$\%\ \boldsymbol{Lattice\ Mismatch} = \frac{\boldsymbol{a_{surface} - a_{layer}}}{\boldsymbol{a_{surface}}}\ \boldsymbol{x\ 100\%}$$

Therefore, the lattice mismatch between Au (FCC, a = 0.4078nm) and ZnS (Wurtzite, a = 0.3811nm, c = 0.6234nm) is 7% in two directions and 34.6% in the third direction.

3.5.12 EDX characterization of Au TP products from QD particle precursors

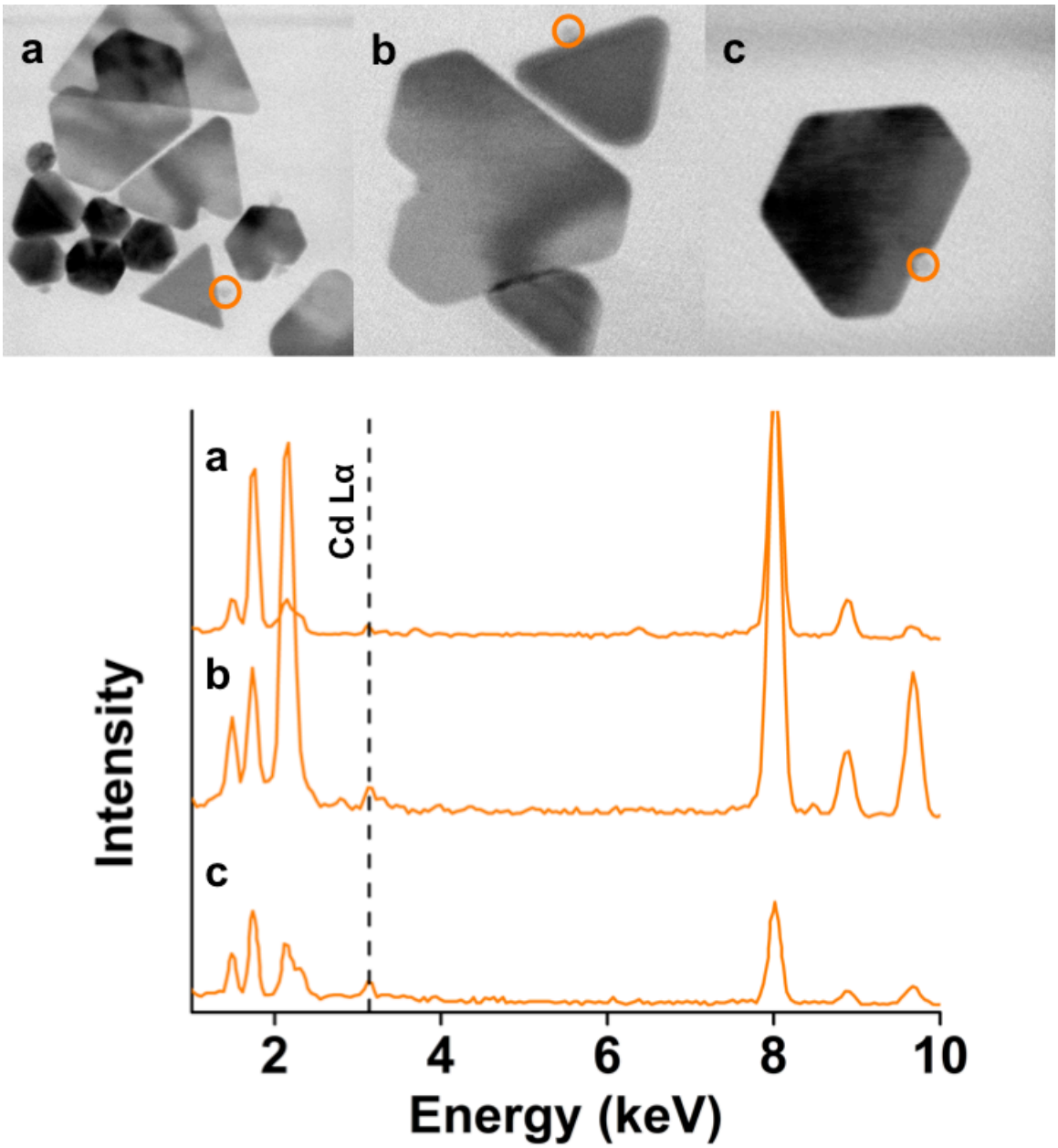

Figure 28. EDX analysis of three separate Au TP samples (a, b, c) synthesized with CdSe@ZnS NP precursors identifies the composition of nanoparticle products. EDX of low contrast particles close to the gold prism surface demonstrates the presence of cadmium.

3.5.13 TEM characterization of Au TP products from QD particle precursors

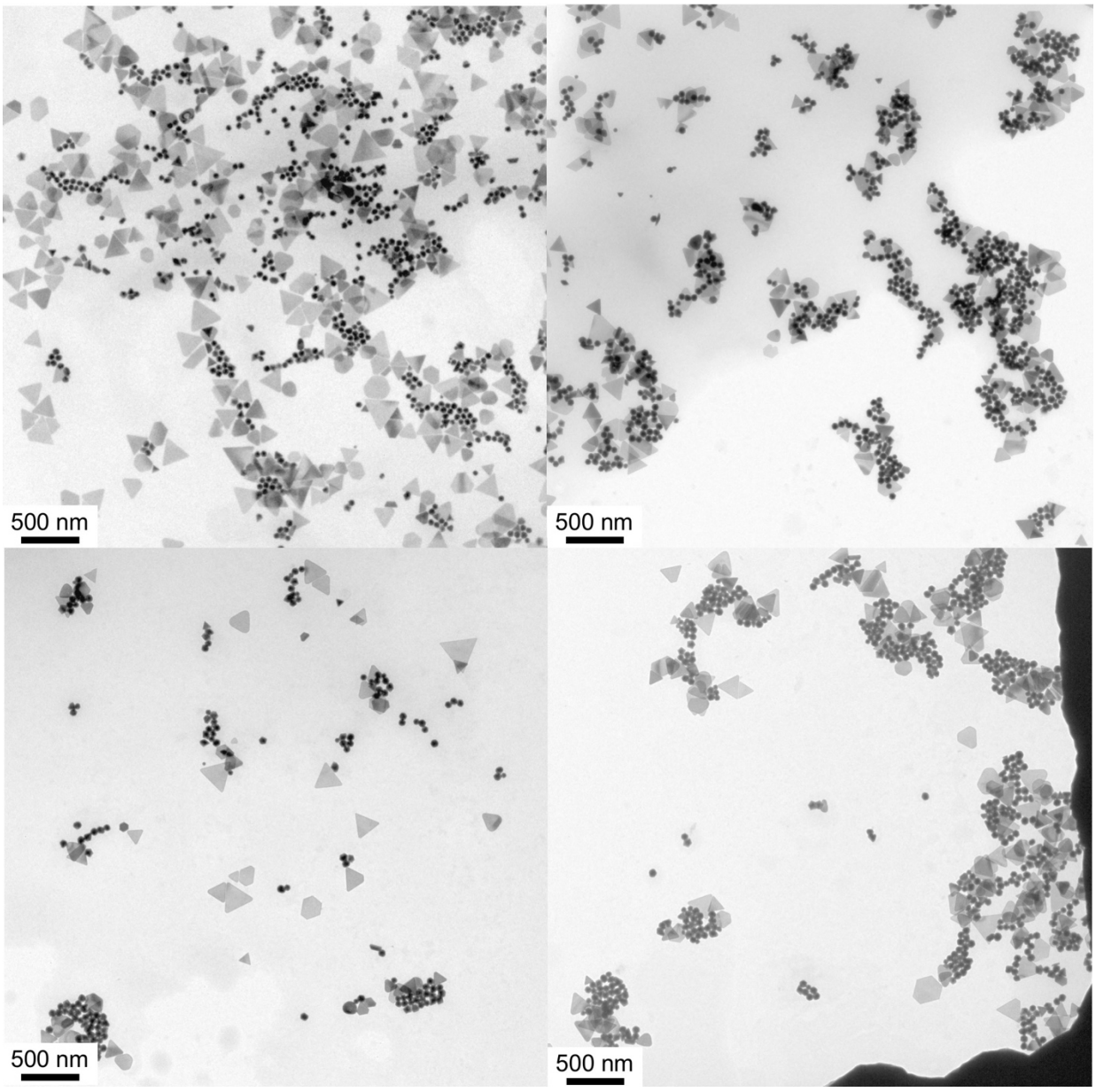

Figure 29. Representative TEM images show the products of the Au TP synthesis when CdSe@ZnS particles are used as NP precursors.

Concave edge features and holes were observed in the Au TP products synthesized with QD particles. Measurement from EM images of these features reveals that the average hole diameter is (5.88 ± 1.3 nm, n = 24 particles) comparable to the size of the QD particles. Features

of this size (~5nm) are highly prone to Au rearrangement which limits the accuracy of size measurement. Further, concave edge features appeared with greater frequency than holes. In order to study this phenomenon further and with greater accuracy, the same measurements were performed on the resultant products of larger particle precursors (e.g. Pd).

3.5.14 Synthesis of Pd spheres from Pd cubes

Pd single crystalline spheres were synthesized based on a Pd single crystalline cube synthesis by Niu et. al.[4] Briefly, as synthesized Pd cubes were centrifuged for 25 minutes at 11,000 rpm and resuspended in 50mM CTAB, twice. The cubes were brought approximately 1 OD (λ = 338) in 50mM CTAB. This solution was brought to 85°C. Aqua regia was added such that the final dilution was 20,000x. After 1 hour the solution was centrifuged for 25 minutes at 11,000 rpm and resuspended in 50mM CTAB, twice. This solution was used as a concentrated NP precursors solution for subsequent Au TP growth experiments.

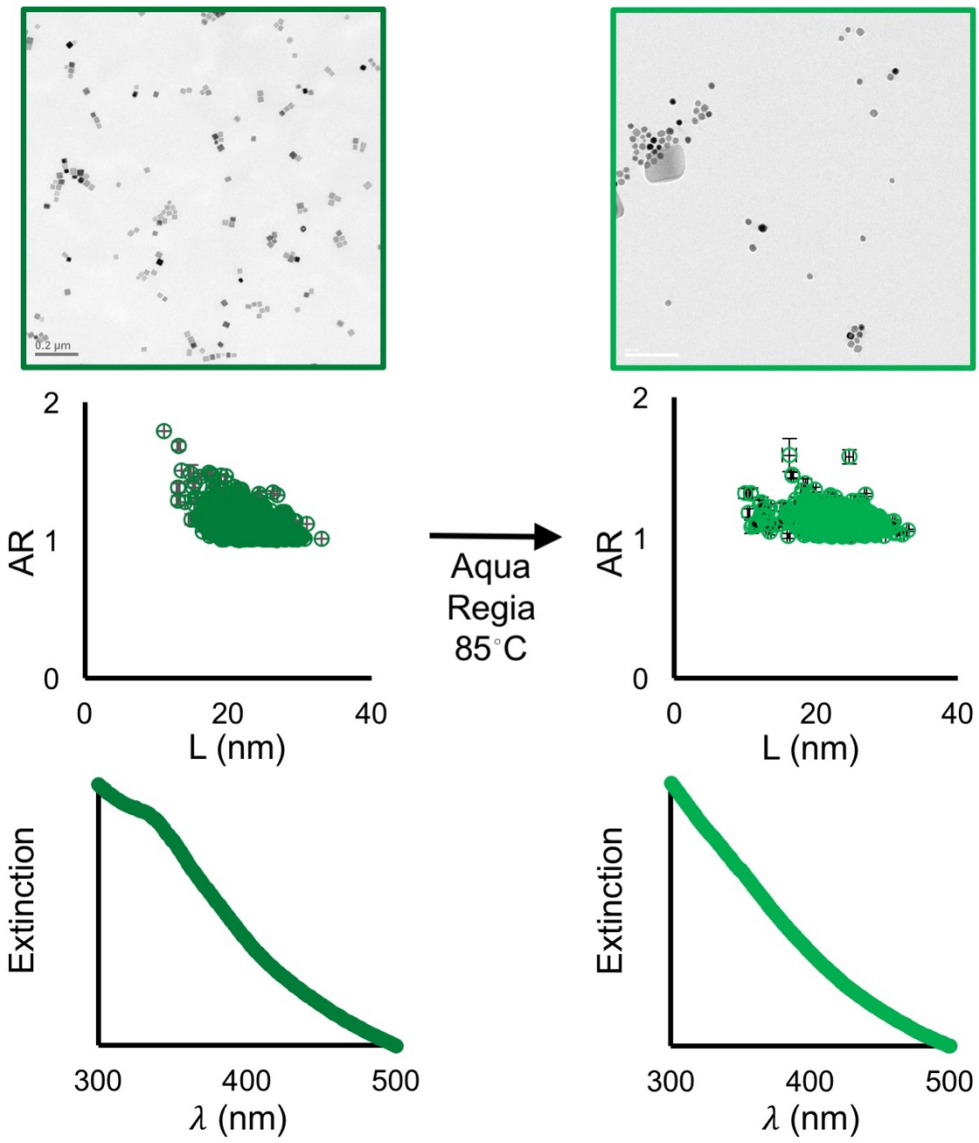

Figure 30. Characterization of Pd particles before and after etching treatment. Initial synthesis follows method by Niu et al. method.[4] Algorithmic EM and UV-Vis Spectroscopy characterization of a Pd single crystalline cubes and b Pd single-crystalline spheres.[7]

3.5.15 EDX spectroscopy of Au TP products grown from Pd particle precursors

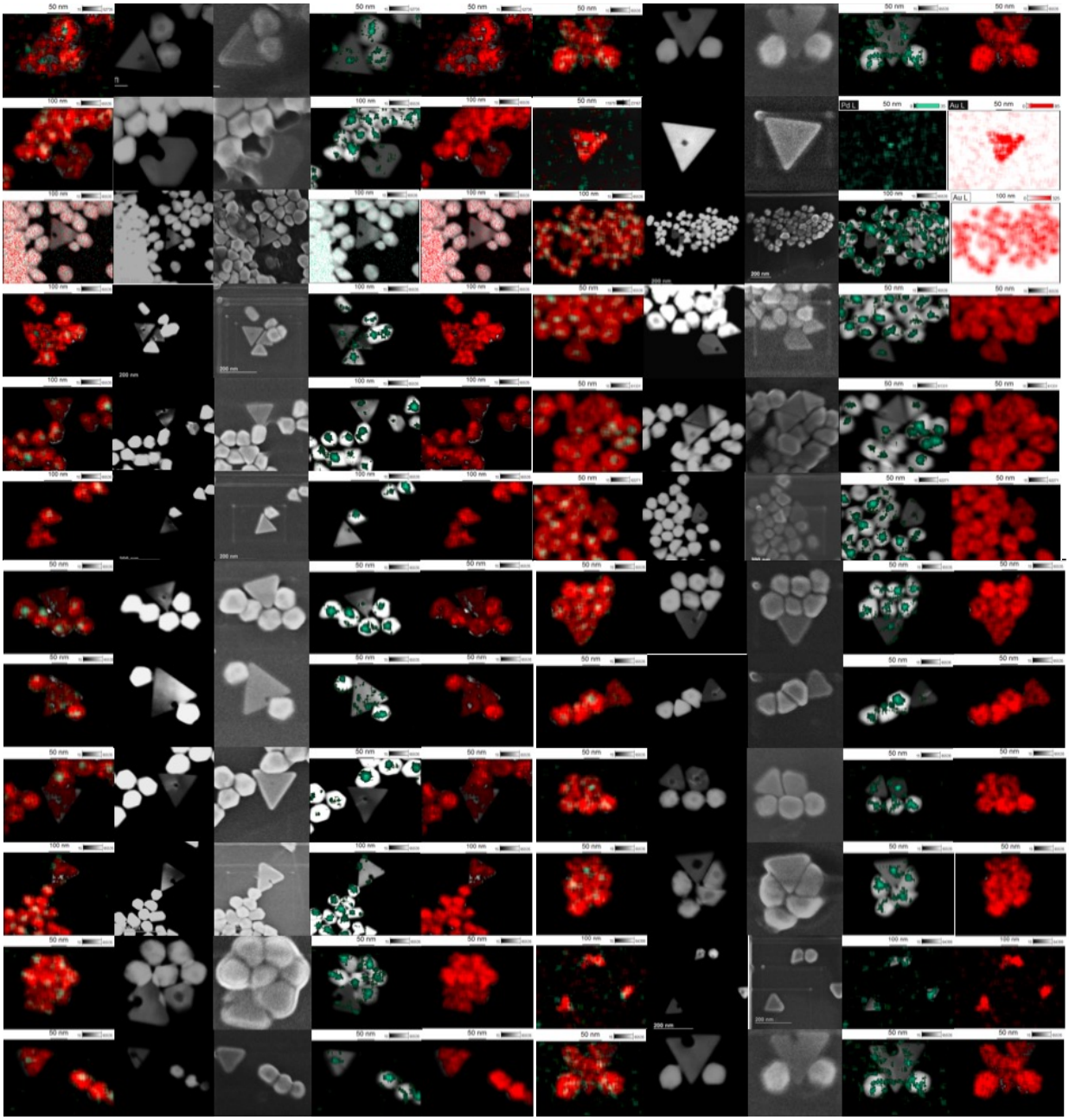

Figure 31. EDX analysis identifies composition of Au TP products when grown from Pd NP precursors. From left to right, images show a compositional overlay of Au and Pd onto the TEM image, a TEM image, a SEM image, a compositional overlay of Pd onto the TEM image, and a compositional overlay of Au onto the TEM image.

With respect to the pseudospherical impurity particles, the Pd particle study indicates that the particle precursors may act as templates for the impurity products. Intuitively, this observation

makes sense since palladium and gold are both FCC metals with similar lattice parameters (lattice mismatch of 4.6%). The presence of palladium at the core of impurity particles implies that the same particle population may be both structurally (e.g. act as a seed) and chemically (e.g. act as a catalyst) relevant for product nucleation. In comparison, the QD particle was not observed in the core of impurity particles. This may be a result of the low X-ray emission intensity of cadmium relative to gold. Alternatively, this may suggest that the nanoparticle precursor can catalyze homogeneous nucleation of products other than Au TP. This implication is supported by the population of pseudospherical impurity products from the Pd particle study with a core composed of entirely gold, as opposed to palladium (Figure S10).

3.5.16 Characterization of Pd core in products grown with Pd particle precursors

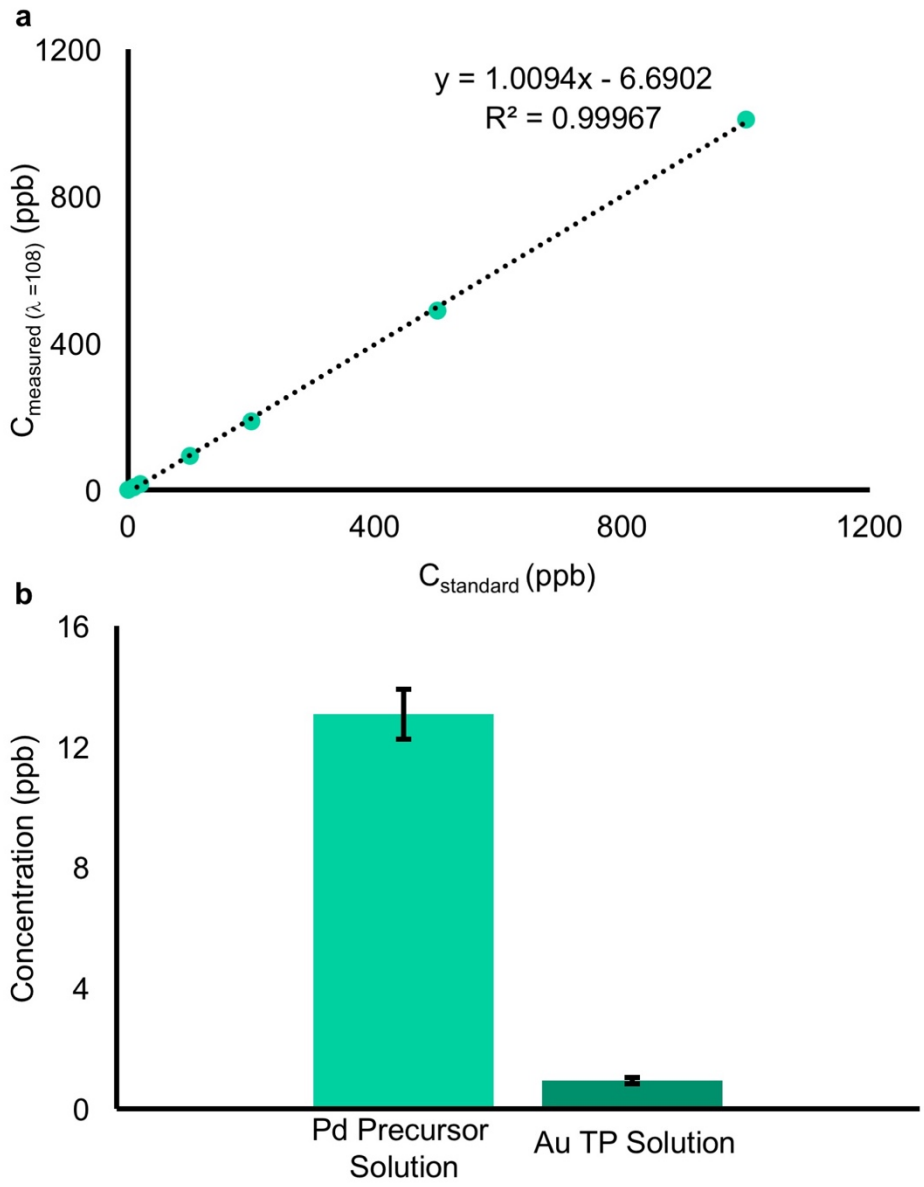

Figure 32. ICP-MS measurements show that the concentration of palladium species in solution in the supernatant of an Au TP synthesis is less than in the supernatant of the Pd particle precursors. a) The standard curve used to determine concentration with ICP-MS. b) Measured concentration of palladium in the supernatant of a solution of 5 pM Pd particle precursor and in the supernatant of a solution of Au TP grown from 5 pM Pd particle precursor. Error bars represent the standard deviation of 3 measurements.

The presence of palladium on the surface of Au TP and other products may be explained by the trace amounts of remaining Pd^{2+} in the Pd particle precursor solution. In order to test this 50

mL of two comparable solutions were prepared. One was a solution of Pd particle precursors brought to 5 pM in 50 mM CTAB with 50 μM NaI. The second solution was a standard Au TP growth solution using 5 pM Pd particle precursors. After 24 hours, three 10 mL aliquots of each solution were centrifuged twice at 10,000 rcf for 90 minutes to remove solid nanoparticles. The solutions were brought to 1% (by volume) of HCl to ensure solubility of remaining Pd^{2+} in solution. Each of these aliquots was stored at 4 °C for 12 hours to precipitate CTAB. These solutions were then centrifuged, the supernatant collected, stored at 4 °C for one hour, and repeated until CTAB crystals were no longer present. ICP-MS was performed on both sets of solutions to determine palladium concentration. Similar to gold, palladium may be reduced by ascorbic acid so the Pd^{2+} in the Pd particle precursor solution may be the source of palladium found on the surface of the products of the Au TP synthesis with Pd particle precursors.

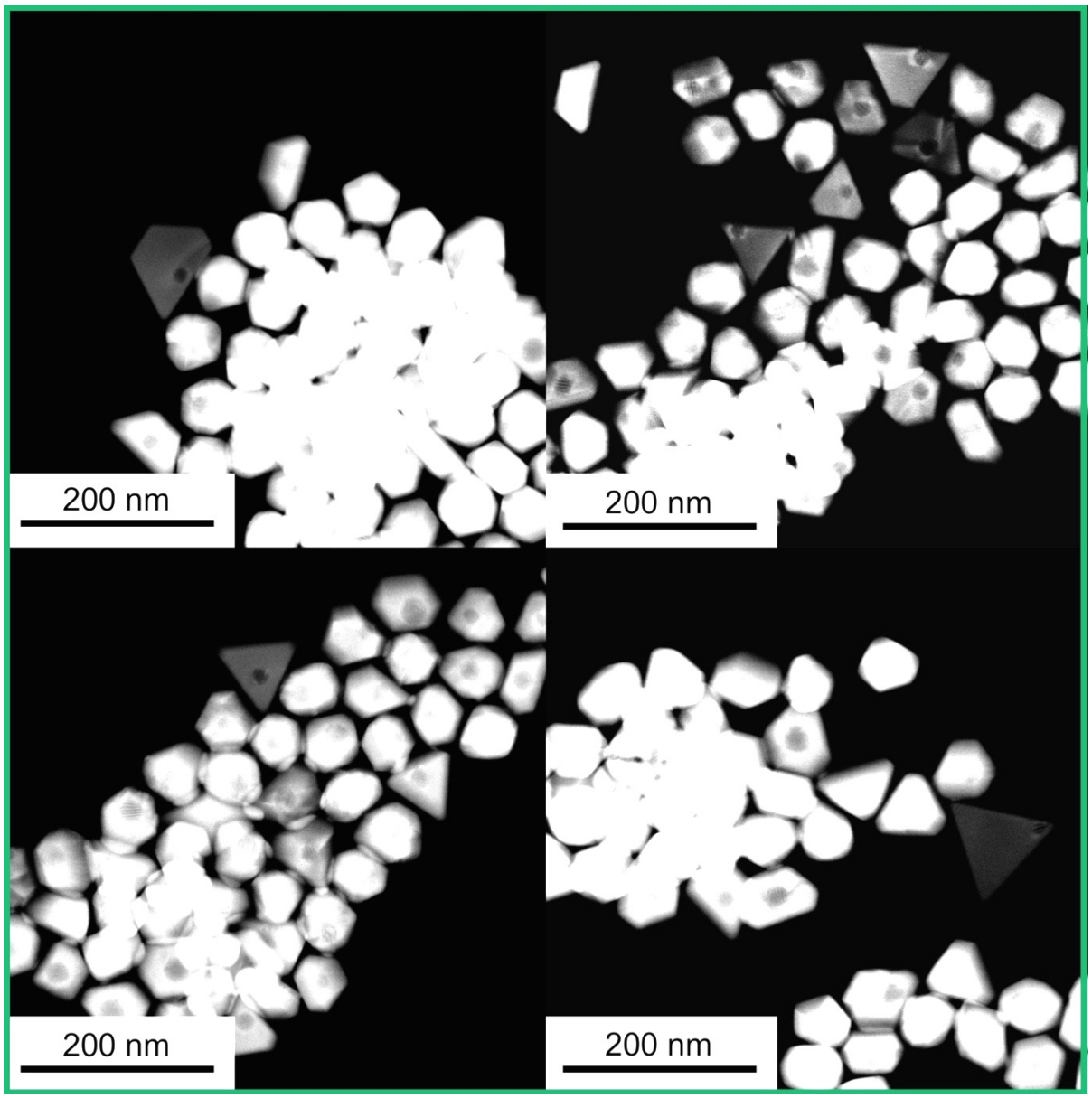

Figure 33. Representative Z-Contrast TEM images of Au TP and pseudospherical impurity particles synthesized with Pd NP precursors show Pd particles at the core of pseudospherical impurity products. Z-Contrast TEM uses particle thickness to create a difference in intensity. Therefore, lighter particles represent thin plate-like shapes, such as Au TP. Intensity is also determined by elemental identity. Palladium appears darker than gold (due to a difference in electron density) resulting in the darker cores observed in most of the pseudospherical impurity particles. These darker cores were measured from Z Contrast TEM images to determine the size of Pd cores.

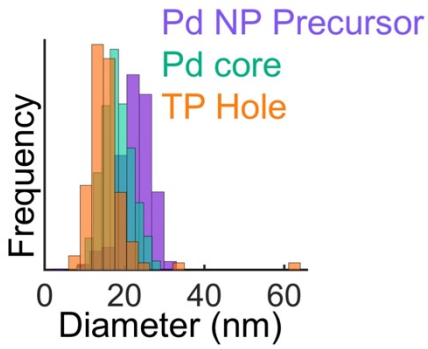

Figure 34. Histogram of size distribution of initial Pd particle precursors, the size of the Pd core in pseudospherical impurity products, and the hole found in resultant Au TPs shows that NP precursor size decreases. The size of the hole in Au TP is comparable to the size of the Pd core in the pseudospherical impurity products.

Additionally, catalysts often undergo degradation processes. The Millstone group recently highlighted the possibility of competing reductive and oxidative processes at the nanoparticle surface.[301] Therefore, an additional source of palladium may be a result of oxidative dissolution of Pd particle precursors. Indeed, EM measurements revealed that the Pd core volume in the pseudospherical impurity products was 48% smaller than the initial Pd NP precursors (SI Figure S12, S13). This reduction in size poses an interesting potential source of electrons in the system which may partially contribute to the reduction of Au ions (accounting for <1% of the total electrons required for reduction of all Au^{1+} to Au^{0} based on the density of palladium and assuming all Pd^{0} oxidizes to Pd^{2+} and all Au^{3+} has been reduced to Au^{1+}). Section XI discusses the likely primary electron source. A more in depth study of this process would benefit from the development of additional techniques for characterizing the redox properties of nanoparticles, which likely differ from bulk properties. Note: Although EM measurements represent one of the best available techniques for determining the size of the Pd cores, it is also possible that this technique may underestimate the size of the core.

3.5.17 Characterization of Pd core in products grown with Pd particle precursors

Ascorbic acid may donate up to two electrons per molecule to reduce Au. Each oxidation event results in the loss of one proton per ascorbic acid. Here, we use these deprotonation events as a proxy for the potential number of electrons donated by ascorbic acid into the reaction system (Table 2). The values in the "Expected pH" column are determined using the pH measured from the growth solution prior to ascorbic acid and nanoparticle precursor addition to calculate the initial $[H^+]$. The changes in pH are monitored from the initial addition of nanoparticle precursors (t = 0) through 90 minutes after addition. The final pH indicates that ~1.5 protons/ascorbic acid are in solution. Since two molar equivalents of ascorbic acid are added to one molar equivalent of $HAuCl_4$, this suggests that ascorbic acid provides enough electrons to reduce all Au^{3+} to Au^0.

Table 2. pH measurements of Au TP growth solutions before and after nanoparticle precursor addition suggest ascorbic acid protonation state.

Experiment	Expected pH	Measured pH
CTAB NaI $HAuCl_4$ NaOH	NA	6.33 ± 0.05
+Ascorbic Acid	3.27 ($1H^+$: 1AA)	3.2 ± 0.05
+NP Precursor t = 0	3.27	3.22 ± 0.05
t = 30 min	3.1 - 2.97 (1.5-$2H^+$: 1AA)	3.08 ± 0.05
t = 90 min	3.1 - 2.97	3.06 ± 0.05

3.5.18 Characterization of resultant Au TP solution with TiO_2 particle precursors

As a negative control, 21nm TiO_2 particle precursors are shown to be unable to induce nucleation of Au TP. In order to test this, Au^+ concentration in a series of experimental conditions was monitored with UV-Vis. Au^+ concentration would remain constant if nucleation does not occur. Since the CTAB:Au^+ complex has a characteristic peak at 260nm, the absorption at this wavelength may be monitored as a proxy for Au^+ concentration. Experimental conditions with TiO_2 particle concentrations spanning several orders of magnitude were monitored with UV-Vis spectroscopy. After 24 hours, the absorption at 260nm between every experimental condition was comparable to that of a growth solution without added nanoparticle precursors (Figures S14-S17).

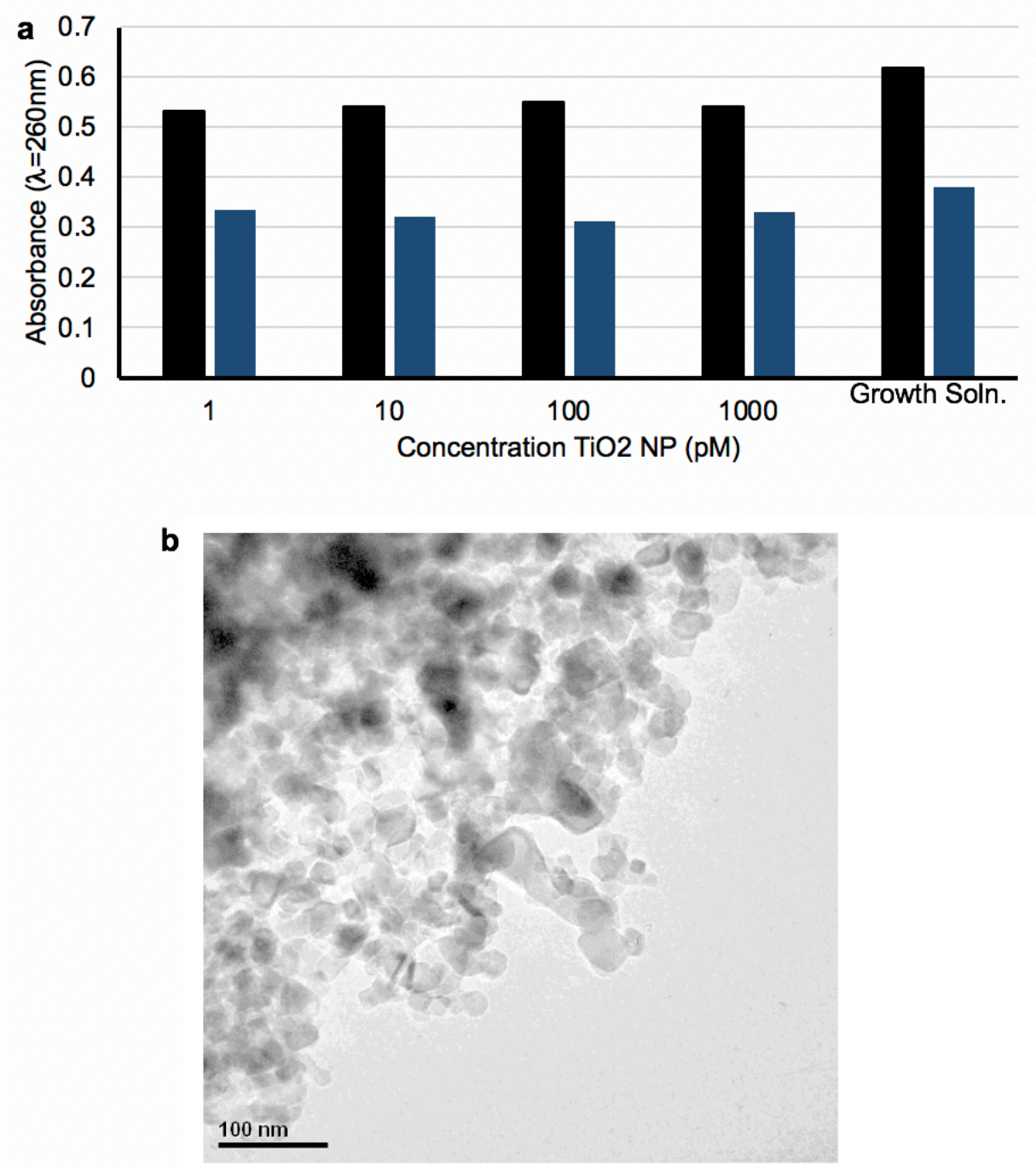

Figure 35. Analysis of resultant solution from Au TP synthesis with TiO_2 particle precursors. a) Au TP growth solutions with and without TiO_2 (21nm) nanoparticle precursors show comparable changes in absorption (260nm) over a 24-hour period. Black bars indicate the initial absorption for each growth solution before nanoparticle precursor addition. Grey bars show absorption after 24 hours. b) TEM image of TiO_2 found in AuTP growth solution with 1000pM TiO_2 nanoparticle precursor added. Solution was concentrated 10-fold for imaging, but less than 10% of grid space was occupied. No evidence of gold nucleation was found among agglomerated TiO_2. An average diameter of 23nm was measured for non-agglomerated particles.

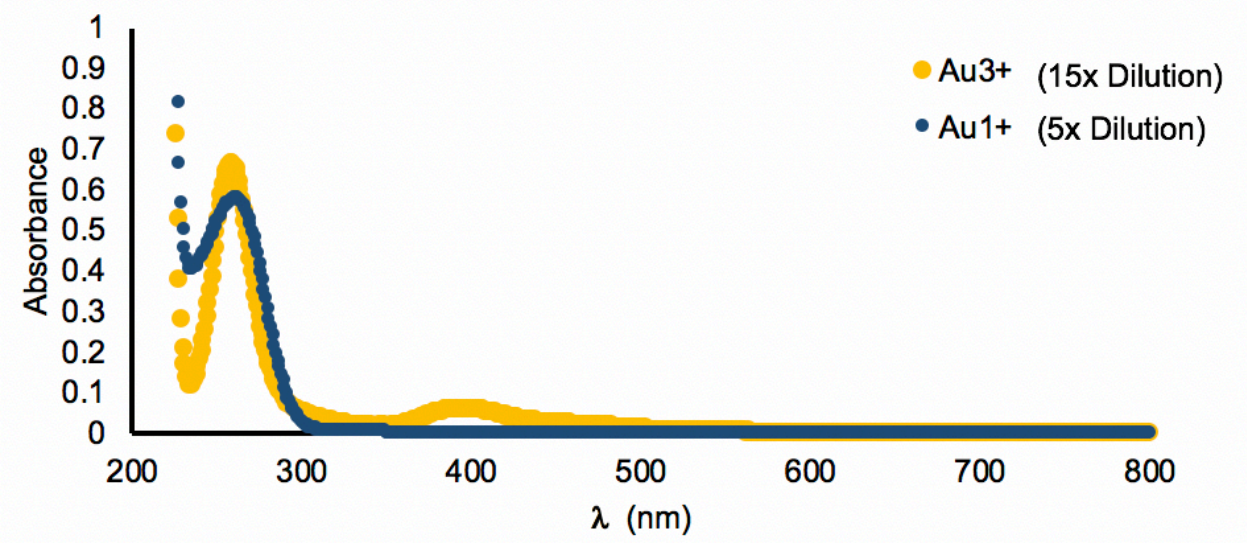

Figure 37. UV-Vis characterization of Au TP growth solution before and after addition of ascorbic acid suggests that most Au^{3+} is converted to Au^{1+} based on the disappearance of a peak at 398nm. The peak at 260nm likely corresponds to CTAB:Au^{+} complex. The initial concentration of Au^{3+} in a growth solution is 267.4 μM.

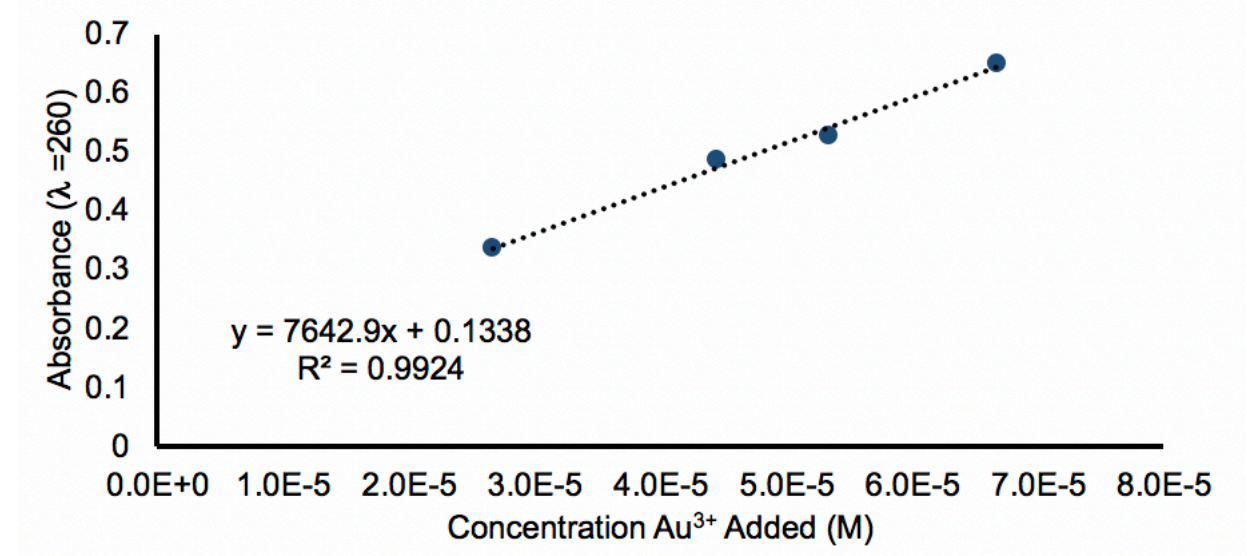

Figure 36. UV-Vis characterization of dilutions of Au TP growth solution after ascorbic acid addition shows a linear relationship between the concentration of Au^{3+} added and the absorption at 260nm. Assuming that all Au^{3+} added to the Au TP growth solution is reduced to Au^{1+}, this curve can be used to determine the concentration of Au^{1+} in an Au TP growth solution.

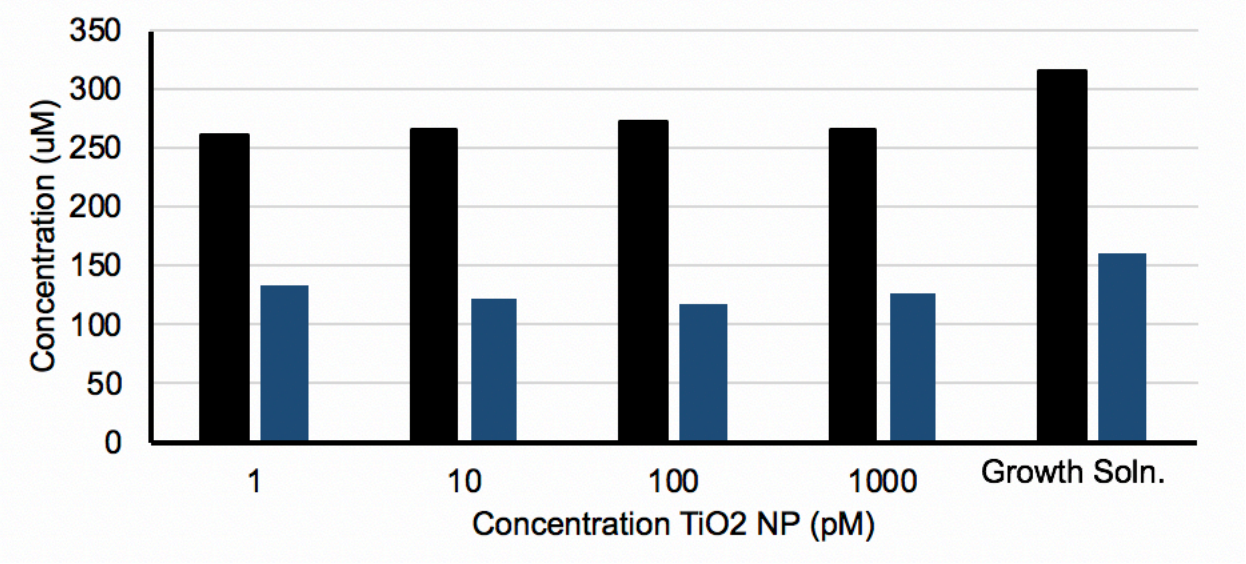

Figure 38. Au TP growth solutions with and without TiO_2 (21nm) nanoparticle precursors show comparable changes in concentration of Au^+ over a 24-hour period. Black bars indicate the initial concentration of Au^+ for each growth solution before nanoparticle precursor addition. Grey bars show concentration of Au after 24 hours. Concentration was calculated based on the calibration curve for Au^+ and assuming all Au^{3+} is converted to Au^+ upon addition of ascorbic acid.

3.5.19 Products of reaction conditions, which favor homogeneous nucleation

In addition to tracking a particle by composition, shape may act as a probe for determining NP precursor location. Here, an Au single crystalline rod particle was added as a NP precursor to the growth solution (Figure S13). Au TP reaction conditions were tuned to either favor homogeneous or heterogeneous reaction conditions by varying the number of sites of homogeneous nucleation (e.g. NP precursor concentration) or the strength of the reducing agent (e.g. increasing pH). Under conditions favoring heterogeneous nucleation, overgrown rods or dumbbells are the only products observed (Figure S13e). Conversely, when the pH is increased Au TP appear as products along with dumbbell products (Figure S13f). Similarly, when NP precursor concentration is decreased Au TP appear as products along with a number of other multiply-twinned products which may be a result of homogeneous nucleation (Figure S13d).

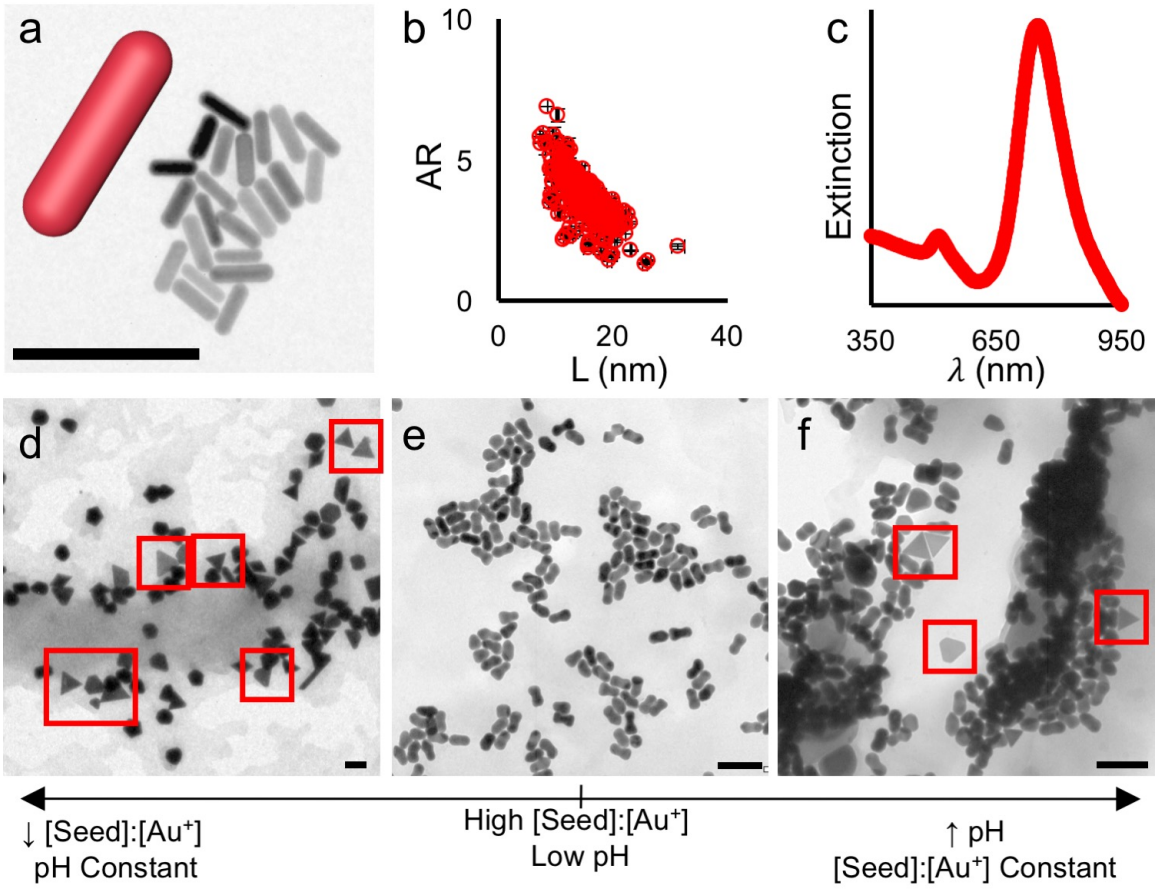

Figure 39. When Au TP reaction conditions are tuned to favor homogeneous nucleation Au TP appear as products. Conversely, when conditions favor heterogeneous nucleation Au TP are not found. Scale bars represent 200nm. a) Representative EM image of Au single crystalline rod NP precursors for algorithmic analysis. b) Algorithmic analysis of rod NP precursors reveals the particles have a diameter of 15.7± 2.9 nm and an aspect ratio of 3.6 ± 0.7 (N = 701 particles). c) UV-Vis characterization of NP precursors. d) Conditions that favor homogeneous nucleation by decreasing NP precursor concentration. e) Conditions favoring heterogeneous nucleation. f) Conditions favoring homogeneous nucleation by increasing the strength of the reducing agent.

4 CHAPTER FOUR: SYNTHESIS OF BROKEN SYMMETRY AU NANOPARTICLES WITH TUNABLE ANISOTROPY

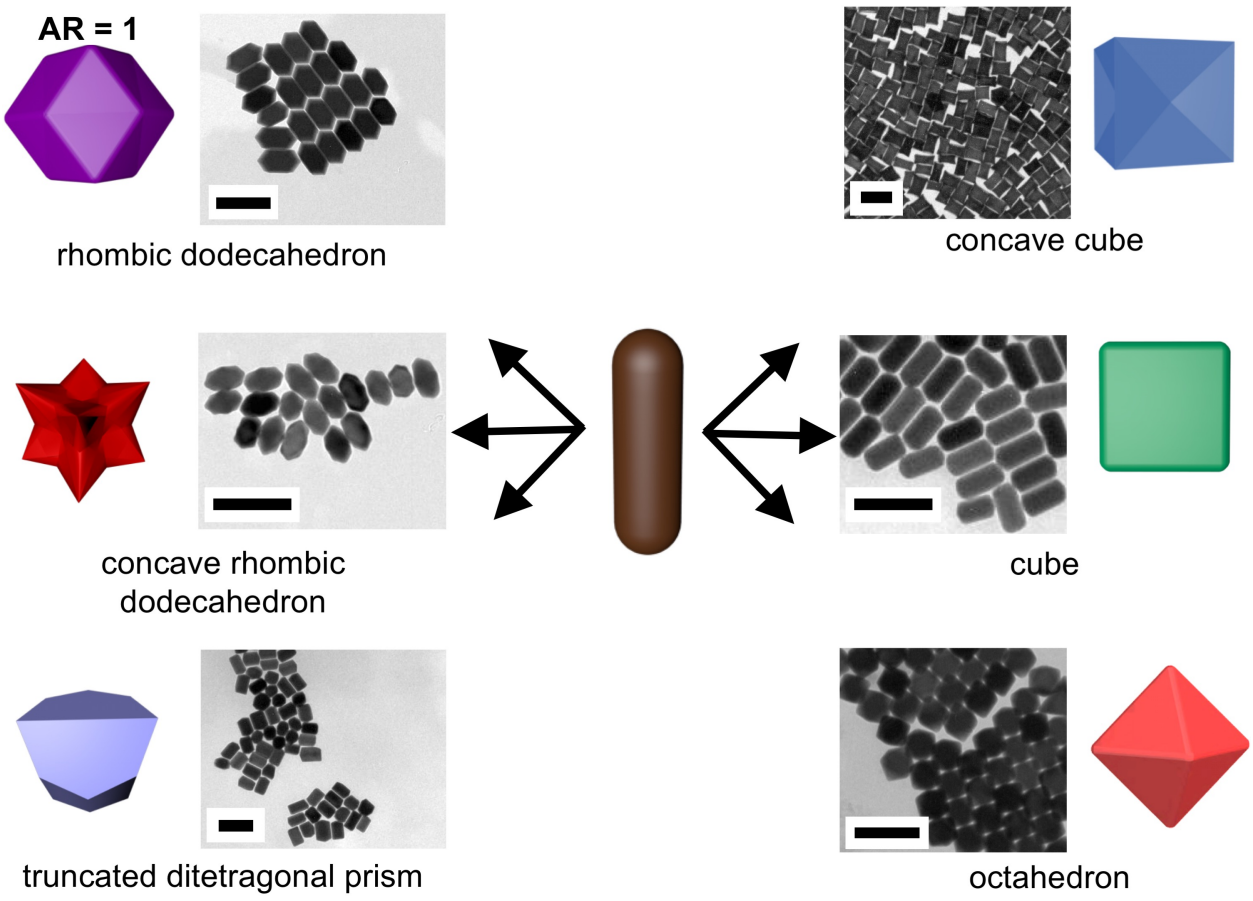

Material in this chapter is based upon published work:

C.R. Laramy, H. Lopez-Rios, M.N. O'Brien, M. Girard, R.J. Stawicki, B. Lee, M. Olvera de la Cruz, C.A. Mirkin. *Submitted*.

4.1 Abstract

Nanoparticles represent highly tunable material building blocks which may be modified in size, shape, and composition for applications ranging from optoelectronics, catalysis, and the study of crystallization processes. While significant advances have been made in the synthesis of non-spherical, anisotropic nanoparticles, most approaches result in high symmetry and volume fraction particles. Herein, we report an approach to realize a series of broken symmetry particles with synthetically adjustable dimensions and tunable aspect ratios. As a result of this approach, the aspect ratio of particles may be tuned by up to an order of magnitude while maintaining a high yield of uniform products. This degree of structural control enables systematic exploration of the impact of anisotropy on particle properties. Indeed, Chapter Five utilizes one class of these particles with the same general shape but increasing aspect ratio to study the implications of particle anisotropy in DNA-directed crystallization.

4.2 Background

The ability to control matter on the nanoscale results in particles with distinctly different and useful properties relative to their bulk counterparts.[65] In addition to size and composition, nanoparticle shape often dictates these properties.[65, 312] Robust syntheses to control the shape of nanocrystals require precise control over the placement of millions of atoms.[52] One strategy to achieve this control is to spatiotemporally separate homogeneous particle nucleation from heterogeneous growth onto existing particles, and thereby improve control over each step.[52] In this "seed-mediated" approach, a pre-formed particle surface (i.e. "seed") is separately nucleated and added to finely tuned, mildly reducing growth solutions, such that the seed acts as a preferential site for heterogeneous nucleation.[232, 234, 264, 313] In many cases, this approach enables one to

preferentially guide particles toward a single anisotropic product with high uniformity and yield.[52] Despite these advances, most syntheses result in high symmetry and volume fraction products[65, 312] due to the thermodynamic preference for highly symmetric products and the poor understanding of symmetry breaking events.[244, 245, 312, 314] Successful examples often result from trial-and-error, where kinetic processes trap structures in local energetic minima that are prone to subtle fluctuations in reaction conditions.[120, 232, 265, 312]

Although significant advances have been in preparing low symmetry anisotropic particles,[65, 312] to realize their full potential a larger library is required. In particular, it would be useful to have sets of structures, defined by general shape, but with tunable aspect ratios. Such structures may enable access to materials with new properties, including colloidal crystallization behavior driven by particle anisotropy as is explored in Chapter Five.

One strategy that may enable such control is to use the structure of the nanoparticle seed to direct the growth of the nanoparticle product.[12, 181, 315] Herein, inspired by this work, we demonstrate a nanoparticle synthesis platform where the shape of a seed can be used to initiate symmetry breaking (rather than relying upon poorly understood and controlled nucleation events) and to manipulate the anisotropy of the nanoparticle product.

4.3 Results and Discussion

4.3.1 Development of broken symmetry seeds

An ideal low-symmetry particle seed should be accessible in high yield with broadly tunable anisotropy (Figure 40a). For this purpose, we chose the well-studied syntheses for single crystalline Au rods, a particle in which symmetry is broken along a single axis.[265] The anisotropy of these particles can be defined by the ratio of the rod length divided by the rod diameter (aspect

ratio, *AR*), and directly measured via electron microscopy (EM). The shape and size of the particles (seeds and products) can be analytically determined for hundreds of particles per sample via algorithmic analysis of EM images in order to approximate population-level statistics (Chapter Two).[7, 12] The electronic structure of these particles further enables structural changes to be measured via UV-Vis spectroscopy, where the broken symmetry manifests in two, spectrally separated localized surface plasmon resonances (LSPRs), which correspond to each dimension.[52, 234]

Several syntheses exist to control the *AR* of single crystalline Au rod seeds through the inclusion of different amounts of shape-directing additives (e.g. Ag^{+}). However, these syntheses simultaneously change both particle length and diameter.[12, 267, 316] An ideal platform to control seed *AR* would permit control over length, while holding the diameter constant (or vice versa). One strategy to achieve such control could begin with high *AR* rods and selectively remove material from their tips; an approach previously demonstrated via the addition of an oxidizing agent (*e.g.* Au^{3+} salt).[12, 261] Importantly, EM of *AR*=8 rods etched to different extents enables access to rods of *AR* down to 4.4, while maintaining the uniformity and diameter of the original particles (Figure 41-Figure 43, Table 3). Starting the etching process with a lower *AR* rod (~3.4) similarly afforded access to a range of low *ARs* down to 1.7 (Figure 42, Figure 44).

4.3.2 Overgrowth of rod seeds into products

To study the impact of seed anisotropy on product anisotropy, Au rods with the same diameter, but different *ARs* (1.7, 3.4, 4.4, 5.2, and 8, Figure 43, Figure 44, and Table 4) were added to a seed-mediated synthesis that conventionally produces Au rhombic dodecahedra, a particle

with twelve equal rhombus faces. While this synthesis has been shown to primarily yield a single product from single crystalline Au spherical seeds, it was uncertain whether the trace amount of Ag or the different faceting/surface curvature of the rod seeds would result in multiple products or impact the resultant shape. EM and UV-Vis revealed the formation of unique, anisotropic products that resembled elongated rhombic dodecahedra. More specifically, facets adjacent to the axis of four-fold symmetry remained fixed in surface area and formed the "tips", while the four remaining facets (at 90 degrees to this axis) elongated and increased in surface area (Figure 40a). Algorithmic image analysis of hundreds of particles confirmed the formation of this single product in >95% yield, as fit to an elongated hexagonal cross-section in EM image analysis (Figure 40b, c, Figure 45). The *AR* of the elongated rhombic dodecahedra directly correlated with the *AR* of the seeds (Figure 40b, c, Figure 46) and an EM image tilt series of products grown from the highest *AR* seeds revealed a consistent elongated rhombic dodecahedron shape, with the preservation of a square cross-section along the four-fold symmetry axis (Figure 47). Importantly, the introduction of rod seeds into several other syntheses for anisotropic shapes (e.g. concave cubes, ditetragonal prisms) yielded similarly shifted LSPRs and elongated products (Figure 48-Figure 50, Table 5), in support of this as a platform-type approach.

4.3.3 Tune particle AR

The anisotropy of elongated particles can be further tuned by varying the ratio of rod concentration to Au concentration in the growth solution, with higher ratios leading to more anisotropic products (Figure 40b, Figure 46, Figure 49). With this approach, products from a single rod seed can be tuned by up to a factor of two in *AR* (here defined as the longest edge length

divided by the shortest, Figure 43) and a factor of 3 in minor edge length. In totality, both approaches enabled realization of a library of elongated rhombic dodecahedra that span from a regular rhombic dodecahedron with an *AR*, by definition, of 1.15 to the most anisotropic with an *AR*=9, with similar minor edge lengths (Figure 45).

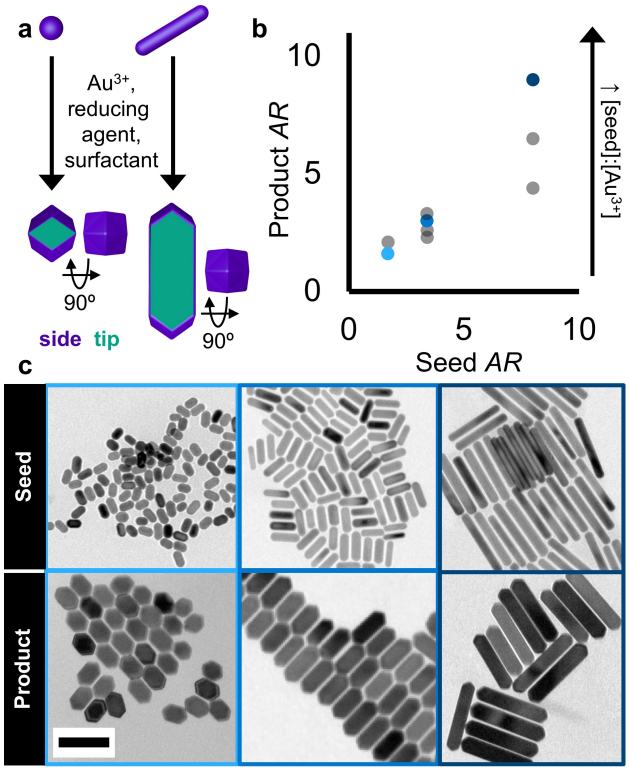

Figure 40. A rod-based seed-mediated synthesis can be used to generate elongated rhombic dodecahedra with tunable *AR*s. a Schematics show a seed-mediated synthesis with a sphere or a rod seed and their resultant products. Green indicates an elongated side facet, and purple indicates a tip facet. **b** Seed *AR* and different [seed] to [Au^{3+}] ratios can be used to tune product *AR*. The algorithmic analysis of several hundred nanoparticles per sample from transmission electron microscopy (TEM) images can be used to quantitate this relationship. **c** Representative TEM images show seed and product particles that correspond to the colors in the plot in b. The scale bar represents 100 nm.

4.4 Conclusion

In summary, systematic modification of seed aspect ratio can act as a platform approach for the synthesis of broken symmetry particles with highly tunable anisotropy, in some cases over an order of magnitude. This approach enables *AR* and minor edge length to be tuned independently in order to access a number of products with high yield and uniformity. The resultant library of particles enables isolation of particle anisotropy in the exploration of particle properties, such as their crystallization behavior. Chapter 5 utilizes this platform to access and understand a series of anisotropy-driven phase transitions in colloidal crystallization processes directed by DNA.

4.5 Experimental Details and Supplementary Materials

4.5.1 Synthesis of Au Rod Seeds with High AR

Au rods with *AR* = 8.0 were synthesized according to literature protocol.[316] After synthesis, rods were centrifuged (7,000 rpm, 40 min) in 50 mL Falcon tubes three times and resuspended in 10 mM CPC, 50 mM CPC, and 100 mM CPC, respectively. UV-Vis revealed an unexpected peak near 600nm and analysis of particle yield from EM images (Hitachi H-8100) show rods represent 77% of products with 23% impurity particles (N = 1183, Figure 41). EM samples were prepared according to literature protocol.[7]

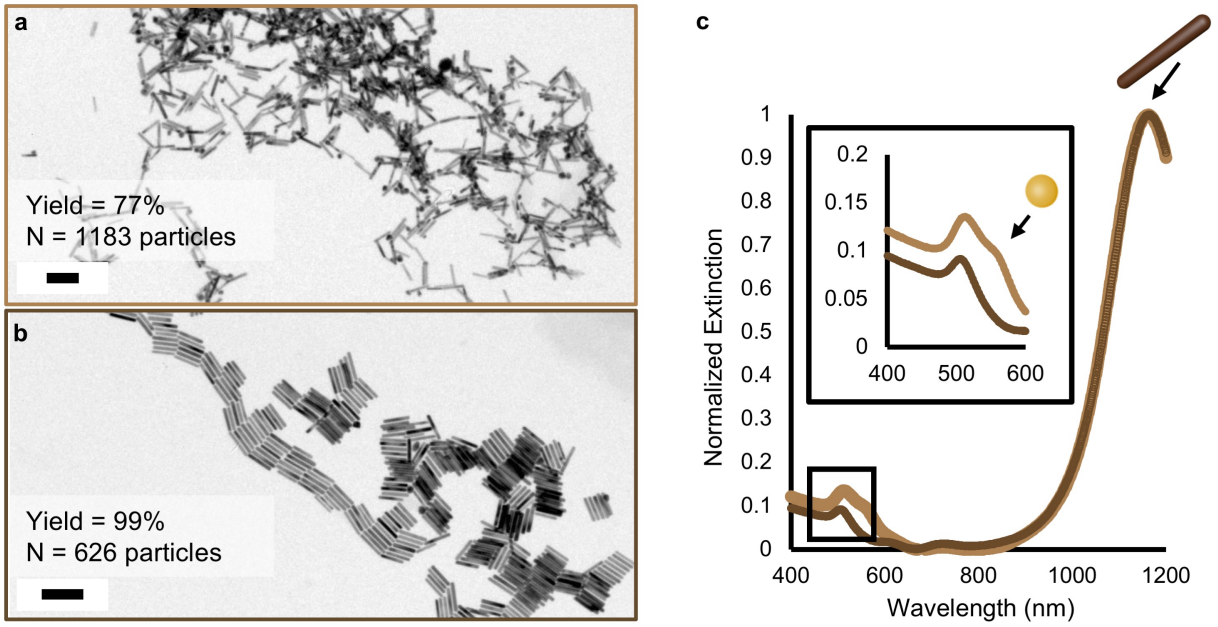

Figure 41. Sedimentation purifies high AR Au rods. a EM image of unpurified, high AR rods. Inset indicates yield determined by EM image analysis. **b** EM image of purified high AR rods. Inset indicates yield determined by EM image analysis. **c** UV-Vis spectroscopy of purified and unpurified rods from a and b. Inset shows zoomed region of spectra indicated by the black box. Scale bars indicate 200 nm.

4.5.2 Tune AR of rod seeds

Au rods with *AR*=3.4 were synthesized according to literature protocol.[12] In order to etch rods selectively from the tips and reduce the aspect ratio of particles, Au rods with AR=3.4 and AR=8 were diluted to 2 OD. 1.5 mL Eppendorf tubes were filled with 0.5 mL aliquots of 2 OD rods and brought to 40°C in a shaker at 1000 rpm. Aliquots were then brought to a particular concertation of [$HAuCl_4$] indicated in Figure 42 below. These acted as test batches to determine the ideal [$HAuCl_4$] to synthesize a rod with a desired AR. UV-Vis spectroscopy (Cary 5000) was used to determine the LSPR of the resultant rods and correlated to expected AR (Figure 42).[267]

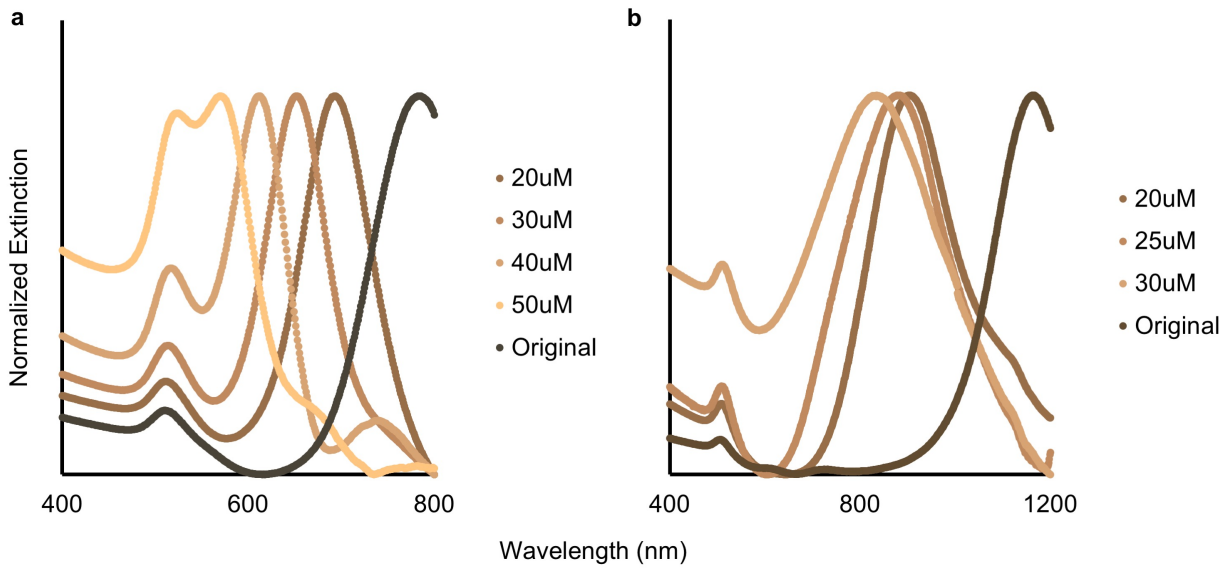

Figure 42. UV-Vis spectroscopy confirms etched Au rods. **a** Etching of AR=3.4 rods. Legend indicates the concentration of $HAuCl_4$ added to each test batch. Original indicates the as-synthesized rods. **b** Etching of AR=8.0 rods. Legend indicates the concentration of $HAuCl_4$ added to each test batch. Original indicates the as-synthesized rods.

Table 3. **Algorithmic analysis of EM images determined structure of AR=3.4 rods.**

Number of particles	2411
% Rod	93
% Impurity	7

4.5.3 Characterization of rod seeds with different AR

All TEM images were collected using a Hitachi H-8100.

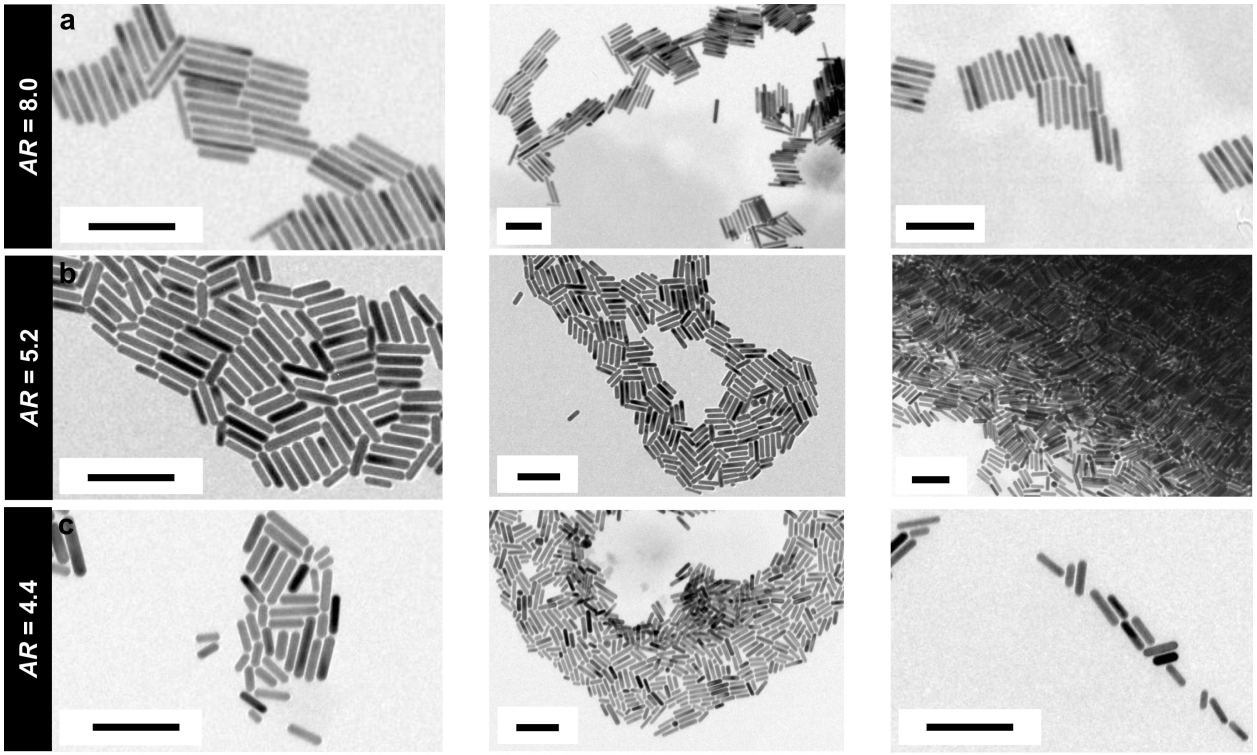

d

	L_{minor} (nm)	St. Dev. L_{minor} (nm)	L_{major} (nm)	St. Dev L_{major}(nm)	*AR*	N measured	[Au^{3+}] (uM), LSPR (nm)	[Rod] (OD)
High *AR* Seed	17.3	2.7	136.2	15.4	8.0	158	N/A, 1170	N/A
Etched Seed	18.1	2	94.3	19.5	5.2	606	20, 952	2
Etched Seed	15.5	2.3	67.9	20.3	4.4	812	30, 834	2

e

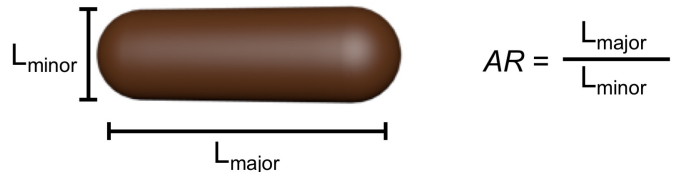

Figure 43. EM reveals structure of high AR rod seeds. a High and low magnification EM images of rods with AR=8.0. **b** High and low magnification EM images of rods with AR=5.2. **c** High and low magnification EM images of rods with AR=4.4 **d** Table that indicates statistical analysis of nanoparticle structure from EM images and etching conditions used to achieve this structure. **e** Model of Au rod that indicates the major and minor edge lengths as well as defines AR for rod shapes. Scale bars represent 200 nm.

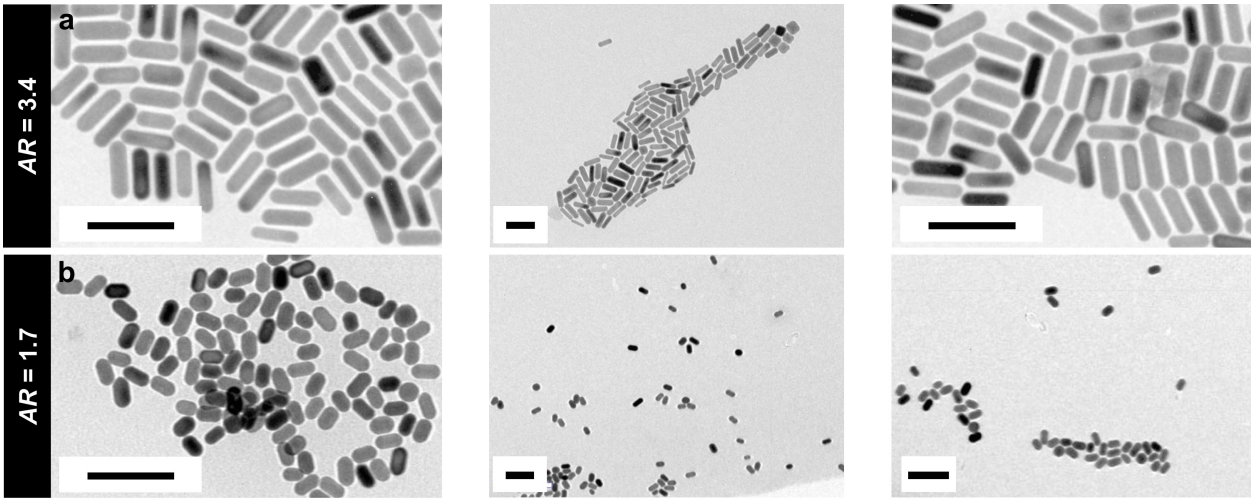

c	L_{minor} (nm)	St. Dev. L_{minor} (nm)	L_{major} (nm)	St. Dev L_{major}(nm)	*AR*	N measured	$[Au^{3+}]$ (uM), LSPR (nm)	[Rod] (OD)
Low *AR* Seed	16.5	2.6	54.6	5.6	3.4	2238	N/A, 726	N/A
Etched Seed	21.2	2.7	36.4	4.4	1.7	383	50, 581	2

Figure 44. EM reveals structure of intermediate and low AR rod seeds. a High and low magnification EM images of rods with AR=3.4. **b** High and low magnification EM images of rods with AR=1.7. **c** Table that indicates statistical analysis of nanoparticle structure from EM images and etching conditions used to achieve this structure. Scale bars represent 100 nm.

Table 4. Table contains the final concentration of concentrated seed particles used for synthesis of elongated rhombic dodecahedra and other elongated products.

AR	Concentration (OD)	Ext. Coeff. ($M^{-1}cm^{-1}$)	Concentration (nM)
1.1	17.22	4.14E-08	712.9
1.7	10.4	4.66E-09	2.2
3.4	35.6	4.47E-09	8.0
4.4	14.1	5.39E-09	2.6
5.2	35	6.55E-09	5.3
8.0	56.3	7.90E-09	44.5

4.5.4 Algorithmic analysis of elongated RD from EM images

TEM images which contained many particles per sample were collected using a Hitachi H-8100. For shape yield calculations ~1000 particles per sample were counted. For determination of structural parameters > 100 RD or elongated RD (most often several hundred) were analyzed. This analysis fits the 2D projection of a RD or an elongated RD to a regular or elongated hexagon,

respectively. All analysis was performed using software that is freely available on the MATLAB File Exchange (https://de.mathworks.com/matlabcentral/fileexchange/54101-high-throughput-algorithmic-determination-of-nanoparticle-structure-from-electron-microscopy-images).[7, 12] Samples were prepared according to literature precedent in order to collect appropriate images for analysis.[7]

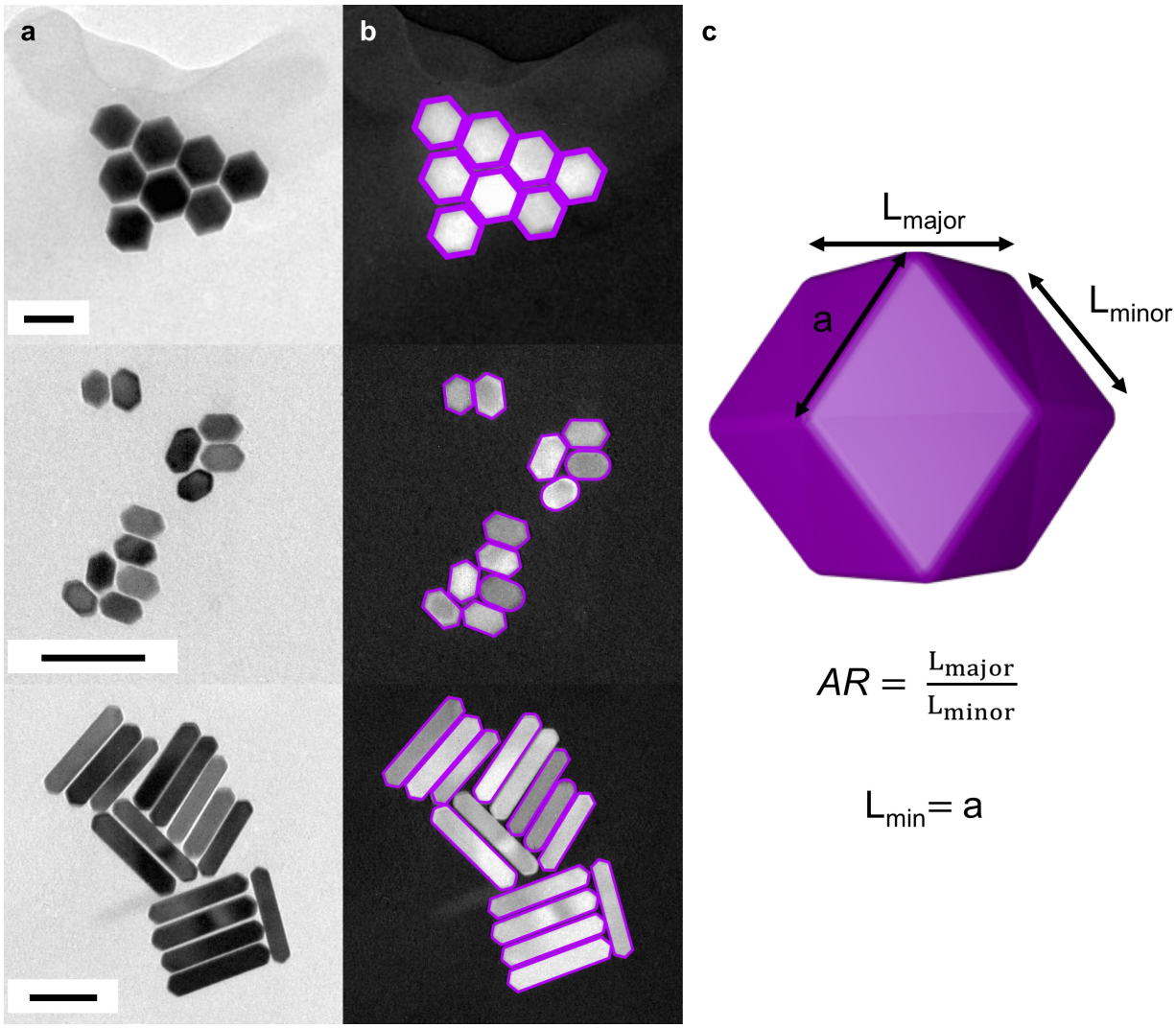

Figure 45. Algorithmic analysis reveals elongated RD structure from EM images. a EM images of regular (top) and elongated RD to be analyzed by fitting to a regular or elongated hexagon. **b** Analyzed EM image overlaid with the best fit (purple outline) as determined by algorithmic analysis. This analysis accounts for elongation and corner rounding. (bottom) The two particles that lack a purple outline were excluded from analysis since the particles overlap with each other. **c** Model of a regular RD with the major and minor lengths labeled. Equations below define an AR for this shape and relate the minor length with the edge length of a rhombus-shaped facet. Scale bars indicate 100nm.

4.5.5 Synthesis and characterization of elongated RD

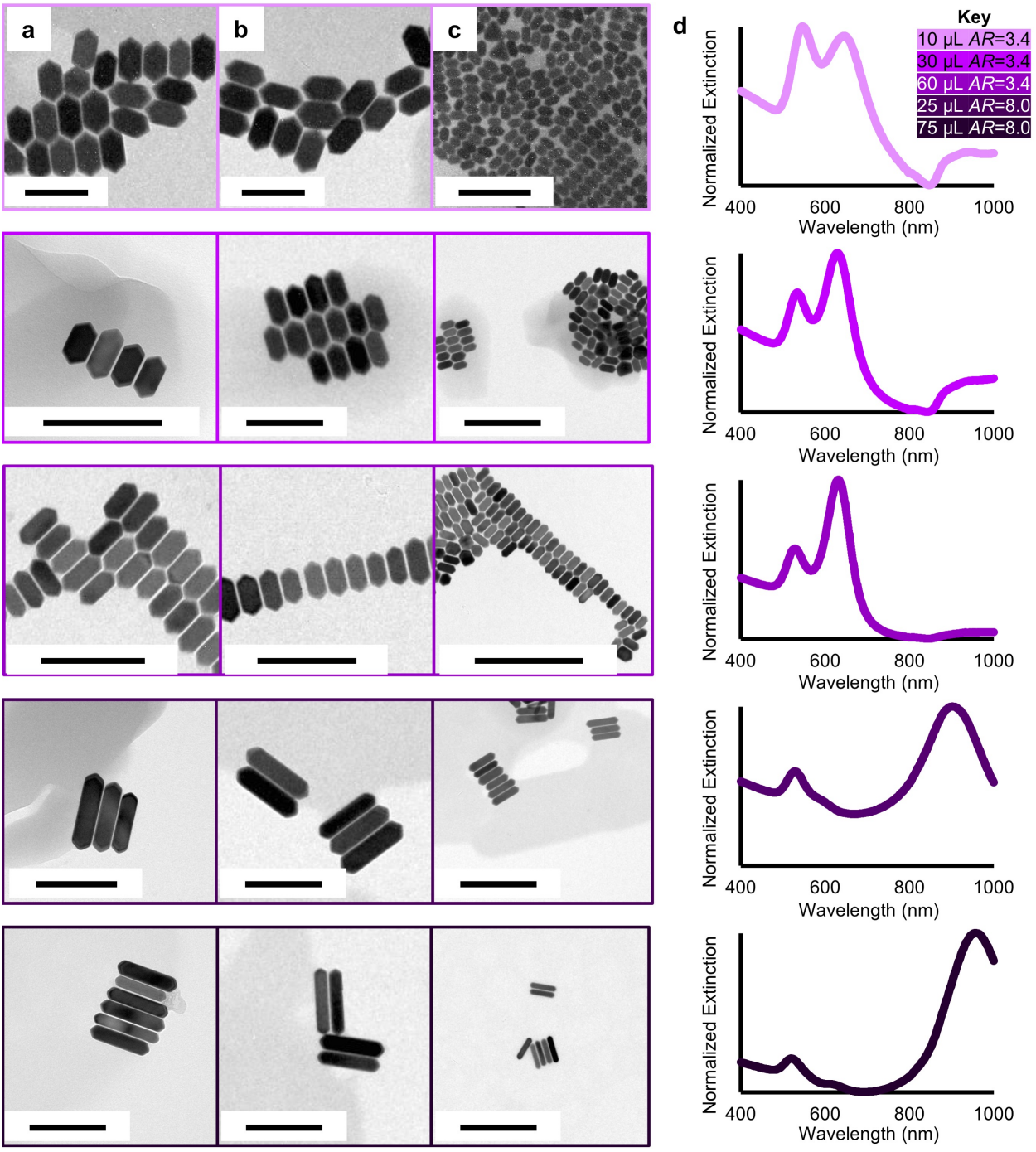

Figure 46. EM and UV-Vis characterize elongated rhombic dodecahedra with various AR. a High magnification EM images of elongated rhombic dodecahedra grown from either AR=3.4 or AR=8.0 rod seeds and with different [seed]:Au^{3+} ratios. Scale bars represent 200 nm. **b** Additional high magnification EM images of elongated rhombic dodecahedra grown from either AR=3.4 or AR=8.0 rod seeds and with different [seed]:Au^{3+} ratios. Scale bars represent 200 nm. **c** Low magnification EM images of elongated rhombic dodecahedra grown from either AR=3.4 or AR=8.0 rod seeds and with different [seed]:Au^{3+} ratios. Scale bars represent 500 nm. **d** UV-Vis Spectroscopy measurement of elongated rhombic dodecahedra. Plot colors correspond to EM image outline colors. Key indicates seed AR and seed volume.

Syntheses for elongated rhombic dodecahedra followed previously reported protocols with the addition of various amounts of rod seeds (example volumes indicated in the Key in Figure 46) from seed stocks with concentrations indicated in Table 4.[12] Briefly, 250 μL of 1M HCl, 250 μL of 10mM $HAuCl_4$, 13μL of 10mM $AgNO_3$, and 30μL 100mM AA were added in this order to 5mL of 100mM CPC. The solution was briefly mixed between each addition. After the addition of AA the solution turned clear and seeds were added. The solution was briefly vortexed and allowed to react for 5 hours before characterization with EM (Hitachi H-8100) and UV-Vis spectroscopy. For larger batch sizes, all volumes could be scaled up.

4.5.6 EM characterization of elongated RD from AR=8 seed

Tilt series TEM images were collected using a Hitachi HD-2300. SEM images were collected using a Hitachi SU8030.

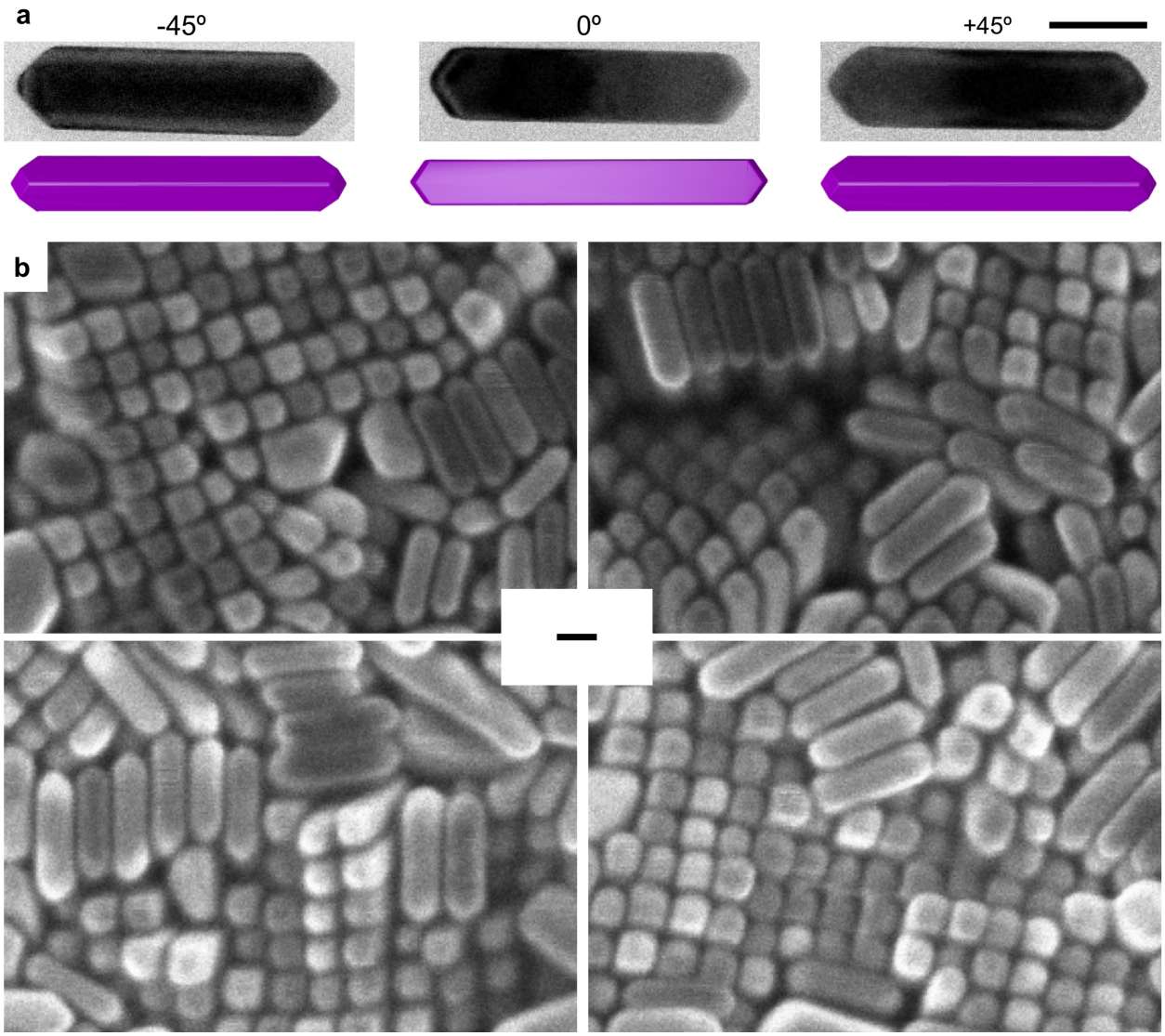

Figure 47. Tilt series and scanning electron microscopy (SEM) reveal preservation of elongated rhombic dodecahedra square cross-section when grown from AR=8 seed. a Tilt series of EM images of a single elongated rhombic dodecahedron (AR=9.0). Angle indicated above image. Particle models indicate the orientation the particle in EM image. **b** Scanning electron microscopy (SEM) images of elongated rhombic dodecahedra (AR=6.5) dried on a silicon substrate. Images show particles resting on their long axis or tip-on. Tip-on orientations allow visualization of the square cross-section of elongated rhombic dodecahedra. Scale bars represent 50 nm.

4.5.7 Elongated products grown from broken symmetry seeds

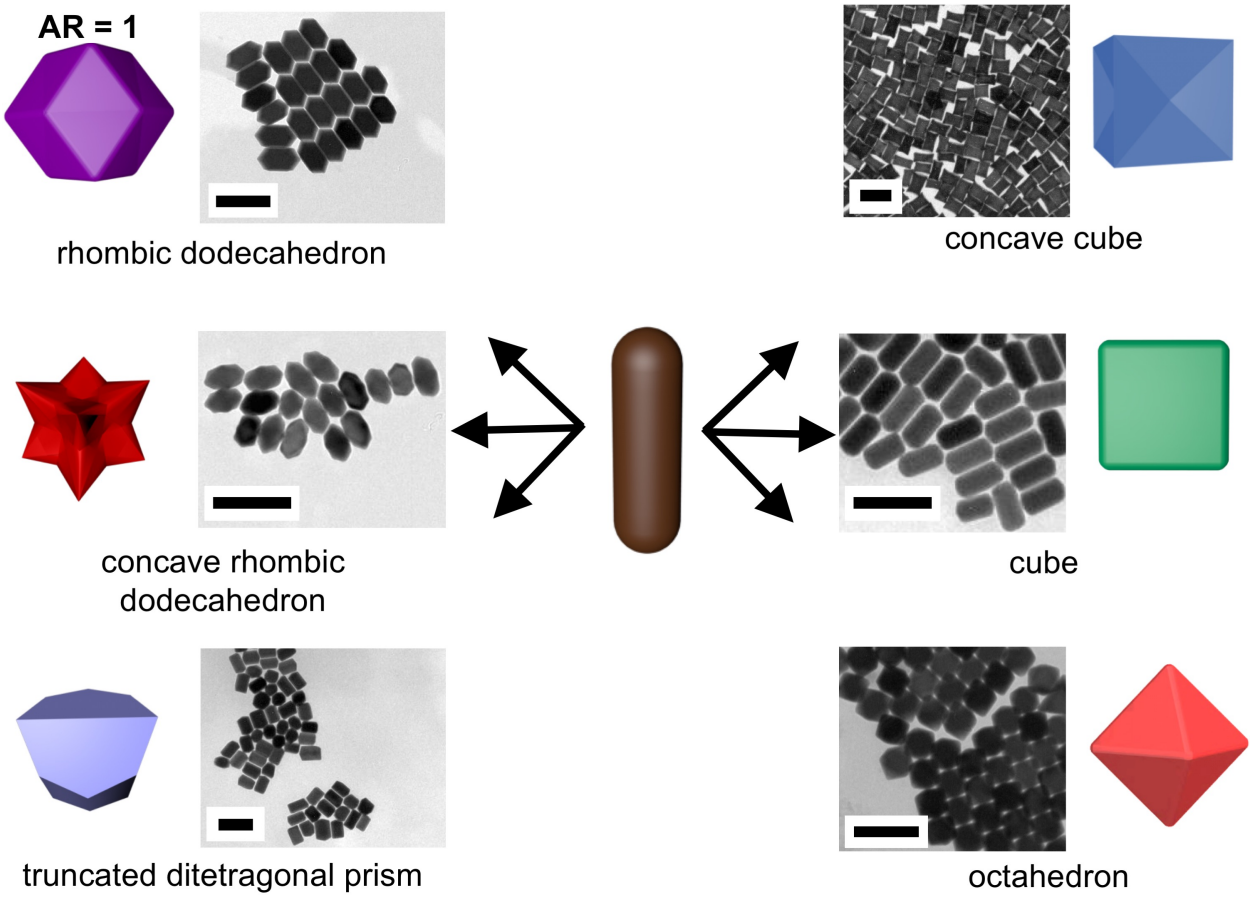

Figure 48. Elongated products can be grown from broken symmetry seeds shown in Figure 44a. Particle models represent the regular particle shape, expected when grown from spherical seeds.

Table 5. Table includes reaction conditions for elongated concave cubes corresponding to data points in Figure 49 below. Volumes correspond to a 5 mL batch size for a concave cube synthesis reported by O'Brien et al.

Volume Seed (µL)	Lmin Seed (nm)	L STD Seed (nm)	AR Seed	AR STD (Seed)	N Seed	AR Product	AR STD	Lmin Product (nm)	L STD	N product
10	16.5	2.6	3.4	0.6	2238	1.4	0.2	102.6	10.4	53
30	16.5	2.6	3.4	0.6	2238	1.6	0.2	73.6	6.5	31
100	16.5	2.6	3.4	0.6	2238	2	0.3	42.3	5.7	155
25	17.3	2.7	8	1.1	158	2.6	0.3	83.4	11.8	82
75	17.3	2.7	8	1.1	158	3.4	0.4	54.8	5.4	99
150	17.3	2.7	8	1.1	158	4.1	0.6	41.1	6	90
200	17.3	2.7	8	1.1	158	4.3	0.4	38	3.9	64

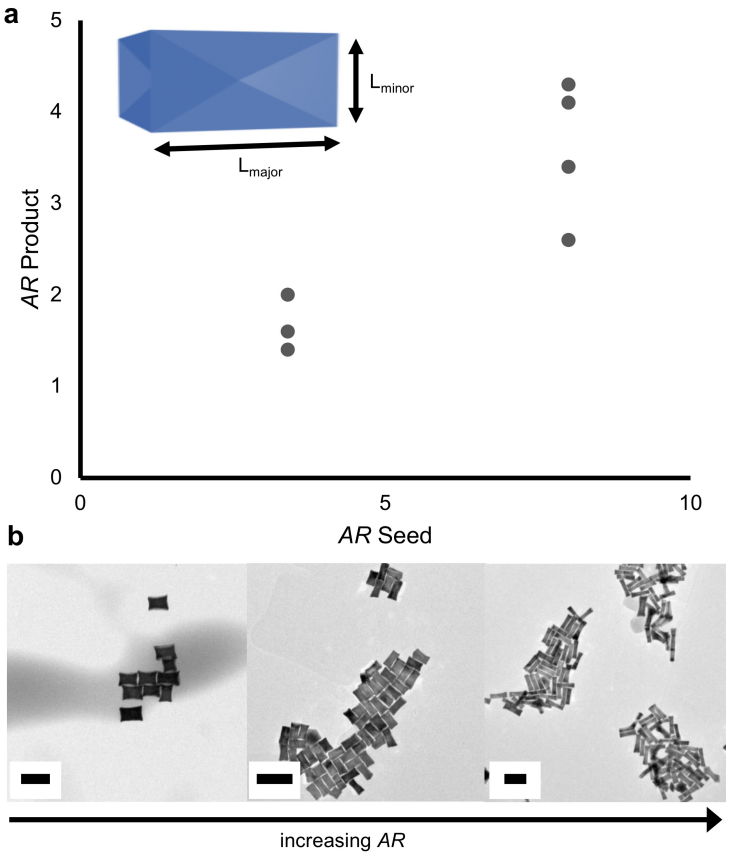

Figure 49. Seed AR and Au^{3+}:[seed] tune elongated concave cube AR. a Plot of seed AR vs. elongated concave cube AR as measured from ~100 particles in EM images. Particle model indicates the major and minor lengths used to calculate AR for elongated concave cubes. **b** Representative EM images of elongated concave cube with increasing AR.

Syntheses for elongated concave rhombic dodecahedra, concave cube, truncated ditetragonal prism, and cube followed previously reported protocols with the addition of various amounts of rod seeds (example volumes and product statistics given in Table 5 for elongated concave cubes) from stock solutions with concentrations indicated in Table 4.[12] The inclusion of seeds with an AR of 3.4 in a previously reported synthesis for cubes[12] produced irregular particle shapes, while their inclusion in a previously synthesis for tetrahexahedra[12] resulted in elongated cube/rectangular

prism products. Interestingly, the overgrowth of rod seeds in a previously reported synthesis for octahedra[12] could produce regular octahedra with sharp features (Figure 48).

Similar to elongated rhombic dodecahedra, the *AR* and minor edge length of concave cubes may be tuned through the overgrowth of various amounts of seeds with different *AR* in a constant growth solution. Briefly, 250μL of 1M HCl, 250μL of 10mM $HAuCl_4$, 62.5μL of 10mM $AgNO_3$ and 47.5μL of 100mM AA were added, in order, to 5mL of 100mM CPC. The solution was briefly mixed after each addition. After the addition of AA the solution turned clear and seeds were added. The solution was briefly vortexed and allowed to react for 5 hours before characterization with EM (Hitachi H-8100) and UV-Vis spectroscopy. Example volumes and resultant products are given in Table 5.

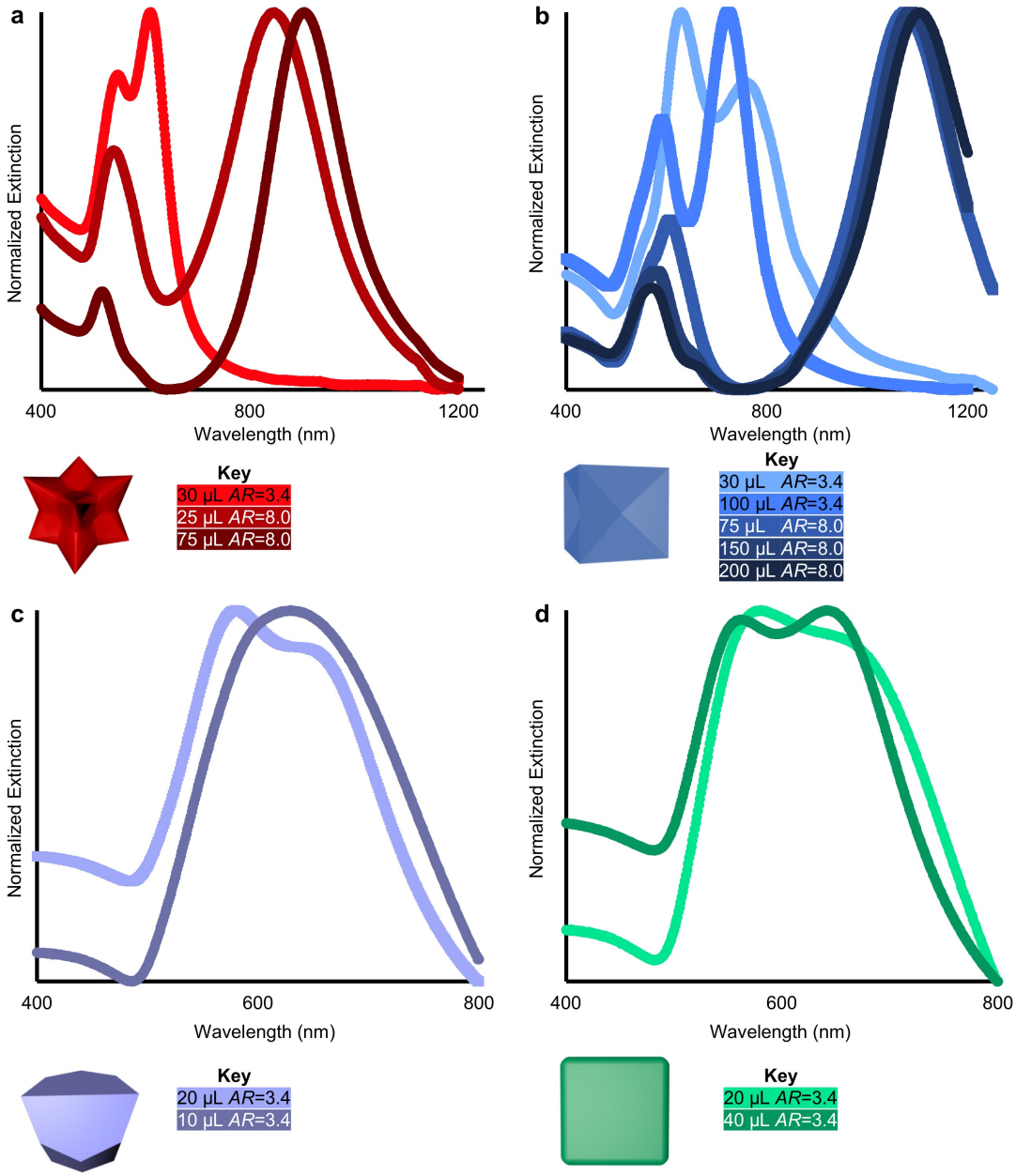

Figure 50. UV-Vis spectroscopy confirms elongation of concave rhombic dodecahedra, concave cubes, truncated ditetragonal prisms, and cubes. a Extinction spectra for elongated concave rhombic dodecahedra grown from various [seed]:Au^{3+} and seeds with either AR=3.4 or AR=8.0. Model shows a regular concave rhombic dodecahedron grown from spherical seeds. Key indicates seed AR and volume. **b** Extinction spectra for elongated concave cubes grown from various [seed]:Au^{3+} and seeds with either AR=3.4 or AR=8.0. Model shows a regular concave cube grown from spherical seeds. Key indicates seed AR and volume. **c** Extinction spectra for elongated truncated ditetragonal prisms grown from various [seed]:Au^{3+} and seeds with AR=3.4. Model shows a regular truncated ditetragonal prism grown from spherical seeds. Key indicates seed AR and volume. **d** Extinction spectra for elongated cubes grown from various [seed]:Au^{3+} and seeds with AR=3.4. Model shows a regular cube grown from spherical seeds. Key indicates seed AR and volume.

SECTION THREE – ENGINEERING LOW SYMMETRY LATTICES

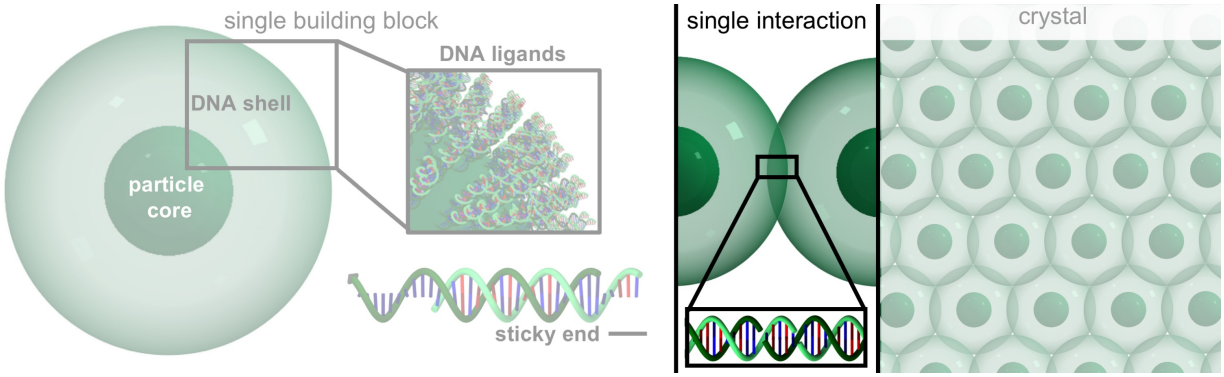

5 CHAPTER FIVE: CONTROLLED SYMMETRY BREAKING IN COLLOIDAL CRYSTAL ENGINEERING WITH DNA

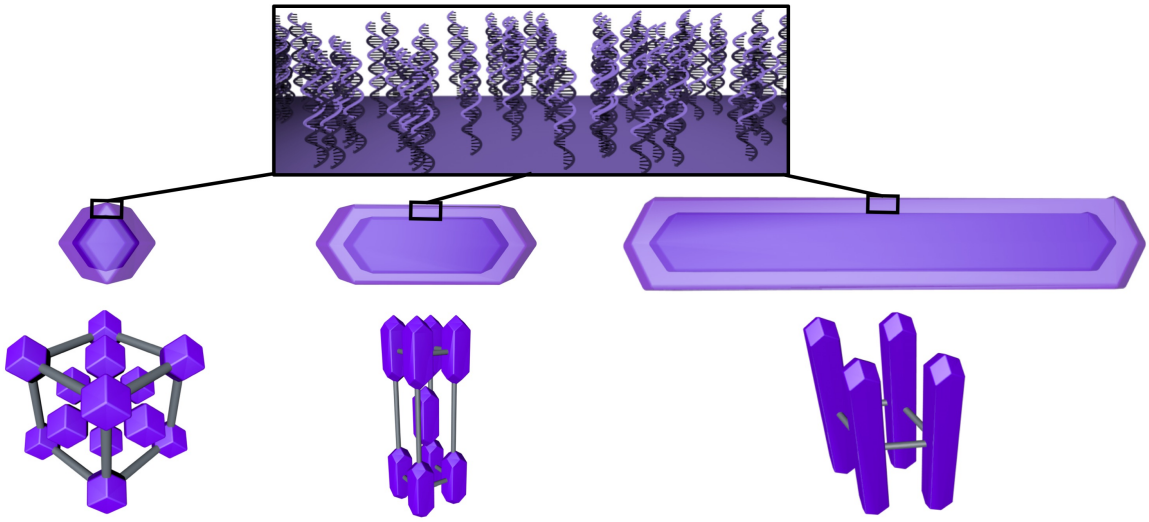

Material in this chapter is based upon published work:

C.R. Laramy, H. Lopez-Rios, M.N. O'Brien, M. Girard, R.J. Stawicki, B. Lee, M. Olvera de la Cruz, C.A. Mirkin. *Submitted*.

5.1 Abstract

The programmed crystallization of particles into low symmetry lattices represents a major synthetic challenge in the field of colloidal crystal engineering. Herein, we report an approach to realizing such structures that relies on particles with tunable anisotropy developed in Chapter Four. When modified with DNA ligands, and used as building blocks for colloidal crystal engineering, these structures enable one to expand the types of accessible lattices and to answer mechanistic questions about phase transitions that break crystal symmetry. Indeed, crystals formed from a library of elongated rhombic dodecahedra yield a rich phase space, including low symmetry lattices (body-centered tetragonal and hexagonal planar). Molecular dynamics simulations corroborate and provide insight into the origin of these phase transitions. In particular, we identify unexpected asymmetry in the DNA shell, distinct from both the particle and lattice symmetries, which enables directional, but non-close packed interactions.

5.2 Background

The ability to arrange colloidal particles into crystalline lattices with controlled spacing and symmetry enables the construction of next generation materials.[65] In these materials, particles represent tunable building blocks that can be engineered in composition and structure, and assembled into sophisticated architectures with functionalities relevant for fields ranging from optoelectronics to catalysis.[65, 189, 190, 192] One powerful strategy to imbue these building blocks with chemical crystallization instructions, and thereby "program" their organization, is to attach DNA molecules, as ligands, to their surfaces.[36, 43, 56, 117, 317] Over two decades of research have yielded an optimized DNA design for this purpose, comprised of a rigid, double-stranded region near the

particle surface and a solution-exposed, single-stranded terminus (known as a "sticky end").[3, 9] Watson-Crick base pairing between sticky ends on adjacent particles drives crystallization through collective interactions between particles, where the most favorable configuration often maximizes the total number of hybridization events (known as the complementary contact model).[9] Researchers have used this approach to program the formation of over 50 different crystal symmetries and more than 500 different structures (e.g. same symmetry but different compositional building blocks or lattice parameters).[9, 15, 22] However, the majority of these lattices are high symmetry, cubic lattices.[9, 15, 146] Low symmetry lattices (i.e. lattices comprised of unit cells with few symmetry operators) represent some of the most desirable, yet synthetically challenging structures to realize,[55, 65] and necessitate a more complex set of crystallization instructions to break the symmetry of interparticle interactions.[175]

Recent experimental and theoretical work suggests that anisotropic building blocks can be used to direct interactions and, when combined with the encoding capabilities of DNA, provide access to structures not attainable with isotropic building blocks.[8, 10, 22, 118, 318-320] With this approach, the particle core acts as a template to arrange the DNA into a conforming shell.[8, 22] Anisotropic shapes can thus encode spatially discrete, collective DNA interactions localized along each facet or spatial region of the particle. The number, geometry, and relative strength (*i.e.* the number of DNA molecules within each collective interaction) of these "bonds" can be tuned to produce different symmetries.[8, 9, 22, 321] Furthermore, recent work shows that flexible DNA ligands can deform to enable symmetries beyond those predicted by particle shape alone.[8, 321]

Realization of low-symmetry lattices via this approach is dependent on the availability of suitable chemical syntheses that produce the desired shapes with sufficient uniformity and yield,

such as those developed in Chapter 4. Herein, we report the DNA-directed crystallization of a series of particles with tunable aspect ratios (*ARs*). As a case study, a base shape of a rhombic dodecahedron is systematically elongated, which enables the realization of broken symmetry lattices, including a body-centered tetragonal (BCT) lattice and a new hexagonal planar (HP) lattice. When paired with molecular dynamics simulations, this platform enables one to probe the key factors that underlie a series of anisotropy-driven phase transitions. Simulations accurately predict each phase and reveal a unique symmetry breaking in the DNA shell that leads to the formation of the non-close packed HP lattice.

5.3 Results and Discussion

5.3.1 Development of building blocks with varied AR

Synthetic access to this library of elongated rhombic dodecahedra, with precise control of particle anisotropy, allows one to probe the effects of *AR* on colloidal crystallization with DNA. In principle, the ability to systematically manipulate *AR* allows one to probe the symmetries that form before, throughout, and after a phase transition. By mapping the boundaries of the transition, one can gain experimental insight into why particular phases occur in order to gain greater predictive power. Therefore, elongated Au rhombic dodecahedra with *ARs* spanning from 1.15 to 9 (1.1, 1.6, 2.0, 2.8, 3.5, 4.3, 5.0, 9.0, analyzed via the method introduced in Chapter 2), and minor edge lengths that differed by no more than 10 nm, were functionalized with thiol-modified DNA according to literature protocols (Figure 51a, b, Table 6-Table 8 and Figure 53, Figure 54).[88, 166]

The extent to which an anisotropic building block displays directional interactions arises from an interplay between the shape of the particle core and the structure of the DNA. As the DNA

increases in length, it can become more flexible, splay, and obscure particle anisotropy.[8] Therefore, the DNA was designed to be short and rigid enough to preserve the directional interactions templated by the underlying particle. This DNA design was kept constant for all particle cores in order to isolate the role of particle anisotropy (Table 7). A self-complementary DNA sticky end sequence was utilized, such that all particles could hybridize to each other. In order to remove kinetic traps and study the thermodynamically-preferred state of DNA-assembled particles, samples were heated above their collective DNA hybridization temperature and slowly cooled to room temperature (0.1°C/10 min).[1] Subsequently, the structure of these assemblies was directly visualized via EM and probed via small angle x-ray scattering (SAXS).[53] Since EM requires *in vacuo* conditions, aggregates were transferred to the solid state through a previously reported method shown to preserve the solution-phase structure.[322] Further embedding of these solid state aggregates in a polymer resin allowed the samples to be cut into ~200 – 400 nm sections to visualize particles within lattices.[9]

Rhombic dodecahedra possess 12 facets of equal surface area and thus are capable of 12 equally strong, directional DNA interactions.[8, 22] Based on shape, at the lowest *AR* (1.15), one would thus expect a face-centered cubic (FCC) crystal symmetry, where the 12 directional interactions enable hybridization to 12 nearest neighbors.[8, 22] An increased facet surface area, as seen for the elongated rhombic dodecahedra, should contain a proportionally greater number of DNA molecules (assuming that each facet can be functionalized with a comparable DNA density). Consequently, the DNA along elongated side facets should be able to engage in a greater number of total DNA hybridization events and thereby exhibit an increased collective DNA "bond strength."[22] Thus, elongated rhombic dodecahedra should be capable of four equal, directional

DNA interactions on each tip and four directional interactions that increase in strength as the *AR* increases.

5.3.2 Characterization of resultant crystals

EM and SAXS of crystals formed from this library of elongated rhombic dodecahedra revealed the formation of several phase transitions (Figure 51, Figure 54-Figure 68, Table 9). Both techniques confirm that the control sample, a rhombic dodecahedron, formed the expected FCC lattice (Figure 51b, c, e, f, Figure 56). As the symmetry of the rhombic dodecahedron breaks and particles begin to elongate (*AR* of 1.6), SAXS peaks broaden, but their positions remain correlated with a FCC symmetry (Figure 51e, Figure 56). If all of the particles were uniformly oriented along their long axes, it would not be possible to maintain a cubic unit cell. Thus, particles must orient irregularly to maintain face-to-face alignment with neighboring particles (*i.e.* the long axes of each particle differ in orientation throughout the crystal, but are randomly rotated in 90° increments to align facets; Figure 51f). EM images confirm this plastic FCC (pFCC) lattice (Figure 51c, Figure 64, Figure 68, plasticity here refers to the irregular orientation of the particles). The loss of orientational order likely causes the increased SAXS peak breadth (Figure 51e). As the *AR* of the particles continues to increase (*AR* of 2.0 to 2.8), particles further lose order in the formation of a disordered FCC-like structure (Figure 56, Figure 62, Figure 63). Above this *AR* (*AR* of ~3.5 to 4.3), SAXS indicates the formation of 2D lattices with square in-plane arrangements (indexed peaks in Figure 51e, Figure 56), and EM images reveal BCT lattices where up to ~5 planes are in registry (Figure 51c, f, Figure 60, Figure 61, Figure 67). The absence of the expected *00l* reflections for a BCT lattice likely results from the limited extent of three-dimensional growth; for

crystals with few “layers”, these SAXS peaks would be broad and have a significantly lower intensity than peaks that correspond to in-plane ordering (Figure 51e). Most interestingly, a phase transition is observed as *AR* increases further (*AR* of 5.0 to 9.0), from the expected BCT lattice, to a mixture of BCT and HP lattices (*AR* of 5.0), and then to solely a HP lattice (*ARs* of 5.0 to 9.0; Figure 51b, d, e, f, Figure 58, Figure 59, Figure 65, Figure 66). Throughout this phase transition, particles consistently orient in a face-to-face fashion with respect to their neighbors, but the angle of this orientation shifts from 90 to 60°.

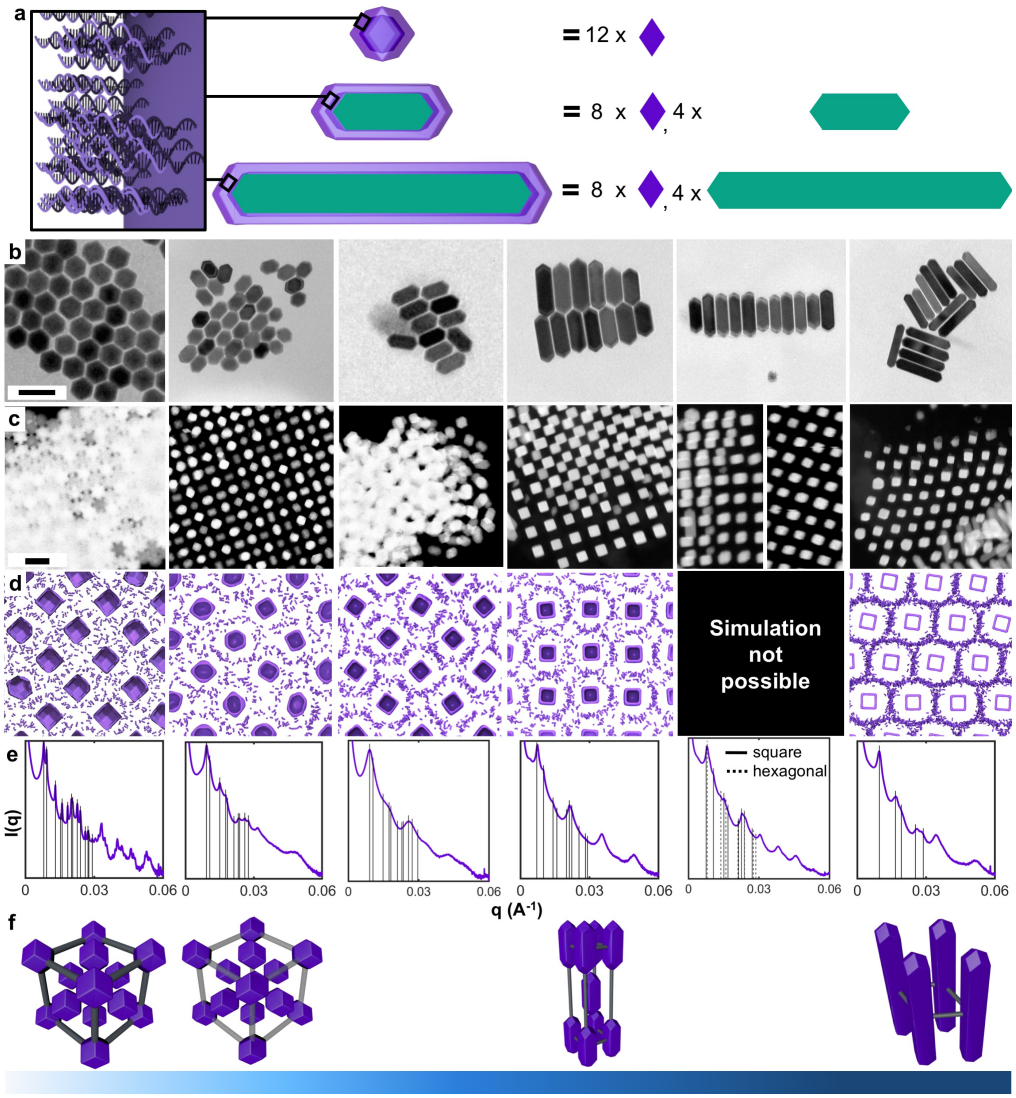

Figure 51. Elongated rhombic dodecahedra building blocks crystallized into multiple unique lattice symmetries. a As the *AR* of building blocks increases, the surface area (and thus number of DNA molecules) on elongated (green) facets increases, while the surface area of the tip (purple) facets remains the same. **b** TEM images show elongated rhombic dodecahedra before functionalization with DNA. From left to right these particles have a minor edge length and corresponding coefficient of variation (CV) and *AR* of: 30.0 ± 4.8 nm (8.0% CV) and 1.1; 20.9 ± 1.4 nm (6.6% CV) and 1.6; 22.3 ± 2.3 nm (10.5% CV) and 2.8 ; 26.2 ± 1.9 nm (7.2% CV) and 4.3; 21.5 ± 2.5 nm (11.3% CV) and 5.0; 16.2 ± 2.4 nm (14.6% CV) and 9.0, as determined by algorithmic analysis of TEM images. The scale bar corresponds to all images in **b**. **c** Z-contrast TEM images show crystals formed from the elongated rhombic dodecahedra in **b**. Images corresponding to *AR*s of 1.6, 4.3, 5.0, and 9.0 were sectioned (section thicknesses of 200 nm, 400 nm, 400 nm, and 400 nm, respectively) to facilitate imaging. The scale bar corresponds to all images in **c**. **d** Simulations show crystals of elongated rhombic dodecahedra with *AR*s that correspond to those in b and c (left to right: *AR*s of 1.15, 1.65, 2.85, 4.5, infinite). Images are cut through particles along the closest-packed plane and include the DNA beads that represent the sticky ends. **e** Indexed SAXS patterns correspond to the crystals in **c**. From left to right patterns index to: FCC, pFCC, disordered FCC-like, square planar (SP), mixture of SP and HP, and HP. **f** Unit cells were determined from the corresponding SAXS patterns and EM images. Transparent unit cell box (grey) indicates a plastic crystal. The color bar indicates the series of phase changes. Scale bars indicate 100 nm.

5.3.3 Molecular dynamics simulations explore experimental crystal symmetries

Under the hypothesis that anisotropic particles create directional interactions perpendicular to their facets, these phase transitions, and notably, the formation of a HP lattice are not intuitive. At higher *AR*s, one might expect that particles would crystallize similarly to rods, which form primarily planar lattices.[22] In particular, one would expect the square cross-section of elongated rhombic dodecahedra to dictate only four in-plane neighbors (*i.e.* square in-plane symmetry) and the potential for inter-plane registry due to face-to-face interactions of the tips (*i.e.* a BCT symmetry if planes are in registry). Due to the novel nature of the elongated rhombic dodecahedron shape, there are limited experiments, simulations, or models in the literature that can be used to predict (or explain) the expected crystallization behavior. Indeed, the closest example simulates the densest packing of rectangular prism-shaped particles (without any ligands) and finds that the four-fold symmetry of the particle's long axis should drive square in-plane arrangements, in line with current understanding.[323, 324] The divergent behavior observed in our system suggests that the exact shape of the particle, or the nature of the attached DNA shell, cause deviations from this densest packing behavior. Thus, we turned to molecular dynamics (MD) simulations to provide more insight into the origin of the BCT to HP phase transition.

MD simulations can aid in understanding phase transitions in colloidal crystal engineering with DNA through the explicit simulation of DNA interactions between particles.[9, 57, 69] Each particle can be modeled based on experimental inputs for both particle shape and DNA density.[8] DNA can be similarly modeled based on experimental inputs, as a chain of beads with mechanical properties analogous to regions of single- or double-stranded DNA, with a terminal region of beads programmed to act as sticky ends.[69] Due to computational limitations, particle size and DNA

length were proportionally scaled down relative to experimental inputs to enable simulation. MD simulations use these models to evaluate the stability of different crystal symmetries by initializing particles in positions that correspond to a particular lattice and then allowing them to relax to their lowest energy state. This modeling strategy has been used previously to accurately predict the DNA-driven crystallization behavior of anisotropic building blocks.[8, 69]

Simulations with these particle models predicted all experimentally observed phase transitions at corresponding *ARs* up to an *AR* of 4.5, with the exception of the disordered region (Figure 51d, Table 10, Figure 69-Figure 73). Prediction of disordered regions can be particularly challenging for this type of simulation. Since particles begin in an ordered lattice, simulations mitigate the formation of any kinetic traps that may prevent the experimental realization of ordered structures. Despite this disparity, simulations show a phase transition occurring near an *AR* of 2.5, analogous to experimental results. Particles with *ARs* between 3.5-4.5 were initialized in either BCT or FCC lattice positions and allowed to equilibrate. FCC lattices represent three-dimensional analogs of the experimentally observed HP lattice. Within this *AR* range, all particles initialized in a FCC lattice rearranged into a BCT lattice upon relaxation. Conversely, those initialized in a BCT lattice remained stable upon relaxation, as expected.

Above an *AR* of 4.5, explicit modeling of building blocks exceeded computational capabilities due to the large number of DNA molecules required for an accurate representation (Table 11, Table 12). As a result, particles with an $AR > 4.5$ were modeled as infinite square prisms (*i.e.* without the tip facets, Figure 51d). This representation reduces computational requirements, because it allows for the simulation of only a single layer of particles, and is reflective of experimental observations, where predominantly planar crystals are observed. Interestingly, infinite square prisms

(approximations for $AR > 4.5$) initialized in square, analogous to a single layer along the (*00l*) of the experimentally observed BCT structure, or hexagonal arrangements both remained stable. To understand the thermodynamic preference between BCT or HP lattices for high *AR*, we analyzed the number of DNA hybridization events between particles in each lattice and used this to calculate a potential energy per particle, with lower energies suggestive of more stable arrangements (Figure 74). Particles initialized in a HP lattice resulted in lower potential energies per particle than those in a square lattice, as seen in experiments.

5.3.4 Simulations reveal number, location and angle of DNA bonds

To explain the phase transition from BCT to HP lattices, we used MD simulations to analyze the number and location of DNA hybridization events between particles (i.e. on an elongated side or tip facet) for different *AR* particles (Figure 52, Figure 75). As the *AR* increases, the ratio of hybridization events on elongated side facets relative to tip facets increases (Figure 52a, Figure 75). In other words, in-plane particle interactions become increasingly dominant over out-of-plane interactions, likely due to the greater surface area, and thus number of DNA molecules per facet. If only in-plane hybridization events are considered for the same particle, the HP symmetry enables more hybridization events per particle than the BCT lattice. Indeed, simulations of infinite square prisms (an extreme case where tip, or out-of-plane, interactions are completely removed) verify this hypothesis. Furthermore, if the symmetry of interplane interactions is considered, BCT lattices may enable face-to-face interactions at the tips, whereas the HP lattice would disrupt such interactions. Therefore, tip interactions are likely key to the stabilization of the BCT lattice. These results suggest that once particles exceed a threshold *AR*, the energetic benefits of DNA

hybridization on elongated side facets in the HP lattice begin to dominate the benefits of DNA hybridization on both elongated side *and* tip facets in the BCT symmetry. Sectioned EM images cut along different lattice planes support this conclusion (Figure 52c). For *AR*=4.3, these images reveal registry between multiple layers, while for *AR*=5.0 the number of layers decreases, and for *AR*=9.0 the images show primarily single layer structures.

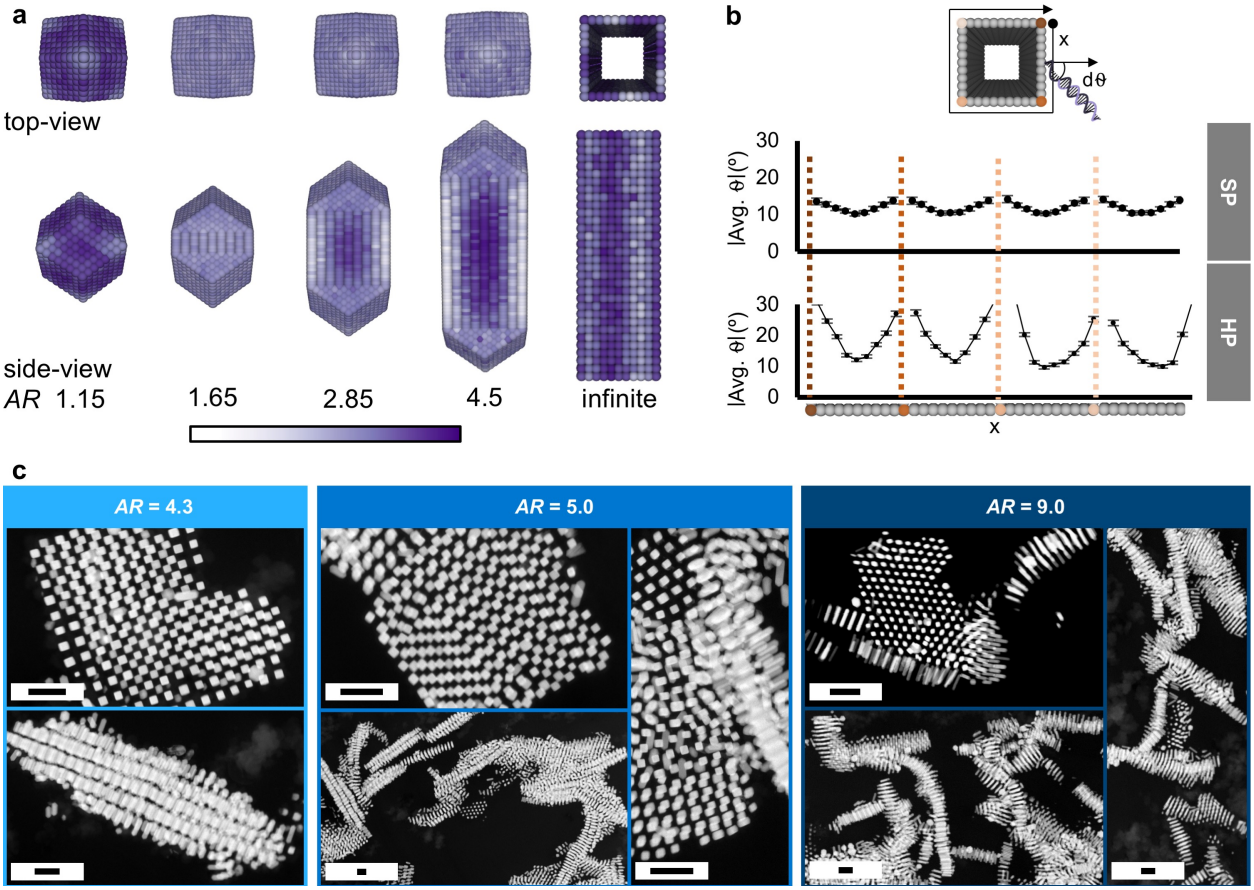

Figure 52. Analysis of the number and location of DNA hybridization events for high *AR* particles. a Models of DNA hybridization probability mapped to the particle surface based on simulations initialized in their most stable lattice (FCC, FCC, BCT, BCT, HP lattices, respectively). Each point on the particle represents a bead that may have DNA attached. Darkest color indicates the maximum (~0.84) and the lightest color indicates the minimum (~0.17) probability that the DNA attached to the bead hybridizes to DNA on an adjacent particle. Color scale corresponds to all models. **b** Analysis of the average DNA angle with respect to the surface normal vector of an infinite rectangular prism initialized in a square planar (SP) vs. HP lattice. The HP plot corresponds to the model in a for the infinite rectangular prism. Dashed lines indicate the location of corners. Error bars represent the standard error determined from the angle of DNA with respect to the reference vector for strands attached to 32 different beads in the same position along the x position over 80 discrete time steps (at equilibrium). **c** Sectioned EM images (section thicknesses of 400nm) show BCT and HP lattices. (top) Images show sections cut across the square cross-section of the particles (approximately parallel to the lattice plane). (bottom and right) Images show sections cut approximately perpendicular to the lattice plane. EM images for particles with *AR*=4.3 show lattices with multiple layers in registry, while images for particles with *AR*=5.0 show multi-layer and single-layer lattices, and images of lattices formed from *AR*=9.0 particles show primarily single layers. Scale bars represent 200 nm.

To understand how a particle with a square cross-section breaks symmetry to engage in six nearest neighbor interactions while remaining oriented, we used MD simulations to examine the

spatial distribution of sticky ends between particles (Figure 52a, b, Figure 76). Interestingly, along each elongated side facet, the DNA shell breaks symmetry to form two directional interactions – a primary face-to-face interaction comprising the majority of the DNA and a secondary face-to-face interaction involving the near-edge DNA (Figure 52a, b, Figure 76). This secondary interaction enables 66% of the simulated edge DNA to hybridize for a HP lattice, compared to only 17% for a SP lattice. Symmetry breaking of a DNA shell along a facet has been observed once previously, for cubes, where the DNA on a single facet split into four equal face-to-face interactions as the DNA length increased.[8] In the work reported here, the symmetry breaking is unique in the following respects: 1) the DNA shell is asymmetrically split along the facet different from both the particle (i.e. four-fold symmetry) and the lattice symmetries (i.e. six-fold symmetry), 2) a face-to-face interaction comprised of near-edge DNA is stabilized, and 3) the phase transition arises from an increase in particle *AR*, rather than in DNA length. This asymmetric split increases the number of DNA hybridization events between particles and likely decreases the repulsion between adjacent DNA molecules by increasing the separation distance. As a result, DNA ligands are able to drive the formation of a non-close packed hexagonal lattice that may not be predicted by densest packing simulations that account only for particle shape.

5.4 Conclusion

The ability to tune the anisotropy of nanoparticles represents a new strategy to access lower symmetry lattices and to stabilize non-standard directional interactions (*i.e.* near-edge face-to-face). Exploration of this phase space reveals a unique phase transition driven by symmetry breaking of the DNA shell, which is induced by particle anisotropy. Importantly, this insight would

not have been possible without precise, systematic control of a particle structure library. Going forward, the synthetic approach used here could be similarly applied to other broken symmetry particles, based on seeds comprised of one-dimensional rods (as shown here), two-dimensional plate-like particles (*e.g.* circular disks, triangular prisms), or three-dimensional polyhedra, or used in multi-step syntheses to create branched structures. These approaches should enable access to novel structures that have yet to be synthesized or modeled and can be used as building blocks in crystal engineering with DNA. Such libraries of building blocks would offer unprecedented insight into phase transitions that lead to low-symmetry lattices and would continue to push the boundaries of accessible lattice symmetries. The resulting low-symmetry lattices could be used to study and unlock access to novel metamaterial properties or afford new control over optoelectronic functionality.

5.5 Experimental Methods and Supplementary Materials

5.5.1 Materials and methods

Materials. The following reagents were purchased from Sigma Aldrich and used as received: sodium borohydride ($NaBH_4$, >99%), tetrachloroaurate trihydrate ($HAuCl_4 \cdot H_2O$, >99%), L-ascorbic acid (AA, >99%), silver nitrate ($AgNO_3$, >99%), potassium bromide (KBr, >99%), dithiothreitol (DTT), concentrated hydrochloric acid (HCl, 37%), potassium cyanide (KCN, >96%), and sodium chloride (NaCl, >99%). The following reagents were purchased from bioWorld and used as received: cetyltrimethylammonium bromide (CTAB, >99%) and cetylpyridinium chloride monohydrate (CPC, >99%). The following reagents were purchased from TCI America and used as received: sodium oleate (>97%).

Au Seed Synthesis. Au seeds (spheres and rods) with aspect ratios of 1, 3.4, and 8 were synthesized as previously reported.[267] The aspect ratio of rod seeds was tuned via addition of different amounts of [Au^{3+}] and subsequent etching over 4 h at 40°C. See Supporting Information for amounts and resultant aspect ratios.

Au Elongated Nanoparticle Synthesis. Au products were synthesized through modifications to previously reported syntheses to incorporate seeds of different sizes and aspect ratios.[12] See Supporting Information for seed and reagent quantities and resultant particle statistics.

EM Image Analysis. Particle structure was analyzed through algorithmic analysis of EM images to directly measure particle edge length, aspect ratio, corner rounding, and shape yield as previously reported.[7] For structural measurements, at least 100 nanoparticles were analyzed in images taken from diverse areas of the EM grid. For yield calculations ~1,000 nanoparticles were analyzed. See Supporting Information for statistical measurements of particle structure, representative EM images, and post analysis EM images where the structure of particles has been fit.

DNA Synthesis. All DNA sequences were synthesized on a solid-support MM48 synthesizer (BioAutomation) with reagents purchased from Glen Research. The resultant DNA, synthesized with a 5' trityl group, were cleaved from the support according to Glen Research procedures. DNA was purified using reverse-phase high-performance liquid chromatography (RP-HPLC; Agilent) and subsequently deprotected following standard procedures. The molecular weight of the DNA was confirmed with matrix-assisted laser desorption ionization time-of-flight mass spectrometry (MALDI-TOF-MS). Extinction coefficients for DNA were determined using IDT's "Oligonucleotide Analyzer" tool and UV-Vis spectroscopy measurements were used to

determine DNA concentration. DNA was aliquoted in small volumes, dried, and kept at 2-8°C until use. See Supporting Information for DNA sequences.

DNA Functionalization. Nanoparticles were functionalized with 3' thiolated DNA according to previously reported procedures.[166, 325] After washing via three rounds of centrifugation and replacement with fresh buffer (0.5M NaCl, 0.01M phosphate buffer, 0.01 wt. % sodium dodecyl sulfate), DNA functionalization density was confirmed by liberating DNA strands through dissolution of the Au nanoparticle core with 150mM KCN for 1 h at 40°C. Serial dilution of a solution of fresh DNA and KCN was used to create a standard curve from UV-Vis spectroscopy measurements to determine an extinction coefficient. After dissolution, each sample was measured with UV-Vis to determine the concentration of DNA. Comparison of this with an estimate of particle concentration and surface area yielded a surface density. See Supporting Information for details of these estimations and resultant DNA ligand density.

Superlattice Assembly. Nanoparticle superlattices were synthesized following previously reported methods with final nanoparticle to DNA linker ratios of 25,000 DNA molecules per particle or 50,000 molecules per particle and 0.5 M NaCl or 0.35 M NaCl.[8] See Supporting Information for data not included in the text.

Transfer of Superlattices to Solid State. Superlattices were encapsulated in silica following previously reported procedures.[322] In order to prepare superlattices for sectioning, silica-encapsulated samples were further embedded in a polymeric resin (Embed 812, Electron Microscopy Sciences) following previously reported procedures.[9] Resin-embedded samples were then microtomed into 200 nm (lattices comprised of particles with an aspect ratio of 1.6) or 400

nm (all other lattices) thick sections in order to visualize particles within the lattice with electron microscopy.

Electron Microscopy. Transmission electron microscopy images of Au nanoparticles were collected using a Hitachi 8100. Scanning electron (SE) and Z-contrast mode images of superlattices were collected using a Hitachi HD2300 STEM.

SAXS Measurements. Solution phase samples were transferred to a 1.5mm quartz capillary tube. SAXS measurements were collected at the Dupont-Northwestern Dow Collaborative Access Team (DND-CAT) following previously reported methods.[197]

DNA-Nanoparticle Models. All nanoparticles were comprised of spherical beads, which remained bare, had an "anchor" DNA attached, or had a "linker" DNA strand attached. The DNA surface density was constant across all systems and consistent with experimental values. Moreover, effective interaction parameters, developed by Li et al.[69] and later modified by O'Brien and Girard et al.[8] were used to establish interactions between particles, including an attractive pairwise force between DNA sticky ends.

MD Simulations. All particle models were initialized in an ordered lattice and allowed to relax and equilibrate. The equilibration period was implemented using NPT integration as in HOOMD-blue.[326, 327] Particle models with ARs < 4.5 were initialized in both FCC and BCT lattices. Infinite rectangular prism models were initialized in both SP and HP lattices. Every simulation contained the same number of periods of Bravais lattices. See Supporting Information for additional simulation results.

5.5.2 Characterization of elongated RD for DNA-Mediated Crystallization

Table 6. Summary of synthetic conditions and resultant elongated rhombic dodecahedra products. Seed volumes correspond to seed stock solutions indicated in Table 4. N seed and N product columns indicate the number of particles which were analyzed to determine the listed structural parameters (i.e. L_{minor}, L_{major}, AR).

Volume Seed (μL)	L_{minor} Seed (nm)	L_{minor} STD Seed (nm)	*AR* Seed	N Seed	*AR* Product	L_{minor} Product (nm)	L_{minor} STD (nm)	L_{major} Product (nm)	L_{major} STD (nm)	N product	Yield (%)
75	21.2	2.7	1.7	383	1.6	20.9	1.4	33.4	4.4	955	96
180	21.2	2.7	1.7	383	2.0	16.1	1.6	31.5	4.1	1843	99
60	16.5	2.6	3.4	2238	2.8	22.3	1.2	61.6	9.1	2288	96
64	15.5	2.3	4.4	812	3.5	24.8	1.2	85.4	23.7	790	95
31	18.1	2	5.23	606	4.3	26.2	1.9	111.2	20.0	751	97
52	18.1	2	5.23	606	5.0	21.5	2.4	106.0	19.1	1117	95
75	17.3	2.7	8	158	9.0	16.2	2.4	143.7	17.8	661	95

Each elongated rhombic dodecahedron sample was analyzed with TEM (Hitachi H-8100) in order to quantify shape yield and structural parameters. Since the extinction coefficient of Au rods may be calculated,[267] yield measurements enabled estimation of the extinction coefficient at the localized surface plasmon resonance (LSPR) for each elongated rhombic dodecahedron, based on the following formulas:

$$[\text{elongated rhombic dodecahedron}] = [\text{rod seed}] \times (\text{yield}/100)$$

$$\varepsilon_{LSPR} = (\text{extinction}_{LSPR} \times \text{path length}) / [\text{elongated rhombic dodecahedron}]$$

5.5.3 Functionalization of elongated RD for DNA-mediated crystallization

Particles were functionalized with thiol modified DNA ("A" anchor in Table 7) and salt aged according to literature protocol.[88, 166] Briefly, ~1 mL of DTT was brought to 100mM in 0.01M phosphate buffer. 10OD of lyophilized DNA was resuspended in 150uL of 0.01M phosphate buffer. 150uL of 100mM DTT solution was added to reduce any disulfide bonds and allowed to

react for 1 hour at room temperature. After 1hour, 300uL of DNA solution plus 200uL of nanopore water was loaded into a Nap-5 size exclusion column (GE Healthcare) and DNA was eluted in 1mL according to listed protocols. 30OD of DNA was used to functionalize 24mL of particles, such that functionalization occurred with ~1.25OD DNA per 1mL of particles.

Table 7. Table contains sequences for DNA-mediated crystallization of elongated rhombic dodecahedra. Blue regions on "A" Linker d40 (self) and "A" Anchor are complementary and green regions on "A" Linker d40 (self) and Duplexer d40 are complementary. Red bases indicate the "sticky end." The extinction coefficient was determined using the Integrated DNA Technologies (IDT) OligoAnalyzer.

Name	ε_{260} ($M^{-1}cm^{-1}$)	MW (g/mol)	Sequence (5' to 3')	# Bases
"A" Anchor	286100	8729.9	TCA ACT ATT CCT ACC TAC AAA AAA AAA A - SH	28
"A" Linker d40 (self)	654700	20157.1	GTA GGT AGG AAT AGT TGA A TT TAG TCA CGA CGA GTC ATT ATT TAG TCA CGA CGA GTC ATT A GCGC	65
Duplexer d40	410500	12616	AAT GAC TCG TCG TGA CTA AAT AAT GAC TCG TCG TGA CTA AA	40

In order to prepare particles for functionalization with DNA, the surfactant present from synthesis conditions must be removed. Therefore, as synthesized particles were aliquoted into 1.5mL Eppendorf tubes, centrifuged once (Table 8), the supernatant removed. The pellet resuspended in 1mL of nanopure water and 75µL of 0.1% SDS. Particles were centrifuged a second time (Table 8) and resuspended with 125µL of freshly purified DNA solution (~1.25OD/mL particle). After 30 minutes the solution was brought up to 0.01M phosphate buffer and 0.01 wt. % SDS in 1mL total volume.

Table 8. Table contains centrifugation conditions for functionalization of elongated rhombic dodecahedron (at each AR) with DNA. Columns labeled "1st" and "2nd" indicate the conditions used prior to addition of thiol modified DNA. Columns labeled "Post Funct." Indicate the conditions used to remove excess thiol modified DNA after particle functionalization and salt aging steps.

AR	1st Speed (rpm)	1st Time (min)	2nd Speed (rpm)	2nd Time (min)	Post Funct. Speed (rpm)	Post Funct. Time (min)
1.1	8000	8	8000	8	9000	9
1.6	9500	9	11000	12	11000	12
2.0	6000	8	7000	12	9000	9.5
2.8	6000	6	6500	8	8000	8
3.5	9200	8	10000	10	10000	10
4.3	8000	6	8800	7	8800	7
5.0	8000	7	8600	8	8600	10
9.0	8000	8	8500	10	10000	10

After 30 minutes, particles were salt aged up to a final concentration of 0.5M NaCl in order to screen the charges of the DNA backbone and enable dense functionalization on the particle surface. Every thirty minutes the concentration of NaCl (stock solution at a concentration of 2M) was incrementally increased from 0.05M to 0.1M to 0.2M to 0.3M to 0.4M to 0.5M with sonication after each salt addition. The particles were allowed to shake for 12 hours at 0.5M NaCl. In order to remove excess DNA and to concentrate functionalized particles, particles were centrifuged according to conditions listed in Table 8 and resuspended in 0.5M NaCl, 0.01M phosphate buffer, and 0.01 wt. % SDS. UV-Vis spectroscopy revealed particles maintained their original structure after functionalization with DNA (Figure 53). Furthermore, the concentration of functionalized particles was determined from their extinction value at their LSPR using the equation listed above in Section VIII. Figure 54 shows the average anchor DNA density on each particle. These values match or exceed reported values for densely DNA-functionalized, large spherical particles (250nm).[88]

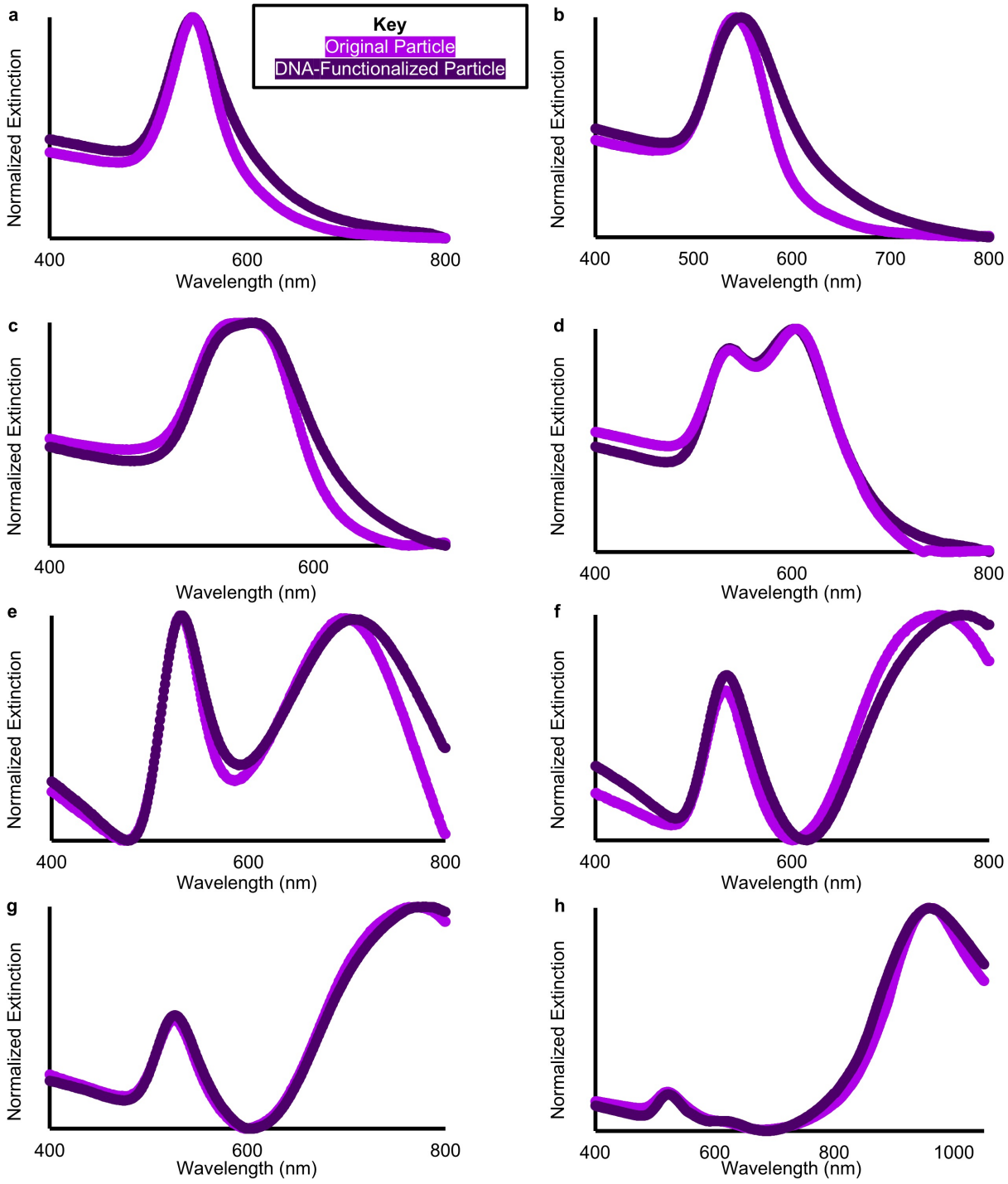

Figure 53. UV-Vis shows elongated rhombic dodecahedra particles before and after functionalization with DNA. Spectra correspond to particles with ARs of: **a** 1.1, **b** 1.6, **c** 2.0, **d** 2.8, **e** 3.5, **f** 4.3, **g** 5.0, and **h** 9.0. The key indicates the spectra for **a-h**.

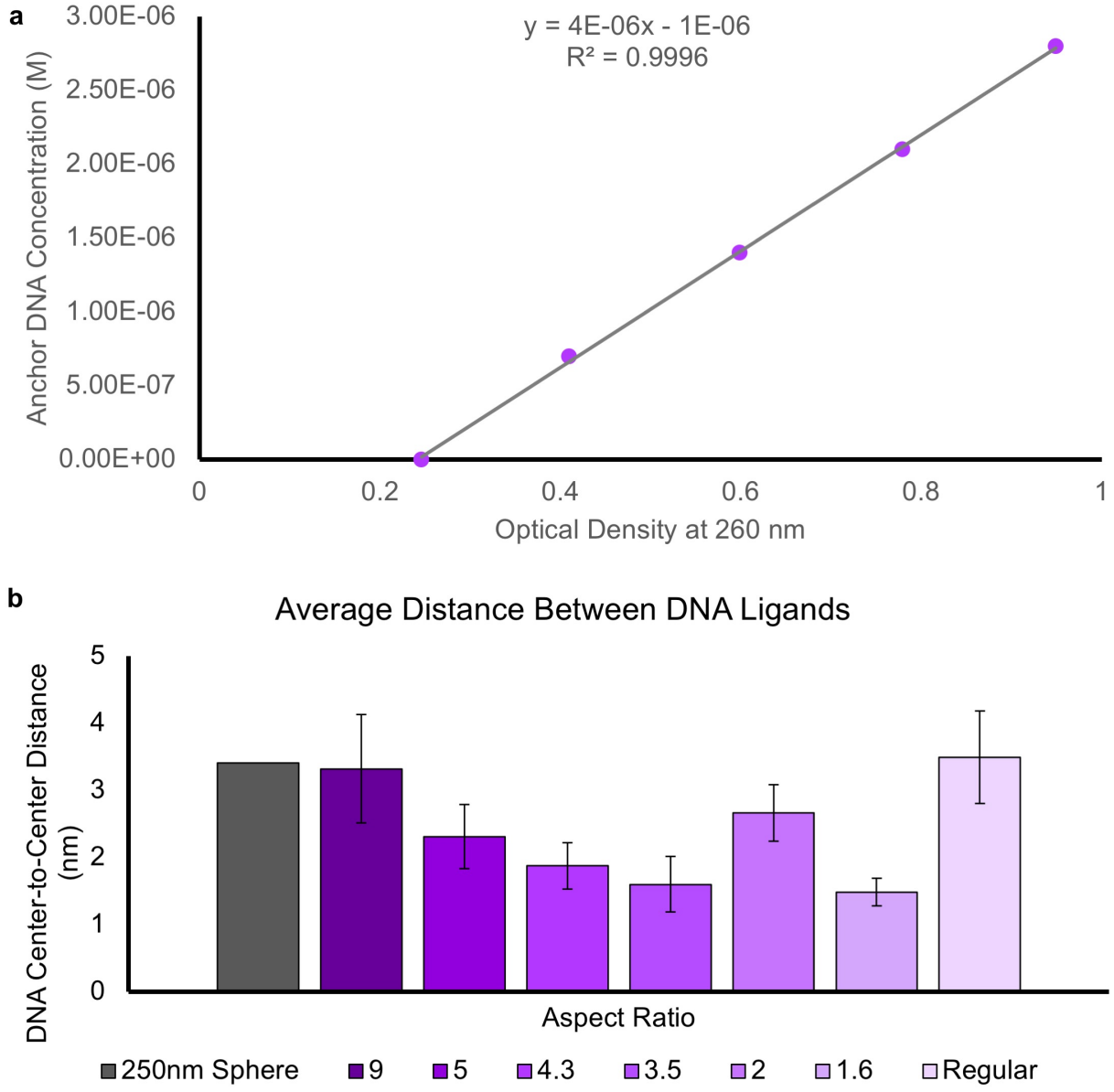

Figure 54. UV-Vis spectroscopy enables calculation of anchor DNA density on particle surfaces. a Standard curve to quantitatively relate the concentration of anchor DNA in a solution of 150mM KCN, 0.5M NaCl, 0.01M phosphate buffer, and 0.01 wt. % SDS to its absorption. **b** Calculation of the average distance between the center of DNA strands on a particle surface. The 250nm Sphere value was previously reported by Hurst et al. and serves as a comparison of densely functionalized large spheres with a high radius of curvature. Error bars represent error propagation that accounts for deviation in particle surface area and particle extinction coefficient.

5.5.4 DNA-mediated crystallization of elongated RD

Crystallization of DNA-functionalized particles was initiated through the addition of a "linker" DNA strand partially duplexed with a "duplexer" DNA strand (Table 7) according to literature precendent.[25] One region of the "linker" strand is complementary to the anchor strand attached to the particle and at the opposite end 5 bases remain unpaired. These unpaired bases act as a self-complementary "sticky end" such that all particles may favorably interact.

First, lyophilized linker and duplexer strands were resuspended in 0.5M NaCl and 0.01M phosphate buffer and combined in a 1:1 ratio. Strands were annealed at 55°C for 30 minutes to favor hybridization. Next, these duplexed strands were added to functionalized particles such that in 1mL total volume:

- [particles] = 50pM
- [NaCl] = 0.2-0.5M
- [SDS] = 0.01 wt. %
- [phosphate buffer] = 0.01M
- Number of linker strands per particle = 25,000 – 250,000 (in excess of the number of DNA strands attached to the particle surface)

Solutions of functionalized particles and linker/duplexer strands were annealed at 40°C for 30 minutes and allowed to cool to room temperature. Once cooled, dark aggregates formed. This solution was mixed and 100μL aliquots were distributed into 200μL PCR 8-tube strips. These strips were loaded into a thermal cycler (Veriti 96-Well Fast Thermal Cycler) and slowly cooled from 60°C to 20°C at 0.1°C/10 minutes.

5.5.5 SAXS characterization of DNA-directed crystals

SAXS samples were prepared by loading 40μL of slow cooled solution into a quartz capillary (Quarzkapillaren, 1.5mm outside diameter, 80mm length, 0.01mm thick). All SAXS data was collected at the DuPont-Northwestern-Dow Collaborative Access Team beamline of the Advanced Photon Source at Argonne National Laboratory. One-dimensional patterns were generated from an azimuthal average of two-dimensional scattering patterns collected with a 10keV collimated beam calibrated against a silver behenate standard with 0.1 to 0.5s exposure time. SAXS patterns shown in the main text and this supplementary information plot scattering intensity (I(q)) versus the scattering vector (q), where q is related to the scattering angle (2θ) and the wavelength of X-ray radiation (λ) by:

$$q = 4\pi\sin(\theta)/\lambda$$

Scattering related to both the crystal lattice (i.e. regular particle arrangement) and the individual particles contribute to I(q). Therefore, SAXS scattering of discrete, functionalized particles was collected and is represented in Figure 54 as the Form Factor (P(q)). Relative to the scattering of gold, peaks from DNA and solvent were assumed to be negligible.

Figure 54 shows SAXS patterns for crystals grown at different NaCl concentrations and linker to particle ratios for each particle. Although peaks may shift in position (indicative of lattice parameter differences) or broaden (indicative of differences in the degree of ordering), the same peaks appear for each particle under the various conditions. This indicates that the arrangement of particles remains largely unchanged over the parameters explored.

The position of SAXS peaks can be compared to modeled peaks for perfect crystals, such as those shown in black in Figure 51e, to approximate lattice parameter (a). Using geometry to calculate the dimensions of particles in a particular lattice direction, DNA length between particles could be estimated for all ordered samples shown in the main text (Table 9). Particles with an AR of 1.6 do not prefer a single orientation, so DNA length was calculated for the largest possible distance which occurs when elongated facets align in a face-to-face fashion. These DNA lengths confirm that modeled lattices reasonably match expected experimental conditions (i.e. "sticky ends" between adjacent particles should be able to hybridize).

Table 9. Table lists outcome of SAXS pattern analysis shown in Figure 51e. Rise per base considers all DNA between the particles, including single-stranded regions.

AR	Symmetry	Lattice Parameter (nm)	[NaCl]	# Linker/Particle	Approx. DNA Length (nm)	Rise per base (nm)
1.1	FCC	136.4	0.5	25,000	47.4	0.325
1.6	pFCC	118.4	0.5	25,000	49.5 or less	0.339 or less
3.5	BCT	85.0	0.35	25,000	44.7	0.306
4.3	BCT	89.0	0.35	25,000	46.2	0.316
5.0	BCT, HP	83.6, 91.2	0.5	25,000	48.4, 56.0	0.331, 0.383
9.0	HP	75.7	0.5	25,000	49.3	0.338

In addition, the BCT and FCC lattices are related structures where the elongation of both the FCC lattice and RDs along the c-axis leads to the BCT. Since particles are better oriented due to the elongated shapes and with larger side face area, the in-plane interaction increases as reflected in shorter rise per base pair of ~0.31 (Table 9).

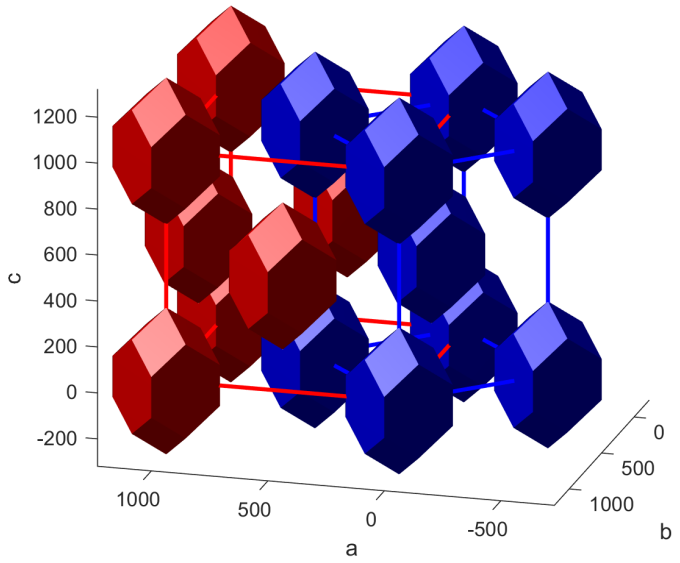

Figure 55. The BCT lattice is analogous to an FCC lattice where the long facets of particles align. Two BCT unit cells with models of elongated RD are shown to illustrate their similarity to an FCC lattice.

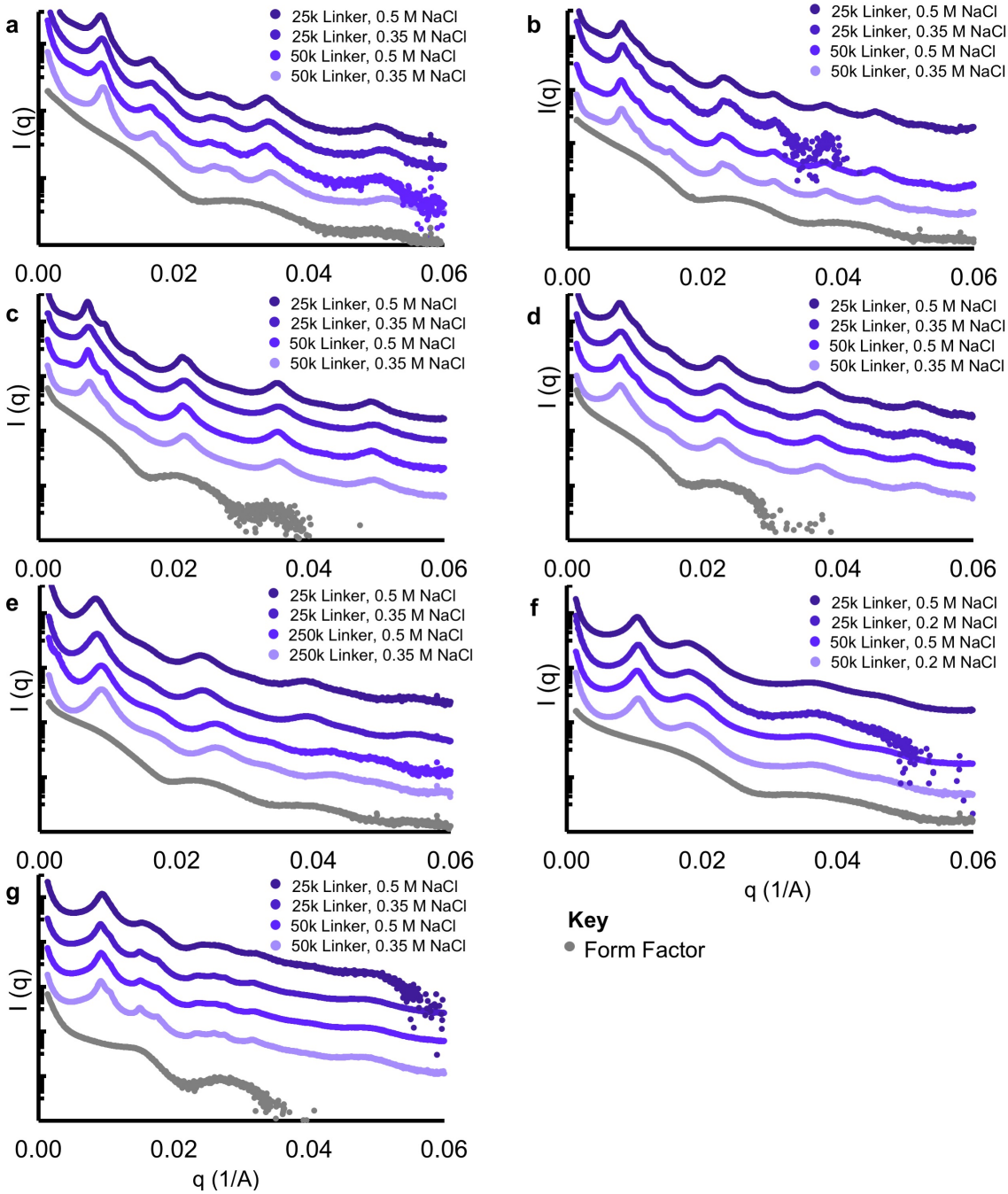

Figure 56. SAXS patterns show structure of DNA-mediated crystallization of all particles over several linker strand to particle molar ratios and salt concentration conditions. I(q) is shown on a log scale and is scaled to show several patterns on a single plot. **a** SAXS pattern corresponding to particles with AR=9.0, **b** SAXS pattern corresponding to particles with AR=5.0, **c** SAXS pattern corresponding to particles with AR=4.3, **d** SAXS pattern corresponding to particles with AR=3.5, **e** SAXS pattern corresponding to particles with AR=2.8, **f** SAXS pattern corresponding to particles with AR=2.0, **g** SAXS pattern corresponding to particles with AR=1.6. The key corresponds to all plots.

5.5.6 EM characterization of DNA-directed crystals

EM sample preparation required the transfer of crystals to the solid state. One strategy is to encase the materials in silica, which has been shown to preserve the solution phase structure of the materials. This was done according to literature protocol.[322] Once encased, EM samples were prepared by drop casting the solution onto a copper TEM grid and wicking away liquid with VWR grade 413, quantitative filter paper. This was repeated 5 times. All EM images were recorded using a Hitachi HD-2300 STEM in either the SE or the Z-contrast mode.

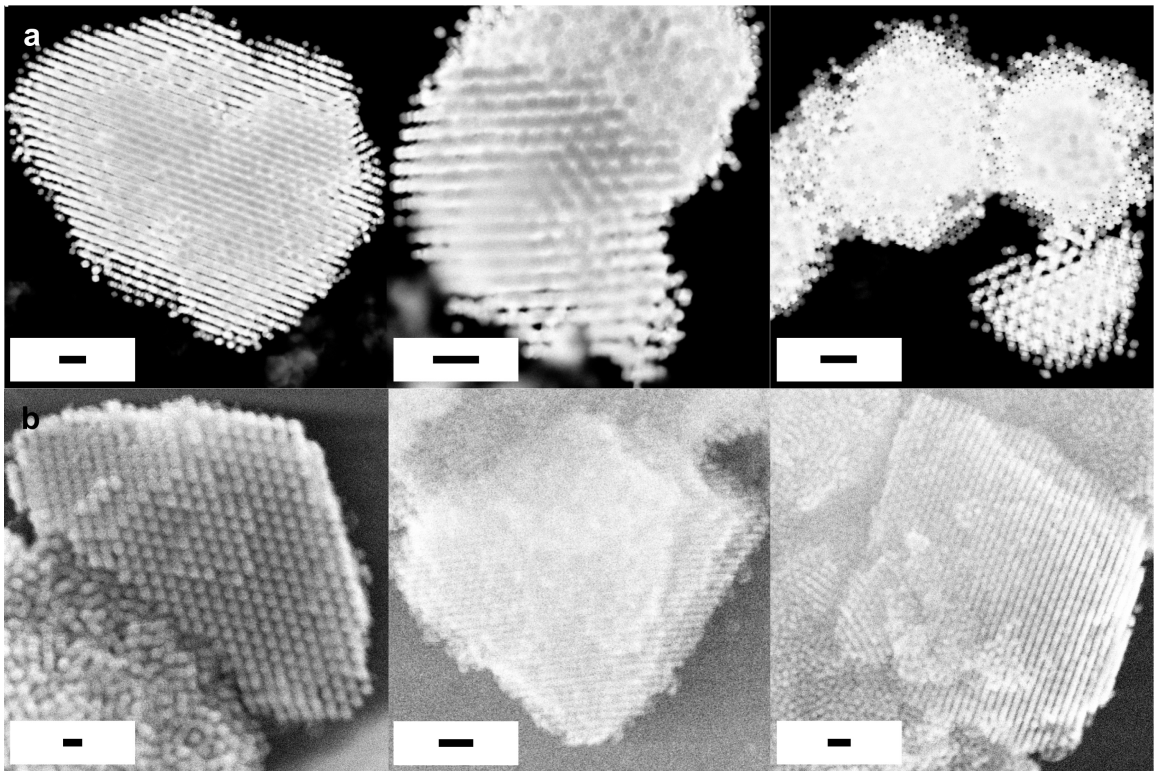

Figure 57. Figure shows additional EM images of superlattices grown from particles with AR = 1.1. a Z-contrast mode images of superlattices crystallized at 0.5M NaCl and with 25,000 linkers per particle. **b** SE mode images of superlattices crystallized at 0.5M NaCl and with 75,000 linkers per particle. Scale bars represent 200nm.

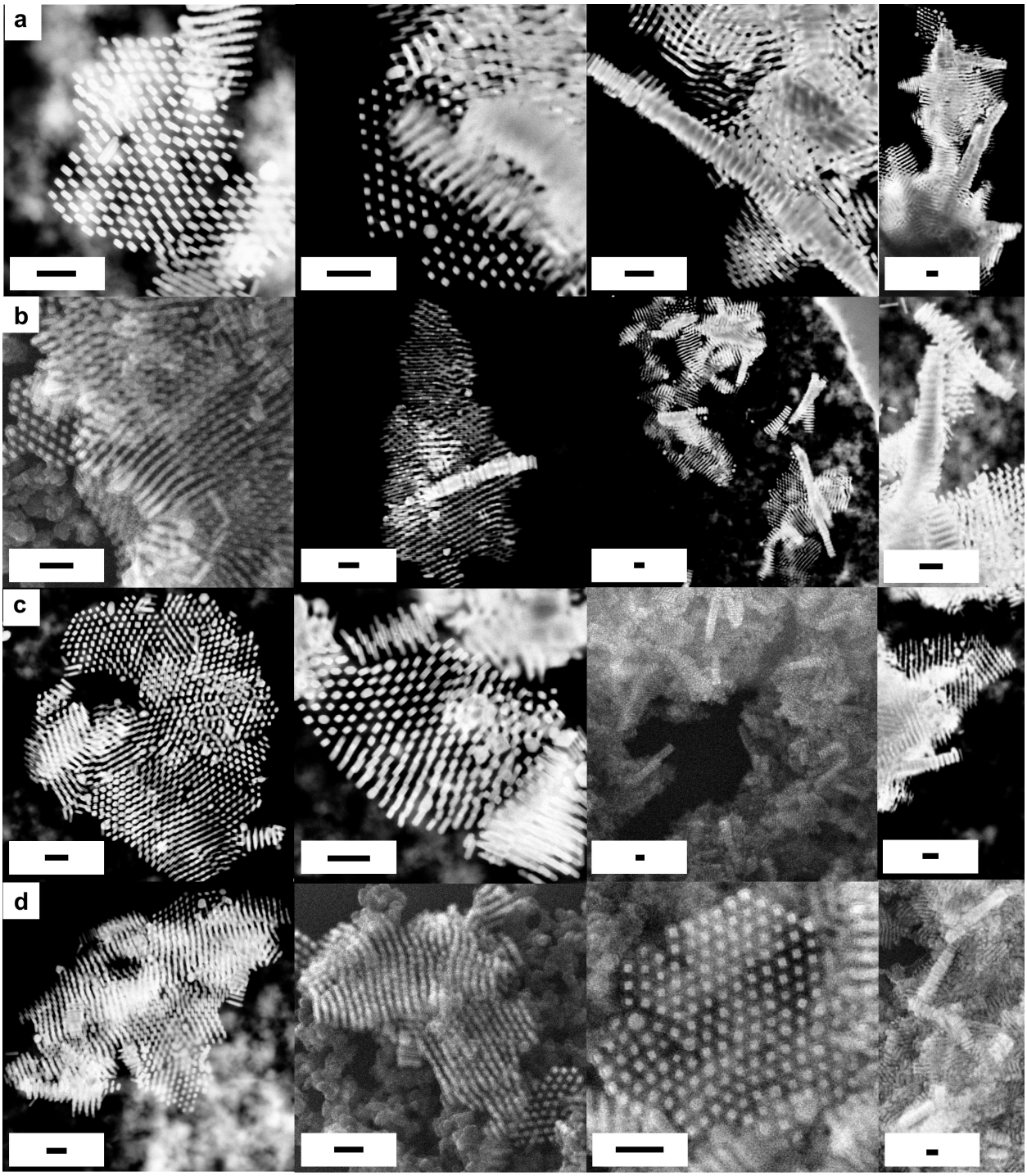

Figure 58. Figure shows additional EM images (SE and Z-Contrast mode) of superlattices formed from particles with AR=9.0 which correspond to a in Figure 56. Superlattices grown with 25,000 linkers in 0.5M NaCl (**a**), 25,000 linkers in 0.35M NaCl (**b**), 50,000 linkers in 0.5M NaCl (**c**), 50,000 linkers in 0.35M NaCl (**d**). Scale bars represent 200 nm.

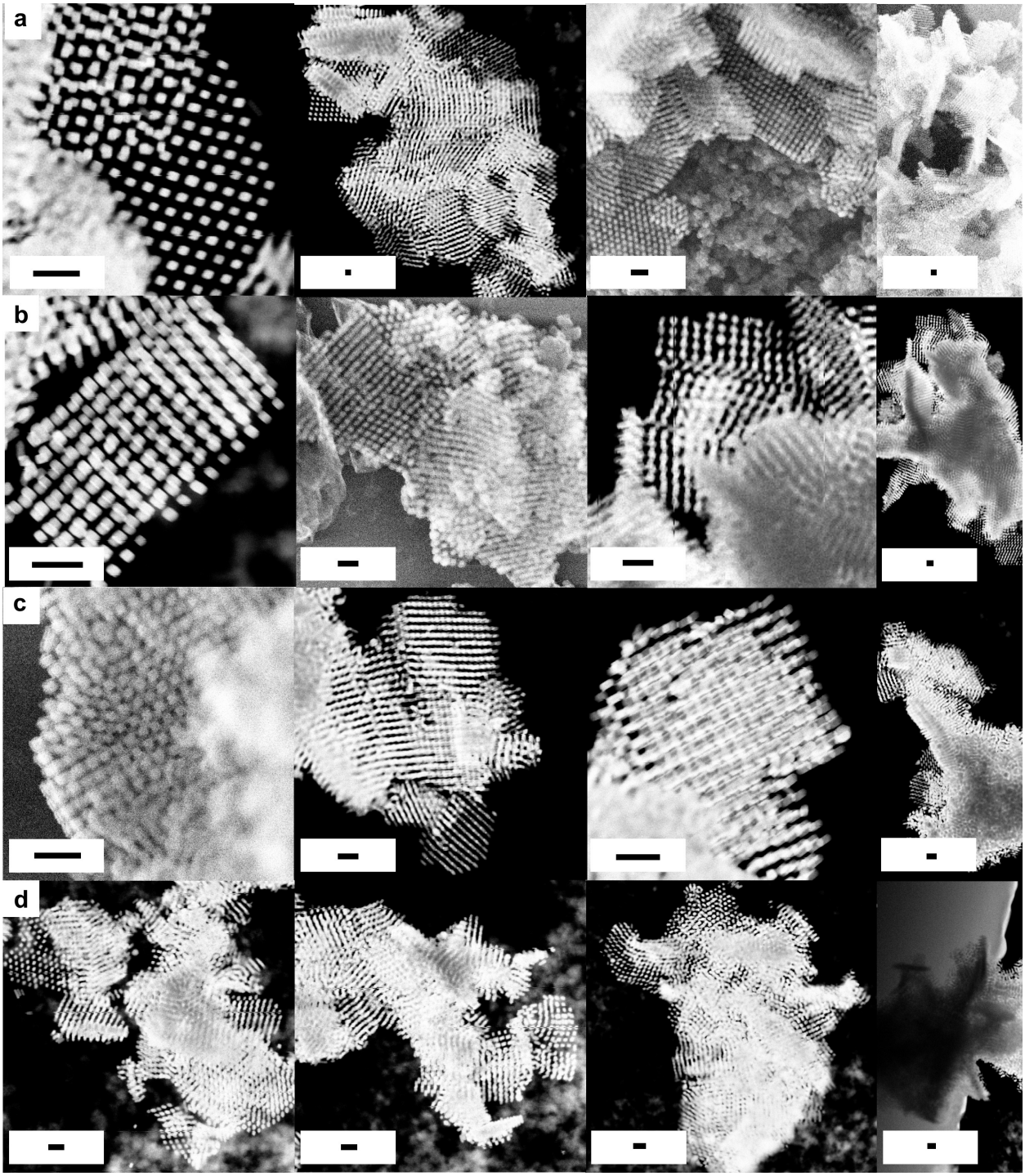

Figure 59. Figure shows additional EM images (SE and Z-Contrast mode) of superlattices formed from particles with AR=5.0 which correspond to b in Figure 56. Superlattices grown with 25,000 linkers in 0.5M NaCl (**a**), 25,000 linkers in 0.35M NaCl (**b**), 50,000 linkers in 0.5M NaCl (**c**), 50,000 linkers in 0.35M NaCl (**d**). Scale bars represent 200 nm.

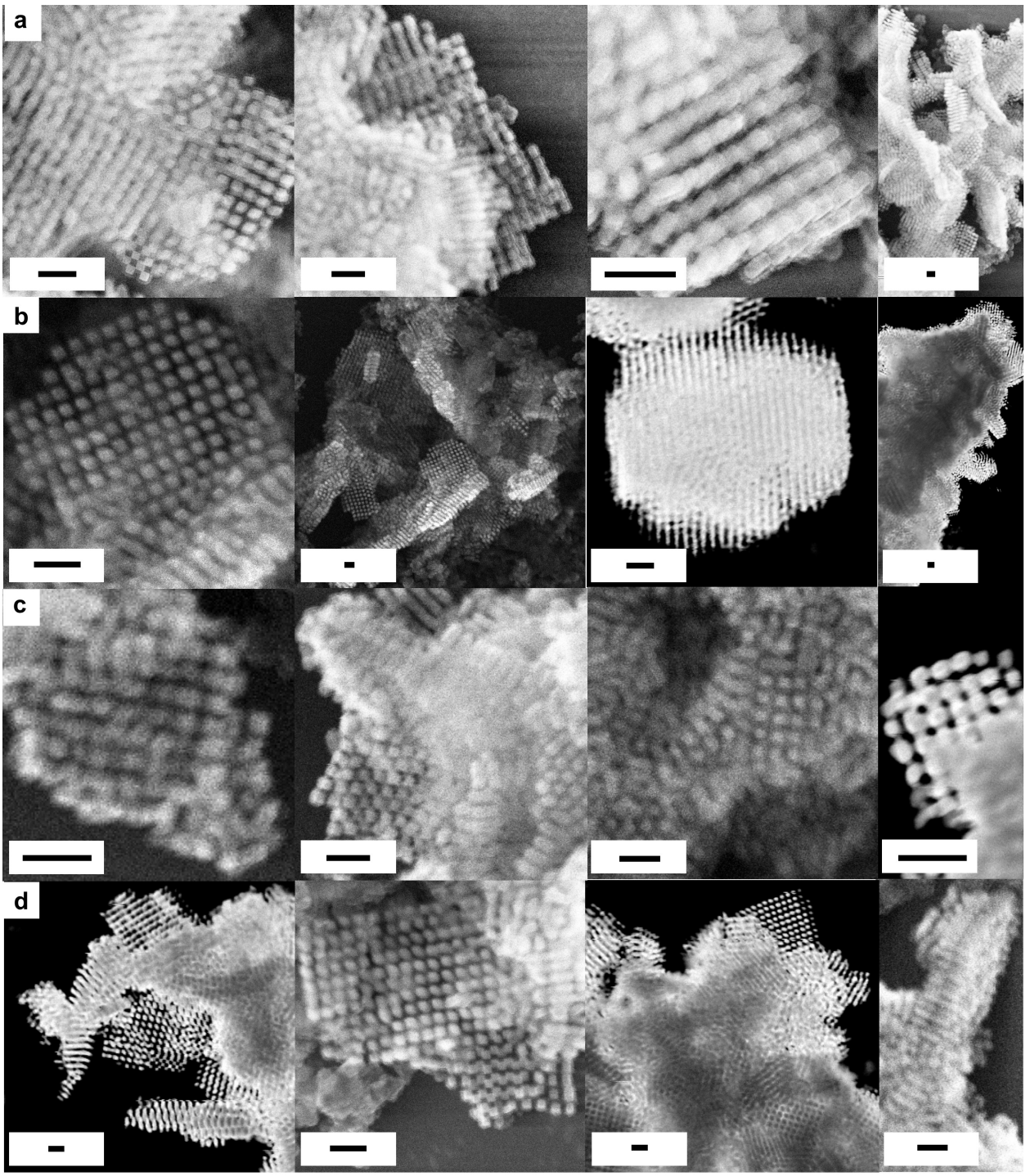

Figure 60. Figure shows additional EM images (SE and Z-Contrast mode) of superlattices formed from particles with AR=4.3 which correspond to c in Figure 56. Superlattices grown with 25,000 linkers in 0.5M NaCl (**a**), 25,000 linkers in 0.35M NaCl (**b**), 50,000 linkers in 0.5M NaCl (**c**), 50,000 linkers in 0.35M NaCl (**d**). Scale bars represent 200 nm.

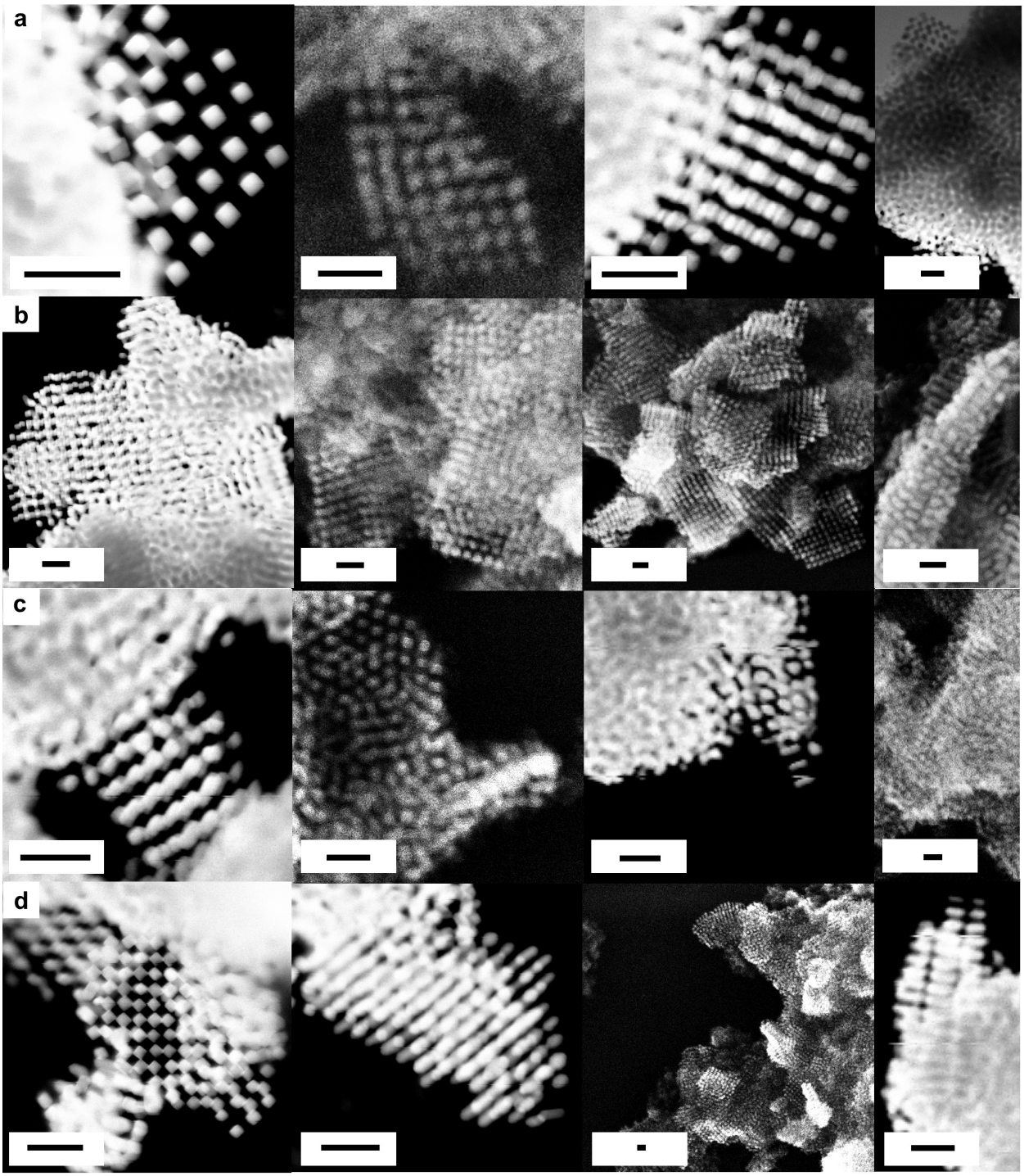

Figure 61. Figure shows additional EM images (SE and Z-Contrast mode) of superlattices formed from particles with AR=3.5 which correspond to d in Figure 56. Superlattices grown with 25,000 linkers in 0.5M NaCl (**a**), 25,000 linkers in 0.35M NaCl (**b**), 50,000 linkers in 0.5M NaCl (**c**), 50,000 linkers in 0.35M NaCl (**d**). Scale bars represent 200 nm.

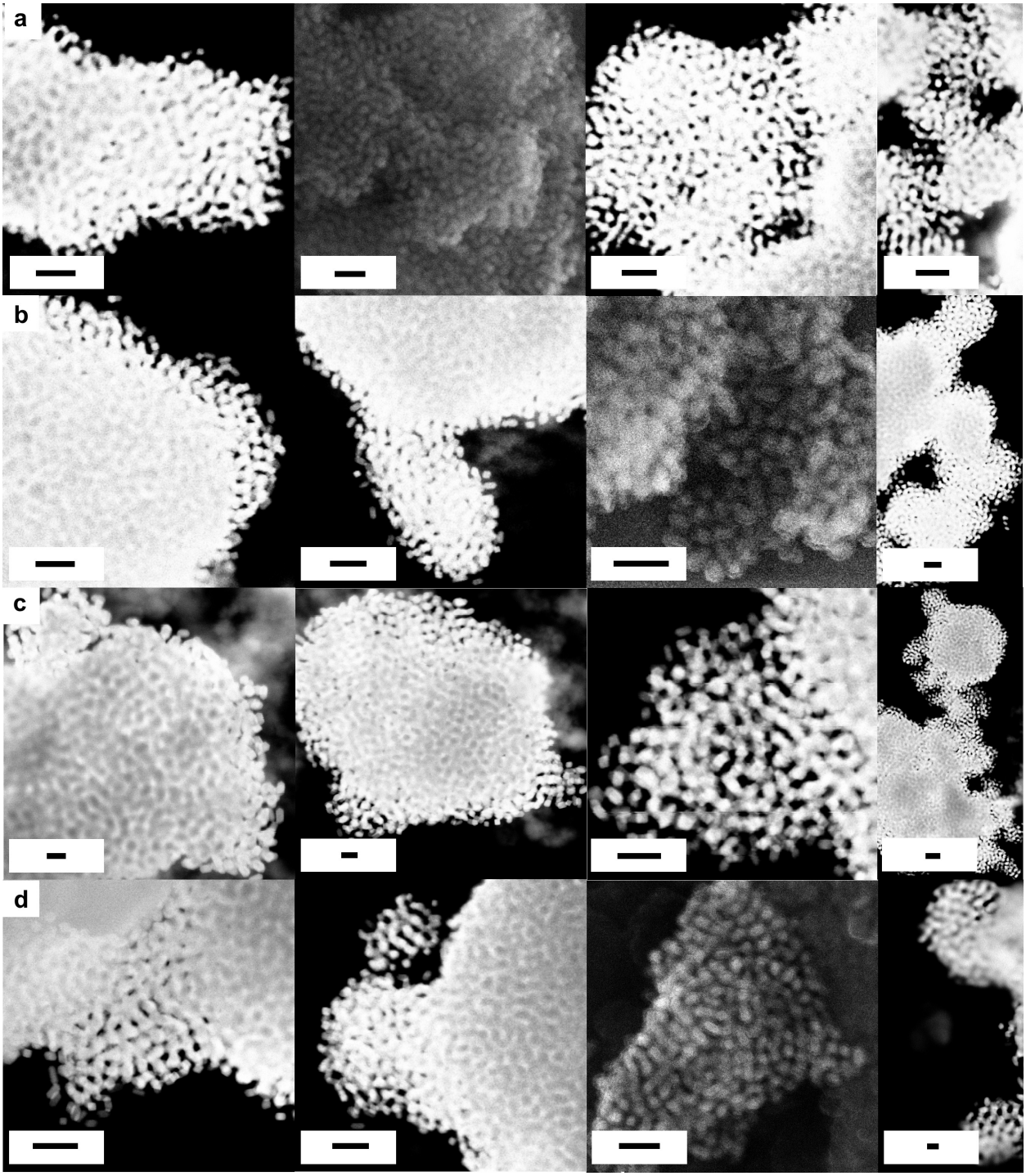

Figure 62. Figure shows additional EM images (SE and Z-Contrast mode) of superlattices formed from particles with AR=2.8 which correspond to e in Figure 56. Superlattices grown with 25,000 linkers in 0.5M NaCl (**a**), 25,000 linkers in 0.35M NaCl (**b**), 250,000 linkers in 0.5M NaCl (**c**), 250,000 linkers in 0.35M NaCl (**d**). Scale bars represent 200 nm.

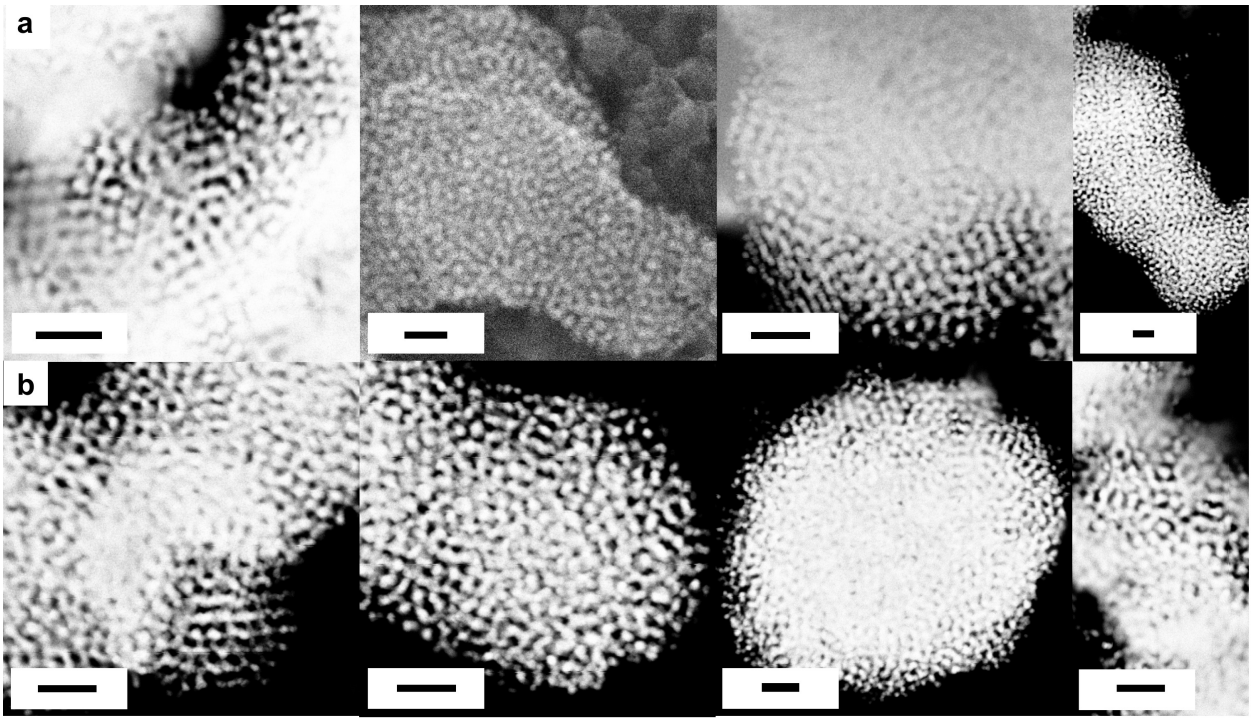

Figure 63. Figure shows additional EM images (SE and Z-Contrast mode) of superlattices formed from particles with AR=2.0 which correspond to f in Figure 56. Superlattices grown with 25,000 linkers in 0.5M NaCl (**a**), 25,000 linkers in 0.2M NaCl (**b**). Scale bars represent 200 nm.

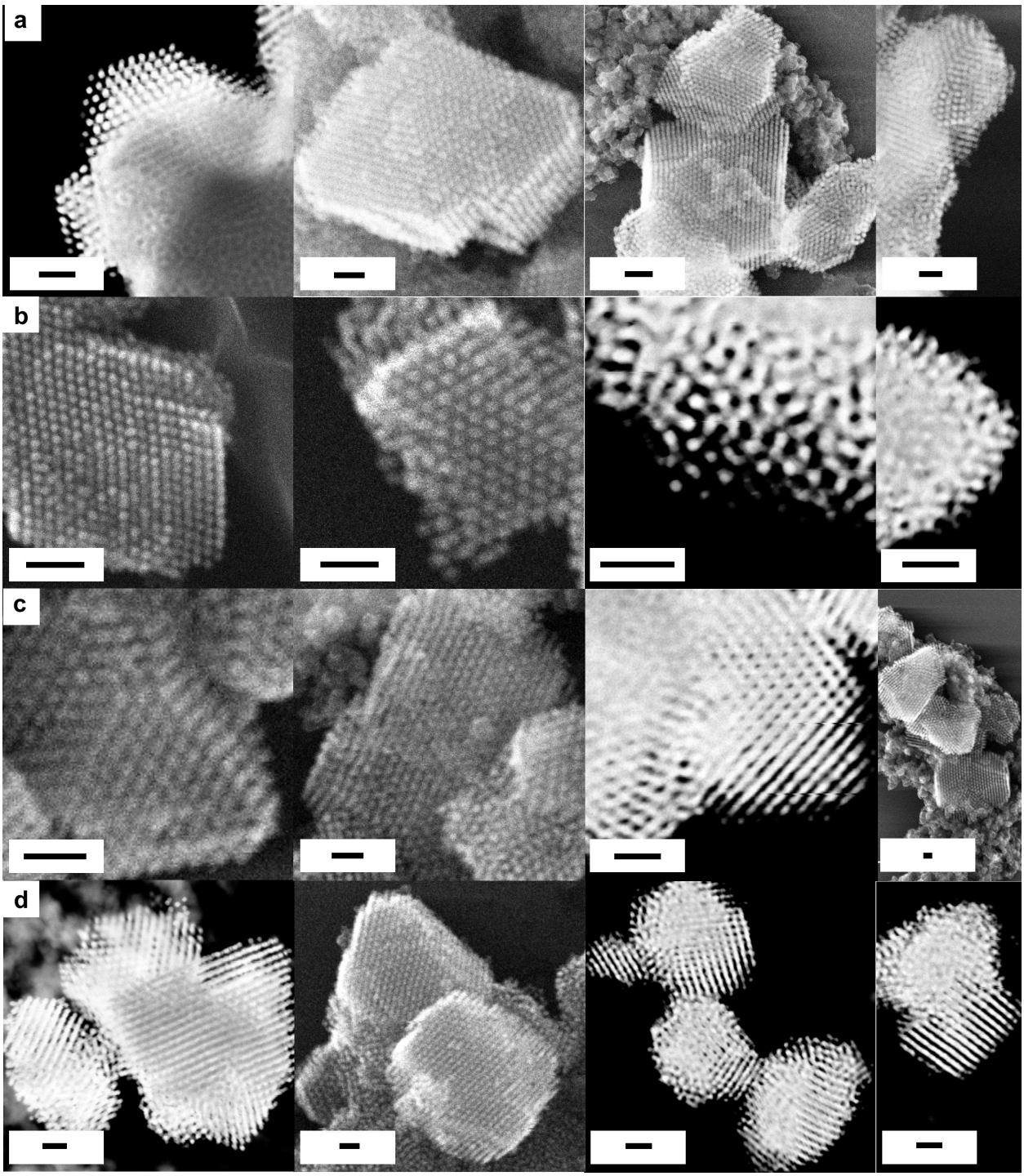

Figure 64. Figures show additional EM images (SE and Z-Contrast mode) of superlattices formed from particles with AR=1.6 which correspond to g in Figure 56. Superlattices grown with 25,000 linkers in 0.5M NaCl (**a**), 25,000 linkers in 0.2M NaCl (**b**). 50,000 linkers in 0.5M NaCl (**c**), 50,000 linkers in 0.35M NaCl (**d**). Scale bars represent 200 nm.

After embedding within silica, samples were further embedded in a polymer resin (Embed 812, Electron Microscopy Sciences) in order to microtome crystals into thin sections to enable visualization of particles within the crystal.[9] Sections were transferred to a copper grid. All EM images were recorded using a Hitachi HD-2300 STEM in Z-contrast mode.

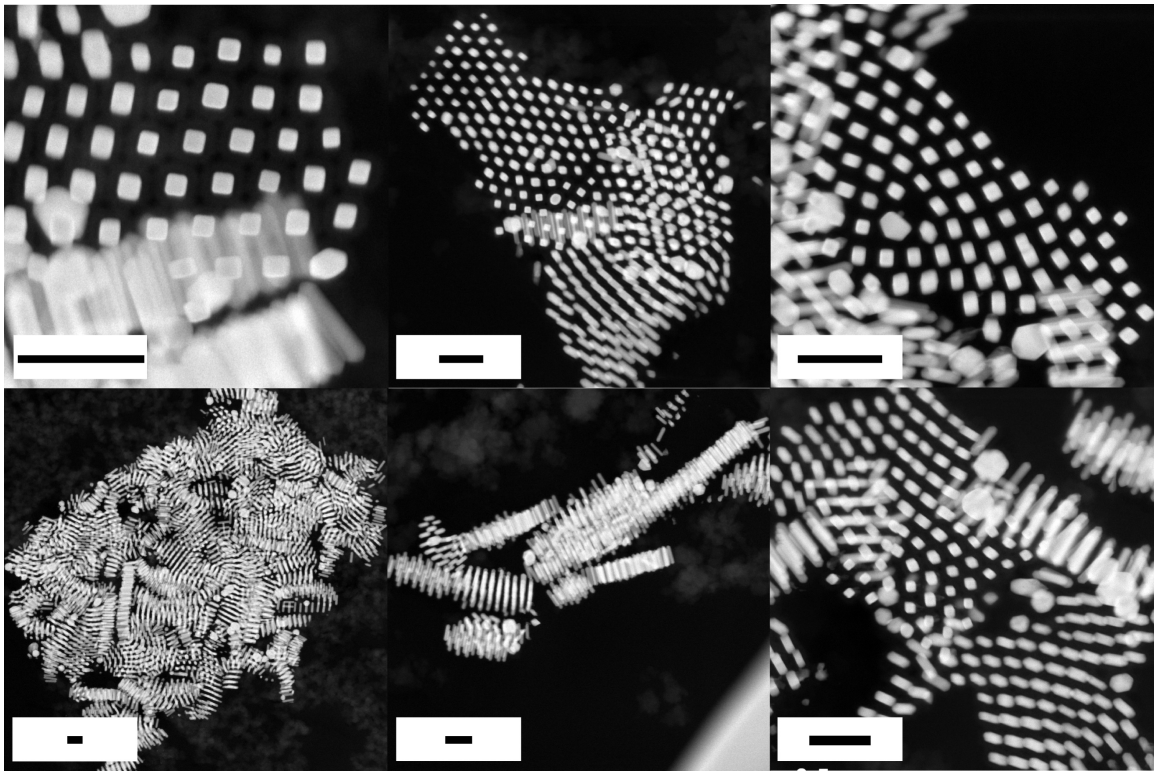

Figure 65. Figure shows additional EM images of resin-embedded and sectioned (400 nm thickness) superlattices formed from particles with AR=9.0 (0.5M NaCl, 25,000 linkers per particle). Images show sections that cut across (top, bottom right) and through layers (bottom left and middle). Scale bars represent 200 nm.

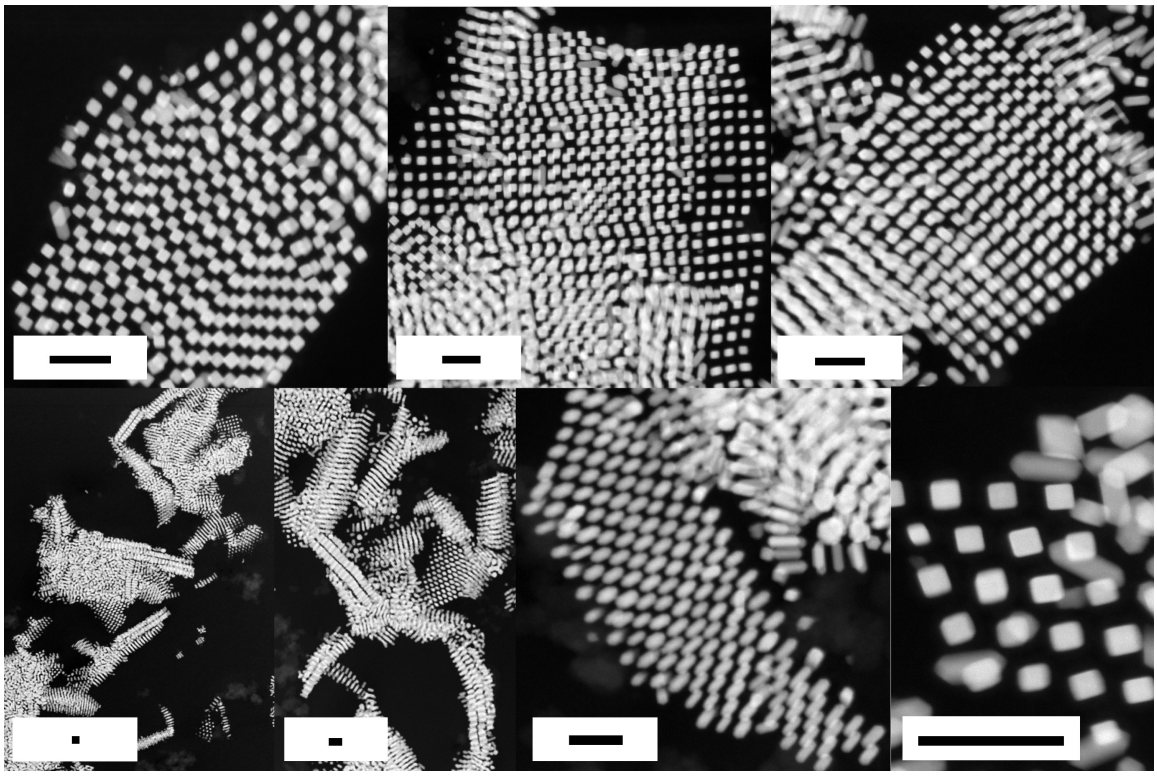

Figure 66. Figure shows additional EM images of resin-embedded and sectioned (400 nm thickness) superlattices formed from particles with AR=5.0 (0.5M NaCl, 25,000 linkers per particle). Images show sections that cut across (BCT: top, HP: bottom right) and through layers (bottom left). Scale bars represent 200 nm.

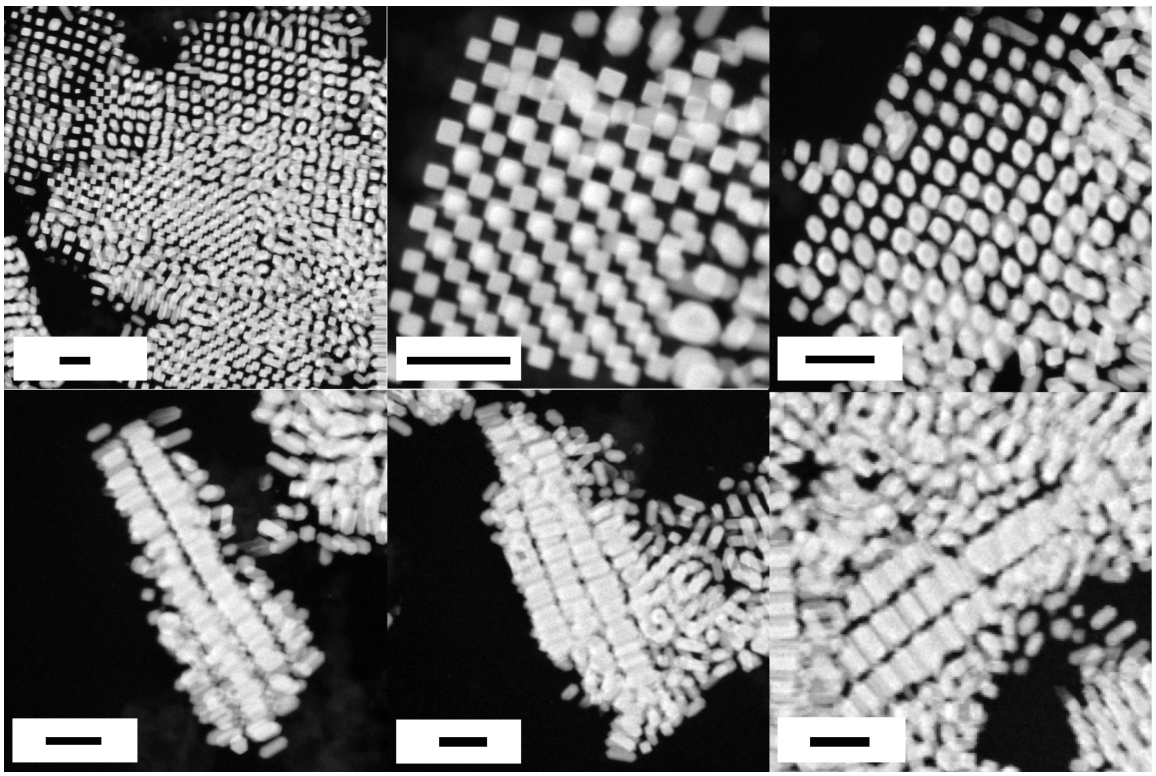

Figure 67. Figure shows additional EM images of resin-embedded and sectioned (400 nm thickness) superlattices formed from particles with AR=4.3 (0.35M NaCl, 25,000 linkers per particle). Images show sections that cut across (BCT: top) and through layers (bottom). Scale bars represent 200 nm.

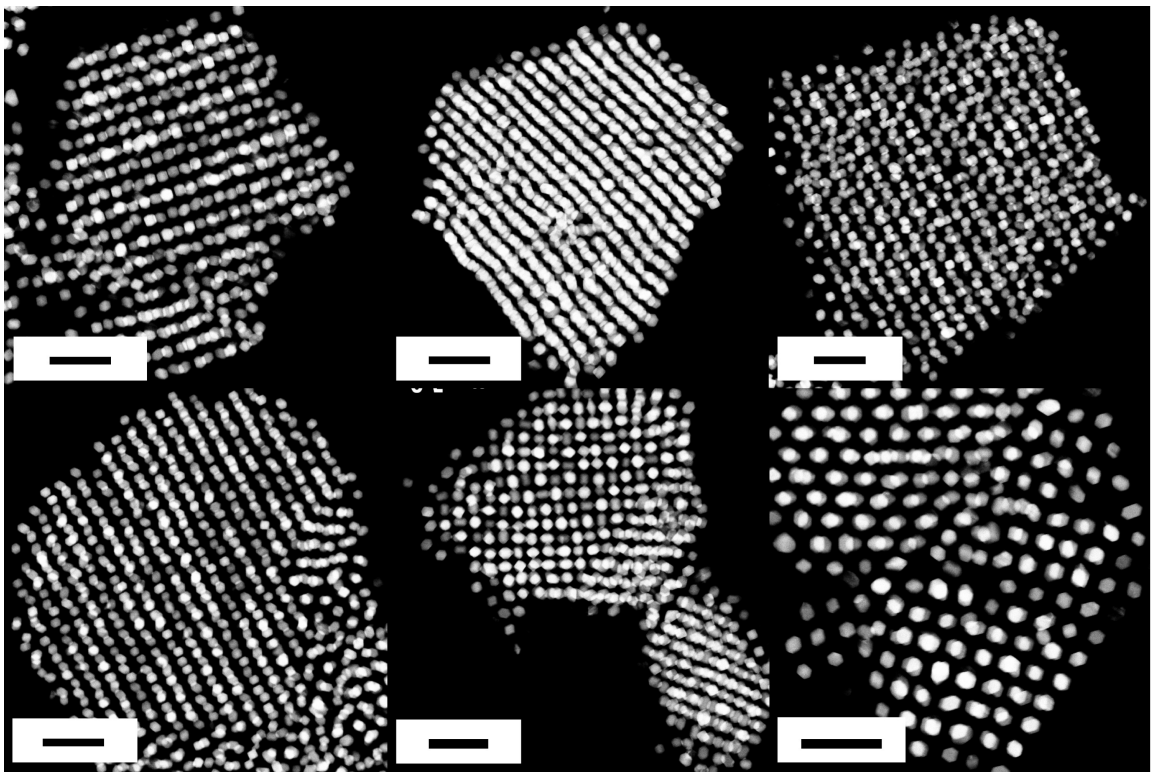

Figure 68. Figure shows additional EM images of resin-embedded and sectioned (200 nm thickness) superlattices formed from particles with AR=1.6 (0.5M NaCl, 25,000 linkers per particle). Scale bars represent 200 nm.

5.5.7 Summary of MD simulation conditions and results

Simulations were run using the HOOMD-blue molecular dynamics engine.[326, 327] Initial conditions were provided by the hoobas package (https://bitbucket.org/NUAztec/hoobas). The system is initialized in an ideal crystal lattice, then relaxed using integration in the microcanonical regime with a limit on displacement. It is then thermalized using a Langevin integrator with friction constant γ =1 over 10^5 time steps. The system is afterwards equilibrated using a Nosé-Hoover thermostat and barostat with coupling constants for temperature and pressure of $\tau = 0.85$ and $\tau_P = 2.0$ over 10^7 timesteps.

The size of a timestep is kept constant at $\Delta t = 0.003\ \delta t$, where δt is the natural time unit of the system. The force-field used to model DNA was previously developed[69, 77] and has been used

to model the DNA-mediated crystallization of spherical and anisotropic particles in excellent agreement with experimental results.[8]

Simulations were scaled according to literature precedent[8] in order to match experimental conditions. The ratio between the average L_{minor} of the experimental particles and the DNA "linker" length (B), in units of double stranded beads (nds, which each represent 4 base pairs) was approximately maintained constant over all simulations. For example, a DNA "linker" of four beads (approximately 16 bps) hybridized to "anchor" strands on a particle with L_{minor} = 6.1 nm satisifies this condition for finite AR particles. For infinite ARs, an L_{minor} = 7.3 nm with B = 6 nds maintains a size ratio comparable to experimental conditions. Since the ratio of DNA length to L_{minor} is approximate, additional DNA lengths were explored to further support simulated and experimental results. Results of these simulations are reported in Table 10 and Table 11. Figure 69 toFigure 72 show results labeled as Unstable for B=4 in Table 9.

Table 10. Table summarizes simulation conditions and results for all finite particles. a and c represent lattice parameters for unit cells. B indicates the length of the DNA "linker" strand in terms of number of double-stranded beads (nds).

AR	B (nds)	Initial Symmetry	a, initial (nm)	c, initial (nm)	c, initial / a, initial	Final Symmetry	a, final (nm)	c, final (nm)	c, final / a, final
1.15	2	FCC	37	37	1	FCC	34.4	34.4	1
1.35	4	FCC	36	36	1	pFCC	40.5	40.5	1
		BCT	32	38.4	1.2	pFCC	29	41.3	1.4
	5	FCC	37	36	1	pFCC	44.2	44.2	1
		BCT	33	39.6	1.2	pFCC	31.7	44.8	1.4
1.65	4	FCC	36	36	1	pFCC	41.2	41.3	1
		BCT	32	38.4	1.2	pFCC	29.2	42.8	1.4
	5	FCC	37	36	1	pFCC	45	45.1	1
		BCT	33	39.6	1.2	pFCC	32.2	45.7	1.4
1.85	4	FCC	36	36	1	pFCC	41.7	41.8	1
		BCT	32	38.4	1.2	pFCC	29.5	43.8	1.5
	5	FCC	37	36	1	pFCC	45.5	45.6	1
		BCT	33	39.6	1.2	pFCC	32.5	46.3	1.4
2	4	FCC	36	36	1	pFCC	41.8	43	1
		BCT	32	38.4	1.2	BCT	29.2	46.3	1.6
	5	FCC	37	36	1	pFCC	46.2	45.9	1
		BCT	33	39.6	1.2	pFCC	32.8	46.8	1.4
2.15	4	FCC	36	36	1	pFCC	41.5	45.3	1.1
		BCT	32	38.4	1.2	BCT	29	48.7	1.7
	5	FCC	37	36	1	pFCC	46.3	46.5	1
		BCT	33	39.6	1.2	BCT	32.7	48.7	1.5
2.65	4	FCC	36	36	1	Unstable			
		BCT	32	38.4	1.2	Unstable			
	5	FCC	37	36	1	Unstable			
		BCT	33	39.6	1.2	Unstable			
2.85	4	FCC	36	36	1	Unstable			
		BCT	32	38.4	1.2	Unstable			
	5	FCC	37	36	1	Unstable			
		BCT	33	39.6	1.2	Unstable			
3	4	FCC	30	42	1.4	BCT	29.3	58.5	2
		BCT	40	68	1.7	BCT	29.3	58.1	2
	5	FCC	31	43.4	1.4	BCT	32.2	61.1	1.9
		BCT	41	69.7	1.7	BCT	32.1	61.3	1.9
3.5	4	FCC	30	42	1.4	BCT	29.4	64.6	2.2
		BCT	40	68	1.7	BCT	29.4	64.9	2.2
	5	FCC	31	43.4	1.4	BCT	32.3	67.5	2.1
		BCT	41	69.7	1.7	BCT	32.3	67.5	2.1
4	4	FCC	30	42	1.4	Unstable			
		BCT	40	68	1.7	BCT	29.6	70.7	2.4
	5	FCC	31	43.4	1.4	Unstable			
		BCT	41	69.7	1.7	BCT	32.5	73.2	2.25
4.5	4	FCC	30	42	1.4	Unstable			
		BCT	40	68	1.7	BCT	29.5	76.5	2.6
	5	FCC	31	43.4	1.4	Unstable			
		BCT	41	69.7	1.7	BCT	32.4	79.4	2.45

Table 11. **Table summarizes simulation results for infinite rectangular prisms.**

AR	B (nds)	Initial Lattice	Final Lattice	a, final (nm)	angle, final (deg)
Infinite	5	HP	HP	35.4	120
		SP	SP	35.4	90
	6	HP	HP	38.4	118
		SP	SP	38.4	90
	7	HP	HP	41.4	120
		SP	SP	41.4	90

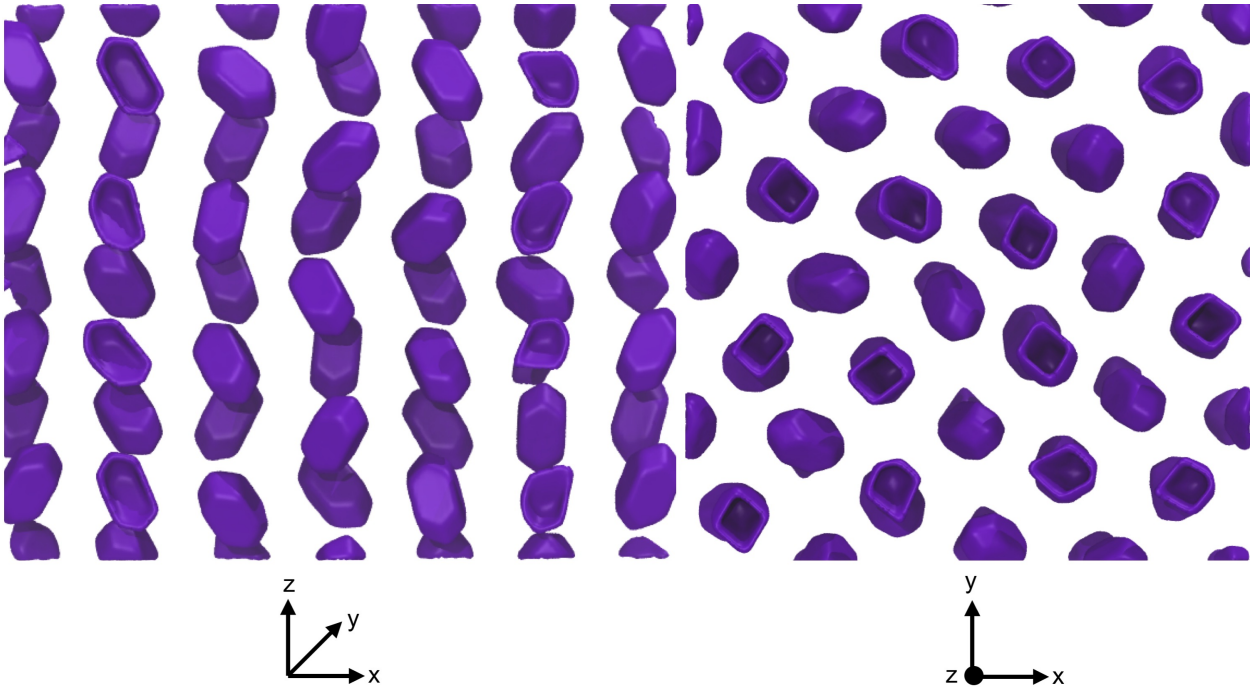

Figure 69. **Simulations show that lattices comprised of particles with AR=2.65 initialized in an FCC lattice are unstable (B=4nds).** Screenshots show two different views of the result of this simulation that include multiple layers of particles. Images do not show DNA for clarity.

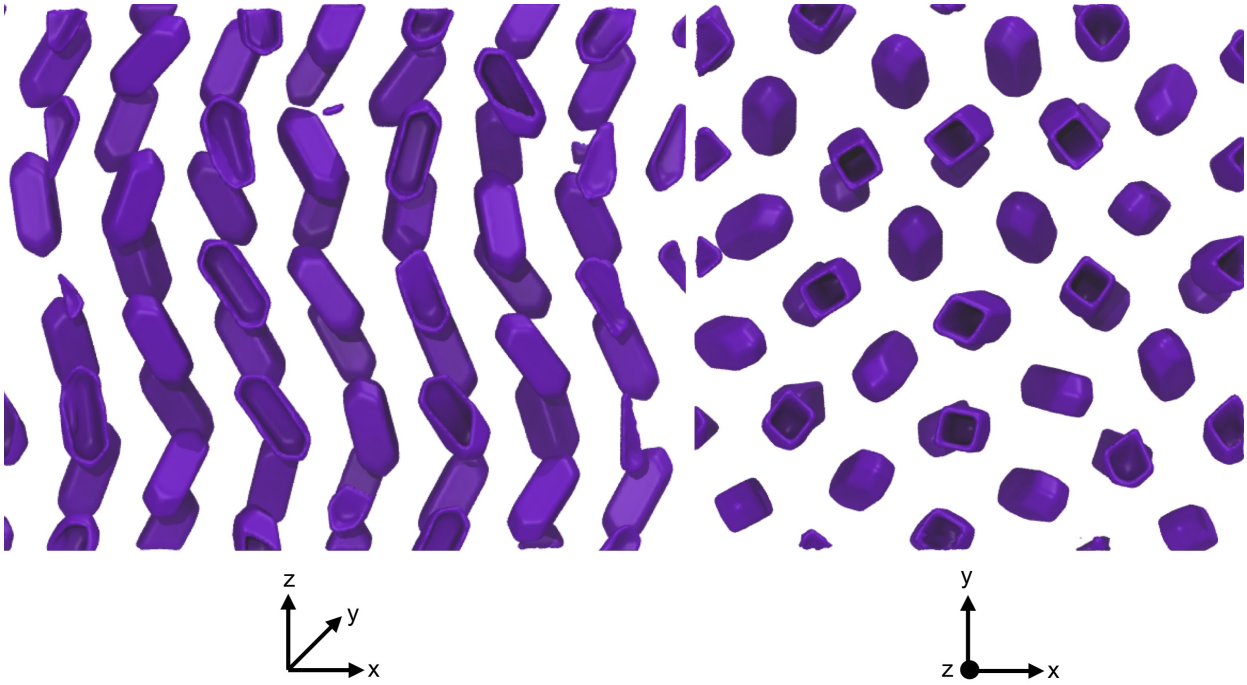

Figure 71. Simulations show that lattices comprised of particles with AR=4 initialized in an FCC lattice are unstable (B=4nds). Screenshots show two different views of the result of this simulation that include multiple layers of particles. Images do not show DNA for clarity.

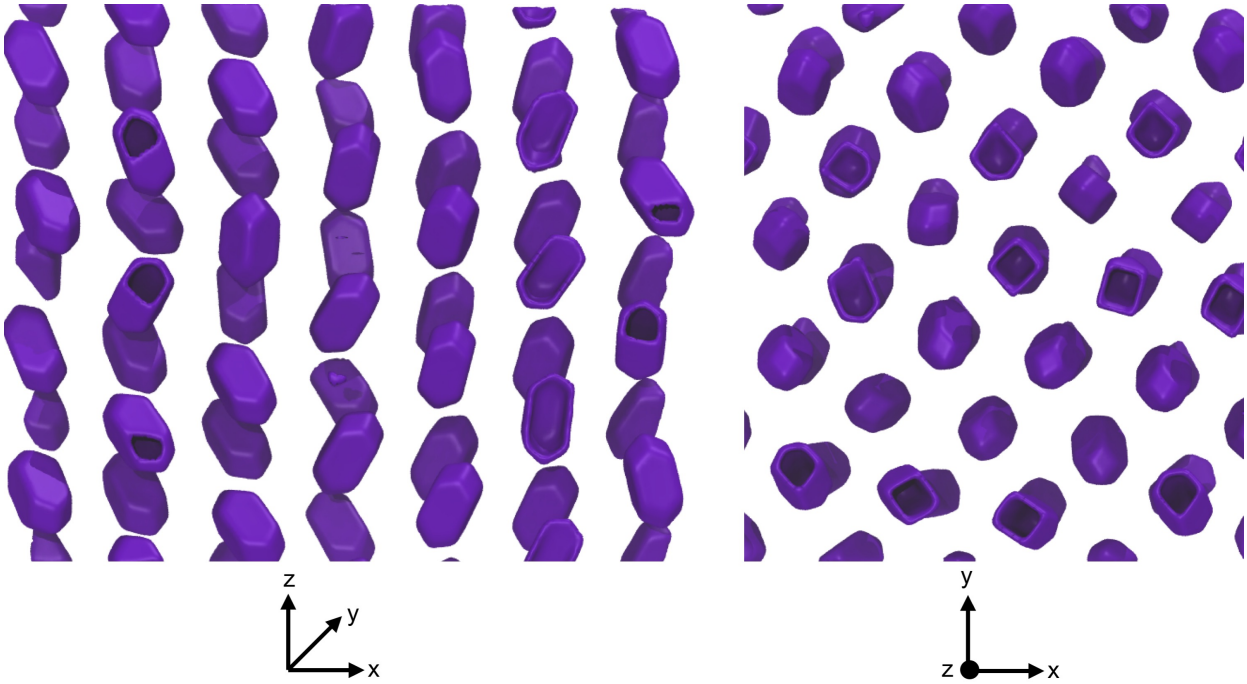

Figure 70. Simulations show that lattices comprised of particles with AR=2.85 initialized in an FCC lattice are unstable (B=4nds). Screenshots show two different views of the result of this simulation that include multiple layers of particles. Images do not show DNA for clarity.

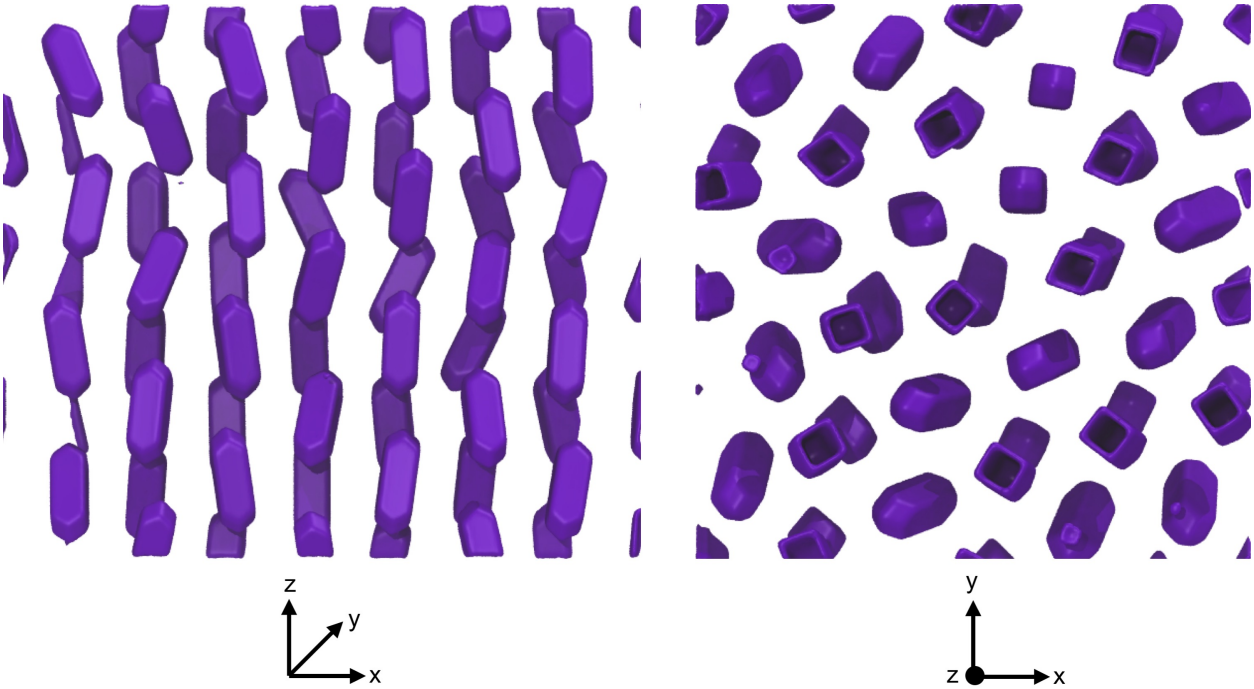

Figure 72. Simulations show that lattices comprised of particles with AR=4.5 initialized in an FCC lattice are unstable (B=4nds). Screenshots show two different views of the result of this simulation that include multiple layers of particles. Images do not show DNA for clarity.

5.5.8 MD simulation of elongated RDs initialized in a BCT lattice

Every simulation was initialized such that L_{miajor} began aligned with the z axis. In order to simulate particles with different aspect ratios, the size of the square cross section was kept constant while L_{miajor} was increased. Thus, L_{minor} remained constant for all *AR*s (6.1nm). The number of beads that comprised the particle surface was chosen to accommodate an appropriate density of anchor DNA strands (i.e. anchor strands present in up to a 20% excess of linker strands). DNA strands were randomly grafted onto to surface beads with a maximum of one strand per bead. Anchor surface density was maintained at 0.34 strands/nm^2 while linker strand surface density was set to 0.14 strands/nm^2, in accordance to experimental measurements.

Simulations modeled superlattices as 4x4x4 Bravais unit cells for each initial lattice symmetry. Thus, FCC lattices contained a total of 256 particles (AR < 3) with while BCT lattices contained 128 particles. In order to preserve face-to-face interactions and to prevent metastable FCC lattices, FCC lattices for particles with AR >= 3 were initialized as BCT with $c/a = 2^{1/2}$. All elongated RDs in the superlattice were treated as rigid bodies.

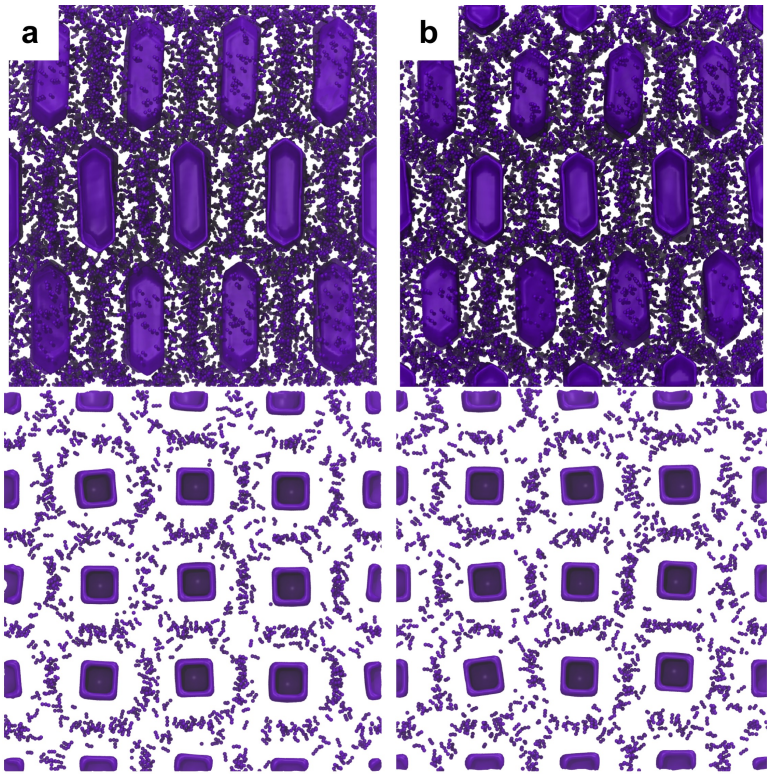

Figure 73. Snap shots show simulation of particles with AR = 4.5 (a) and 3.5 (b). Sticky ends are shown with purple beads surrounding purple particle models. Top: Lattices cut across their long axis. Particles in the front plane are cut across their long dimension. Bottom: Lattices cut across their short axis. Particles cut across their short dimension.

5.5.9 Near phase transition MD simulations and estimation of AR at which transition occurs

For particles with *AR* = 4.5 simulations show that the BCT lattice is likely the most stable lattice. As the *AR* increases above 4.5, systems become more challenging to simulate. In particular,

since simulation uses a limited number of particles to represent an experimental system with orders of magnitude more particles, artifacts arise from the size of the simulation domain. These are usually termed finite-size effects. They become more prominent near phase boundaries. In the case of particles with $AR > 4$, simulations initialized in FCC lattices begin to equilibrate into multiple unexpected lattices. Further, these irregularities persist and increase in magnitude as the simulation is reduced in size (i.e. includes fewer particles) which suggests that particles with $AR=5$ are near to a phase transition. Table 12 illustrates this instability through the large fluctuations in unit cells size (represented as a c/a and b/a ratio where a, b, and c represent the three lattice dimensions) as the number of particles per simulation changes. Computational requirements are prohibitive to exploring this question further with simulations that include more particles.

Table 12. Particles with AR>4 begin to approach a phase transition. This table summarizes the results of simulation of these particles initialized in an FCC lattice. The c/a and b/a ratios indicate that the unit cells vary based on the number of particles in the system, although the particles, DNA length, and initial symmetry remain the same.

AR	Initial Symmetry	B (nds)	System Size by Dimension (# unit cells)	c/a	a/b
4	FCC	4	4 x 4 x 4	1	1.1
			3 x 4 x 4	1.3	0.9
			4 x 4 x 3	0.8	1
		5	4 x 4 x 4	1.1	1
			3 x 4 x 4	1.3	0.8
			4 x 4 x 3	0.8	1
4.5	FCC	4	4 x 4 x 4	1.1	1.1
			3 x 4 x 4	1.4	0.9
			4 x 4 x 3	0.8	1
		5	4 x 4 x 4	1.1	1
			3 x 4 x 4	1.5	0.8
			4 x 4 x 3	0.8	1
5	FCC	4	4 x 4 x 4	1.2	1
			3 x 4 x 4	1.5	0.8
			4 x 4 x 3	0.9	1
		5	4 x 4 x 4	1.15	0.9
			3 x 4 x 4	1.5	0.8
			4 x 4 x 3	0.9	1

Based on the enthalpy associated with hybridization determined from MD simulations for infinite rectangular prisms arranged in either a HP or SP lattice and approximation of tip values from simulations of particles with $3.5 < AR < 4.5$ (i.e. BCT lattice), it is possible estimate the AR for which a phase transition should occur (i.e. the $AR_{transition,}$ where the hexagonal lattice begins to

allow more hybridization in-plane interactions than are possible in a BCT lattice with both in-plane and out-of-plane interactions). This was estimated using the following inequality:

$$\mathbf{U_{HP,\,side} > U_{BCT,\,tip} + U_{SP,\,side}}$$

$$\mathbf{U_{lattice,\,facet} = H \times Z_{lattice,\,facet} \times A}$$

$$\mathbf{Z_{HP,\,side} \times 4 \times A_{side} > Z_{BCT,\,tip} \times 8 \times A_{tip} + Z_{SP,\,side} \times 4 \times A_{side}}$$

$$\mathbf{Z_{BCT,\,tip} = 0.54}$$

$$\mathbf{Z_{SP,\,side} = 0.52}$$

$$\mathbf{Z_{HP,\,side} = 0.61}$$

U is the internal energy for a particle facet in a lattice with the given symmetry, A is the area of either a tip or side facet, H is the enthalpy of sticky end hybridization, and Z is the probability of sticky end hybridization for a particle facet in a lattice with the given symmetry. For this calculation A_{side} increases as the *AR* increases while A_{tip} remains constant. The type of facet (tip or side) was classified by its dimensions and orientation on the particle. In this approximation, we assume that entropic contributions are negligible compared to the enthalpic differences. Since DNA linker surface density and enthalpy of sticky end hybridization remain constant, enthalpic terms cancel out to leave hybridization rate (determined from simulations). Therefore, $AR_{transition}$ can be derived from through the following expressions:

$$\mathbf{A_{side} = A_{tip} + q \times l}$$

$$\mathbf{q \times l \times (Z_{HP,\,side} - Z_{SP,\,Side}) > (2 \times U_{BCT,\,tip} + Z_{SP,\,side} - Z_{HP,\,side}) \times A_{tip}}$$

$$\mathbf{L_{major} = l + p}$$

Add p to both sides in order to introduce L_{major}. Divide by L_{minor} to find *AR.:*

$$\mathbf{[(2\ x\ Z_{BCT,\ tip} + Z_{SP,\ side} - Z_{HP,\ side})/(\ Z_{HP,\ side} - Z_{SP,\ Side})]\ x\ (A_{tip}\ /q\ x\ L_{minor}) + p\ /\ L_{minor} <}$$

$$\mathbf{L_{major}/L_{minor} = AR}$$

$$\mathbf{L_{minor} = 7.3\ nm}$$

$$\mathbf{p\ (by\ geometry) = 4.2\ nm}$$

$$\mathbf{q\ (by\ geometry) = 6\ nm}$$

p and q correspond to the shortest and longest line distance between opposite vertices of a regular rhombus facet, respectively, and l is the length of the long edge of an elongated facet. Upon substitution of known values, MD simulations predict that a phase transition should occur as particles approach an *AR* of ~7, in agreement with experimental and simulation results.

5.5.10 MD simulation of infinite rectangular prisms initialized in HP and SP lattices

In order to simulate nanoparticles with very large aspect ratio, we approximate them as infinite rectangular prisms. This prism was allowed to translate in space, but only rotate about its long axis. Furthermore, the barostat was only allowed to rescale the x and y lengths as well as the xy tilt factor of the box. The prism length (Lz = 20σ = 40nm) was chosen equal to the box z dimension to obtain an effectively continuous translation symmetry along z. Crystals were initialized in square or hexagonal lattices and equilibrated. Both phases were stable, but a

comparison of their potential energies (Fig. S27) reveals that the internal energy of the hexagonal lattice is lower than the square. This difference is larger for longer DNA chains.

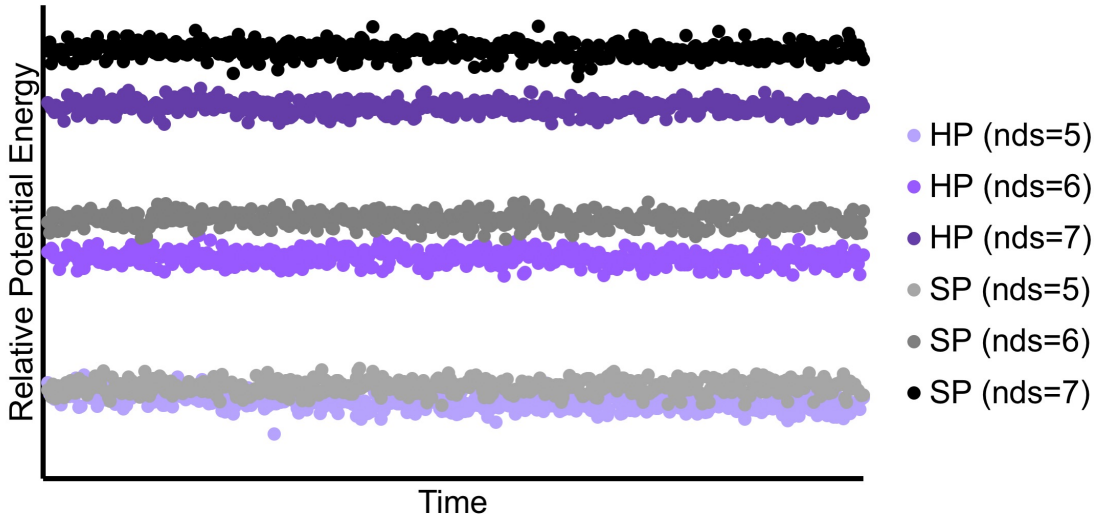

Figure 74. Infinite rectangular prisms initialized in HP lattices with different lengths of DNA (represented as double-stranded beads (nds)) are consistently lower in potential energy than those initialized in SP lattices. Lower potential energies indicate the more stable lattice.

5.5.11 Analysis of DNA hybridization from MD simulations for additional ARs

In order to obtain rates and probabilities of hybridization per bead, every simulated elongated dodecahedron was projected on to a reference particle. This enabled computation of the distance between adjacent sticky ends. If this distance satisfied r < 1.5 * 1.2nm sticky ends were classified as hybridized, since 1.2 nm is the typical hydrogen bond length.[69] Subsequently, the location of hybridized sticky ends could be projected onto the particle surface based on the bead attached to the DNA strand. Averages of multiple time points (80 time frames separated by 20,000 time steps) after equilibration enabled calculation of the average number of binding events per

bead. These values were normalized by the number of linker strand attachment on a particular bead and visualized as shown in Figure 75.

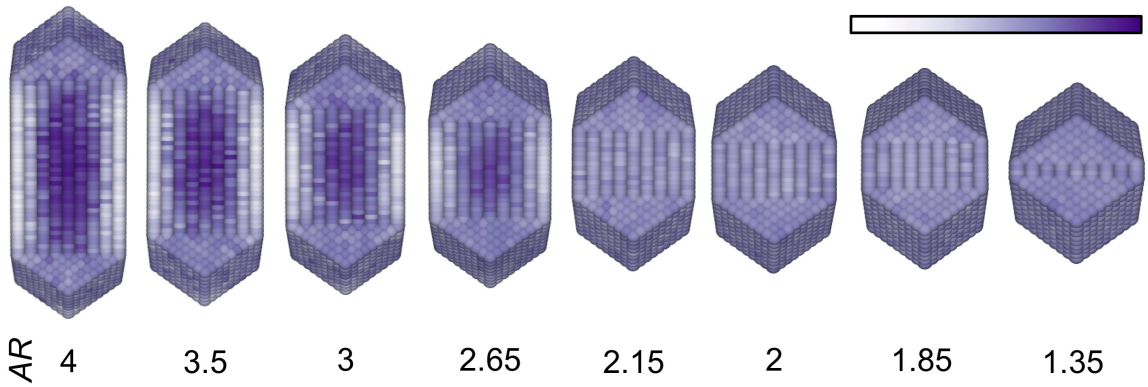

Figure 75. Models show DNA hybridization probability mapped to the particle surface based on simulations initialized in BCT, BCT, BCT, BCT, FCC, FCC, FCC, FCC lattices, respectively. Each point on the particle represents a bead that may have DNA attached. Darker colors indicate a higher probability that the DNA attached to the bead hybridizes to DNA on an adjacent particle. Color scale corresponds to all models and is consistent with the color scale in Figure 52.

For infinite rectangular prisms, MD enabled comparison of the fraction of DNA on edge beads vs. face beads that hybridized with DNA on an adjacent particle, on average (Figure 76). This analysis revealed that placement of particles in a hexagonal lattice facilitates a greater number of DNA hybridization interactions (relative to a square lattice) through increased hybridization of edge and near edge DNA. In particular, in a hexagonal lattice, ~66% of face DNA (88% of which is hybridized to DNA on another facet and 12% to DNA on an edge) and ~60% of edge DNA (93% of which is hybridized to DNA on a facet and 7% to DNA on an edge) can be hybridized. In contrast, square lattices permit ~56% of face DNA (97% of which is hybridized to DNA on a facet and 3% to DNA on an edge) and 17% of edge DNA (87% of which is hybridized to DNA on a facet and 13% to DNA on an edge) to be hybridized.

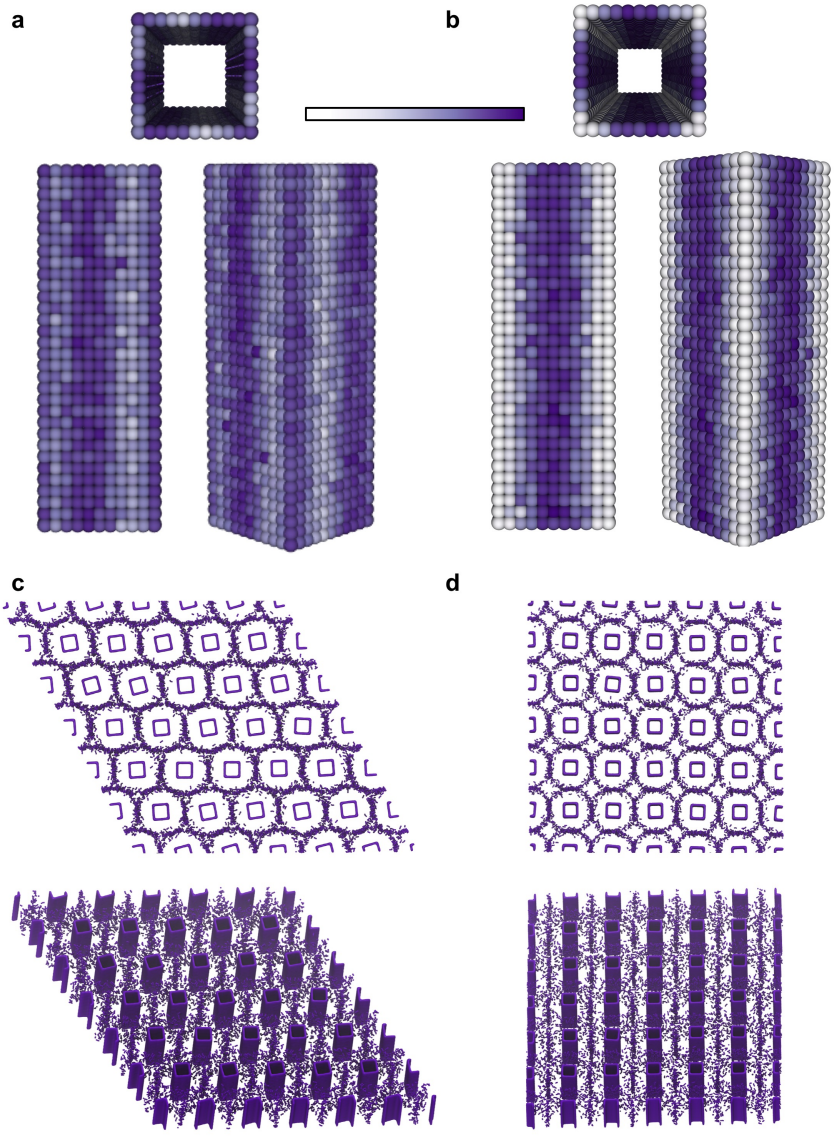

Figure 76. MD simulations of an infinitely long rectangular prism reveal that a HP, rather than a SP, lattice favors more DNA hybridization interactions. a Models of DNA hybridization probability mapped to the particle surface (from top, side and edge views) based on simulations initialized in a HP lattice. Color bar corresponds to a and b and is consistent with Figure 3 in the main text. **b** Models of DNA hybridization probability mapped to the particle surface (from top, side and edge views) based on simulations initialized in a SP lattice. Color bar corresponds to a and b and is consistent with Figure 3 in the main text. **c** Snapshot of particle models and their sticky ends arranged in a HP lattice captured perpendicular to their closest-packed plane (top) and at an angle <90° from their closest packed plane (nds=6). **d** Snapshot of particle models and their sticky ends arranged in a SP lattice captured perpendicular to their closest-packed plane (top) and at an angle <90° from their closest packed plane (nds=6).

SECTION FOUR – RESPONSIVE CRYSTALS DRIVEN BY DNA BONDS

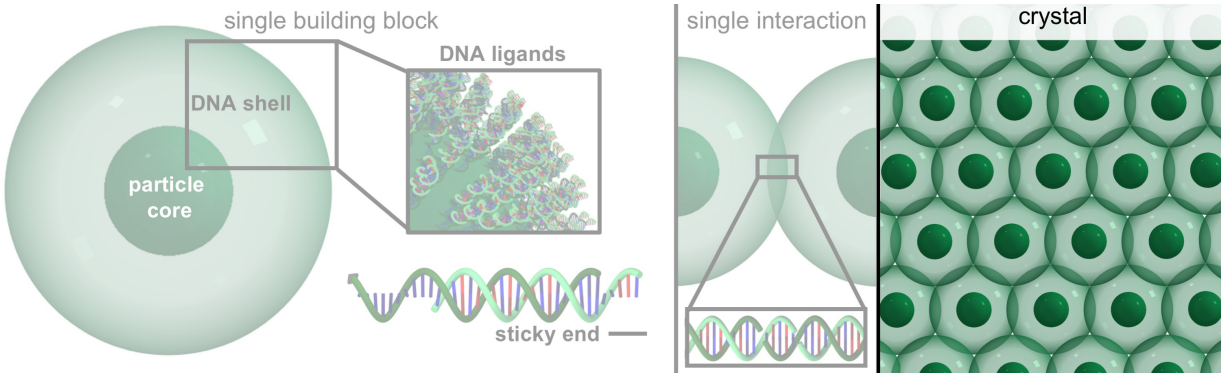

6 CHAPTER SIX: CONTRACTION AND EXPANSION OF STIMULI-RESPONSIVE DNA BONDS IN FLEXIBLE COLLOIDAL CRYSTALS

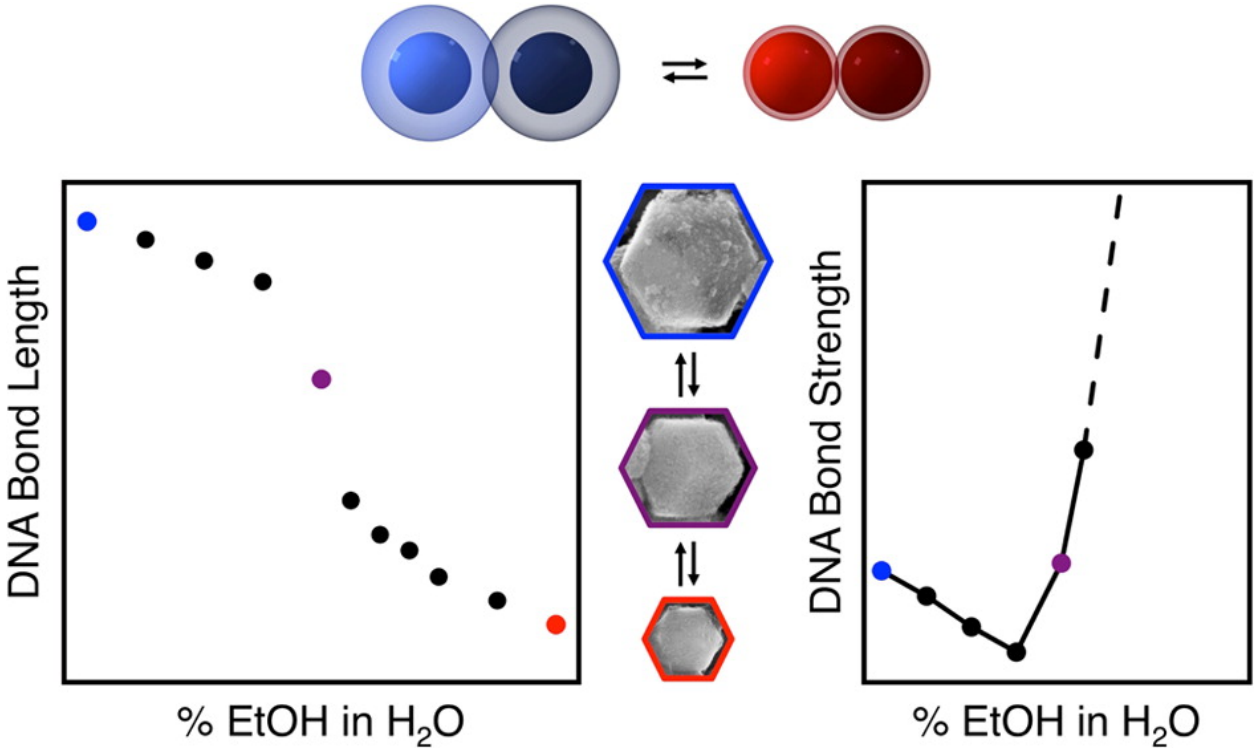

Material in this chapter is based upon published work:

J.A. Mason, C.R. Laramy, C.T. Lai, M.N. O'Brien, Q.Y. Lin, V.P. Dravid, G.C.Schatz, C.A. Mirkin. *Nano Letters* **2015**, *15*, 1012-1017.

6.1 Abstract

DNA surface ligands can be used as programmable "bonds" to control the arrangement of nanoparticles into crystalline lattices. Here, we study the intrinsic responsiveness of these DNA bonds to changes in local dielectric constant (ε_r) as a new approach to dynamically modulate superlattice structure. Remarkably, ethanol (EtOH), addition can be used to controllably tune DNA bond length from 16 to 3 nm and to increase bond stability by >40 °C, while retaining long-range order and crystal habit. Interestingly, we find that these structural changes, which involve the expansion and contraction of crystals by up to 75% in volume, occur in a cooperative fashion once a critical percentage of EtOH is reached. These results provide a facile and robust approach to create stimuli-responsive lattices, to access high volume fractions, and to improve thermal stability.

6.2 Background

Due to their highly tunable structure and sequence-specific interactions, nucleic acids have emerged as powerful surface ligands to direct the assembly of nanoparticles into one-, two-, and three-dimensional colloidal crystals.[2, 3, 9, 36, 37, 117] In this context, nanoparticles coated with a dense shell of nucleic acids function as programmable atom equivalents (PAEs), where nucleic acid "bonds" arrange nanoparticle "atoms" into superlattices with precisely defined spacing, symmetry, and, in some cases, crystal habit.[317] Because many physical properties of nanoparticles are dramatically affected by the location and arrangement of neighboring nanoparticles, the high level of structural control afforded by this approach is extremely useful for the synthesis of both fundamentally interesting and functional materials.[117]

While significant advances have been made in the structural control of DNA-assembled colloidal crystals,[15, 25] less is known about the physical and chemical properties of the DNA bonds within these crystals and of their intrinsic ability to change in response to external stimuli. The use of external stimuli to post-synthetically tune DNA bond length and strength is particularly intriguing for the development of responsive colloidal crystals, where material properties can be changed on-demand.[220, 328] Several strategies have been developed to introduce such dynamic control, including the use of DNA hairpins, molecular intercalators, osmotic pressure, and solvent evaporation techniques.[9, 18, 194-196, 199, 200, 329-332] While each approach possesses certain advantages, there are still no general methods that allow DNA bonds to be rapidly, precisely, and reversibly tuned over a wide range of lengths and strengths.

Although many techniques have been developed to manipulate the structure of free DNA,[333] few of these have been adapted to post-synthetically modify DNA bonds in nanoparticle superlattices. For instance, the effect of alcohols on the structure and hybridization interactions of double-stranded DNA has been the subject of many detailed experimental and theoretical studies,[203, 334-339] and ethanol (EtOH) precipitation reactions are routinely used in molecular biology laboratories to purify and concentrate DNA extracted from cells.[202] Inspired by the ability of EtOH to modulate the intra- and interhelical structure of free DNA, we hypothesized that EtOH could be similarly used to provide a convenient and controllable external stimulus to induce structural changes in DNA-assembled colloidal crystals (Figure 77). In particular, one would expect that DNA bonds in high salt concentration solutions should be sensitive to changes in solvent ε_r and, perhaps, be able to undergo an EtOH-induced precipitation reaction, even when confined inside a superlattice.

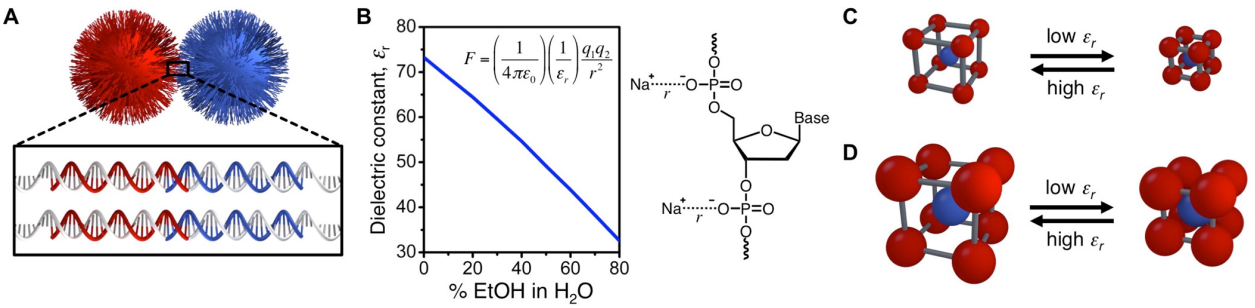

Figure 77. Schematic shows superlattice structural changes as DNA responds to changes in solution dielectric constant. (A) DNA-functionalized nanoparticles can be assembled through complementary hybridization interactions that collectively form DNA "bonds". (B) The dielectric constant, ε_r, of H_2O decreases as EtOH is added,[5] leading to a greater Coulombic force, *F*, between the negatively charged PO_4^- backbone of DNA and positively charged Na^+ ions in solution. (C, D) Scheme illustrating the EtOH-induced contraction and expansion of bcc superlattices composed of 15 nm (C) or 30 nm (D) spherical nanoparticles.

In a conventional EtOH precipitation, DNA is dissolved in an aqueous salt solution (~0.3 M NaOAc or NaCl), and the solution is brought to 65–75% EtOH. As a less polar molecule, EtOH cannot solvate charged species as effectively as H_2O, and the solvent ε_r decreases as EtOH is added (Figure 77b).[5] As a result, the Coulombic attraction between the positively charged Na^+ ions in solution and the negatively charged PO_4^- groups of the DNA backbone increases to such an extent that ionic bonds form, neutralizing the charge on the DNA backbone and inducing precipitation.[340] Depending on the salt concentration, addition of EtOH can also cause double-stranded DNA to transition from the B-form to A-form, with a concurrent ~25% decrease in DNA length, prior to precipitation.[203, 335]

6.3 Results and Discussion

6.3.1 Determination of superlattice structural response to changes in percent of EtOH

To investigate the ability of EtOH to post-synthetically modulate DNA bonds, two populations of 30 nm diameter spherical PAEs were prepared, designed to specifically interact

with each other via complementary DNA sequences (Figure 81). Slow cooling of these samples through their melting temperature resulted in single crystalline body-centered cubic (bcc) superlattices with well-defined rhombic dodecahedron habits.[1, 9] Prior to EtOH addition, crystals were washed repeatedly with 0.3 M NaCl (aq) to remove any excess DNA, nanoparticles, buffers, and surfactants from solution. Crystals were then partitioned and brought to different volume percentages of EtOH in H_2O, ranging from $\varepsilon_r = 73.3$ at 0% EtOH to $\varepsilon_r = 32.6$ at 80% EtOH, at a constant 0.3 M NaCl. Superlattices were then characterized by *in situ* small-angle X-ray scattering (SAXS), electron microscopy (EM), and variable-temperature UV–vis spectroscopy.

To examine the effect of EtOH on DNA bond length, unit cell parameters were determined from the comparison of experimental and modeled SAXS patterns, and these values were used to calculate the minimum distance between nanoparticle surfaces.[341] Initially, SAXS data show a small, continuous contraction of the bcc unit cell of 13% by volume as the amount of EtOH is increased from 0 to 30% (Figure 78). Once the percentage of EtOH rises above 30%, however, there is a dramatic contraction of the unit cell that is suggestive of a cooperative phase transition. Specifically, the unit cell volume decreases by 42% when increasing from 30% to 45% EtOH, and the average gap between nanoparticles, or effective "DNA bond length", decreases from 14 to 7 nm. After the sharp transition, the superlattice continues to moderately contract as more EtOH is added, reaching a gap distance of only 3 nm—an 80% decrease from the original DNA bond length—at 80% EtOH. Note that this is much greater than the ~25% contraction expected for a classical transition from B-DNA to A-DNA.[335] Moreover, access to this distance regime is particularly important to realize materials with strong magnetic and optical coupling and has been challenging with existing DNA-mediated assembly techniques.[24]

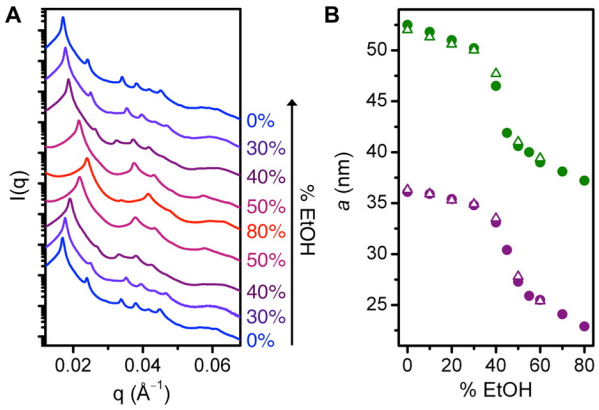

Figure 78. Superlattices reversibly contract in response to changes in the percentage of EtOH. A) SAXS data for bcc superlattices of 30 nm PAEs at different volume percentages of EtOH in H_2O. (B) The bcc unit cell length, *a*, for superlattices of 30 nm PAEs (green) and 15 nm PAEs (purple) at different volume percentages of EtOH in H_2O. Solid and empty symbols correspond to values during contraction and re-expansion, respectively.

Despite the large contraction, SAXS data show that, regardless of the amount of EtOH added, PAEs are still arranged in a well-ordered bcc lattice (Figure 78, Figure 84 - Figure 123, **Table 15**). This ordering was further confirmed by directly imaging superlattices at 0%, 41%, and 80% EtOH using EM, with crystals embedded in silica to preserve the solution-phase DNA bonds in the solid state (Figure 79).[322] Significantly, EM images also demonstrate that the well-defined rhombic dodecahedron habit is preserved after EtOH addition.

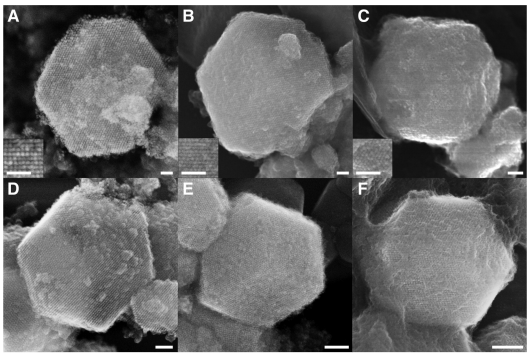

Figure 79. Electron microscopy reveals that lattice symmetry and crystal habit are retained at up to 80% EtOH. Top: Scanning electron microscopy (SEM) images of silica-encapsulated superlattices of 30 nm PAEs at (A) 0%, (B) 41%, and (C) 80% EtOH confirm rhombic dodecahedron crystal habits. Insets: High-magnification SEM images. Bottom: SEM images of silica-encapsulated superlattices of 15 nm PAEs at (D) 0%, (E) 45%, and (F) 80% EtOH. Scale bars, 200 nm.

Remarkably, the EtOH-induced transition is fully reversible, and SAXS patterns collected before and after exposure to 80% EtOH possess no noticeable changes (Figure 78A). To investigate how this reversibility holds up to many cycles of expansion and contraction, a single sample was transitioned repeatedly between 0% and 80% EtOH. Significantly, SAXS data did not indicate any changes in crystallinity after five complete cycles (Figure 104). In all contracted phases, there is, however, a noticeable increase in SAXS peaks widths, which is typically indicative of an increase in lattice strain or decrease in effective crystallite size.[341] Since the SAXS peak widths return to their original values upon re-expansion, this effect can be predominantly attributed to increased lattice strain in the contracted phases.

6.3.2 The effect of percent of EtOH on DNA "bond strength"

To characterize the effects of EtOH on DNA "bond strength", we used UV–vis spectroscopy measurements of extinction to determine the temperature at which superlattice crystals dissociate, or melt, into discrete nanoparticles (Figure 126, Figure 125).[72, 342] As the

percentage of EtOH is increased, the melting temperature of the superlattice slowly decreases from 41.1 °C at 0% EtOH to 33.1 °C at 30% EtOH (Figure 80A). This can be attributed to weaker DNA hybridization interactions as ε_r and the bulk solvent polarity decrease.[203] At 40–45% EtOH the melting transition begins to broaden, and the melting temperature rapidly increases. After the solution reaches 50% EtOH, we no longer observe evidence of melting by UV–vis analysis over the 20 to 70 °C temperature range. *In situ* SAXS experiments further reveal that the bcc crystal structure is intact to at least 80 °C in 80% EtOH (Figure 124). This dramatically increased thermal stability after the phase transition is consistent with an EtOH-induced DNA precipitation reaction occurring inside the superlattice to increase the collective stability of DNA bonds.

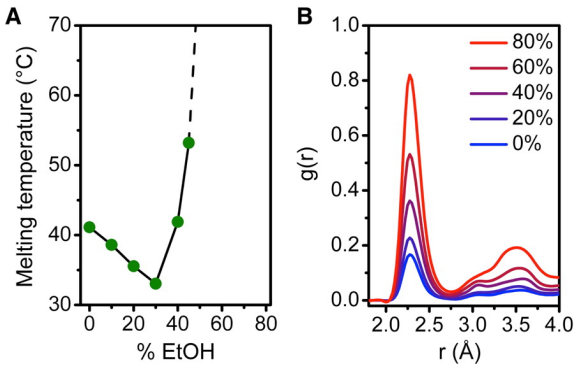

Figure 80. As the percent of EtOH increases, the melting temperature initially declines before sharply increasing. (A) Melting temperatures for bcc superlattices of 30 nm PAEs at different volume percentages of EtOH in H_2O. (B) Simulated radial distribution function, g(r), of the distance, r, between Na^+ and PO_4^- groups at different EtOH percentages.

To evaluate the effect of nanoparticle size on the ability of EtOH to modulate DNA bonds, crystals were similarly prepared using 15 nm diameter spherical PAEs. While *in situ* SAXS experiments indicate that the superlattice undergoes a similar phase transition in response to EtOH (Figure 78B), the crystallinities of the contracted phases are reduced compared to those of the 30 nm PAEs (Figure 105 - Figure 123). Still, SAXS simulations and EM images confirm that the 15

nm PAEs contract by 75% in volume to a strained bcc lattice, with a decrease in DNA bond length from 17 to 6 nm, as the EtOH percentage is increased from 0% to 80%. Interestingly, the midpoint of the phase transition for 15 nm PAEs occurs at 45% EtOH compared to 41% EtOH for 30 nm PAEs. Since 15 and 30 nm PAEs are expected to have a similar DNA surface coverage,[88] the increased amount of EtOH required to induce the transition in 15 nm PAEs can likely be attributed to a radius of curvature effect.[343] Specifically, the lower radius of curvature of the 30 nm PAEs leads to a smaller average distance between duplexed DNA strands above the surface. This should lead to a higher local salt concentration around the PO_4^- backbones and, consequently, less EtOH required for Na^+ cations to fully neutralize the DNA backbones and induce a precipitation transition.

6.3.3 Atomistic molecular dynamics simulations reveal origin of DNA structural changes

All-atom molecular dynamics (MD) simulations were performed to gain additional insight into the mechanism of the EtOH-induced superlattice contraction. Below 80% EtOH, simulations show that the DNA conformation remains exclusively in the B-form, and the sharp contraction at 40–45% EtOH cannot, therefore, be attributed to a transition from B-DNA to A-DNA. Instead, the contraction likely results from changes in the spacing and arrangement of DNA strands relative to each other. It is important to consider that the DNA bonds between nanoparticles have single-stranded regions of DNA that impart substantial conformational flexibility, and the MD simulations show a significant bending angle of 70° at the center of the DNA bond at 40% EtOH (Figure 82). This bending should allow neighboring DNA strands to pack more tightly between nanoparticle surfaces and, in so doing, draw the nanoparticles closer together.

Current computational methods, including both MD and coarse-grained simulations, are not capable of capturing the large contraction that occurs above 40% EtOH. Based on studies of free DNA in solution, however, it is reasonable to assume that after ε_r decreases below a critical value, Na^+ cations in solution effectively form ionic bonds with the PO_4^- groups of the DNA backbone,[344, 345] leading to counterion correlations between neighboring DNA strands that trigger DNA–DNA attractions and cause DNA strands to rearrange into a more condensed phase.[338] Indeed, MD simulations confirm an increased local concentration of Na^+ ions around PO_4^- groups with increasing EtOH (Figure 80B). While it is exceedingly difficult to determine the exact structure and chemical nature of DNA bonds in the contracted superlattice phases with existing experimental techniques, condensed DNA is known to adopt a range of liquid crystalline and crystalline phases.[346]

6.4 Conclusion

Taken together, these results demonstrate the intrinsic responsiveness of nanoparticle-based DNA bonds and provide a powerful general approach to the synthesis of responsive colloidal crystals with precisely controlled interparticle distances and increased thermal stability. The extension of this work to different alcohols, multivalent cations, DNA sequences, and non-spherical nanoparticle shapes should enhance our fundamental understanding of condensed DNA bonds and lead to new possibilities for the post-synthetic manipulation of superlattice structures. This ability to rapidly, predictably, and reversibly modulate DNA bonds has great potential for the development of dynamic materials with optical,[219] magnetic, and mechanical properties that can be tuned on-demand.

6.5 Experimental Methods and Supplementary Materials

6.5.1 Nanoparticle synthesis and characterization

Gold spherical nanoparticles capped with citrate ligands were purchased from Ted Pella, Inc. with nominal diameters of 15 and 30 nm. Two techniques were used to determine the actual size distribution of the nanoparticles (Table 13). First, algorithmic analysis of transmission electron microscopy (TEM) images was performed for > 2000 particles from each sample. This data returns an average diameter and standard deviation for nanoparticles, assuming a spherical nanoparticle shape.[7] Second, small angle X-ray scattering (SAXS) experiments were used to measure an experimental form factor for discrete nanoparticles. Measured form factors were then fit with simulated form factors for spherical particles using the following parameters: diameter and diameter dispersity.[25, 53, 341, 347] In all cases, the simulated form factors demonstrate excellent agreement with the experimental form factors (Figure 84, Figure 85). Note that the diameters determined by TEM and SAXS are in very good agreement, and the average values from SAXS were used to calculate all interparticle gaps reported in this work.

Table 13. Nanoparticle size is consistent, within error, between TEM and SAXS measurements.

Ted Pella Gold Colloid	Average Diameter, TEM (nm)	Average Diameter, SAXS (nm)
15 nm	14.3 ± 1.4	13.9 ± 1.3
30 nm	30.3 ± 4.5	29.4 ± 2.9

6.5.2 DNA synthesis and characterization

All oligonucleotides used in this work were synthesized on a solid-support MM48 synthesizer (BioAutomation) using reagents purchased from Glen Research. Oligonucleotides were synthesized with a 5′ trityl group and purified with reversephase high-performance liquid

chromatography (HPLC; Agilent), followed by standard deprotection procedures. Matrix-assisted laser desorption ionization time-of-flight mass spectrometry was used to confirm the molecular weight of the HPLC-purified oligonucleotides. The OligoAnalyzer tool from Integrated DNA Technologies was used to determine an extinction coefficient for each DNA strand, and UV-vis spectroscopy was used to determine concentrations.

6.5.3 DNA design

The DNA design in this work follows previous literature protocols.[3, 266] Briefly, gold nanoparticles were densely functionalized with one of two unique single-stranded oligonucleotides composed of three regions (from 3′ to 5′): 1) 3′ alkylthiol moiety (−CH2CH2CH2SH) to anchor the DNA to the nanoparticle surface, 2) an A10 spacer region to distance the DNA from the surface and provide some degree of flexibility, and 3) an 18-base pair sequence. To each of these "anchor" strands, we hybridized a second "linker" strand composed of three regions (from 5′ to 3′): 1) an 18-base pair sequence complementary to the anchor strand, 2) a single unpaired A base for DNA flexibility, and 3) a 5-base terminus, or "sticky end", designed such that the terminus on nanoparticle "A" is complementary to the terminus on nanoparticle "B". Specific sequences used in this work are listed in Table 14 and Figure 81.

Table 14. Nanoparticles were functionalized with anchor DNA and crystallized with sticky ends on linker

DNA Description	DNA Sequence (5′ to 3′)
"A" Anchor	TCA ACT ATT CCT ACC TAC AAA AAA AAA A $(CH_2)_3SH$
"A" Linker	GTA GGT AGG AAT AGT TGA ATC TCT
"B" Anchor	TCC ACT CAT ACT CAG CAA AAA AAA AAA A $(CH_2)_3SH$
"B" Linker	TTG CTG AGT ATG AGT GGA AAG AGA

Figure 81. Hybridization between complementary linker strands leads to superlattice formation. The above schematic shows the design implemented for this work.

6.5.4 DNA design

Nanoparticles were functionalized with 3′ oligonucleotides as previously reported.[3, 266] Briefly, thiolated oligonucleotides were treated with a 100 mM solution of dithiothreitol (DTT) in 170 mM sodium phosphate buffer (pH = 7.4) for 1 h. Residual DTT was removed using Nap-5 size exclusion columns (GE healthcare), and the DNA was added directly to the spherical nanoparticle colloids (5 nmol and 8 nmol of DNA were added per mL of 15 nm and 30 nm nanoparticle solution, respectively). After 12 h, each nanoparticle solution was brought to 0.01 M sodium phosphate buffer (pH = 7.4) and 0.01 wt % sodium dodecyl sulfate (SDS) in water, briefly sonicated, and then placed on a shaker for 2 hours. After this step, 2 M NaCl (aq) was added to the nanoparticle solutions every half hour such that the final concentration of each solution was 0.05 M, 0.1 M, 0.2 M, 0.3 M, 0.4 M, and 0.5 M NaCl after each successive addition. After each addition of 2 M NaCl (aq) the nanoparticle solution was briefly sonicated. Following the last NaCl addition, the nanoparticles were placed on a shaker at 1000 rpm for 12 h to ensure a dense loading of oligonucleotides. After this time, each nanoparticle solution was centrifuged three times to remove excess DNA, with the supernatant removed each time and replaced with 0.5 M NaCl, 0.01 M sodium phosphate buffer (pH = 7.4), and 0.01 wt % SDS. Centrifugation conditions used in this process were 25 min at 21,130 and 9,400 rcf for 15 nm and 30 nm particles, respectively.

6.5.5 Linker DNA hybridization

Linker strands were hybridized to nanoparticles by adding 500 and 5000 equivalents per 15 nm and 30 nm particle, respectively.

6.5.6 Superlattice assembly

A stock solution was prepared by combining concentrated stocks of functionalized nanoparticles and linker strands A and B (at the above ratios) in 0.5 M NaCl, 0.01 M sodium phosphate buffer (pH = 7.4), and 0.01 wt % SDS such that the final concentration of each particle type (A and B) was 12 nM (15 nm particles) or 3 nM (30 nm particles). Aggregates formed within 5 minutes. The solution was then heated above 50 °C to dissociate the aggregates. While maintaining a temperature above 50 °C, this solution was transferred in 100 μL aliquots to 200 μL PCR 8-tube strips (Life Technologies). The solutions were then slowly cooled in a Life Technologies PCR Thermocycler from 55 °C to 20 °C at a rate of 0.01 °C/min. [1] Some crystals were transferred to the solid state via silica embedding for visualization by scanning transmission electron microscopy (STEM; Hitachi HD-2300).

6.5.7 Preparation of superlattice samples in EtOH

After assembly, the as-synthesized superlattices were combined in a 1.5-mL Eppendorf tube and washed repeatedly with an aqueous solution of 0.3 M NaCl. Aliquots of superlattice crystals (50 μL) were then added to a series 0.5-mL Eppendorf tubes. A stock solution of 0.3 M NaCl in 80% EtOH (EtOH) and 20% H_2O was then added incrementally to bring each sample sequentially to 10%, 20%, 30%, 40%, 45%, 50%, 55%, 60%, and 70% EtOH. A sample in 80% EtOH was prepared from a superlattice suspended in 70% EtOH by replacing the supernatant with 50 μL of the 80% EtOH stock solution. After reaching 80% EtOH, a stock solution of 0.3 M NaCl

in H_2O was then added incrementally to bring a series of samples sequentially to 60%, 50%, 40%, 30%, 20%, and 10% EtOH. A sample in 0% EtOH was then prepared from a superlattice suspended in 10% EtOH by replacing the supernatant with 50 μL of 0.3 M NaCl in H_2O.

6.5.8 Silica embedding superlattice samples

Silica embedding and EM sample preparation was performed as previously reported for 0% EtOH samples. [322] Briefly, 4 100 μL aliquots were combined from PCR 8-tube strips after slow cooling. The solution was brought to 0.3 NaCl, 0.01 M sodium phosphate buffer (pH = 7.4), and 0.01 wt % SDS in 1 mL total volume. 1.5 μL of N-trimethoxysilylpropyl -N,N,N-trimethylammonium chloride (50% in methanol, Gelest, Inc.) was added to the solution. The solution was placed on a shaker at 1000 rpm for 10 min. After 10 min, 4 μL of triethoxysilane (Sigma-Aldrich) was added and the solution was returned to the shaker for 12 hours. After 12 hours, the solution was washed by briefly centrifuging (~10 sec), removing the supernatant and resuspending in ~1mL nanopure water. This process was repeated 1-2 more times to remove excess silica. 9μL of solution was drop cast on a copper TEM grid (Ted Pella) and wicked away using Qualitative 413 filter paper (VWR). This was repeated 3-5 times. The samples were imaged within 1 week of preparation.

Silica embedding and EM sample preparation of 41%, 45%, and 80% EtOH samples were performed similar to the above procedure with some changes. After combining 4 100 μL aliquots of solution containing slow cooled superlattices, the solution was brought to the desired percent EtOH using a stock of 80% EtOH and 0.3 M NaCl in a volume of 1 mL total. For 80% EtOH samples this required brief centrifugation (~10 seconds) and removal of supernatant. As above, 1.5 μL of N-trimethoxysilylpropyl-N,N,N-trimethylammonium chloride (50% in methanol,

Gelest, Inc.) was then added. The solution was placed on a shaker at 1000 rpm for 10 min. After 10 min, 4 μL of triethoxysilane (Sigma-Aldrich) was added and the solution was returned to the shaker for 12 hours. Unlike 0% EtOH samples, samples containing EtOH were not washed. 9μL of solution was directly drop cast on a copper TEM grid (Ted Pella) and wicked away using Qualitative 413 filter paper (VWR). This was repeated 2-3 times. The samples were imaged within 1 week of preparation.

EM images were obtained at the Northwestern University Atomic and Nanoscale Characterization Experimental Center (NUANCE) on a Hitachi HD2300 Scanning Transmission Electron Microscope (STEM) in z-contrast and SE mode at an accelerating voltage of 200 kV

6.5.9 SAXS experiments

Synchrotron small angle X-ray scattering (SAXS) experiments were conducted at the Dupont-Northwestern Dow Collaborative Access Team (DND-CAT) beamline of the Advanced Photon Source at Argonne National Laboratory. The X-ray wavelength for all experiments was 1.24 Å (10 keV). The sample angle was calibrated with a silver behenate standard. Two sets of slits were used to define, and collimate the beam, and parasitic scattering was removed with a pinhole. The X-ray beam cross-section measured 200 μm, and exposure times varied from 0.1 to 0.5 seconds. Scattered radiation was detected with a CCD area detector, and dark current frames were subtracted from all data. 1D SAXS data was obtained by an azimuthal average of the 2D scattering patterns. All SAXS data is presented as scattering intensity, $I(q)$, as a function of the scattering vector, q:

$$q = 4\pi \sin(\theta)/\lambda$$

where q is half of the scattering angle 2θ and l is the wavelength of X-ray radiation. Scattering from the solution, capillary, and DNA were assumed to be negligible.

Note that all SAXS data presented in this work are a combination X-ray scattering from the discrete the discrete nanoparticles described as a form factor, *P*(q), and scattering from nanoparticle ordering described as the structure factor, *S*(q). Together these compose the overall scattering for a given nanoparticle superlattice sample, *I*(q), where *I*(q) = *P*(q) x *S*(q). Due to the orders of magnitude difference in the scattering associate with the gold nanoparticles relative to the DNA, one cannot draw conclusions and DNA structure in superlattices using this technique.

Experimental form factors and structure factors were simulated to reconstruct *I*(q) for each sample (Figures SX-SX). [25, 53, 341, 347] As discussed in the main text, there is an increase in SAXS peaks widths during the EtOH-induced transition of superlattices composed of both 30 nm and 15 nm PAEs. Peak broadening is typically indicative of an increase in lattice strain or decrease in crystallite size. Since the SAXS peak widths return to their original values upon superlattice re-expansion, the peak broadening is likely the result of increased lattice strain, rather than a decrease in crystallite size, during superlattice contraction. As a result, the only SAXS simulation parameters changed when simulating diffraction patterns from 0 to 80% EtOH were: 1) unit cell dimension and 2) crystal microstrain. The unit cell dimensions and space group assignment (*I*m−3m for all samples) were confirmed by comparing the positions of predicted and experimental diffraction peaks for each sample.

In the superlattice samples composed of 15 nm PAEs, we note that there appears to be some SAXS peak splitting that is particularly evident in the region of the EtOH-induced transition (Figure 109 - Figure 111). Although it is difficult to identify its exact origins, this peak splitting can likely be attributed to two different populations of superlattice crystals – perhaps a population of larger, micron-sized single crystals and a population of sub-micron crystallites – going through the transition at slightly different EtOH percentages.

6.5.10 Kinetics of phase transition

Although it was not possible to directly measure the kinetics of the EtOH-induced transition in situ given our experimental setup, the speed of the transition was probed by soaking a fully expanded superlattice in 70% EtOH and collecting a SAXS pattern as rapidly as possible. The superlattice had fully contracted by the 3 minutes required to prepare a sample and collect SAXS data, demonstrating that the transition occurs faster than 3 minutes (Figure 123).

Table 15. SAXS can determine structural parameters of nanoparticle superlattices. Summary of unit cell parameters and nanoparticle gap distances as determined from in situ SAXS experiments.

	15 nm PAE superlattice (BCC)			30 nm PAE superlattice (BCC)		
% EtOH in H_2O (by volume)	*a* (nm)	*V* (nm^3)	DNA bond length (nm)	*a* (nm)	*V* (nm^3)	DNA bond length (nm)
0	36.1	47,000	17.4	52.5	144,000	16.1
10	35.9	46,300	17.2	51.8	139,000	15.5
20	35.4	44,400	16.8	51	133,000	14.8
30	34.8	42,100	16.2	50.2	127,000	14.1
40	33.1	36,300	14.8	46.5	101,000	10.9
45	30.4	28,000	12.4	41.9	73,600	6.9
50	27.3	20,300	9.7	40.6	66,900	5.8
55	25.9	17,400	8.5	40.0	64,000	5.2
60	25.5	16,600	8.2	39.0	59,300	4.4
70	24.1	14,000	7.0	38.1	55,300	3.8
80	22.9	12,000	5.9	37.2	51,500	2.8
60 (re-expansion)	25.4	16,400	8.1	39.4	61,200	4.7
50 (re-expansion)	27.8	21,500	10.2	41.0	68,900	6.1
40 (re-expansion)	33.5	37,600	15.1	47.7	109,000	11.9
30 (re-expansion)	34.9	42,500	16.3	50.0	125,000	13.9
20 (re-expansion)	35.3	44,000	16.7	50.6	130,000	14.4
10 (re-expansion)	35.9	46,300	17.2	51.3	135,000	15.0
0 (re-expansion)	36.3	47,800	17.5	52.0	141,000	15.6

6.5.11 UV-Vis Melting Experiments

Superlattices of 30 nm spherical nanoparticles were suspended in solutions containing 0 to 80% of EtOH in H_2O and 0.3 M NaCl. For melting experiments, 1.5 mL of each sample was loaded in quartz cuvettes with a small cavity at the bottom for a magnetic stir bar and placed in a Varian Cary 5000 UV-vis spectrophotometer. Samples were continuously stirred throughout the experiment to facilitate thermal diffusion and to ensure that assemblies remained suspended in the beam path. Each sample was capped tightly to prevent solution evaporation over the course of the experiment. Samples were then heated from 25 °C to 70 °C at 0.1 °C/min. Temperature was regulated from within the Varian software with an external temperature controller, which drives a

Peltier heat pump attached to a six-cell holder. Thermocouples in the sample holder are used to provide feedback to regulate the sample temperature. Extinction was monitored at the nanoparticle LSPR. Melting transition temperatures were determined *via* a baseline subtraction method. Briefly, the pre- and post-melt extinction baselines were linearly fit for each sample and subtracted from the experimental curve. The resulting curve was further manipulated to normalize the data to fraction of nanoparticles assembled, and the point at which the fraction assembled equals 0.5 corresponds to the melting temperature.

6.5.12 Addition of EtOH to DNA-functionalized nanoparticles

To investigate the effect of EtOH on single-stranded DNA-functionalized nanoparticles dispersed in solution, rather than bound within a superlattice, 30 nm Au spheres were functionalized with single-stranded DNA (see "B" anchor strand in Table S2 for the specific sequence used) and suspended in H2O at 0.3 M NaCl. A solution of 80% EtOH and 20% H2O at 0.3 M NaCl was then added to bring the suspended nanoparticles to 0, 30, 35, 40, 45, 50, and 60% EtOH by volume. UV-vis extinction spectra were measured at each EtOH percentage (Figure 133). Up to 30% EtOH, there are no changes to nanoparticle localized surface plasmon resonance (LSPR). However, at higher EtOH percentages, the LSPR broadens and shifts to higher wavelengths (Figure 135, Figure 134). Additionally, the color of the nanoparticle solution changes from pink to clear (Figure 136). Both of these phenomena are consistent with agglomeration, or precipitation, of the DNA-functionalized nanoparticles at higher EtOH percentages. While it is difficult to define precisely, nanoparticle agglomeration appears to begin at ~30-40% EtOH, which is slightly lower than the percentage of EtOH (40-45%) observed to induce a phase transition in the nanoparticle superlattices (Figure 78B). Note that the LSPR does not shift or broaden when

citrate-capped, rather than DNA-functionalized, Au nanoparticles are suspended in 60% EtOH (Figure 134).

6.5.13 MD simulations

System setup and equilibration. The initial A-DNA structure, which served as the starting point for all MD simulations, was generated using the LEAP module of AMBER 14.[348] The two 3′ DNA strands (see Table 14 for sequences) were attached to two flat Au(111) slabs with a dimension of 29 Å X 30 Å X 5 Å. A hole of 7 Å X 7 Å X 5 Å was made on one slab to enable the solvent to move freely between the two sides of the Au slab. Each system was charge-neutralized with Na+ ions and solvated with a specific number of water and ethanol molecules in a 29 Å X 30 Å X 245 Å box. Exact numbers of water and ethanol molecules are listed in Table S4. The GAFF and ff14SB force fields,[349, 350] which contain the parmbsc0 backbone modification to the ff99 DNA parameters,[351] were used in this study. Gold and ethanol force fields (W-46 project) were adopted from other studies.[352, 353] The partial charges of the alkythiolate linker were calculated using GAMESS with the HF/6-31G* basis set,[354] followed by the RESP fitting procedure.[355] MD simulations were carried out using NAMD.[356] Each system was equilibrated as follows. First, the system was energy minimized in 5000 steps. Then, the system was gradually heated from 100 to 300 K in 200 ps using Langevin dynamics in a constant volume condition, followed by a 200 ps constant volume simulation at 300 K. Next, the system was switched to constant pressure (1 atm) with a damping coefficient of 1 ps-1 at 300 K. Constant surface area at the X-Y plane was turned on so the box volume was only changed along the z axis. A 10.0 kcal/mol Å−2 Cartesian restraint was applied on the DNA and alkythiolate linker during the previous steps. Lastly, the restraints were gradually decreased from 10.0 kcal/mol/Å2 to 1.0 kcal/mol/Å2 in a 500 ps run.

Simulations of Na+ distribution and A-B DNA transformation. A 100 ns unrestrained production run under 1 atm and 300 K condition was performed for every percentage of ethanol considered. The last 50 ns of the trajectories were taken for radial distribution function (RDF) and A-B conformation analyses (Figure 83B, Figure 83). The same strand C1′-C1′ distance (Figure 82B) was used to distinguish the A or B form of DNA. [357] For canonical A and B DNA, the distances are 5.52 Å and 4.95 Å, respectively. Analyses were carried out using cpptarj. [358]

Simulations of DNA bend angle. To match the experimental distance between the Au slabs under different percentages of ethanol, a steered MD simulation approach was used. This was done by gradually moving the distance between the two Au slabs from 188 Å to the specific distance listed in Table 15 in 50 ns with a 100 kcal/mol/Å2 force constant under 1 atm and at 300 K. Because this distance suddenly decreased as the amount of EtOH exceeds 40% by volume, simulations were only run in the range of 0-40% EtOH. An 150 ns unrestrained production run was performed for each percentage of ethanol considered. The last 50 ns trajectories were taken for the bend angle analyses (Figure 83).

Table 16. MD simulations vary the number of water and EtOH molecules. The values used in the current study are listed below.

	% EtOH (by volume)						
	0	10	20	30	40	60	80
H_2O	5600	5040	4480	3920	3360	2240	1120
EtOH	0	172	345	517	690	1035	1379

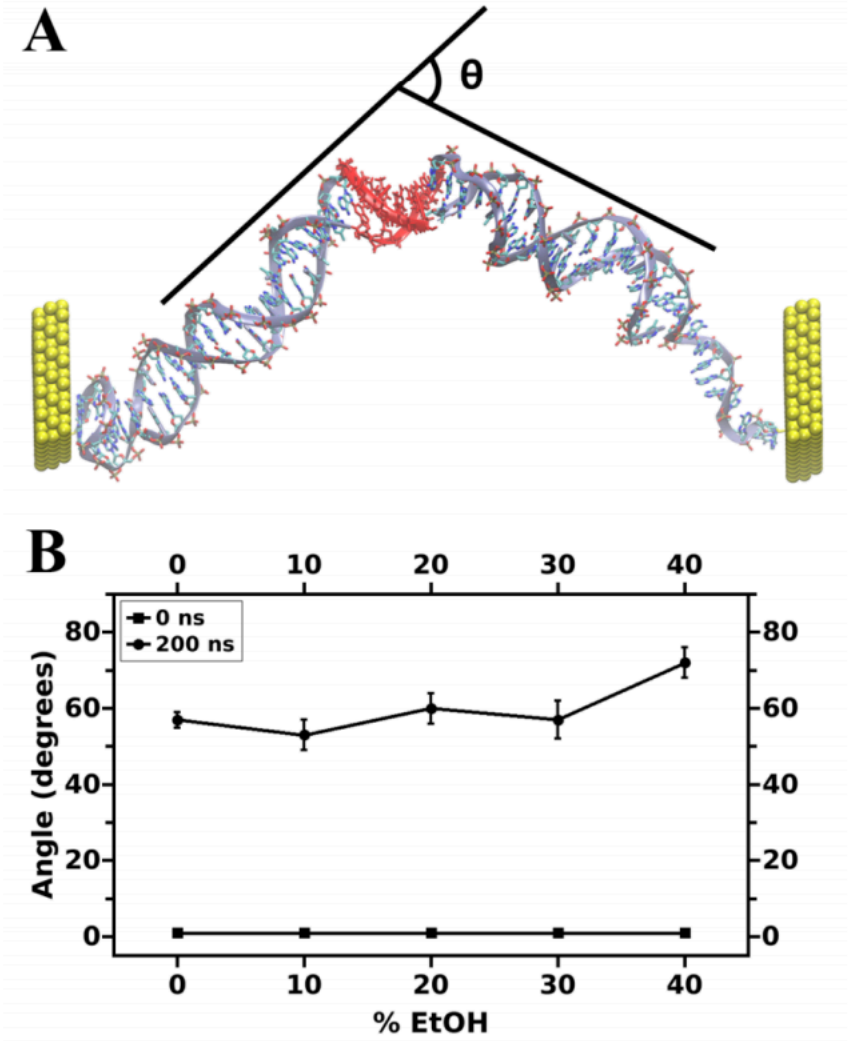

Figure 82. Simulations reveal that as the percent of EtOH increases DNA begins to bend. (A) Schematic showing the model of two DNA strands between two gold surfaces used in MD simulations. The bend angle, θ, represents the amount of bending at the sticky end overlap region between the two strands. (B) The bend angle is plotted for different volume percentages of EtOH in H2O calculated using MD simulations at 200 ns.

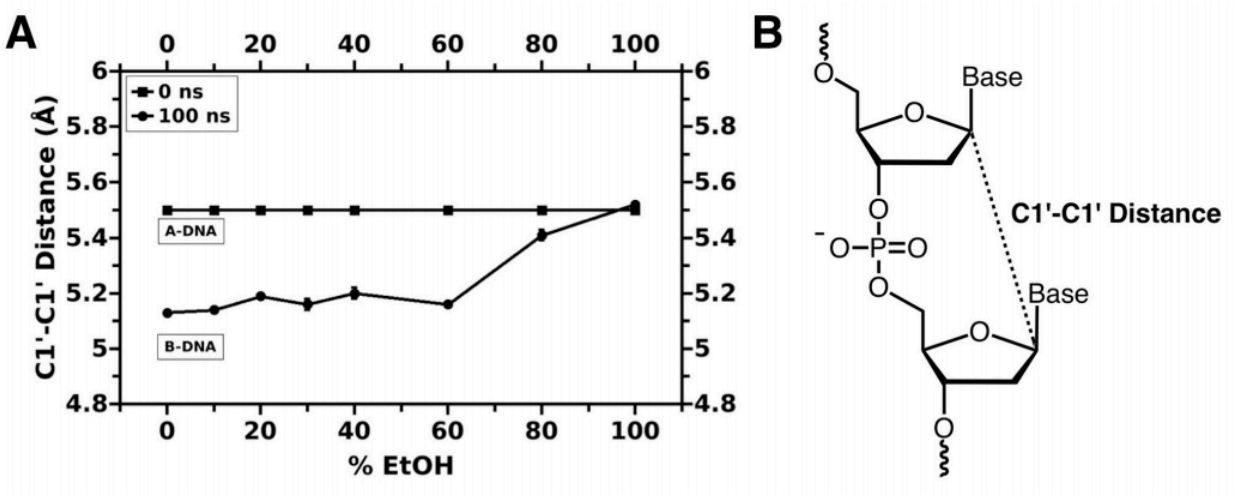

Figure 83. DNA undergoes structural transitions as the percent of EtOH approaches 80%. (A) MD simulations predict that DNA remains in the B-form from 0 to 60% EtOH and transitions to the A-form at 80% EtOH. (B) Definition of C1′-C1′ distance.

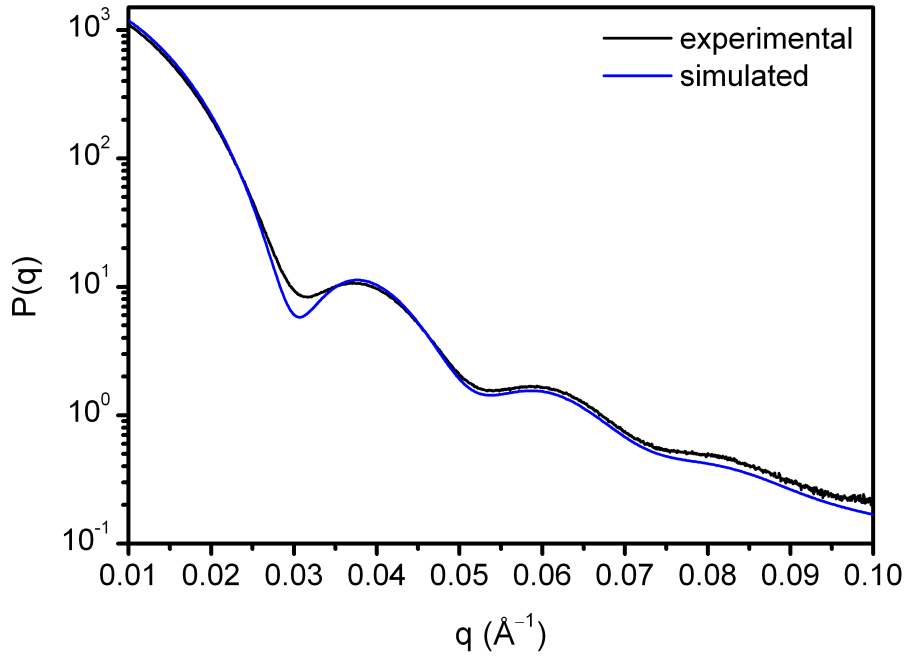

Figure 84. Experimental (black) and simulated (blue) form factors are plotted for the 30 nm spherical nanoparticles used in this work. The simulated sphere diameter was 14.7 Å with a diameter dispersity of 10%.

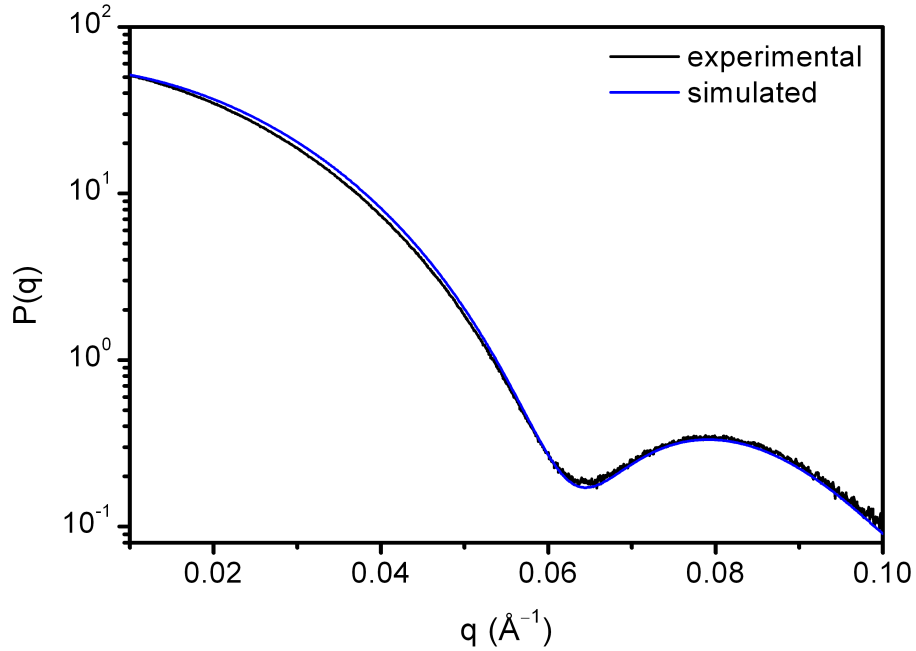

Figure 85. Experimental (black) and simulated (blue) form factors are plotted for the 15 nm spherical nanoparticles used in this work. The simulated sphere diameter was 6.95 Å with a diameter dispersity of 9.5%.

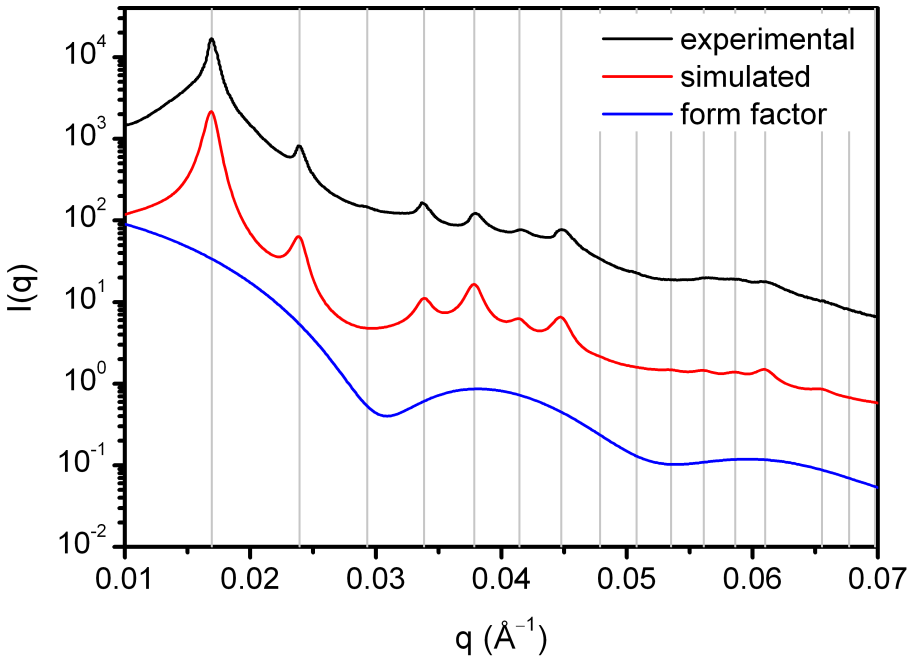

Figure 86. Experimental scattering pattern (black) is shown for a BCC superlattice of 30 nm spherical nanoparticles in 100% H_2O, 0.3 M NaCl. A simulated scattering pattern (red) is shown for a = 52.5 nm along with a simulated form factor (blue). Calculated peak positions are indicated by gray lines.

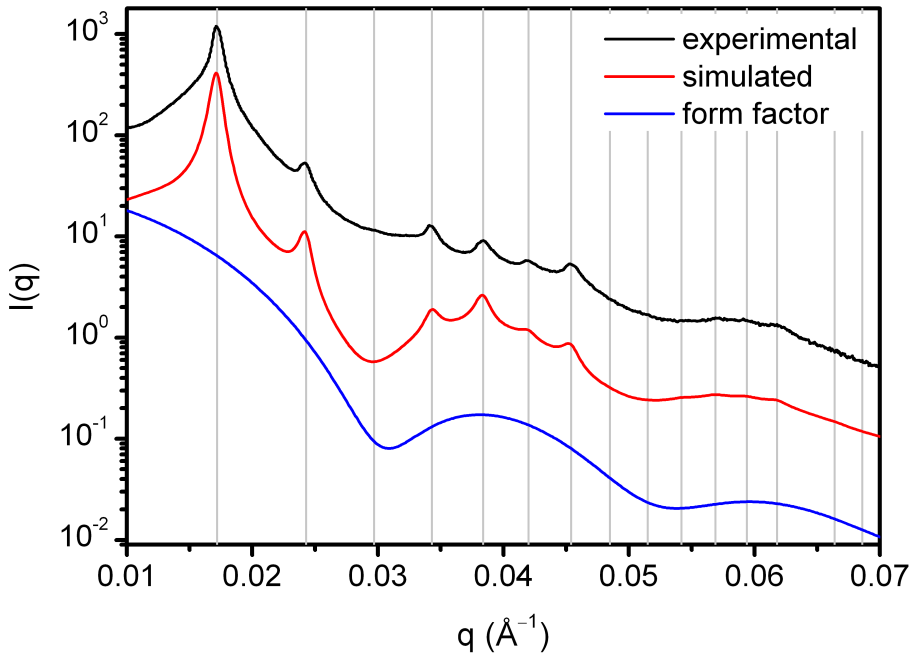

Figure 87. Experimental scattering pattern (black) is shown for a BCC superlattice of 30 nm spherical nanoparticles in 10% EtOH, 90% H_2O, 0.3 M NaCl. A simulated scattering pattern (red) is shown for a = 51.8 nm along with a simulated form factor (blue). Calculated peak positions are indicated by gray lines.

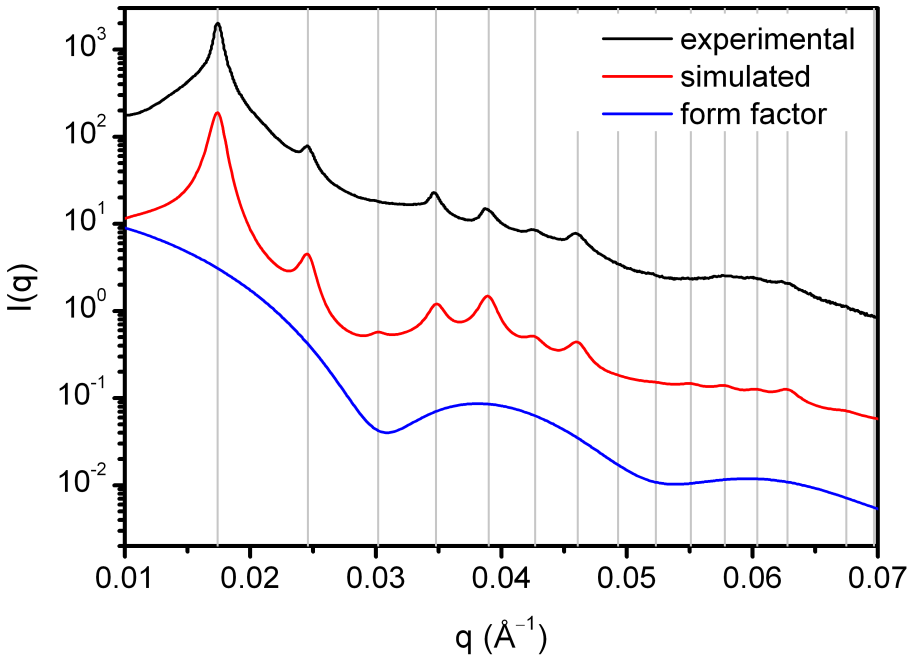

Figure 88. Experimental scattering pattern (black) is shown for a BCC superlattice of 30 nm spherical nanoparticles in 20% EtOH, 80% H_2O, 0.3 M NaCl. A simulated scattering pattern (red) is shown for a = 51.0 nm along with a simulated form factor (blue). Calculated peak positions are indicated by gray lines.

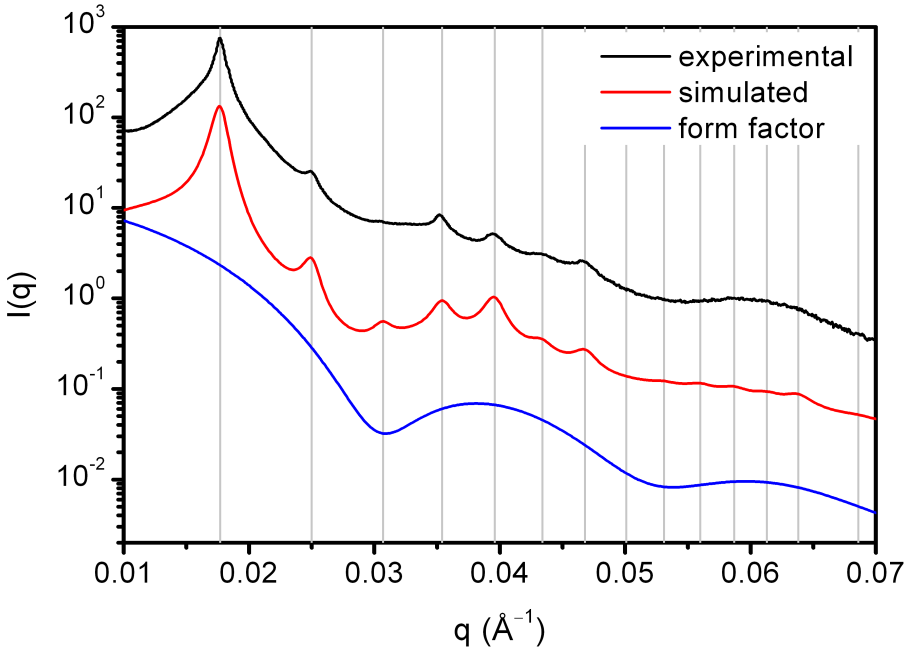

Figure 89. Experimental scattering pattern (black) is shown for a BCC superlattice of 30 nm spherical nanoparticles in 30% EtOH, 70% H_2O, 0.3 M NaCl. A simulated scattering pattern (red) is shown for a = 50.2 nm along with a simulated form factor (blue). Calculated peak positions are indicated by gray lines.

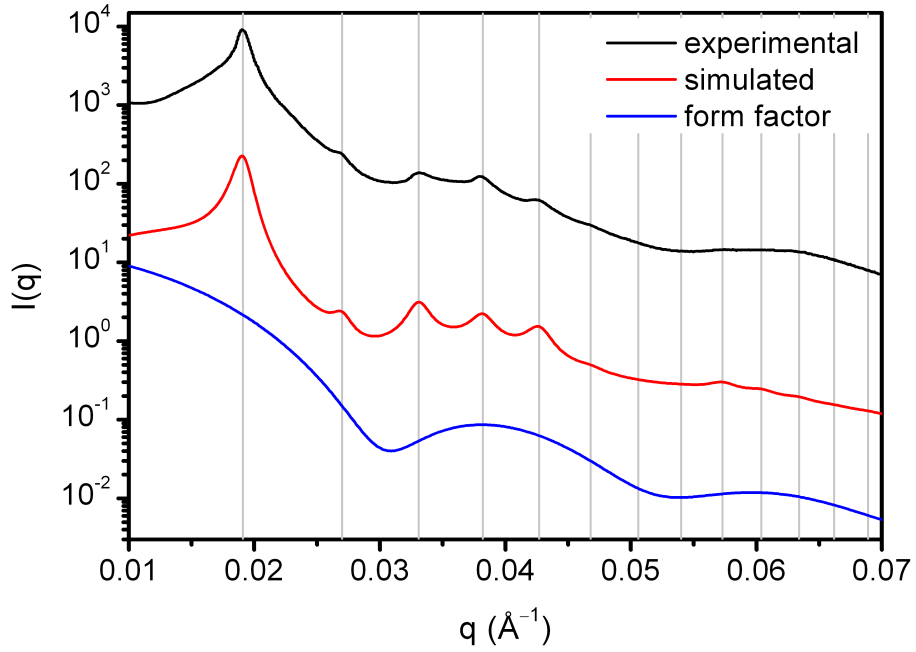

Figure 90. Experimental scattering pattern (black) is shown for a BCC superlattice of 30 nm spherical nanoparticles in 40% EtOH, 60% H_2O, 0.3 M NaCl. A simulated scattering pattern (red) is shown for a = 46.5 nm along with a simulated form factor (blue). Calculated peak positions are indicated by gray lines.

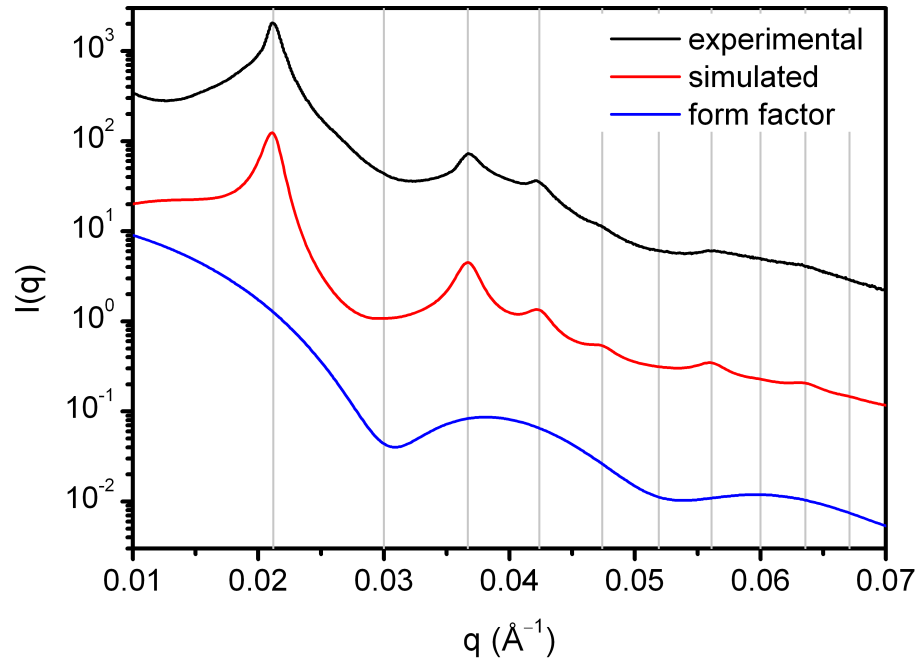

Figure 91. Experimental scattering pattern (black) is shown for a BCC superlattice of 30 nm spherical nanoparticles in 45% EtOH, 55% H_2O, 0.3 M NaCl. A simulated scattering pattern (red) is shown for a = 41.9 nm along with a simulated form factor (blue). Calculated peak positions are indicated by gray lines.

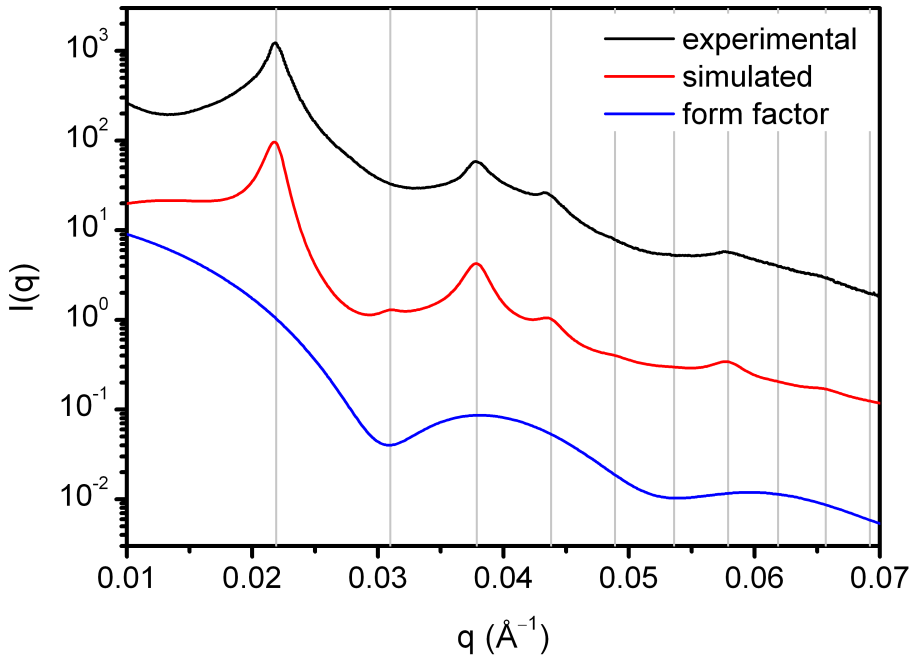

Figure 92. Experimental scattering pattern (black) is shown for a BCC superlattice of 30 nm spherical nanoparticles in 50% EtOH, 50% H_2O, 0.3 M NaCl. A simulated scattering pattern (red) is shown for a = 40.6 nm along with a simulated form factor (blue). Calculated peak positions are indicated by gray lines.

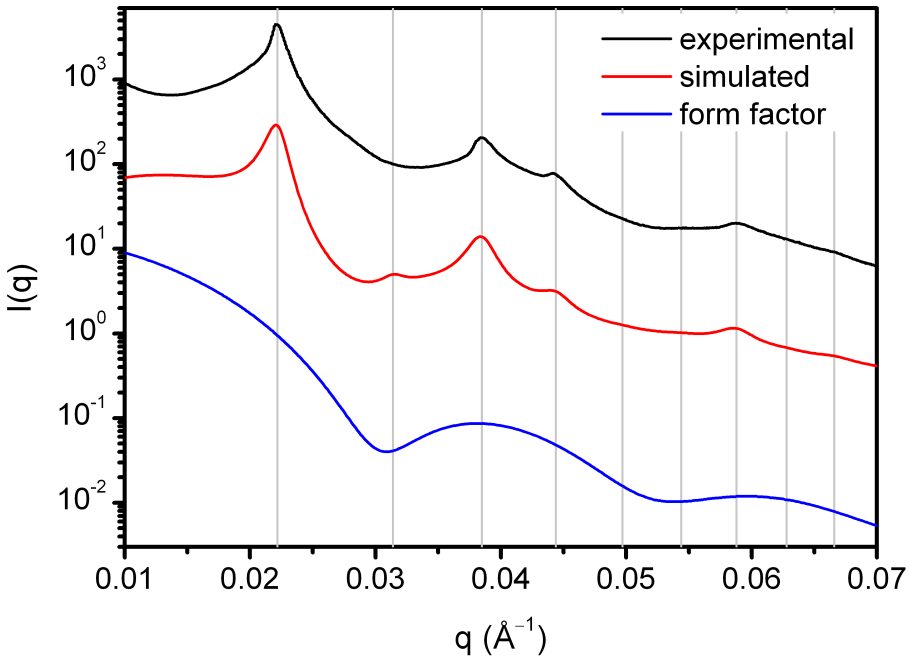

Figure 93. Experimental scattering pattern (black) is shown for a BCC superlattice of 30 nm spherical nanoparticles in 55% EtOH, 45% H_2O, 0.3 M NaCl. A simulated scattering pattern (red) is shown for a = 40.0 nm along with a simulated form factor (blue). Calculated peak positions are indicated by gray lines.

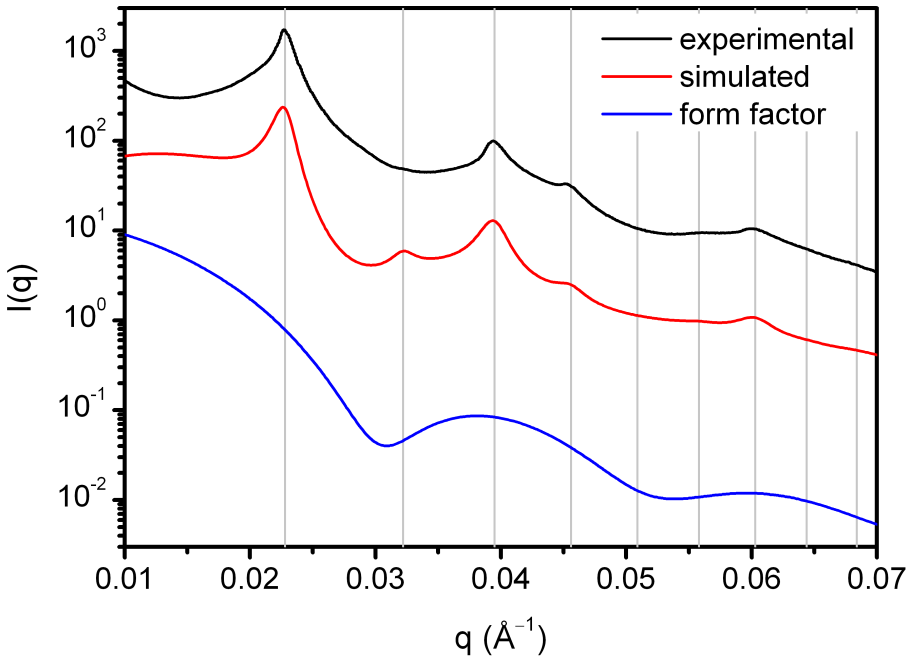

Figure 94. Experimental scattering pattern (black) is shown for a BCC superlattice of 30 nm spherical nanoparticles in 60% EtOH, 40% H_2O, 0.3 M NaCl. A simulated scattering pattern (red) is shown for a = 39.0 nm along with a simulated form factor (blue). Calculated peak positions are indicated by gray lines.

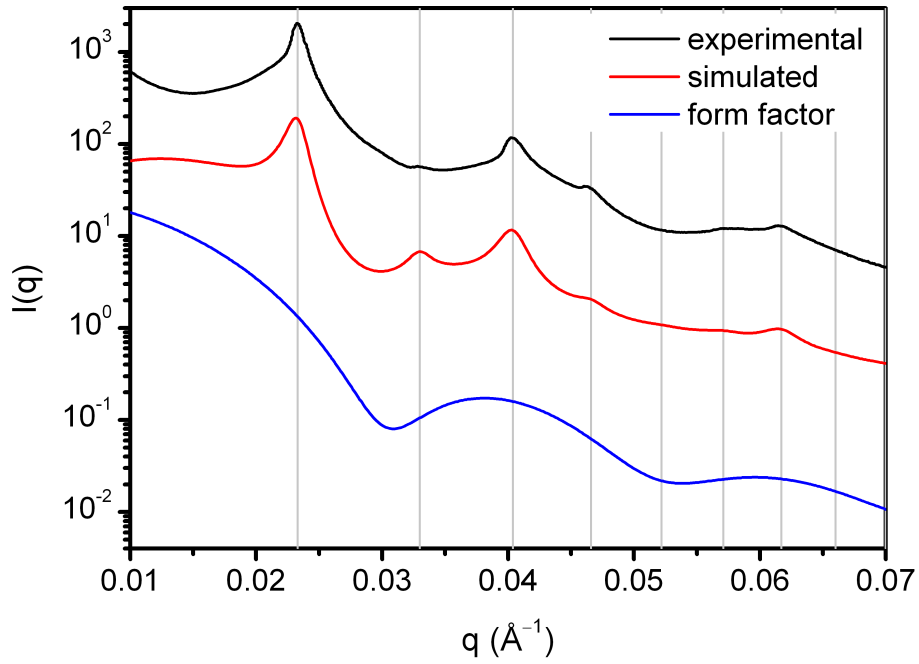

Figure 95. Experimental scattering pattern (black) is shown for a BCC superlattice of 30 nm spherical nanoparticles in 70% EtOH, 30% H_2O, 0.3 M NaCl. A simulated scattering pattern (red) is shown for a = 38.1 nm along with a simulated form factor (blue). Calculated peak positions are indicated by gray lines.

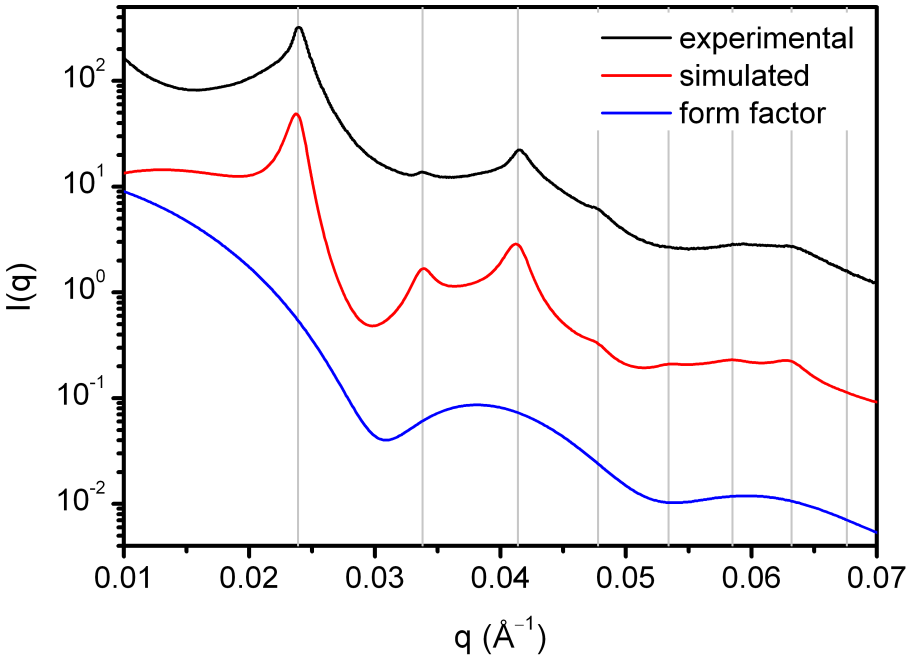

Figure 96. Experimental scattering pattern (black) is shown for a BCC superlattice of 30 nm spherical nanoparticles in 80% EtOH, 20% H_2O, 0.3 M NaCl. A simulated scattering pattern (red) is shown for a = 37.2 nm along with a simulated form factor (blue). Calculated peak positions are indicated by gray lines.

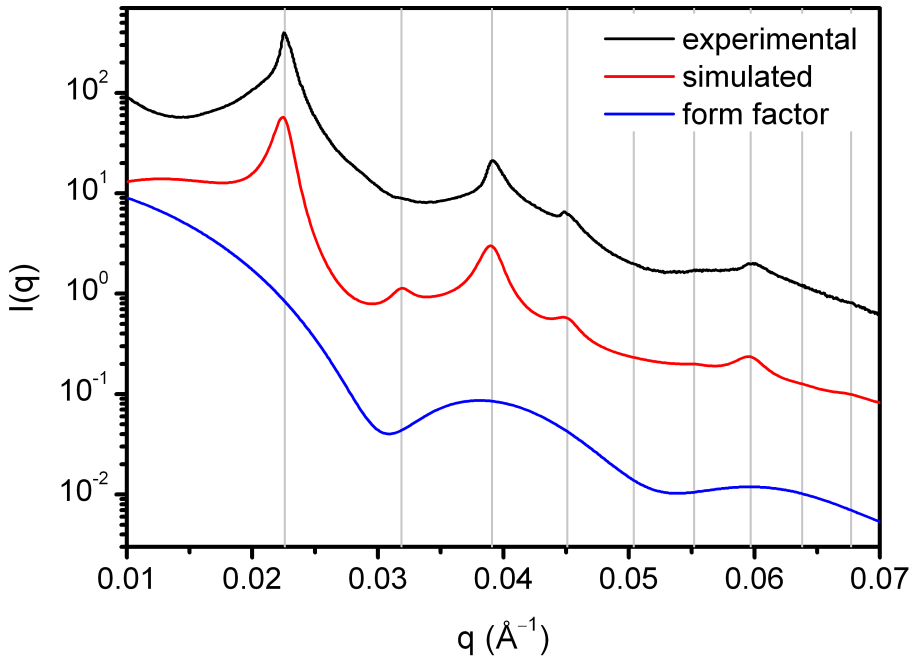

Figure 97. Experimental scattering pattern (black) is shown for a BCC superlattice of 30 nm spherical nanoparticles in 60% EtOH, 40% H_2O, 0.3 M NaCl after equilibrating in 80% EtOH, 20% H_2O, 0.3 M NaCl. A simulated scattering pattern (red) is shown for a = 39.4 nm along with a simulated form factor (blue). Calculated peak positions are indicated by gray lines.

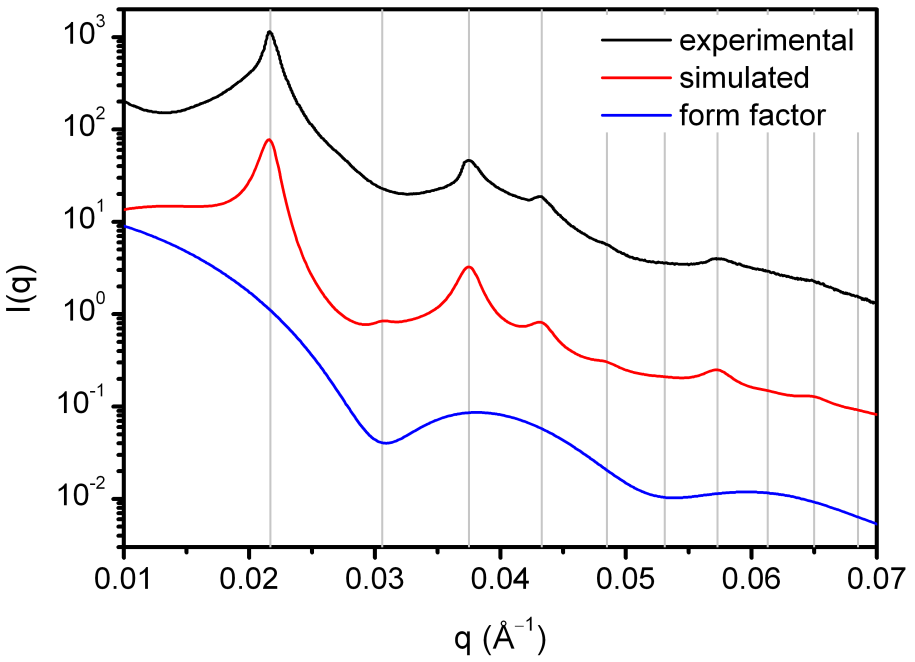

Figure 98. Experimental scattering pattern (black) is shown for a BCC superlattice of 30 nm spherical nanoparticles in 50% EtOH, 50% H_2O, 0.3 M NaCl after equilibrating in 80% EtOH, 20% H_2O, 0.3 M NaCl. A simulated scattering pattern (red) is shown for a = 41.0 nm along with a simulated form factor (blue). Calculated peak positions are indicated by gray lines.

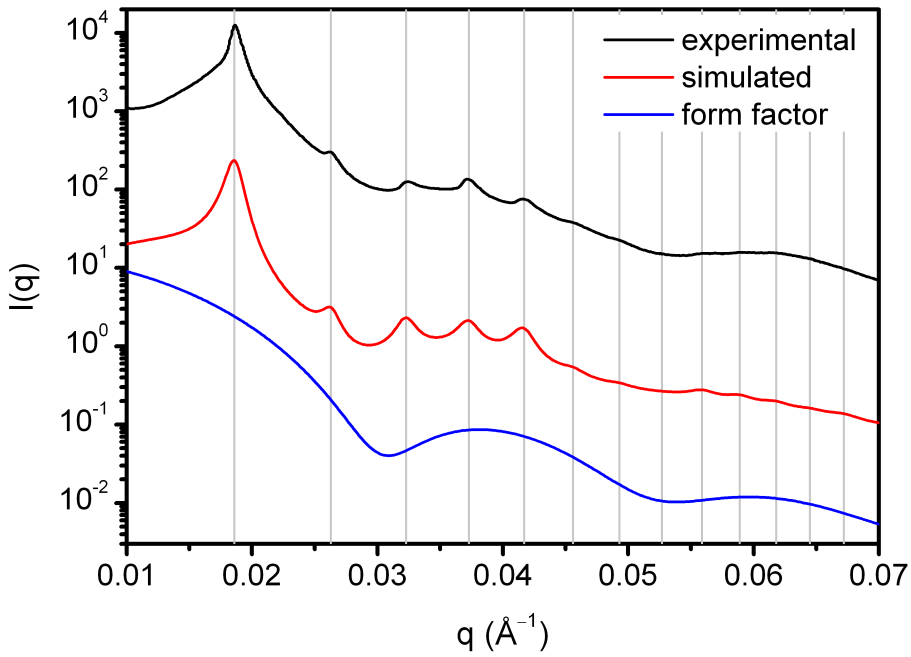

Figure 99. Experimental scattering pattern (black) is shown for a BCC superlattice of 30 nm spherical nanoparticles in 40% EtOH, 60% H_2O, 0.3 M NaCl after equilibrating in 80% EtOH, 20% H_2O, 0.3 M NaCl. A simulated scattering pattern (red) is shown for a = 47.7 nm along with a simulated form factor (blue). Calculated peak positions are indicated by gray lines.

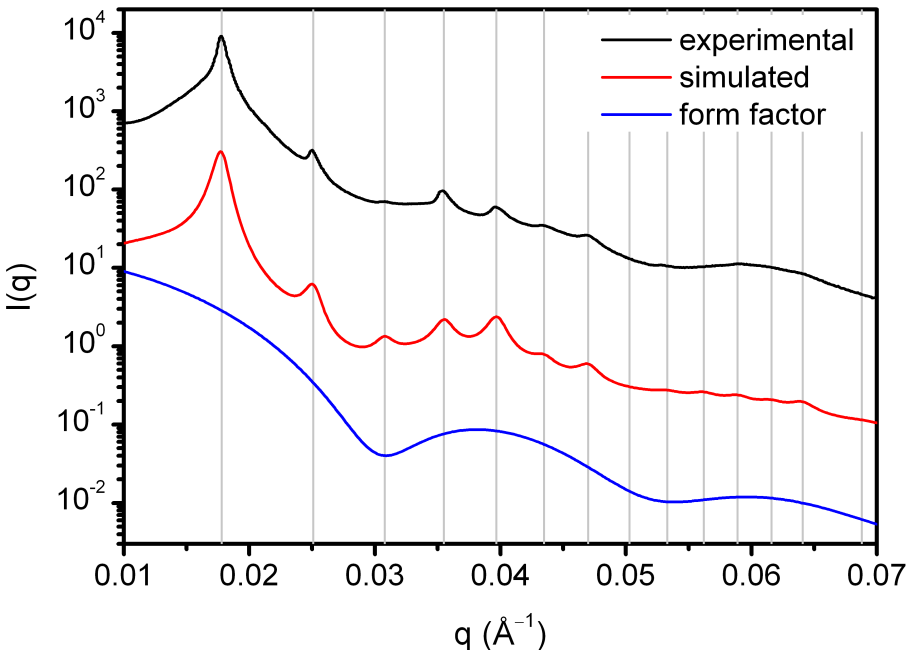

Figure 100. Experimental scattering pattern (black) is shown for a BCC superlattice of 30 nm spherical nanoparticles in 30% EtOH, 70% H_2O, 0.3 M NaCl after equilibrating in 80% EtOH, 20% H_2O, 0.3 M NaCl. A simulated scattering pattern (red) is shown for a = 50.0 nm along with a simulated form factor (blue). Calculated peak positions are indicated by gray lines.

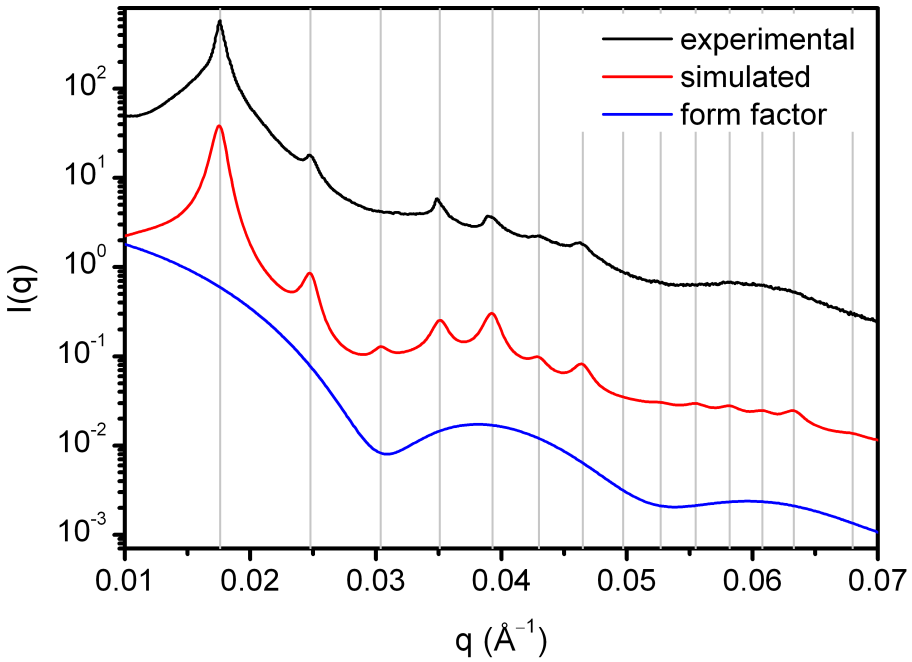

Figure 101. Experimental scattering pattern (black) is shown for a BCC superlattice of 30 nm spherical nanoparticles in 20% EtOH, 80% H_2O, 0.3 M NaCl after equilibrating in 80% EtOH, 20% H_2O, 0.3 M NaCl. A simulated scattering pattern (red) is shown for a = 50.6 nm along with a simulated form factor (blue). Calculated peak positions are indicated by gray lines.

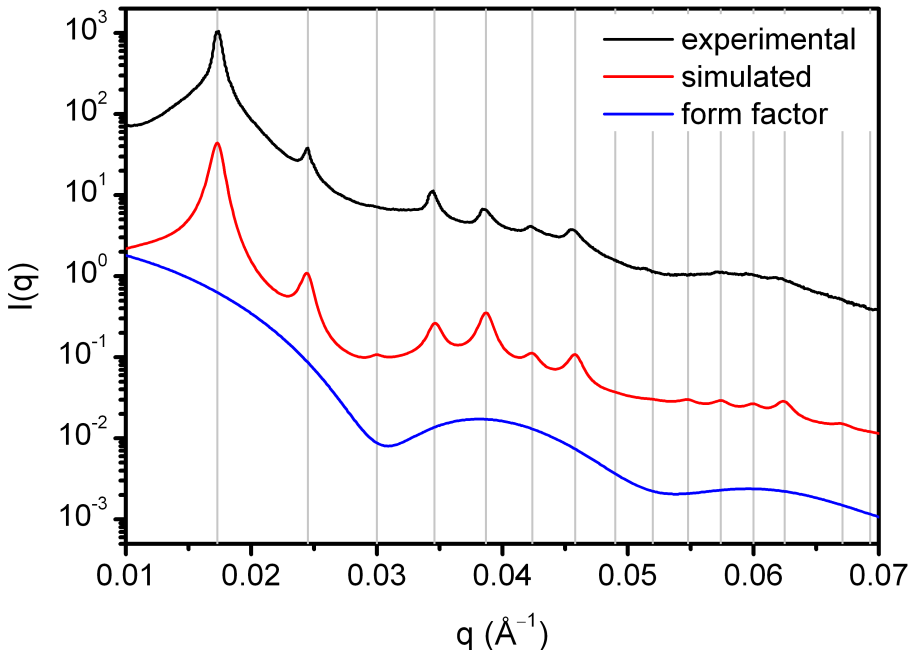

Figure 102. Experimental scattering pattern (black) is shown for a BCC superlattice of 30 nm spherical nanoparticles in 10% EtOH, 90% H_2O, 0.3 M NaCl after equilibrating in 80% EtOH, 20% H_2O, 0.3 M NaCl. A simulated scattering pattern (red) is shown for a = 51.3 nm along with a simulated form factor (blue). Calculated peak positions are indicated by gray lines.

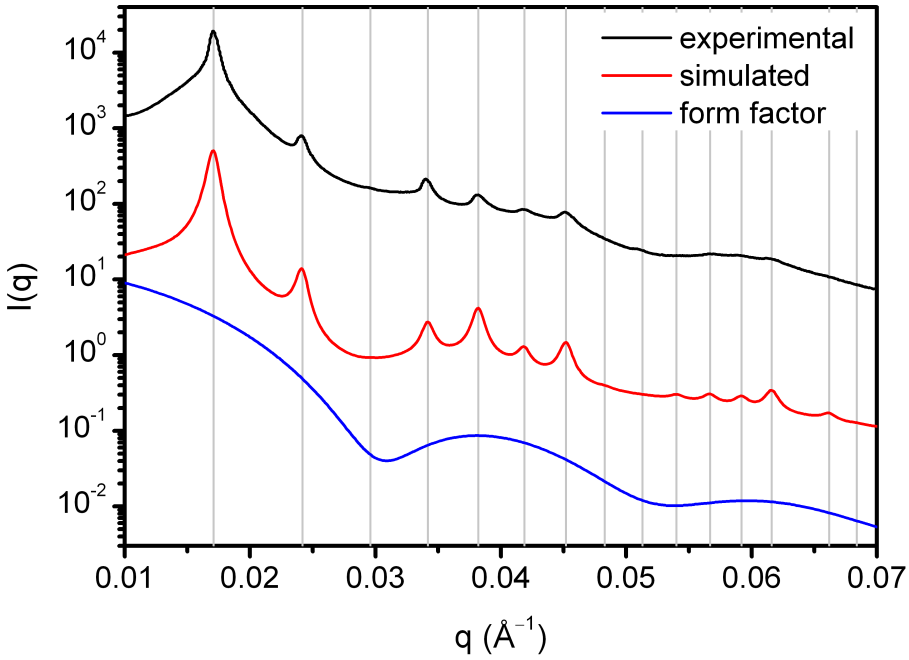

Figure 103. Experimental scattering pattern (black) is shown for a BCC superlattice of 30 nm spherical nanoparticles in 100% H_2O, 0.3 M NaCl after equilibrating in 80% EtOH, 20% H_2O, 0.3 M NaCl. A simulated scattering pattern (red) is shown for a = 52.0 nm along with a simulated form factor (blue). Calculated peak positions are indicated by gray lines.

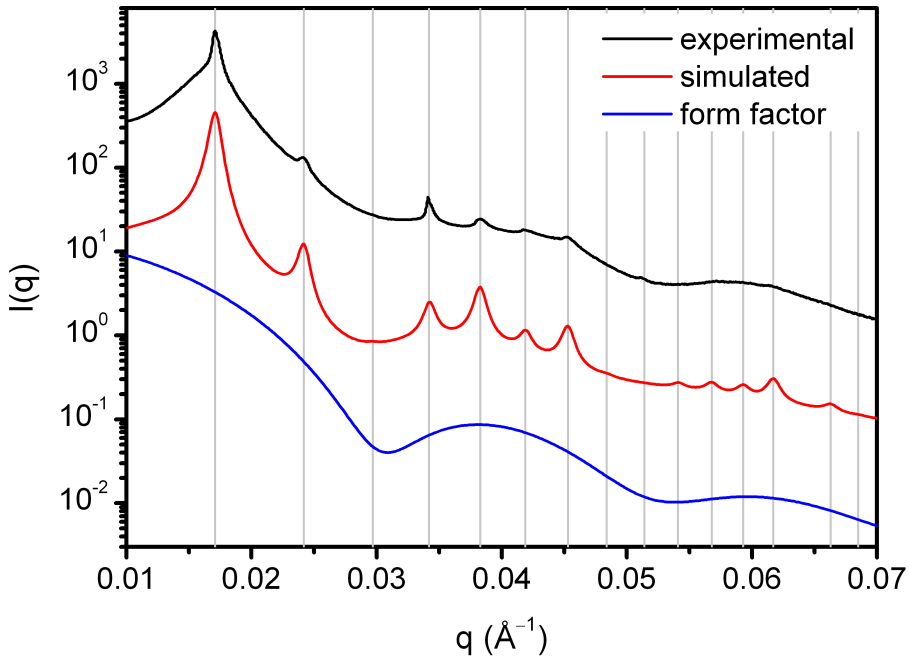

Figure 104. Experimental scattering pattern (black) is shown for a BCC superlattice of 30 nm spherical nanoparticles in 100% H_2O, 0.3 M NaCl after five cycles of equilibrating in 80% EtOH, 20% H_2O, 0.3 M NaCl followed by 100% H_2O, 0.3 M NaCl. A simulated scattering pattern (red) is shown for a = 51.9 nm along with a simulated form factor (blue). Calculated peak positions are indicated by gray lines.

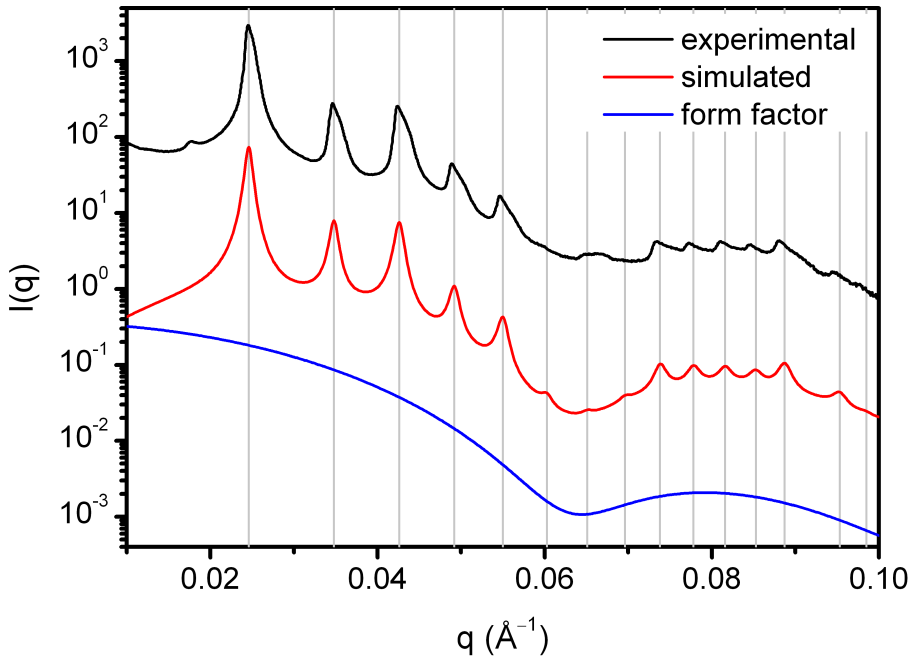

Figure 105. Experimental scattering pattern (black) is shown for a BCC superlattice of 15 nm spherical nanoparticles in 100% H_2O, 0.3 M NaCl. A simulated scattering pattern (red) is shown for a = 52.5 nm along with a simulated form factor (blue). Calculated peak positions are indicated by gray lines.

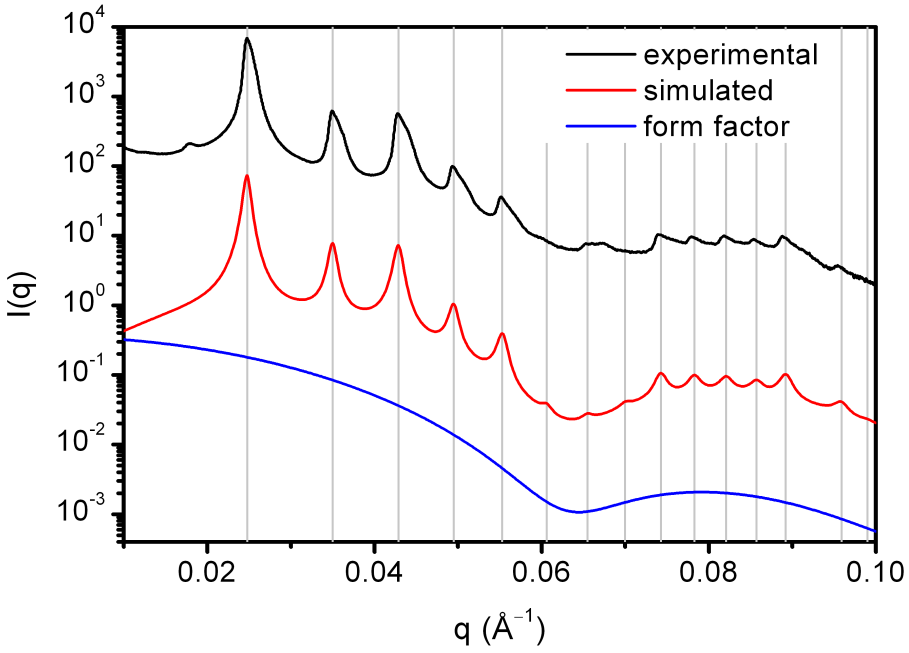

Figure 106. Experimental scattering pattern (black) is shown for a BCC superlattice of 15 nm spherical nanoparticles in 10% EtOH, 90% H_2O, 0.3 M NaCl. A simulated scattering pattern (red) is shown for a = 52.5 nm along with a simulated form factor (blue). Calculated peak positions are indicated by gray lines.

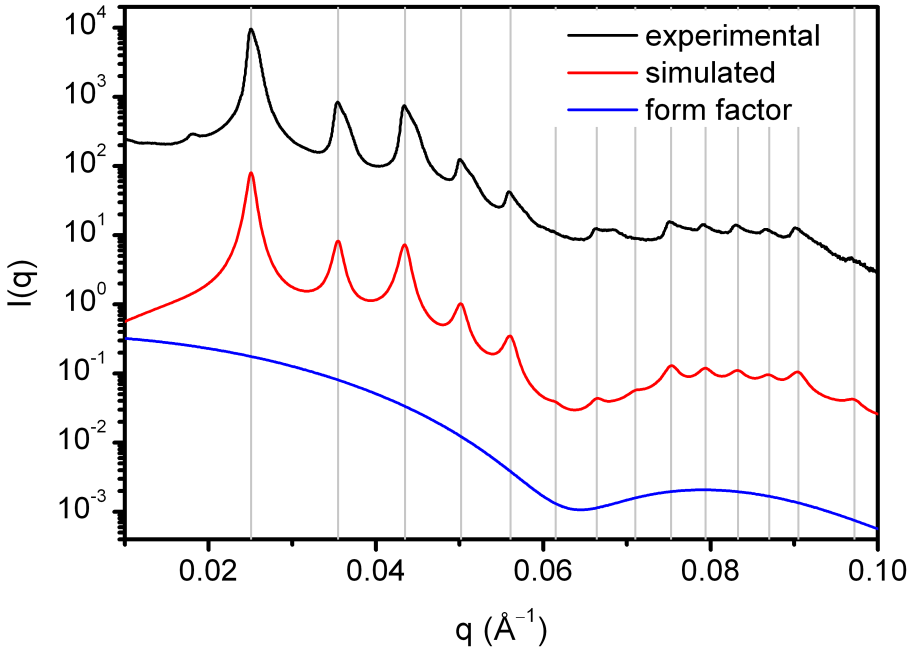

Figure 108. Experimental scattering pattern (black) is shown for a BCC superlattice of 15 nm spherical nanoparticles in 20% EtOH, 80% H_2O, 0.3 M NaCl. A simulated scattering pattern (red) is shown for a = 52.5 nm along with a simulated form factor (blue). Calculated peak positions are indicated by gray lines.

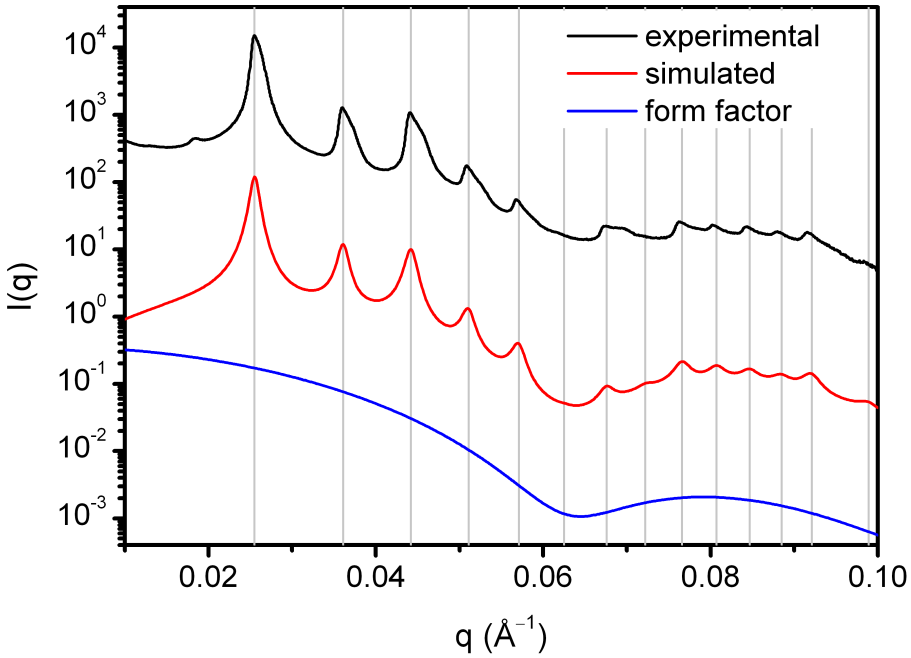

Figure 107. Experimental scattering pattern (black) is shown for a BCC superlattice of 15 nm spherical nanoparticles in 30% EtOH, 70% H_2O, 0.3 M NaCl. A simulated scattering pattern (red) is shown for a = 52.5 nm along with a simulated form factor (blue). Calculated peak positions are indicated by gray lines.

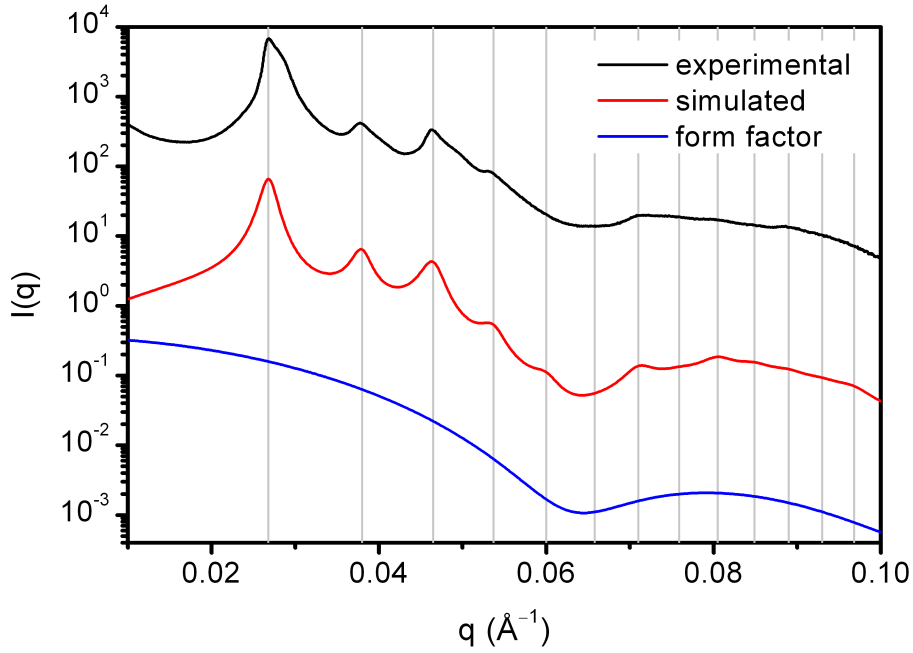

Figure 109. Experimental scattering pattern (black) is shown for a BCC superlattice of 15 nm spherical nanoparticles in 40% EtOH, 60% H_2O, 0.3 M NaCl. A simulated scattering pattern (red) is shown for a = 52.5 nm along with a simulated form factor (blue). Calculated peak positions are indicated by gray lines.

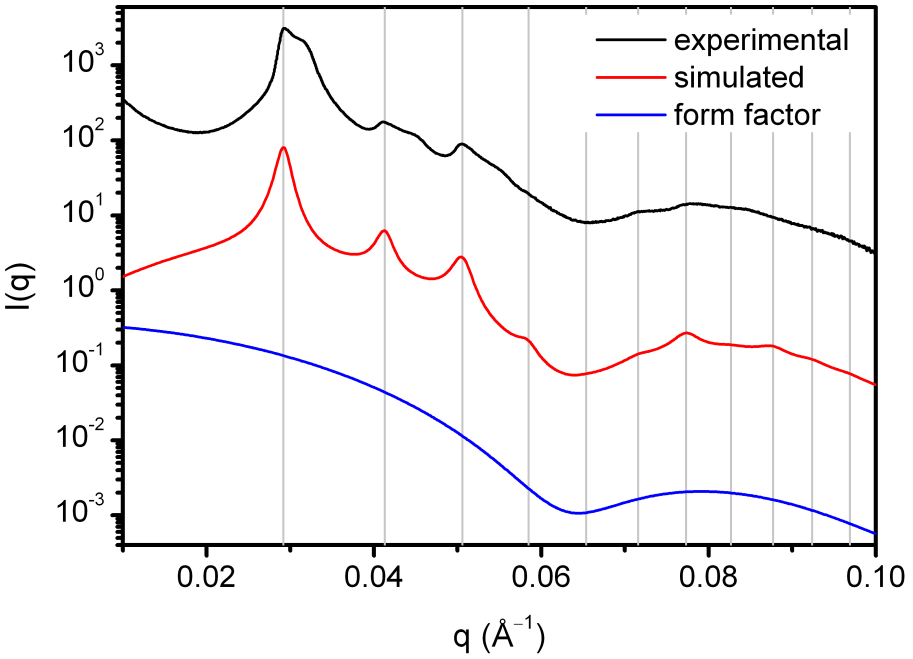

Figure 110. Experimental scattering pattern (black) is shown for a BCC superlattice of 15 nm spherical nanoparticles in 45% EtOH, 55% H_2O, 0.3 M NaCl. A simulated scattering pattern (red) is shown for a = 52.5 nm along with a simulated form factor (blue). Calculated peak positions are indicated by gray lines.

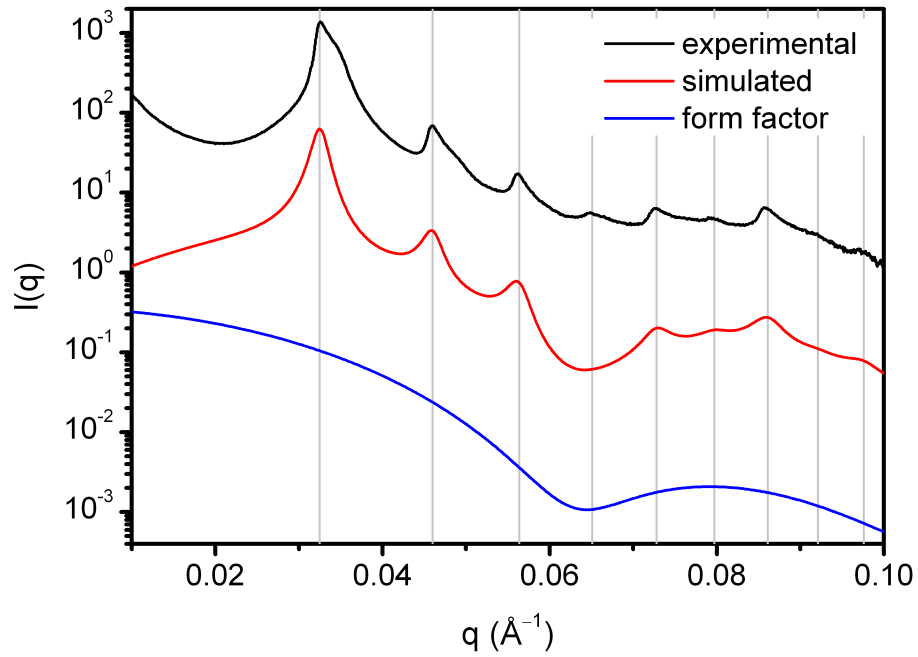

Figure 111. Experimental scattering pattern (black) is shown for a BCC superlattice of 15 nm spherical nanoparticles in 50% EtOH, 50% H_2O, 0.3 M NaCl. A simulated scattering pattern (red) is shown for a = 52.5 nm along with a simulated form factor (blue). Calculated peak positions are indicated by gray lines.

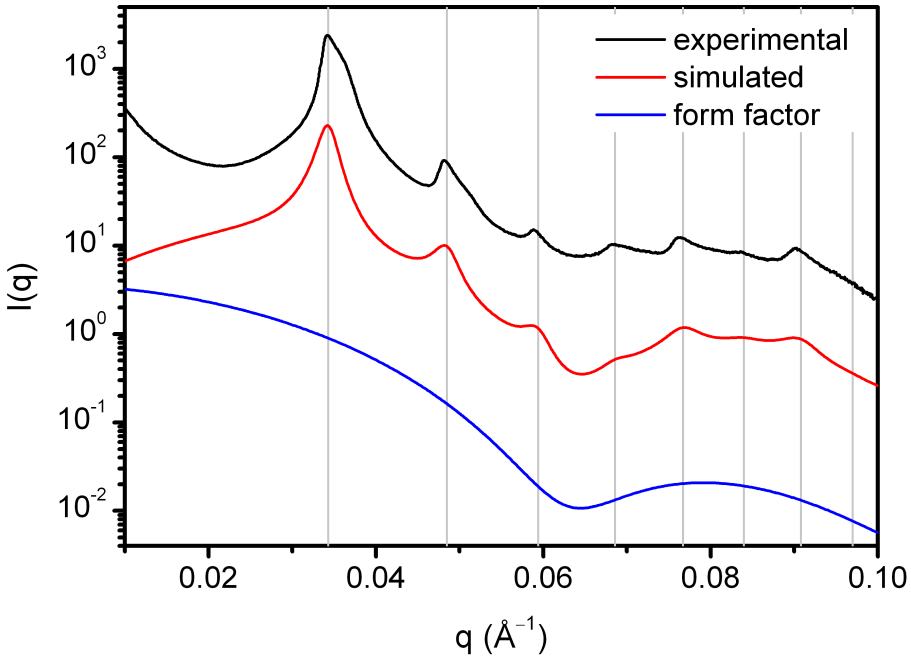

Figure 112. Experimental scattering pattern (black) is shown for a BCC superlattice of 15 nm spherical nanoparticles in 55% EtOH, 45% H_2O, 0.3 M NaCl. A simulated scattering pattern (red) is shown for a = 52.5 nm along with a simulated form factor (blue). Calculated peak positions are indicated by gray lines.

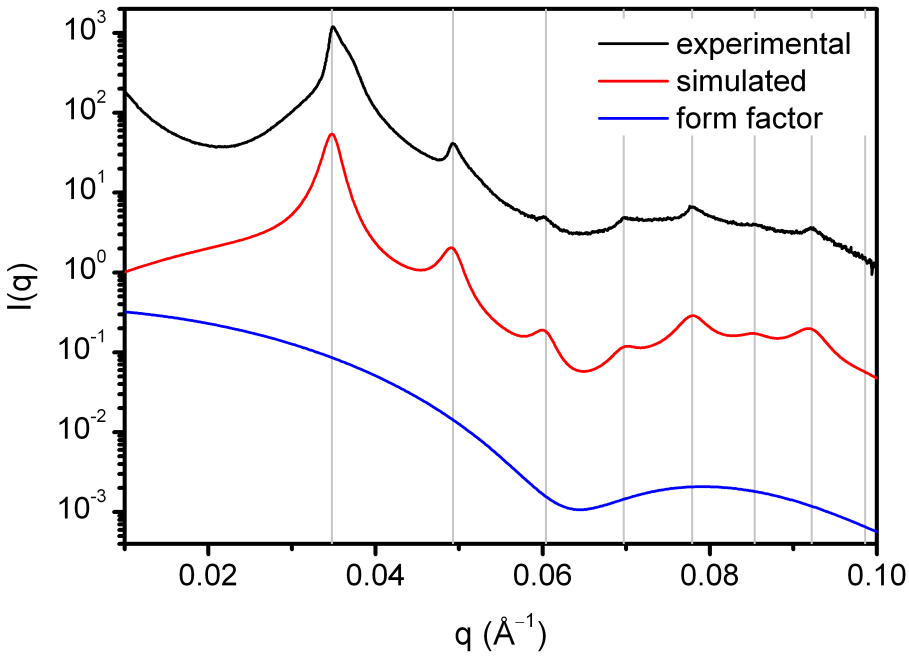

Figure 113. Experimental scattering pattern (black) is shown for a BCC superlattice of 15 nm spherical nanoparticles in 60% EtOH, 40% H_2O, 0.3 M NaCl. A simulated scattering pattern (red) is shown for a = 52.5 nm along with a simulated form factor (blue). Calculated peak positions are indicated by gray lines.

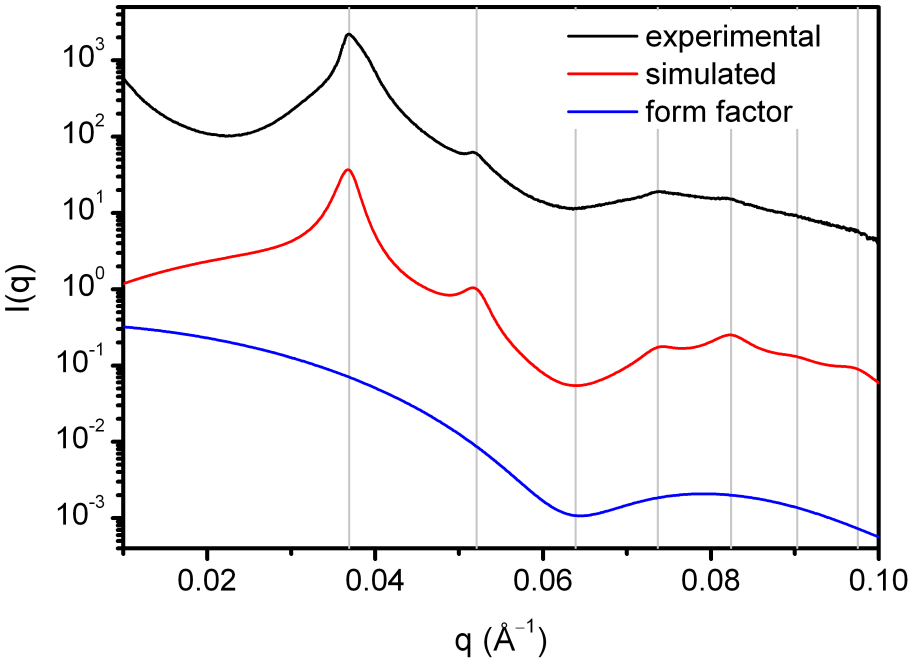

Figure 114. Experimental scattering pattern (black) is shown for a BCC superlattice of 15 nm spherical nanoparticles in 70% EtOH, 30% H_2O, 0.3 M NaCl. A simulated scattering pattern (red) is shown for a = 52.5 nm along with a simulated form factor (blue). Calculated peak positions are indicated by gray lines.

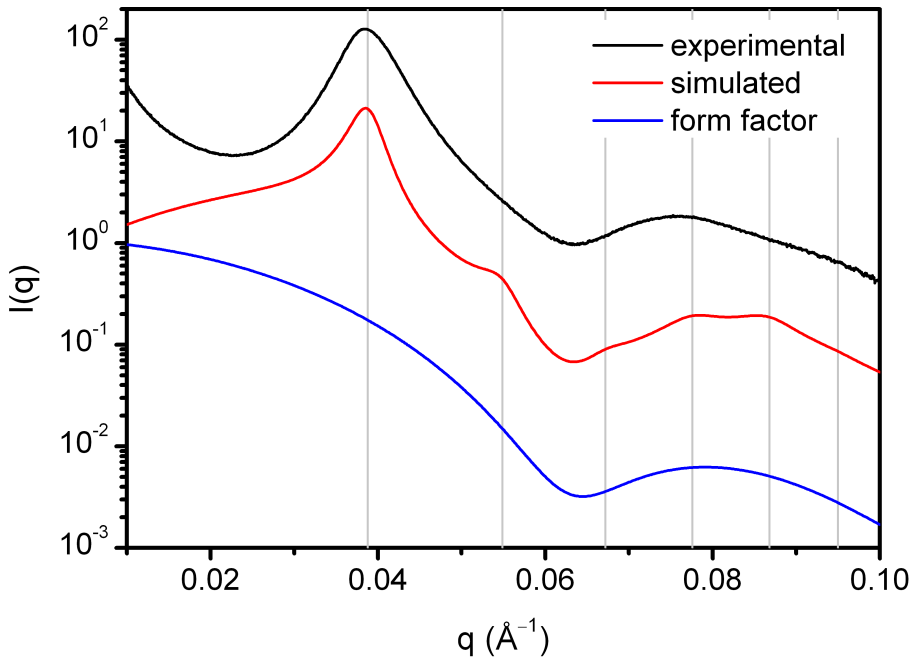

Figure 115. Experimental scattering pattern (black) is shown for a BCC superlattice of 15 nm spherical nanoparticles in 80% EtOH, 20% H_2O, 0.3 M NaCl. A simulated scattering pattern (red) is shown for a = 52.5 nm along with a simulated form factor (blue). Calculated peak positions are indicated by gray lines.

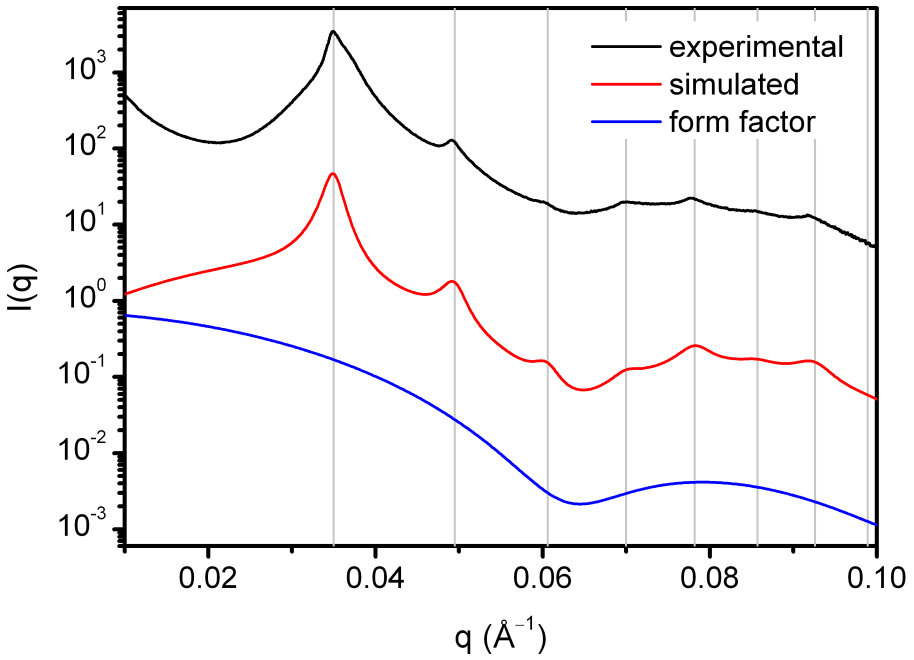

Figure 116. Experimental scattering pattern (black) is shown for a BCC superlattice of 15 nm spherical nanoparticles in 60% EtOH, 40% H_2O, 0.3 M NaCl after equilibrating in 80% EtOH, 20% H_2O, 0.3 M NaCl. A simulated scattering pattern (red) is shown for a = 51.3 nm along with a simulated form factor (blue). Calculated peak positions are indicated by gray lines.

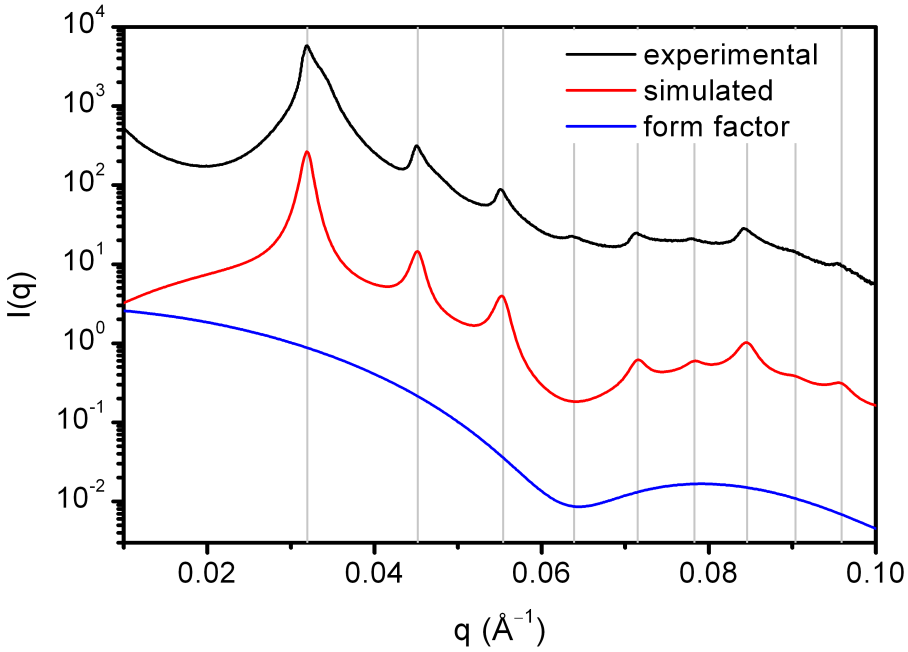

Figure 118. Experimental scattering pattern (black) is shown for a BCC superlattice of 15 nm spherical nanoparticles in 50% EtOH, 50% H_2O, 0.3 M NaCl after equilibrating in 80% EtOH, 20% H_2O, 0.3 M NaCl. A simulated scattering pattern (red) is shown for a = 51.3 nm along with a simulated form factor (blue). Calculated peak positions are indicated by gray lines.

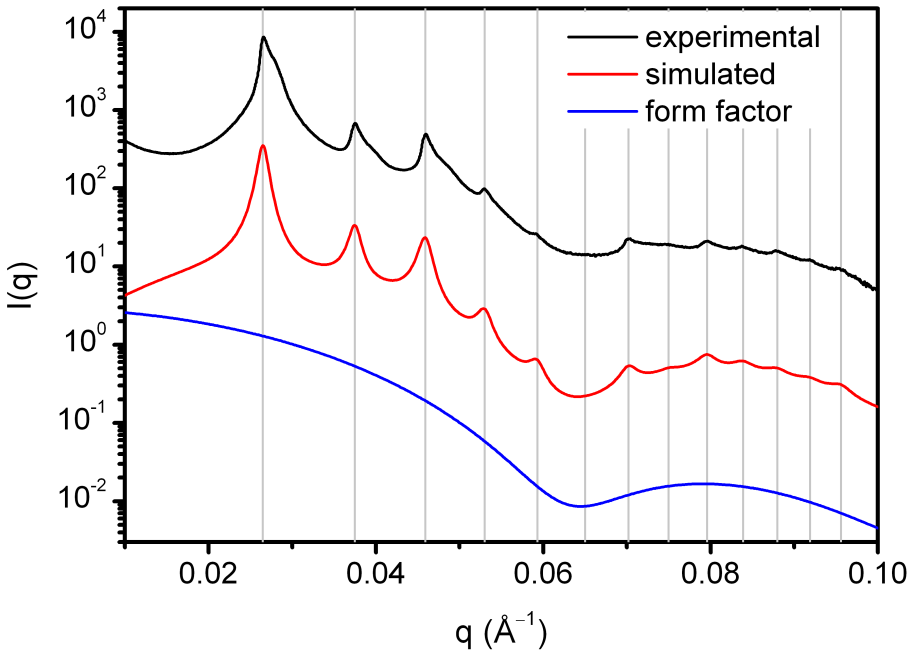

Figure 117. Experimental scattering pattern (black) is shown for a BCC superlattice of 15 nm spherical nanoparticles in 40% EtOH, 60% H_2O, 0.3 M NaCl after equilibrating in 80% EtOH, 20% H_2O, 0.3 M NaCl. A simulated scattering pattern (red) is shown for a = 51.3 nm along with a simulated form factor (blue). Calculated peak positions are indicated by gray lines.

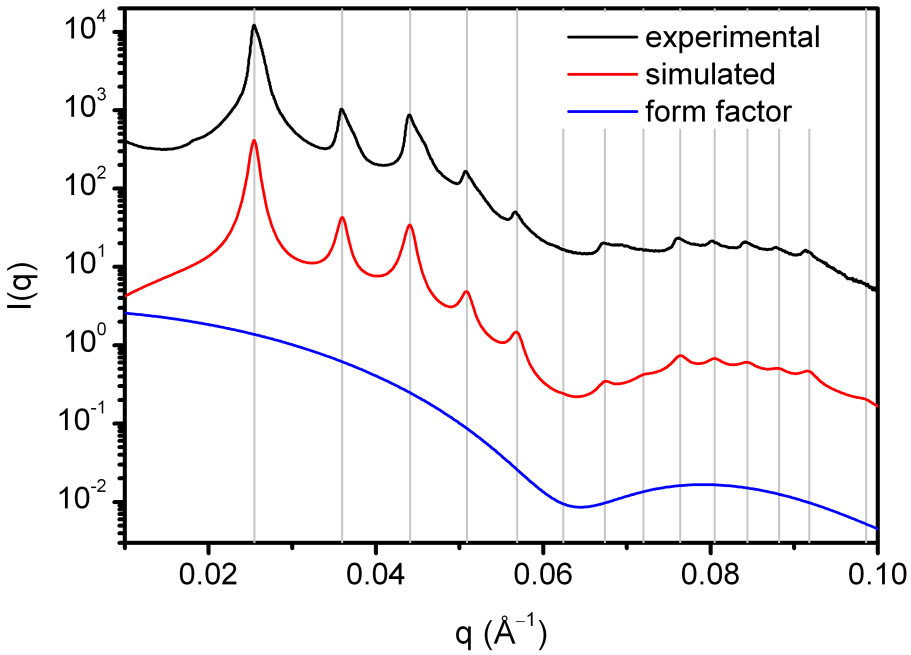

Figure 119. Experimental scattering pattern (black) is shown for a BCC superlattice of 15 nm spherical nanoparticles in 30% EtOH, 70% H_2O, 0.3 M NaCl after equilibrating in 80% EtOH, 20% H_2O, 0.3 M NaCl. A simulated scattering pattern (red) is shown for a = 51.3 nm along with a simulated form factor (blue). Calculated peak positions are indicated by gray lines.

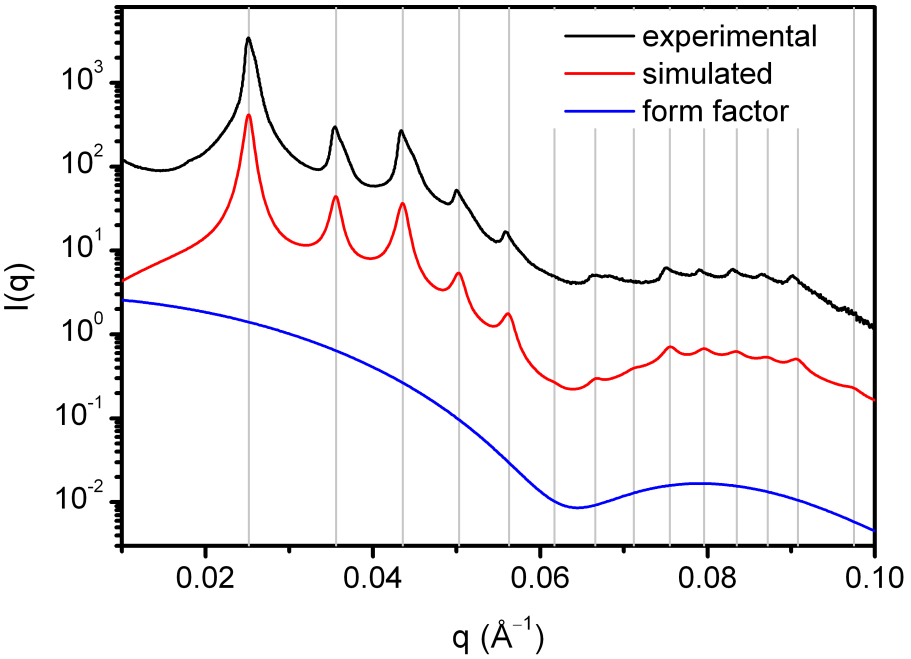

Figure 120. Experimental scattering pattern (black) is shown for a BCC superlattice of 15 nm spherical nanoparticles in 20% EtOH, 80% H_2O, 0.3 M NaCl after equilibrating in 80% EtOH, 20% H_2O, 0.3 M NaCl. A simulated scattering pattern (red) is shown for a = 51.3 nm along with a simulated form factor (blue). Calculated peak positions are indicated by gray lines.

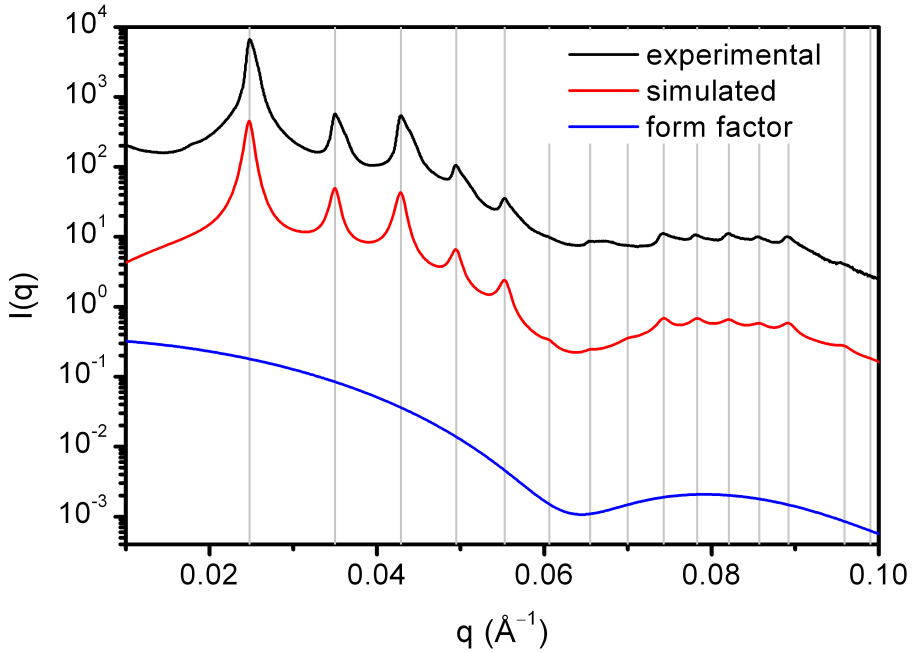

Figure 121. Experimental scattering pattern (black) is shown for a BCC superlattice of 15 nm spherical nanoparticles in 10% EtOH, 90% H_2O, 0.3 M NaCl after equilibrating in 80% EtOH, 20% H_2O, 0.3 M NaCl. A simulated scattering pattern (red) is shown for a = 51.3 nm along with a simulated form factor (blue). Calculated peak positions are indicated by gray lines.

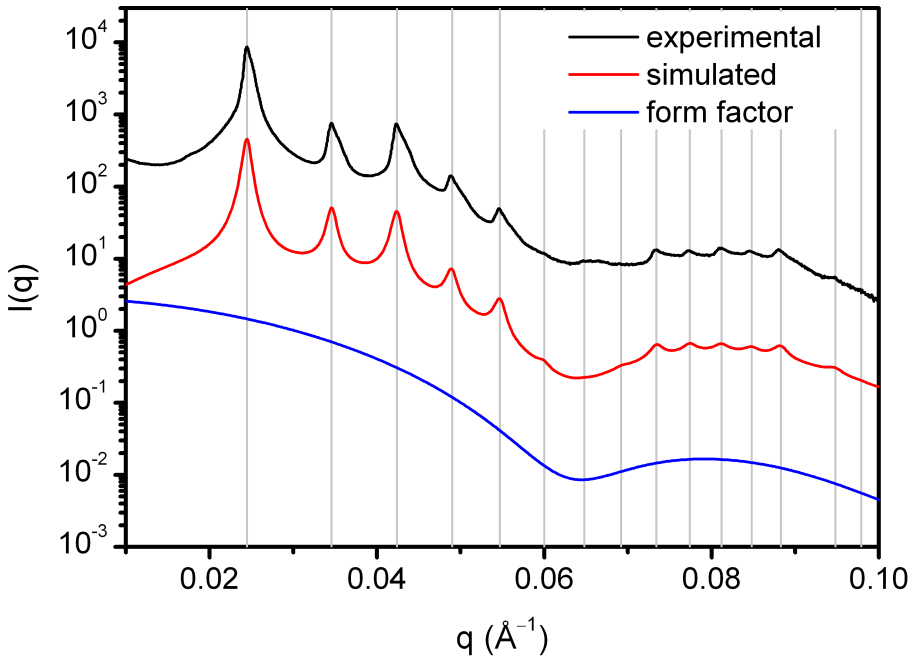

Figure 122. Experimental scattering pattern (black) is shown for a BCC superlattice of 15 nm spherical nanoparticles in 100% H_2O, 0.3 M NaCl after equilibrating in 80% EtOH, 20% H_2O, 0.3 M NaCl. A simulated scattering pattern (red) is shown for a = 51.3 nm along with a simulated form factor (blue). Calculated peak positions are indicated by gray lines.

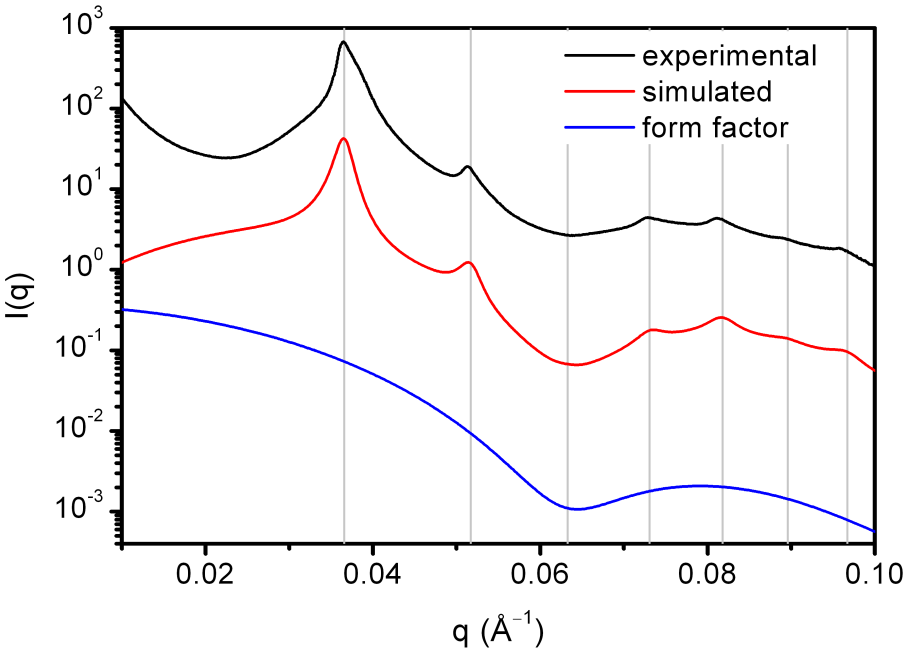

Figure 123. Experimental scattering pattern (black) is shown for a BCC superlattice of 15 nm spherical nanoparticles in 70% ETOH, 30% H_2O, 0.3 M NaCl after equilibrating for 3 min. A simulated scattering pattern (red) is shown for a = 51.3 nm along with a simulated form factor (blue). Calculated peak positions are indicated by gray lines.

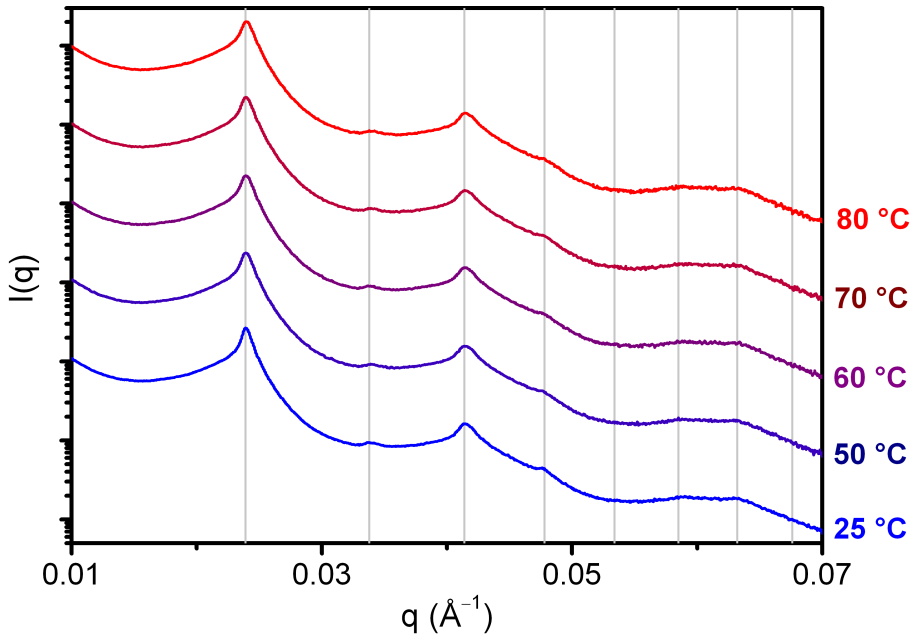

Figure 124. Experimental scattering patterns for a BCC superlattice of 30 nm spherical nanoparticles in 80% ETOH, 20% H_2O, 0.3 M NaCl at 25, 50, 60, 70, or 80 °C. Calculated peak positions for a = 50.6 nm are indicated by gray lines.

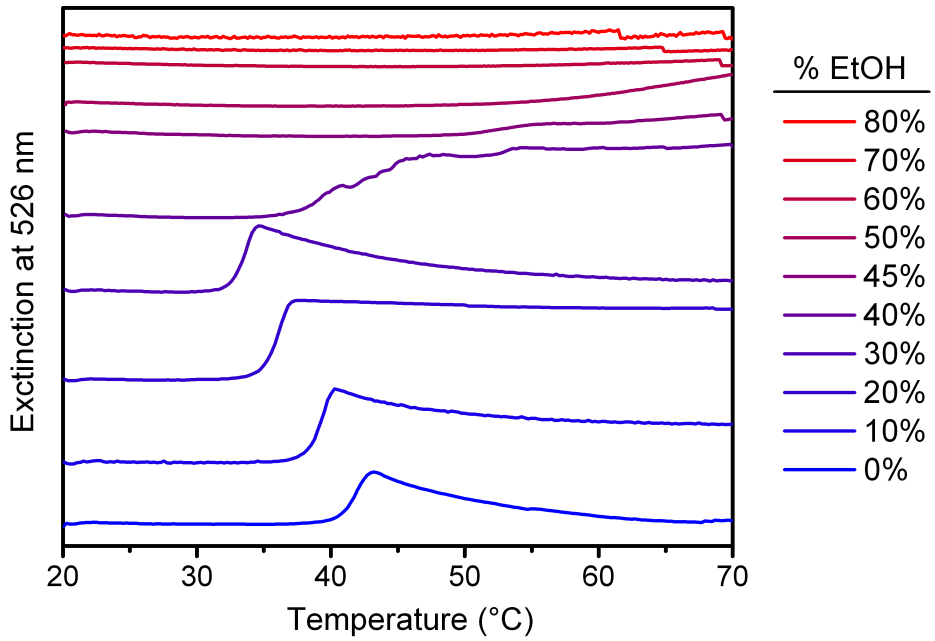

Figure 125. Variable-temperature UV-vis spectroscopy melting curves for BCC superlattices of 30 nm spherical nanoparticles suspended in 0% to 80% EtOH in H_2O at 0.3 M NaCl. Extinction was monitored at the nanoparticle localized surface plasmon resonance frequency of 526 nm. Note that the extinction values are offset to facilitate comparison.

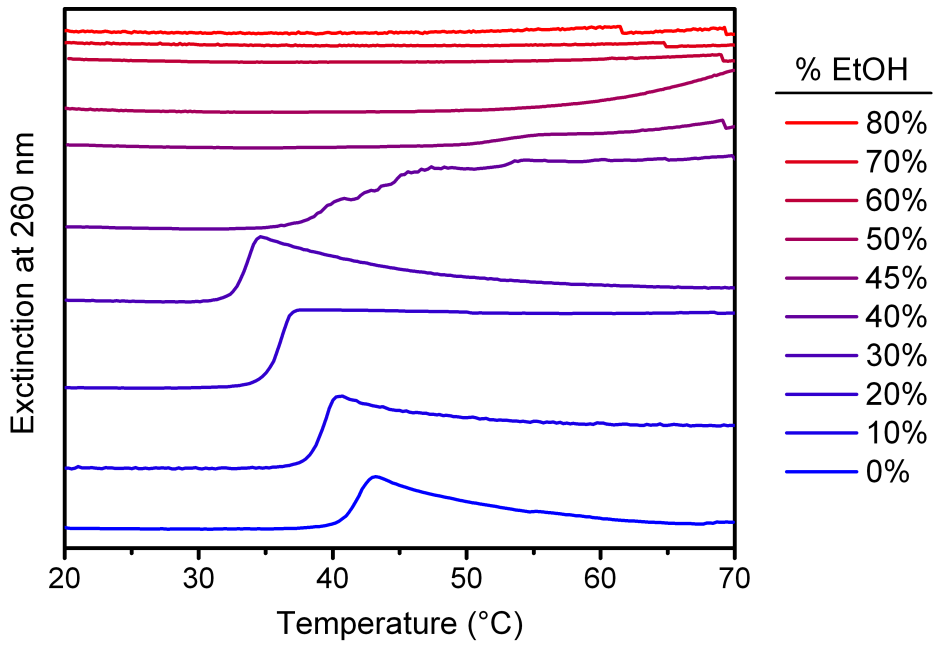

Figure 126. Variable-temperature UV-vis spectroscopy melting curves for BCC superlattices of 30 nm spherical nanoparticles suspended in 0% to 80% EtOH in H_2O at 0.3 M NaCl. Extinction was monitored at 260 nm. Note that the extinction values are offset to facilitate comparison.

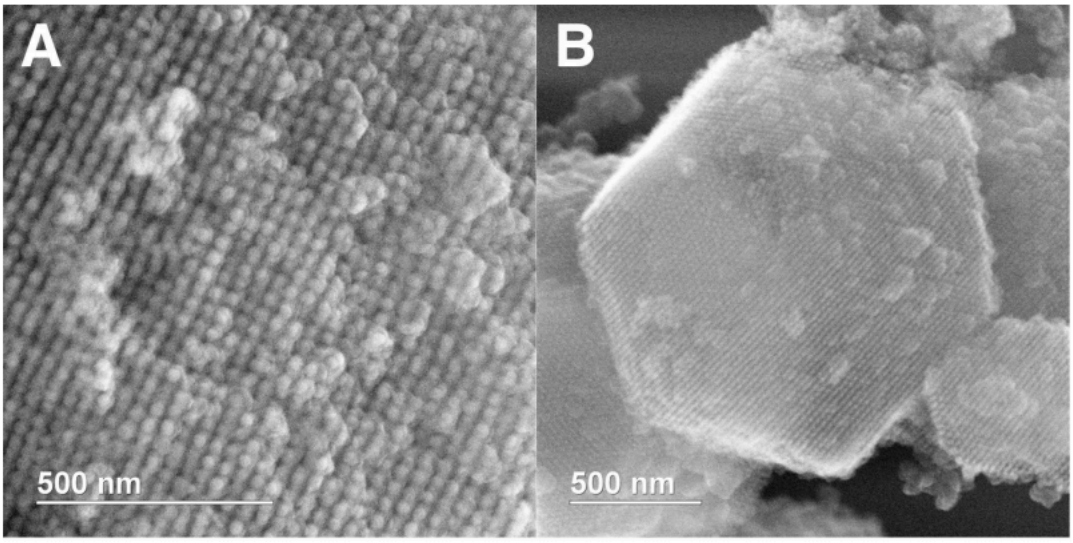

Figure 127. Additional STEM images of silica-encapsulated BCC superlattices of 30 nm spherical nanoparticles previously suspended in 100% H2O at 0.3 M NaCl. Images were obtained in scanning mode.

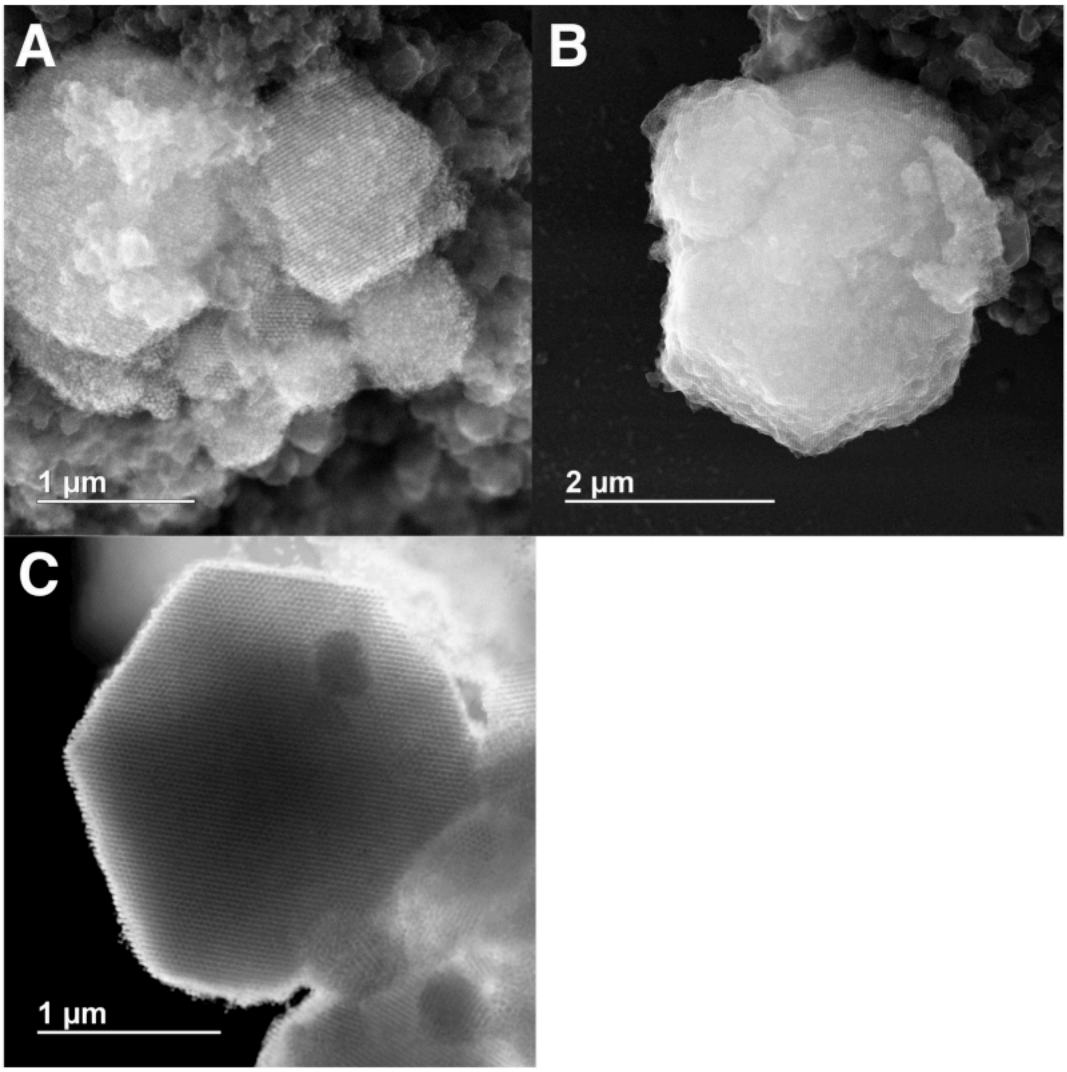

Figure 128. Additional STEM images of silica-encapsulated BCC superlattices of 30 nm spherical nanoparticles previously suspended in 41% EtOH and 59% H_2O at 0.3M NaCl. Top images were obtained in scanning mode, while bottom image was obtained in transmission mode.

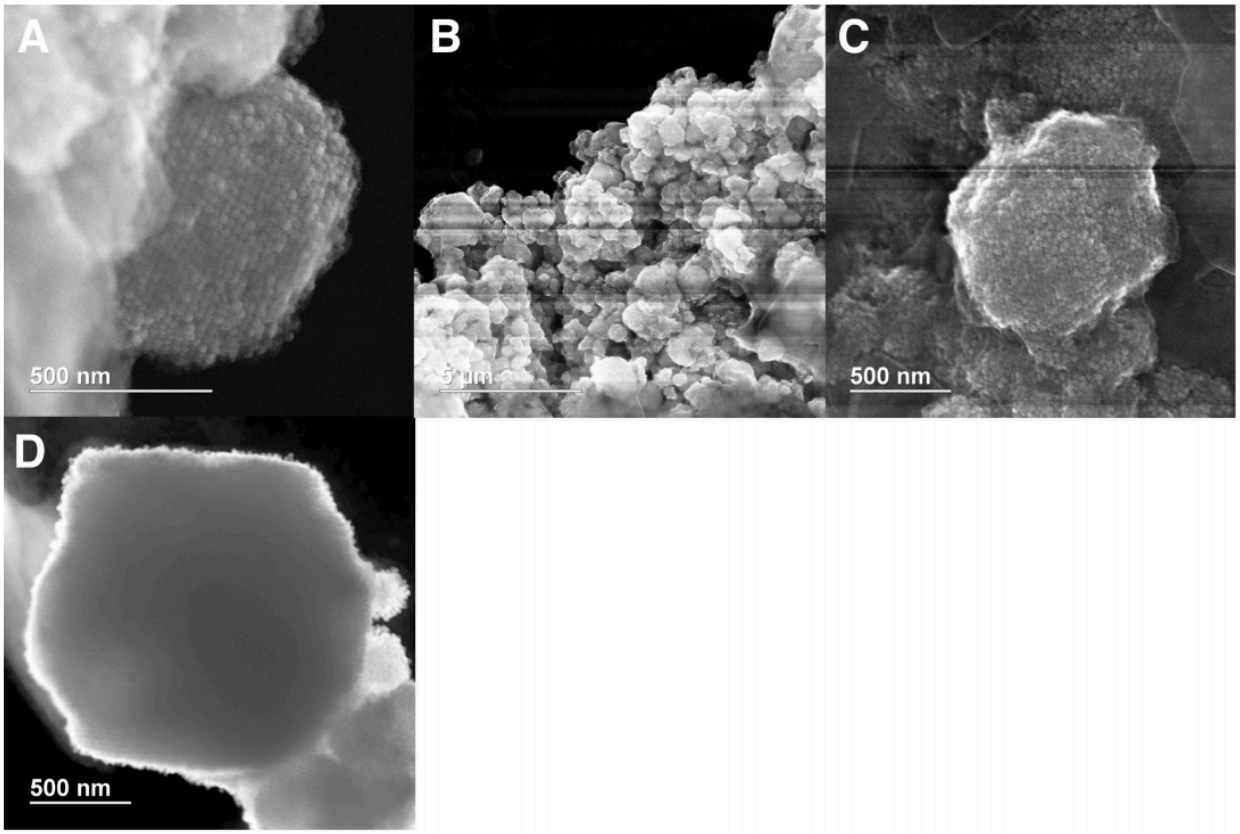

Figure 129. Additional STEM images of silica-encapsulated BCC superlattices of 30 nm spherical nanoparticles previously suspended in 80% EtOH and 20% H2O at 0.3 M NaCl. Top images were obtained in scanning mode, while bottom images were obtained in transmission mode.

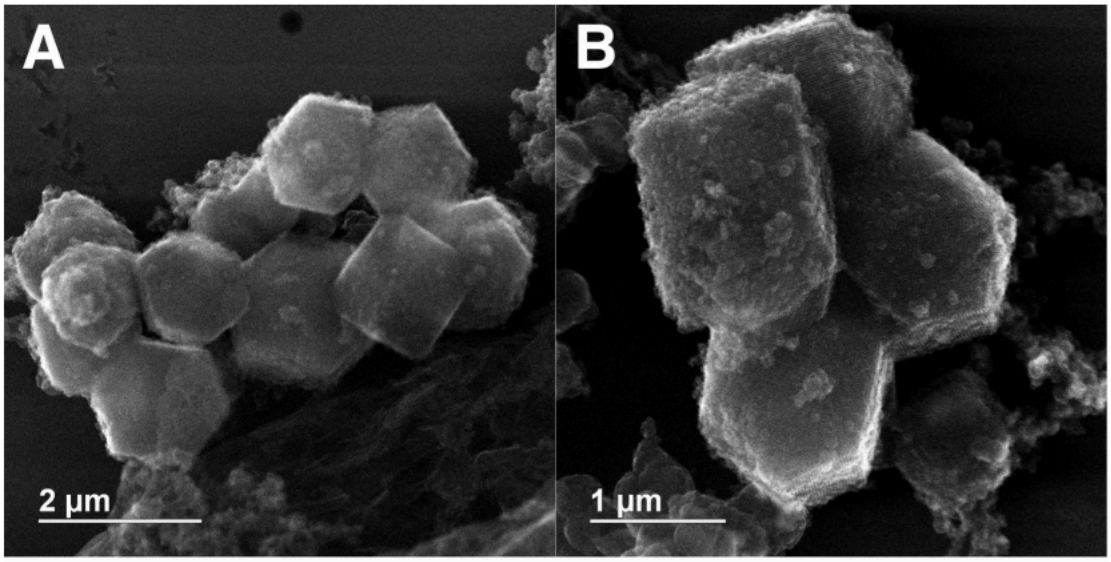

Figure 131. Additional STEM images of silica-encapsulated BCC superlattices of 15 nm spherical nanoparticles previously suspended in 100% H2O at 0.3 M NaCl. Images were obtained in scanning mode.

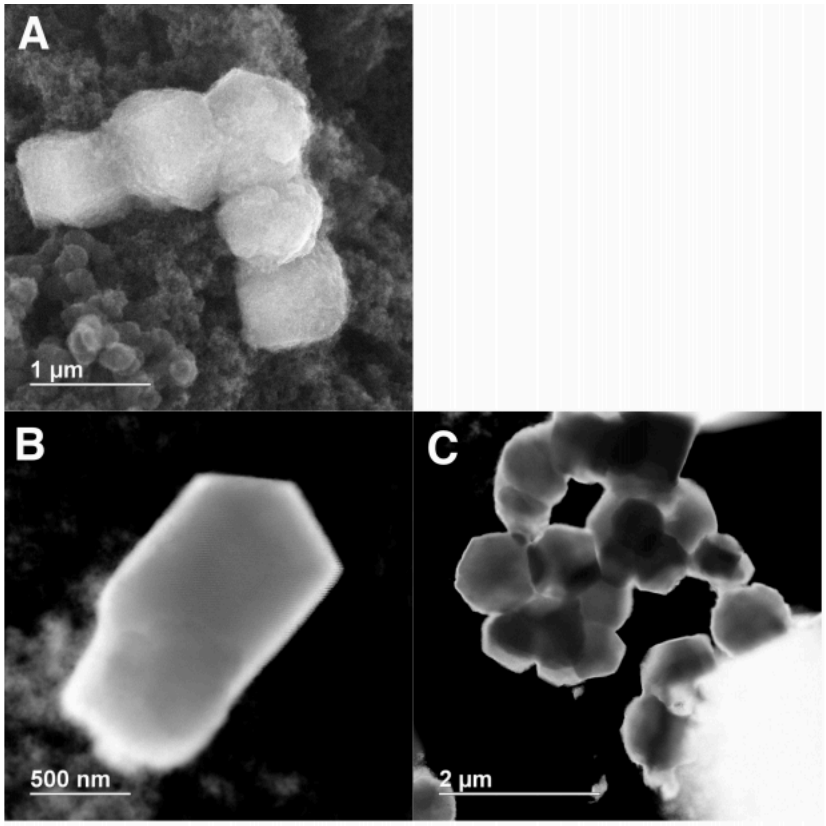

Figure 130. Additional STEM images of silica-encapsulated BCC superlattices of 15 nm spherical nanoparticles previously suspended in 45% EtOH and 55% H2O at 0.3 M NaCl. Top images were obtained in scanning mode, while bottom images were obtained in transmission mode.

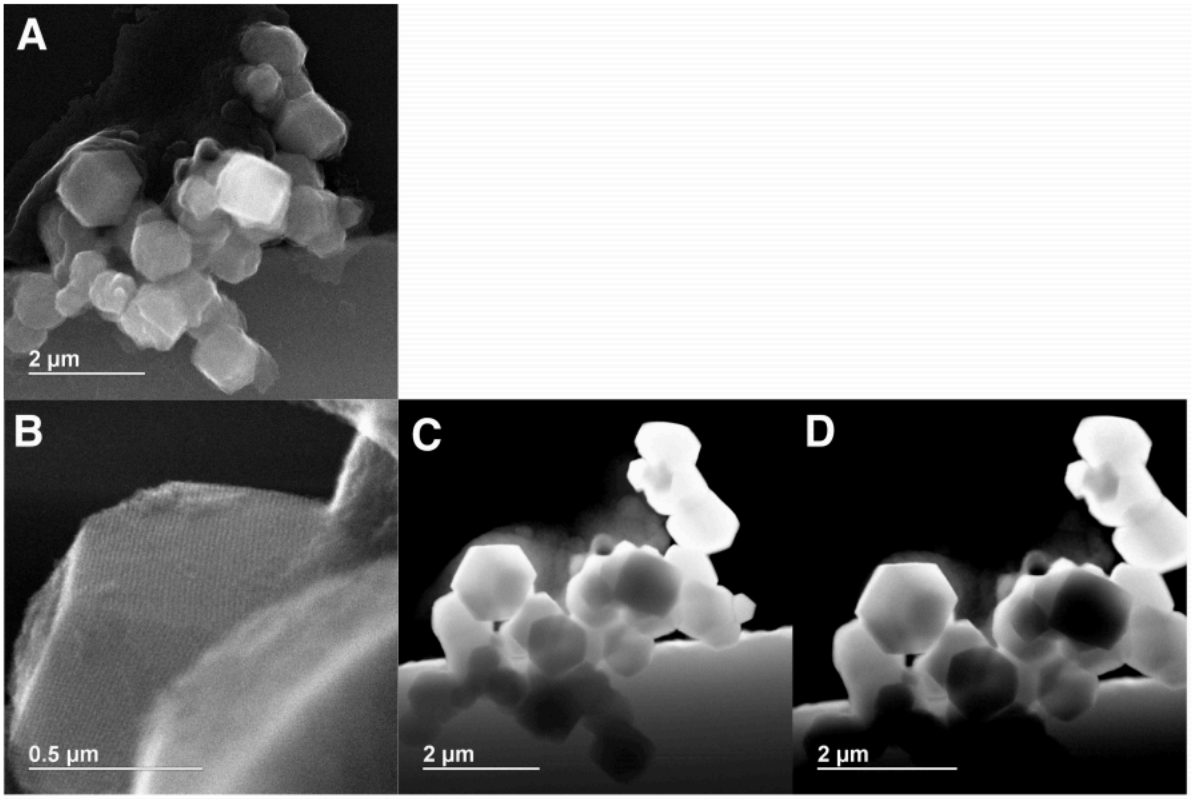

Figure 132. Additional STEM images of silica-encapsulated BCC superlattices of 15 nm spherical nanoparticles previously suspended in 80% EtOH and 20% H2O at 0.3 M NaCl. Top images were obtained in scanning mode, while bottom images were obtained in transmission mode.

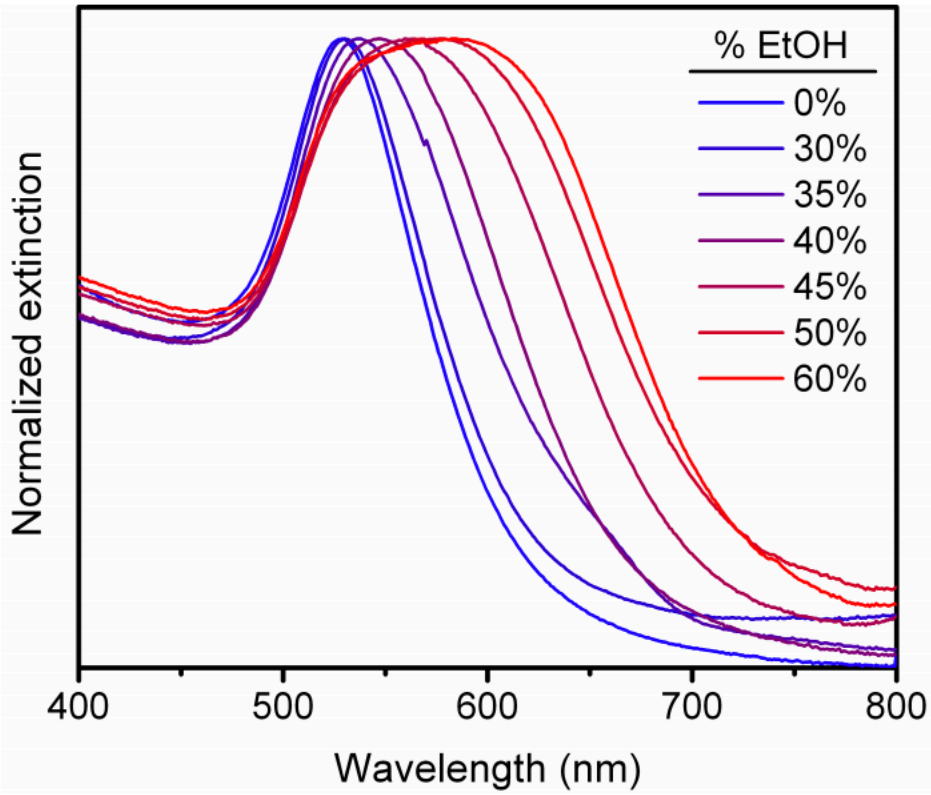

Figure 133. UV-vis spectra of 30 nm Au spheres functionalized with single-stranded DNA (sequence corresponds to the "B" anchor strand in Table S2) at different volume percentages of EtOH in H2O at a constant 0.3 M NaCl. As the EtOH percentage is increased, the localized surface plasmon resonance (LSPR) shifts to higher wavelengths and broadens, which is indicative of particle agglomeration. Note that all spectra were normalized to the maximum intensity of the LSPR.

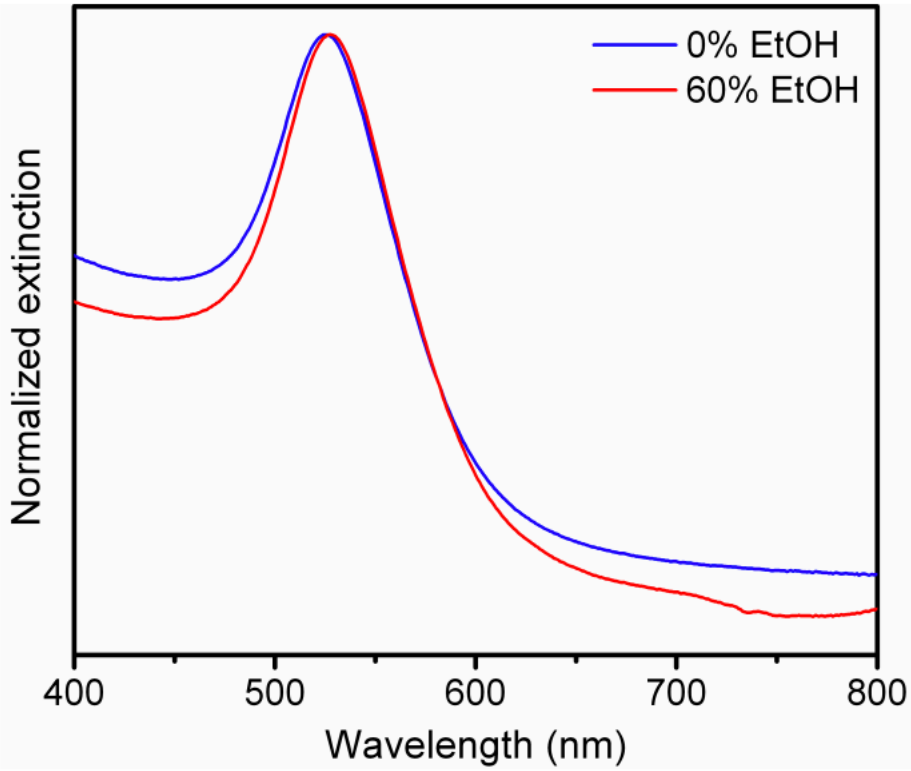

Figure 134. UV-vis spectra of citrate-capped 30 nm Au spheres suspended in H2O (blue) or 60% EtOH and 40% H2O (red). As expected, the position and width of the LSPR are not significantly affected by the change in solvent dielectric constant. Note that the spectra were normalized to the maximum intensity of the LSPR.

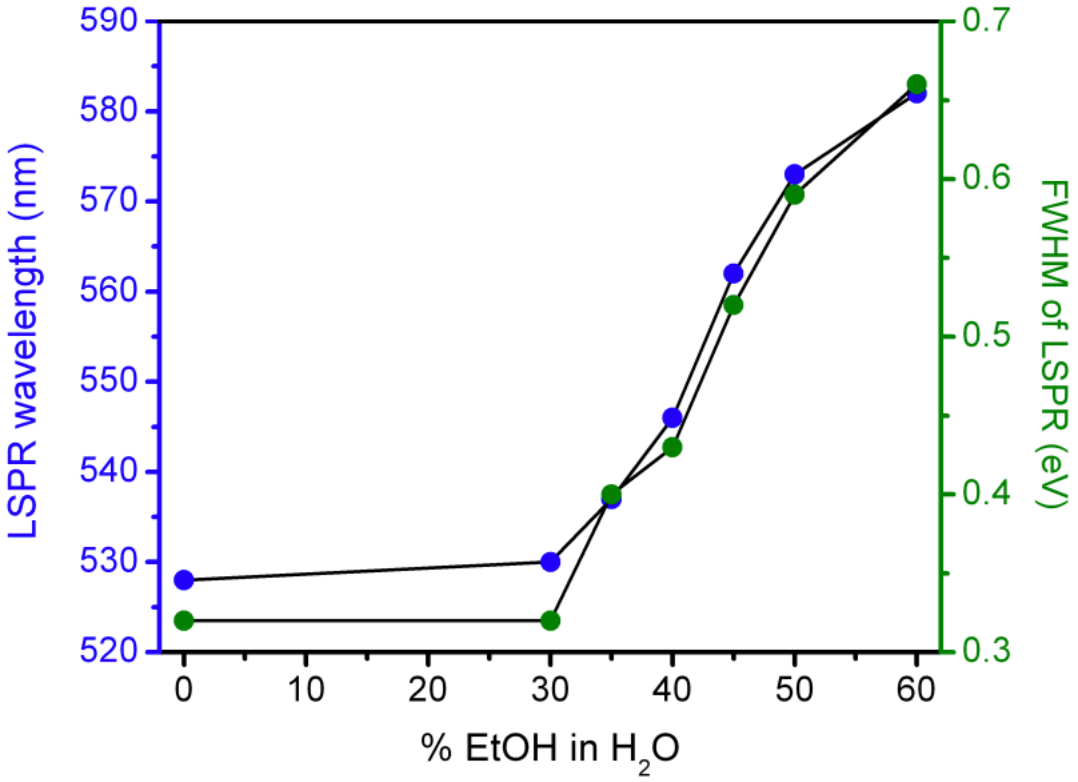

Figure 135. Wavelength (blue) and full width at half maximum (FWHM, green) of the LSPR of 30 nm Au spheres functionalized with single-stranded DNA (sequence corresponds to the "B" anchor strand in Table S2) at different volume percentages of EtOH in H2O at a constant 0.3 M NaCl. The red-shift and peak broadening of the LSPR is indicative of a transition from suspended nanoparticles to agglomerated nanoparticles at 30-60% EtOH.

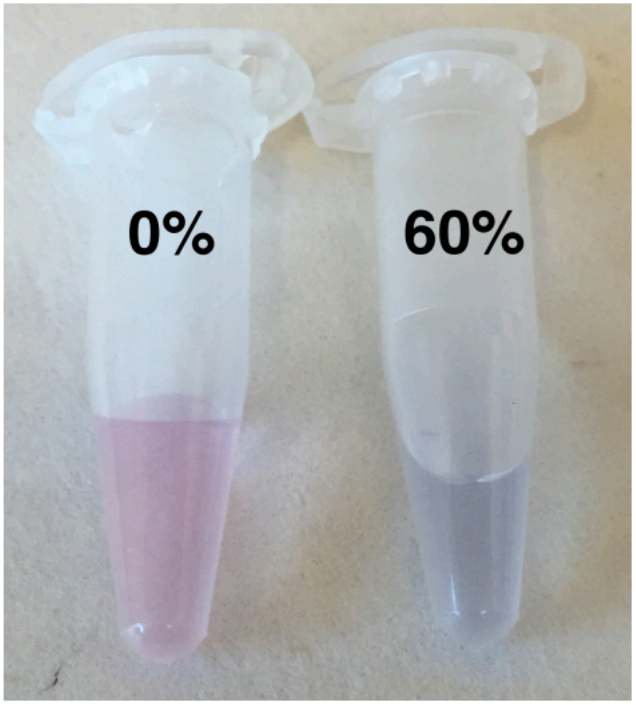

Figure 136. Images of 30 nm Au spheres functionalized with single-stranded DNA (sequence corresponds to the "B" anchor strand in Table S2) at 0% or 60% of EtOH in H2O at a constant 0.3 M NaCl. The change in color is consistent with the red-shift and peak broadening of the nanoparticle LSPR observed by UV-vis at 60% EtOH and is indicative of particle agglomeration.

REFERENCES

1. Auyeung, E.; Li, T. I.; Senesi, A. J.; Schmucker, A. L.; Pals, B. C.; de la Cruz, M. O.; Mirkin, C. A. *Nature* **2014,** *505*, 73-7.
2. Nykypanchuk, D.; Maye, M. M.; van der Lelie, D.; Gang, O. *Nature* **2008,** *451*, 549-552.
3. Park, S. Y.; Lytton-Jean, A. K. R.; Lee, B.; Weigand, S.; Schatz, G. C.; Mirkin, C. A. *Nature* **2008,** *451*, 553-556.
4. Niu, W.; Zhang, L.; Xu, G. *ACS Nano* **2010,** *4*, 1987-1996.
5. Wyman, J. *J. Am. Chem. Soc.* **1931,** *53*, 3292-3301.
6. O'Brien, M. N.; Lin, H.-X.; Girard, M.; Olvera de la Cruz, M.; Mirkin, C. A. *J. Am. Chem. Soc.* **2016,** *138*, 14562-14565.
7. Laramy, C. R.; Brown, K. A.; O'Brien, M. N.; Mirkin, C. A. *ACS Nano* **2015,** *9*, 12488-12495.
8. O'Brien, M. N.; Girard, M.; Lin, H.-X.; Millan, J. A.; Olvera de la Cruz, M.; Lee, B.; Mirkin, C. A. *Proc. Natl. Acad. Sci. U.S.A.* **2016,** *113*, 10485-10490.
9. Macfarlane, R. J.; Lee, B.; Jones, M. R.; Harris, N.; Schatz, G. C.; Mirkin, C. A. *Science* **2011,** *334*, 204-208.
10. Ducrot, E.; He, M.; Yi, G.-R.; Pine, D. J. *Nat. Mater.* **2017,** *16*, 652-657.
11. Wang, M. X.; Seo, S. E.; Gabrys, P. A.; Fleischman, D.; Lee, B.; Kim, Y.; Atwater, H. A.; Macfarlane, R. J.; Mirkin, C. A. *ACS Nano* **2017,** *11*, 180-185.
12. O'Brien, M. N.; Jones, M. R.; Brown, K. A.; Mirkin, C. A. *J. Am. Chem. Soc.* **2014,** *136*, 7603-6.
13. McMillan, J. R.; Mirkin, C. A. *J. Am. Chem. Soc.* **2018,** *140*, 6776-6779.
14. Cigler, P.; Lytton-Jean, A. K. R.; Anderson, D. G.; Finn, M. G.; Park, S. Y. *Nat. Mater.* **2010,** *9*, 918.
15. Liu, W.; Tagawa, M.; Xin, H. L.; Wang, T.; Emamy, H.; Li, H.; Yager, K. G.; Starr, F. W.; Tkachenko, A. V.; Gang, O. *Science* **2016,** *351*, 582-586.
16. Schrodinger, L., The PyMOL Molecular Graphics System, Version 1.8. 2015.
17. Auyeung, E.; Cutler, J. I.; Macfarlane, R. J.; Jones, M. R.; Wu, J.; Liu, G.; Zhang, K.; Osberg, K. D.; Mirkin, C. A. *Nat. Nanotechnol.* **2012,** *7*, 24-28.
18. Macfarlane, R. J.; Jones, M. R.; Lee, B.; Auyeung, E.; Mirkin, C. A. *Science* **2013,** *341*, 1222-1225.
19. Wang, Y.; Jenkins, I. C.; McGinley, J. T.; Sinno, T.; Crocker, J. C. *Nat. Commun.* **2017,** *8*, 14173.
20. Casey, M. T.; Scarlett, R. T.; Benjamin Rogers, W.; Jenkins, I.; Sinno, T.; Crocker, J. C. *Nat. Commun.* **2012,** *3*, 1209.
21. Thaner, R. V.; Eryazici, I.; Macfarlane, R. J.; Brown, K. A.; Lee, B.; Nguyen, S. T.; Mirkin, C. A. *J. Am. Chem. Soc.* **2016,** *138*, 6119-6122.
22. Jones, M. R.; Macfarlane, R. J.; Lee, B.; Zhang, J.; Young, K. L.; Senesi, A. J.; Mirkin, C. A. *Nat. Mater.* **2010,** *9*, 913-917.
23. Jones, M. R.; Kohlstedt, K. L.; O'Brien, M. N.; Wu, J.; Schatz, G. C.; Mirkin, C. A. *Nano Lett.* **2017,** *17*, 5830-5835.

24. Senesi, A. J.; Eichelsdoerfer, D. J.; Brown, K. A.; Lee, B.; Auyeung, E.; Choi, C. H. J.; Macfarlane, R. J.; Young, K. L.; Mirkin, C. A. *Adv. Mater.* **2014,** *26*, 7235-7240.
25. O'Brien, M. N.; Jones, M. R.; Lee, B.; Mirkin, C. A. *Nat. Mater.* **2015,** *14*, 833-839.
26. Lin, H.; Lee, S.; Sun, L.; Spellings, M.; Engel, M.; Glotzer, S. C.; Mirkin, C. A. *Science* **2017,** *355*, 931-935.
27. Lu, F.; Yager, K. G.; Zhang, Y.; Xin, H.; Gang, O. *Nat. Commun.* **2015,** *6*, 6912.
28. Hayes, O. G.; McMillan, J. R.; Lee, B.; Mirkin, C. A. *J. Am. Chem. Soc.* **2018**.
29. McMillan, J. R.; Brodin, J. D.; Millan, J. A.; Lee, B.; Olvera de la Cruz, M.; Mirkin, C. A. *J. Am. Chem. Soc.* **2017,** *139*, 1754-1757.
30. Brodin, J. D.; Auyeung, E.; Mirkin, C. A. *Proc. Natl. Acad. Sci. U.S.A.* **2015,** *112*, 4564-4569.
31. Phillips, R. B.; Kondev, J.; Theriot, J.; Orme, N.; Garcia, H., *Physical biology of the cell*. Garland Science: 2009.
32. Watson, J. D.; Crick, F. H. C. *Nature* **1953,** *171*, 737-738.
33. Franklin, R. E.; Gosling, R. G. *Nature* **1953,** *171*, 740-741.
34. Letsinger, R. L.; Mahadevan, V. *J. Am. Chem. Soc.* **1965,** *87*, 3526-3527.
35. Chen, J.; Seeman, N. C. *Nature* **1991,** *350*, 631-633.
36. Mirkin, C. A., Letsinger, L., Mucic, R.C., Storhoff, J.J. *Nature* **1996,** *382*, 607-609.
37. Alivisatos, A. P.; Johnsson, K. P.; Peng, X.; Wilson, T. E.; Loweth, C. J.; Bruchez, M. P.; Schultz, P. G. *Nature* **1996,** *382*, 609-611.
38. Winfree, E.; Liu, F.; Wenzler, L. A.; Seeman, N. C. *Nature* **1998,** *394*, 539-544.
39. Zheng, J.; Birktoft, J. J.; Chen, Y.; Wang, T.; Sha, R.; Constantinou, P. E.; Ginell, S. L.; Mao, C.; Seeman, N. C. *Nature* **2009,** *461*, 74.
40. Li, X.; Yang, X.; Qi, J.; Seeman, N. C. *J. Am. Chem. Soc.* **1996,** *118*, 6131-6140.
41. Seeman, N. C., Structural DNA Nanotechnology. In *NanoBiotechnology Protocols*, Rosenthal, S. J.; Wright, D. W., Eds. Humana Press: Totowa, NJ, 2005; pp 143-166.
42. Seeman, N. C. *Annu. Rev. Biochem* **2010,** *79*, 65-87.
43. Seeman, N. C.; Sleiman, H. F. *Nat. Rev. Mater.* **2017,** *3*, 17068.
44. Rothemund, P. W. K. *Nature* **2006,** *440*, 297-302.
45. Veneziano, R.; Ratanalert, S.; Zhang, K.; Zhang, F.; Yan, H.; Chiu, W.; Bathe, M. *Science* **2016,** *352*, 1534-1534.
46. Aldaye, F. A.; Palmer, A. L.; Sleiman, H. F. *Science* **2008,** *321*, 1795-1799.
47. Jones, M. R.; Seeman, N. C.; Mirkin, C. A. *Science* **2015,** *347*.
48. Cutler, J. I.; Auyeung, E.; Mirkin, C. A. *J. Am. Chem. Soc.* **2012,** *134*, 1376-91.
49. Choi, C. L.; Alivisatos, A. P. *Annu. Rev. Phys. Chem.* **2010,** *61*, 369-389.
50. Mertz, J. E.; Davis, R. W. *Proc. Natl. Acad. Sci. U.S.A.* **1972,** *69*, 3370-3374.
51. Lodish, H. F., *Molecular cell biology*. Eighth edition. ed.; New York : W.H. Freeman-Macmillan Learning: New York, 2016.
52. O'Brien, M. N.; Jones, M. R.; Mirkin, C. A. *Proc. Natl. Acad. Sci. U.S.A.* **2016,** *113*, 11717-11725.
53. Li, T.; Senesi, A. J.; Lee, B. *Chem. Rev.* **2016,** *116*, 11128-11180.
54. Leunissen, M. E.; Dreyfus, R.; Sha, R.; Seeman, N. C.; Chaikin, P. M. *J. Am. Chem. Soc.* **2010,** *132*, 1903-1913.
55. Silvera Batista, C. A.; Larson, R. G.; Kotov, N. A. *Science* **2015,** *350*.

56. Rogers, W. B.; Shih, W. M.; Manoharan, V. N. *Nat. Rev. Mater.* **2016,** *1*, 16008.
57. Girard, M.; Millan, J. A.; Cruz, M. O. d. l. *Annu. Rev. Mater. Res.* **2017,** *47*, null.
58. Velev, O. D. *Science* **2006,** *312*, 376-377.
59. Hagan, M. F.; Elrad, O. M.; Jack, R. L. *J. Chem. Phys.* **2011,** *135*, 104115.
60. Dobson, C. M. *Nature* **2003,** *426*, 884.
61. Mammen, M.; Choi, S.-K.; Whitesides, G. M. *Angew. Chem. Int. Ed.* **1998,** *37*, 2754-2794.
62. Bishop, K. J.; Wilmer, C. E.; Soh, S.; Grzybowski, B. A. *Small* **2009,** *5*, 1600-30.
63. Philp, D.; Stoddart, J. F. *Angew. Chem. Int. Ed.* **1996,** *35*, 1154-1196.
64. Rogers, W. B.; Crocker, J. C. *Proc. Natl. Acad. Sci. U.S.A.* **2011,** *108*, 15687-15692.
65. Boles, M. A.; Engel, M.; Talapin, D. V. *Chem. Rev.* **2016,** *116*, 11220-11289.
66. Mergny, J.-L., Lacroix, Laurent. *Oligonucleotides* **2003,** *13*, 515-537.
67. Breslauer, K. J.; Frank, R.; Blöcker, H.; Marky, L. A. *Proc. Natl. Acad. Sci. U.S.A.* **1986,** *83*, 3746-3750.
68. Storhoff, J. J.; Lazarides, A. A.; Mucic, R. C.; Mirkin, C. A.; Letsinger, R. L.; Schatz, G. C. *J. Am. Chem. Soc.* **2000,** *122*, 4640-4650.
69. Li, T. I.; Sknepnek, R.; Macfarlane, R. J.; Mirkin, C. A.; de la Cruz, M. O. *Nano Lett.* **2012,** *12*, 2509-14.
70. Angioletti-Uberti, S.; Mognetti, B. M.; Frenkel, D. *Nat. Mater.* **2012,** *11*, 518-522.
71. Li, T. I. N. G.; Sknepnek, R.; Olvera de la Cruz, M. *J. Am. Chem. Soc.* **2013,** *135*, 8535-8541.
72. Jin, R.; Wu, G.; Li, Z.; Mirkin, C. A.; Schatz, G. C. *J. Am. Chem. Soc.* **2003,** *125*, 1643-1654.
73. Valignat, M.-P.; Theodoly, O.; Crocker, J. C.; Russel, W. B.; Chaikin, P. M. *Proc. Natl. Acad. Sci. U.S.A.* **2005,** *102*, 4225-4229.
74. Park, S. Y.; Gibbs-Davis, J. M.; Nguyen, S. T.; Schatz, G. C. *J. Phys. Chem. B* **2007,** *111*, 8785-8791.
75. Callister, W. D., *Materials Science and Engineering: An Introduction*. 7 ed.; John Wiley & Sons Canada, Limited: 2007.
76. Mladek, B. M.; Fornleitner, J.; Martinez-Veracoechea, F. J.; Dawid, A.; Frenkel, D. *Phys. Rev. Lett.* **2012,** *108*, 268301.
77. Knorowski, C.; Travesset, A. *Soft Matter* **2012,** *8*, 12053-12059.
78. Lukatsky, D. B.; Frenkel, D. *Phys. Rev. Lett.* **2004,** *92*, 068302.
79. Dreyfus, R.; Leunissen, M. E.; Sha, R.; Tkachenko, A. V.; Seeman, N. C.; Pine, D. J.; Chaikin, P. M. *Phys. Rev. Lett.* **2009,** *102*, 048301.
80. Park, D. J.; Zhang, C.; Ku, J. C.; Zhou, Y.; Schatz, G. C.; Mirkin, C. A. *Proc. Natl. Acad. Sci. U.S.A.* **2015,** *112*, 977-981.
81. Park, D. J.; Ku, J. C.; Sun, L.; Lethiec, C. M.; Stern, N. P.; Schatz, G. C.; Mirkin, C. A. *Proc. Natl. Acad. Sci. U.S.A.* **2017,** *114*, 457-461.
82. Sun, L.; Lin, H.; Kohlstedt, K. L.; Schatz, G. C.; Mirkin, C. A. *Proc. Natl. Acad. Sci. U.S.A.* **2018**.
83. Milner, S. T. *Science* **1991,** *251*, 905-914.
84. Parak, W. J.; Pellegrino, T.; Micheel, C. M.; Gerion, D.; Williams, S. C.; Alivisatos, A. P. *Nano Lett.* **2003,** *3*, 33-36.

85. Love, J. C.; Estroff, L. A.; Kriebel, J. K.; Nuzzo, R. G.; Whitesides, G. M. *Chem. Rev.* **2005,** *105*, 1103-1170.
86. Fong, L.-K.; Wang, Z.; Schatz, G. C.; Luijten, E.; Mirkin, C. A. *J. Am. Chem. Soc.* **2018,** *140*, 6226-6230.
87. Elghanian, R., Storhoff, James J., Mucic, Robert, C., Letsinger, Robert L., Mirkin, Chad A. *Science* **1997,** *277*, 1078-1081.
88. Hurst, S. J.; Lytton-Jean, A. K. R.; Mirkin, C. A. *Anal. Chem.* **2006,** *78*, 8313-8318.
89. Biancaniello, P. L.; Kim, A. J.; Crocker, J. C. *Phys. Rev. Lett.* **2005,** *94*, 058302.
90. Schade, N. B.; Holmes-Cerfon, M. C.; Chen, E. R.; Aronzon, D.; Collins, J. W.; Fan, J. A.; Capasso, F.; Manoharan, V. N. *Phys. Rev. Lett.* **2013,** *110*, 148303.
91. Mognetti, B. M.; Leunissen, M. E.; Frenkel, D. *Soft Matter* **2012,** *8*, 2213-2221.
92. Dreyfus, R.; Leunissen, M. E.; Sha, R.; Tkachenko, A.; Seeman, N. C.; Pine, D. J.; Chaikin, P. M. *Phys. Rev. E* **2010,** *81*, 041404.
93. Wang, Y.; Wang, Y.; Zheng, X.; Ducrot, É.; Yodh, J. S.; Weck, M.; Pine, D. J. *Nat. Commun.* **2015,** *6*, 7253.
94. Wang, Y.; Wang, Y.; Zheng, X.; Ducrot, É.; Lee, M.-G.; Yi, G.-R.; Weck, M.; Pine, D. J. *J. Am. Chem. Soc.* **2015,** *137*, 10760-10766.
95. van der Meulen, S. A. J.; Leunissen, M. E. *J. Am. Chem. Soc.* **2013,** *135*, 15129-15134.
96. Thaner, R. V.; Kim, Y.; Li, T. I. N. G.; Macfarlane, R. J.; Nguyen, S. T.; Olvera de la Cruz, M.; Mirkin, C. A. *Nano Lett.* **2015,** *15*, 5545-5551.
97. Kuriyan, J.; Konforti, B.; Wemmer, D., *The molecules of life : physical and chemical principles*. Garland Science, Taylor & Francis Group: New York, 2013; Vol. 1.
98. Tinland, B.; Pluen, A.; Sturm, J.; Weill, G. *Macromolecules* **1997,** *30*, 5763-5765.
99. Marko, J. F.; Cocco, S. *Phys. World* **2003,** *16*, 37.
100. Maye, M. M.; Nykypanchuk, D.; van der Lelie, D.; Gang, O. *J. Am. Chem. Soc.* **2006,** *128*, 14020-14021.
101. Whitesides, G. M.; Grzybowski, B. *Science* **2002,** *295*, 2418-2421.
102. Li, T. I. N. G.; Sknepnek, R.; Macfarlane, R. J.; Mirkin, C. A.; Olvera de la Cruz, M. *Nano Lett.* **2012,** *12*, 2509-2514.
103. Srinivasan, B.; Vo, T.; Zhang, Y.; Gang, O.; Kumar, S.; Venkatasubramanian, V. *Proc. Natl. Acad. Sci. U.S.A.* **2013,** *110*, 18431-18435.
104. Martinez-Veracoechea, F. J.; Mladek, B. M.; Tkachenko, A. V.; Frenkel, D. *Phys. Rev. Lett.* **2011,** *107*, 045902.
105. Gang, O.; Tkachenko, A. V. *MRS Bulletin* **2016,** *41*, 381-387.
106. Horst, N.; Travesset, A. *J. Chem. Phys.* **2016,** *144*, 014502.
107. Boles, M. A.; Talapin, D. V. *J. Am. Chem. Soc.* **2015,** *137*, 4494-4502.
108. Kiely, C. J.; Fink, J.; Brust, M.; Bethell, D.; Schiffrin, D. J. *Nature* **1998,** *396*, 444.
109. Kalsin, A. M.; Fialkowski, M.; Paszewski, M.; Smoukov, S. K.; Bishop, K. J. M.; Grzybowski, B. A. *Science* **2006,** *312*, 420-424.
110. Talapin, D. V.; Shevchenko, E. V. *Chem. Rev.* **2016,** *116*, 10343-10345.
111. Zhang, Y.; Pal, S.; Srinivasan, B.; Vo, T.; Kumar, S.; Gang, O. *Nat. Mater.* **2015,** *14*, 840-847.
112. Wang, M. X.; Brodin, J. D.; Millan, J. A.; Seo, S. E.; Girard, M.; Olvera de la Cruz, M.; Lee, B.; Mirkin, C. A. *Nano Lett.* **2017,** *17*, 5126-5132.

113. Seo, S. E.; Li, T.; Senesi, A. J.; Mirkin, C. A.; Lee, B. *J. Am. Chem. Soc.* **2017,** *139*, 16528-16535.
114. Markov, I. V., *Crystal growth for beginners : fundamentals of nucleation, crystal growth and epitaxy*. 2nd ed.. ed.; Singapore ; River Edge, N.J. : World Scientific: Singapore ; River Edge, N.J., 2003.
115. Mackenzie, J. K.; Moore, A. J. W.; Nicholas, J. F. *J. Phys. Chem. Solids* **1962,** *23*, 185-196.
116. Jones, M. R.; Macfarlane, R. J.; Prigodich, A. E.; Patel, P. C.; Mirkin, C. A. *J. Am. Chem. Soc.* **2011,** *133*, 18865-18869.
117. Jones, M. R.; Seeman, N. C.; Mirkin, C. A. *Science* **2015,** *347*, 1260901.
118. Damasceno, P. F.; Engel, M.; Glotzer, S. C. *Science* **2012,** *337*, 453-457.
119. Tao, A. R.; Habas, S.; Yang, P. *Small* **2008,** *4*, 310-325.
120. Personick, M. L.; Mirkin, C. A. *J. Am. Chem. Soc.* **2013,** *135*, 18238-47.
121. Lohse, S. E.; Burrows, N. D.; Scarabelli, L.; Liz-Marzán, L. M.; Murphy, C. J. *Chem. Mater.* **2014,** *26*, 34-43.
122. Xia, Y.; Gilroy, K. D.; Peng, H.-C.; Xia, X. *Angew. Chem. Int. Ed.* **2017,** *56*, 60-95.
123. Manoharan, V. N.; Elsesser, M. T.; Pine, D. J. *Science* **2003,** *301*, 483.
124. Sacanna, S.; Pine, D. J. *Curr. Opin. Colloid Interface Sci* **2011,** *16*, 96-105.
125. Walther, A.; Müller, A. H. E. *Chem. Rev.* **2013,** *113*, 5194-5261.
126. Gi-Ra, Y.; David, J. P.; Stefano, S. *J. Phys. Condens. Matter.* **2013,** *25*, 193101.
127. Wang, Y.; Wang, Y.; Breed, D. R.; Manoharan, V. N.; Feng, L.; Hollingsworth, A. D.; Weck, M.; Pine, D. J. *Nature* **2012,** *491*, 51-55.
128. Porter, C. L.; Crocker, J. C. *Curr. Opin. Colloid Interface Sci* **2017,** *30*, 34-44.
129. Dorsaz, N.; Filion, L.; Smallenburg, F.; Frenkel, D. *Faraday Discuss.* **2012,** *159*, 9-21.
130. Bianchi, E.; Doppelbauer, G.; Filion, L.; Dijkstra, M.; Kahl, G. *J. Chem. Phys.* **2012,** *136*, 214102.
131. Mao, X.; Chen, Q.; Granick, S. *Nat. Mater.* **2013,** *12*, 217.
132. van Anders, G.; Ahmed, N. K.; Smith, R.; Engel, M.; Glotzer, S. C. *ACS Nano* **2014,** *8*, 931-940.
133. Morphew, D.; Shaw, J.; Avins, C.; Chakrabarti, D. *ACS Nano* **2018,** *12*, 2355-2364.
134. Milliron, D. J.; Hughes, S. M.; Cui, Y.; Manna, L.; Li, J.; Wang, L.-W.; Paul Alivisatos, A. *Nature* **2004,** *430*, 190-195.
135. DeVries, G. A.; Brunnbauer, M.; Hu, Y.; Jackson, A. M.; Long, B.; Neltner, B. T.; Uzun, O.; Wunsch, B. H.; Stellacci, F. *Science* **2007,** *315*, 358-361.
136. DeSantis, C. J.; Sue, A. C.; Bower, M. M.; Skrabalak, S. E. *ACS Nano* **2012,** *6*, 2617-2628.
137. Kwon, S. G.; Krylova, G.; Phillips, P. J.; Klie, R. F.; Chattopadhyay, S.; Shibata, T.; Bunel, E. E.; Liu, Y.; Prakapenka, V. B.; Lee, B.; Shevchenko, E. V. *Nat. Mater.* **2015,** *14*, 215-223.
138. Li, H.; Zhang, B.; Lu, X.; Tan, X.; Jia, F.; Xiao, Y.; Cheng, Z.; Li, Y.; Silva, D. O.; Schrekker, H. S.; Zhang, K.; Mirkin, C. A. *Proc. Natl. Acad. Sci. U.S.A.* **2018,** *115*, 4340-4344.
139. Kashiwagi, D.; Sim, S.; Niwa, T.; Taguchi, H.; Aida, T. *J. Am. Chem. Soc.* **2018,** *140*, 26-29.
140. Huo, F.; Lytton-Jean, A. K. R.; Mirkin, C. A. *Adv. Mater.* **2006,** *18*, 2304-2306.
141. Xu, X.; Rosi, N. L.; Wang, Y.; Huo, F.; Mirkin, C. A. *J. Am. Chem. Soc.* **2006,** *128*, 9286-9287.

142. Maye, M. M.; Nykypanchuk, D.; Cuisinier, M.; van der Lelie, D.; Gang, O. *Nat. Mater.* **2009,** *8*, 388-391.
143. Edwardson, T. G. W.; Lau, K. L.; Bousmail, D.; Serpell, C. J.; Sleiman, H. F. *Nat. Chem.* **2016,** *8*, 162-170.
144. Trinh, T.; Liao, C.; Toader, V.; Barłóg, M.; Bazzi, H. S.; Li, J.; Sleiman, H. F. *Nat. Chem.* **2017,** *10*, 184.
145. Feng, L.; Dreyfus, R.; Sha, R.; Seeman, N. C.; Chaikin, P. M. *Adv. Mater.* **2013,** *25*, 2779-2783.
146. Tian, Y.; Zhang, Y.; Wang, T.; Xin, H. L.; Li, H.; Gang, O. *Nat. Mater.* **2016,** *15*, 654-661.
147. Liu, W.; Halverson, J.; Tian, Y.; Tkachenko, A. V.; Gang, O. *Nat. Chem.* **2016,** *8*, 867-873.
148. Wang, T.; Schiffels, D.; Martinez Cuesta, S.; Kuchnir Fygenson, D.; Seeman, N. C. *J. Am. Chem. Soc.* **2012,** *134*, 1606-1616.
149. Seeman, N. C.; Gang, O. *MRS Bulletin* **2017,** *42*, 904-912.
150. Kannan, B.; Kulkarni, R. P.; Majumdar, A. *Nano Lett.* **2004,** *4*, 1521-1524.
151. Taton, T. A.; Mucic, R. C.; Mirkin, C. A.; Letsinger, R. L. *J. Am. Chem. Soc.* **2000,** *122*, 6305-6306.
152. Zou, B.; Ceyhan, B.; Simon, U.; Niemeyer, C. M. *Adv. Mater.* **2005,** *17*, 1643-1647.
153. Park, J.-U.; Lee, J. H.; Paik, U.; Lu, Y.; Rogers, J. A. *Nano Lett.* **2008,** *8*, 4210-4216.
154. Cheng, W.; Park, N.; Walter, M. T.; Hartman, M. R.; Luo, D. *Nat. Nanotechnol.* **2008,** *3*, 682.
155. Noh, H.; Choi, C.; Hung, A. M.; Jin, S.; Cha, J. N. *ACS Nano* **2010,** *4*, 5076-5080.
156. Lalander, C. H.; Zheng, Y.; Dhuey, S.; Cabrini, S.; Bach, U. *ACS Nano* **2010,** *4*, 6153-6161.
157. Senesi, A. J.; Eichelsdoerfer, D. J.; Macfarlane, R. J.; Jones, M. R.; Auyeung, E.; Lee, B.; Mirkin, C. A. *Angew. Chem. Int. Ed.* **2013,** *52*, 6624-6628.
158. Ku, J. C.; Ross, M. B.; Schatz, G. C.; Mirkin, C. A. *Adv. Mater.* **2015,** *27*, 3159-3163.
159. Bartelt, M. C.; Evans, J. W. *Phys. Rev. Lett.* **1995,** *75*, 4250-4253.
160. Hellstrom, S. L.; Kim, Y.; Fakonas, J. S.; Senesi, A. J.; Macfarlane, R. J.; Mirkin, C. A.; Atwater, H. A. *Nano Lett.* **2013,** *13*, 6084-6090.
161. Le, J. D.; Pinto, Y.; Seeman, N. C.; Musier-Forsyth, K.; Taton, T. A.; Kiehl, R. A. *Nano Lett.* **2004,** *4*, 2343-2347.
162. Zheng, J.; Constantinou, P. E.; Micheel, C.; Alivisatos, A. P.; Kiehl, R. A.; Seeman, N. C. *Nano Lett.* **2006,** *6*, 1502-1504.
163. Lin, Q.-Y.; Li, Z.; Brown, K. A.; O'Brien, M. N.; Ross, M. B.; Zhou, Y.; Butun, S.; Chen, P.-C.; Schatz, G. C.; Dravid, V. P.; Aydin, K.; Mirkin, C. A. *Nano Lett.* **2015,** *15*, 4699-4703.
164. Lin, Q.-Y.; Mason, J. A.; Li, Z.; Zhou, W.; O'Brien, M. N.; Brown, K. A.; Jones, M. R.; Butun, S.; Lee, B.; Dravid, V. P.; Aydin, K.; Mirkin, C. A. *Science* **2018**.
165. Lin, Q.-Y.; Palacios, E.; Zhou, W.; Li, Z.; Mason, J. A.; Liu, Z.; Lin, H.; Chen, P.-C.; Dravid, V. P.; Aydin, K.; Mirkin, C. A. *Nano Lett.* **2018,** *18*, 2645-2649.
166. O'Brien, M. N.; Radha, B.; Brown, K. A.; Jones, M. R.; Mirkin, C. A. *Angew. Chem. Int. Ed.* **2014,** *53*, 9532-8.
167. Dong, J.; Liu, J.; Kang, G.; Xie, J.; Wang, Y. *Sci Rep.* **2014,** *4*, 5618.

168. Lo, P. K.; Karam, P.; Aldaye, F. A.; McLaughlin, C. K.; Hamblin, G. D.; Cosa, G.; Sleiman, H. F. *Nat. Chem.* **2010,** *2*, 319.
169. Pinto, Y. Y.; Le, J. D.; Seeman, N. C.; Musier-Forsyth, K.; Taton, T. A.; Kiehl, R. A. *Nano Lett.* **2005,** *5*, 2399-2402.
170. Lan, X.; Lu, X.; Shen, C.; Ke, Y.; Ni, W.; Wang, Q. *J. Am. Chem. Soc.* **2015,** *137*, 457-462.
171. Aldaye, F. A.; Sleiman, H. F. *J. Am. Chem. Soc.* **2007,** *129*, 13376-13377.
172. He, Y.; Ye, T.; Su, M.; Zhang, C.; Ribbe, A. E.; Jiang, W.; Mao, C. *Nature* **2008,** *452*, 198.
173. Douglas, S. M.; Dietz, H.; Liedl, T.; Högberg, B.; Graf, F.; Shih, W. M. *Nature* **2009,** *459*, 414.
174. Kuzyk, A.; Schreiber, R.; Fan, Z.; Pardatscher, G.; Roller, E.-M.; Hogele, A.; Simmel, F. C.; Govorov, A. O.; Liedl, T. *Nature* **2012,** *483*, 311-314.
175. Cademartiri, L.; Bishop, K. J. M. *Nat. Mater.* **2014,** *14*, 2.
176. Yin, Y.; Alivisatos, A. P. *Nature* **2004,** *437*, 664.
177. Sebastian, P. *Adv. Funct. Mater.* **2011,** *21*, 3214-3230.
178. Bealing, C. R.; Baumgardner, W. J.; Choi, J. J.; Hanrath, T.; Hennig, R. G. *ACS Nano* **2012,** *6*, 2118-2127.
179. Ye, X.; Chen, J.; Engel, M.; Millan, J. A.; Li, W.; Qi, L.; Xing, G.; Collins, J. E.; Kagan, C. R.; Li, J.; Glotzer, S. C.; Murray, C. B. *Nat. Chem.* **2013,** *5*, 466-73.
180. Burrows, N. D.; Vartanian, A. M.; Abadeer, N. S.; Grzincic, E. M.; Jacob, L. M.; Lin, W.; Li, J.; Dennison, J. M.; Hinman, J. G.; Murphy, C. J. *J. Phys. Chem. Lett.* **2016,** *7*, 632-641.
181. Lee, J.-H.; Gibson, K. J.; Chen, G.; Weizmann, Y. *Nat. Commun.* **2015,** *6*, 7571.
182. Weiner, R. G.; DeSantis, C. J.; Cardoso, M. B. T.; Skrabalak, S. E. *ACS Nano* **2014,** *8*, 8625-8635.
183. O'Donoghue, P.; Ling, J.; Wang, Y.-S.; Söll, D. *Nat. Chem. Biol.* **2013,** *9*, 594.
184. Liu, C. C.; Schultz, P. G. *Annu. Rev. Biochem* **2010,** *79*, 413-444.
185. Ke, Y.; Ong, L. L.; Shih, W. M.; Yin, P. *Science* **2012,** *338*, 1177-1183.
186. Rothemund, P. W. K.; Andersen, E. S. *Nature* **2012,** *485*, 584.
187. Li, F.; Lu, J.; Kong, X.; Hyeon, T.; Ling, D. *Adv. Mater.* **2017,** *29*, 1605897-n/a.
188. Bell, A. T. *Science* **2003,** *299*, 1688-1691.
189. Talapin, D. V.; Lee, J.-S.; Kovalenko, M. V.; Shevchenko, E. V. *Chem. Rev.* **2010,** *110*, 389-458.
190. Galisteo‐López, J. F.; Ibisate, M.; Sapienza, R.; Froufe‐Pérez, L. S.; Blanco, Á.; López, C. *Adv. Mater.* **2011,** *23*, 30-69.
191. Campolongo, M. J.; Kahn, J. S.; Cheng, W.; Yang, D.; Gupton-Campolongo, T.; Luo, D. *J. Mater. Chem.* **2011,** *21*, 6113-6121.
192. Tan, S. J.; Campolongo, M. J.; Luo, D.; Cheng, W. *Nat. Nanotechnol.* **2011,** *6*, 268-276.
193. Bishop, K. J. M. *Angew. Chem. Int. Ed.* **2016,** *55*, 1598-1600.
194. Maye, M. M.; Kumara, M. T.; Nykypanchuk, D.; Sherman, W. B.; Gang, O. *Nat. Nanotechnol.* **2009,** *5*, 116.
195. Pal, S.; Zhang, Y.; Kumar, S. K.; Gang, O. *J. Am. Chem. Soc.* **2015,** *137*, 4030-4033.
196. Kim, Y.; Macfarlane, R. J.; Jones, M. R.; Mirkin, C. A. *Science* **2016,** *351*, 579-582.
197. Mason, J. A.; Laramy, C. R.; Lai, C.-T.; O'Brien, M. N.; Lin, Q.-Y.; Dravid, V. P.; Schatz, G. C.; Mirkin, C. A. *J. Am. Chem. Soc.* **2016,** *138*, 8722-8725.

198. Zhu, J.; Kim, Y.; Lin, H.; Wang, S.; Mirkin, C. A. *J. Am. Chem. Soc.* **2018,** *140*, 5061-5064.
199. Kim, Y.; Macfarlane, R. J.; Mirkin, C. A. *J. Am. Chem. Soc.* **2013,** *135*, 10342-10345.
200. Leunissen, M. E.; Dreyfus, R.; Cheong, F. C.; Grier, D. G.; Sha, R.; Seeman, N. C.; Chaikin, P. M. *Nat. Mater.* **2009,** *8*, 590.
201. Gehring, K.; Leroy, J.-L.; Guéron, M. *Nature* **1993,** *363*, 561.
202. Bowtell, D. D. L. *Anal. Biochem.* **1987,** *162*, 463-465.
203. Piškur, J.; Rupprecht, A. *FEBS Letters* **1995,** *375*, 174-178.
204. Zhang, C.; Macfarlane, R. J.; Young, K. L.; Choi, C. H. J.; Hao, L.; Auyeung, E.; Liu, G.; Zhou, X.; Mirkin, C. A. *Nat. Mater.* **2013,** *12*, 741-746.
205. Morris, W.; Briley, W. E.; Auyeung, E.; Cabezas, M. D.; Mirkin, C. A. *J. Am. Chem. Soc.* **2014,** *136*, 7261-7264.
206. Banga, R. J.; Chernyak, N.; Narayan, S. P.; Nguyen, S. T.; Mirkin, C. A. *J. Am. Chem. Soc.* **2014,** *136*, 9866-9869.
207. Wang, S.; McGuirk, C. M.; Ross, M. B.; Wang, S.; Chen, P.; Xing, H.; Liu, Y.; Mirkin, C. A. *J. Am. Chem. Soc.* **2017,** *139*, 9827-9830.
208. Shengshuang, Z.; Hang, X.; Pavlo, G.; Jungsoo, P.; A., M. C. *Adv. Mater.* **2018,** *30*, 1707113.
209. Halas, N. J.; Lal, S.; Chang, W.-S.; Link, S.; Nordlander, P. *Chem. Rev.* **2011,** *111*, 3913-3961.
210. Sargent, E. H. *Nat. Photonics* **2012,** *6*, 133.
211. Mostafa, S.; Behafarid, F.; Croy, J. R.; Ono, L. K.; Li, L.; Yang, J. C.; Frenkel, A. I.; Cuenya, B. R. *J. Am. Chem. Soc.* **2010,** *132*, 15714-15719.
212. Andoy, N. M.; Zhou, X.; Choudhary, E.; Shen, H.; Liu, G.; Chen, P. *J. Am. Chem. Soc.* **2013,** *135*, 1845-1852.
213. Hartland, G. V.; Besteiro, L. V.; Johns, P.; Govorov, A. O. *ACS Energy Lett.* **2017,** *2*, 1641-1653.
214. Yu, S.; Wilson, A. J.; Kumari, G.; Zhang, X.; Jain, P. K. *ACS Energy Lett.* **2017,** *2*, 2058-2070.
215. Singh, G.; Chan, H.; Baskin, A.; Gelman, E.; Repnin, N.; Král, P.; Klajn, R. *Science* **2014,** *345*, 1149-1153.
216. García-Torres, J.; Calero, C.; Sagués, F.; Pagonabarraga, I.; Tierno, P. *Nat. Commun.* **2018,** *9*, 1663.
217. Liu, J.; Postupalenko, V.; Lörcher, S.; Wu, D.; Chami, M.; Meier, W.; Palivan, C. G. *Nano Lett.* **2016,** *16*, 7128-7136.
218. Auyeung, E.; Morris, W.; Mondloch, J. E.; Hupp, J. T.; Farha, O. K.; Mirkin, C. A. *J. Am. Chem. Soc.* **2015,** *137*, 1658-1662.
219. Ross, M. B.; Ku, J. C.; Vaccarezza, V. M.; Schatz, G. C.; Mirkin, C. A. *Nat. Nanotechnol.* **2015,** *10*, 453-458.
220. Xiong, H.; Sfeir, M. Y.; Gang, O. *Nano Lett.* **2010,** *10*, 4456-4462.
221. Jain, P. K.; Huang, W.; El-Sayed, M. A. *Nano Lett.* **2007,** *7*, 2080-2088.
222. Ross, M. B.; Ku, J. C.; Lee, B.; Mirkin, C. A.; Schatz, G. C. *Adv. Mater.* **2016,** *28*, 2790-2794.

223. Zhang, Y.; Lu, F.; Yager, K. G.; van der Lelie, D.; Gang, O. *Nat. Nanotechnol.* **2013,** *8*, 865-872.
224. Ross, M. B.; Blaber, M. G.; Schatz, G. C. *Nat. Commun.* **2014,** *5*, 4090.
225. Wasilke, J.-C.; Obrey, S. J.; Baker, R. T.; Bazan, G. C. *Chem. Rev.* **2005,** *105*, 1001-1020.
226. Yamada, Y.; Tsung, C.-K.; Huang, W.; Huo, Z.; Habas, S. E.; Soejima, T.; Aliaga, C. E.; Somorjai, G. A.; Yang, P. *Nat. Chem.* **2011,** *3*, 372.
227. Lohr, T. L.; Marks, T. J. *Nat. Chem.* **2015,** *7*, 477.
228. Sun, L.; Lin, H.; Park, D. J.; Bourgeois, M. R.; Ross, M. B.; Ku, J. C.; Schatz, G. C.; Mirkin, C. A. *Nano Lett.* **2017,** *17*, 2313-2318.
229. Ross, M. B.; Mirkin, C. A.; Schatz, G. C. *J. Phys. Chem. C* **2016,** *120*, 816-830.
230. Arsenault, A.; Fournier-Bidoz, S.; Hatton, B.; Miguez, H.; Tetreault, N.; Vekris, E.; Wong, S.; Ming Yang, S.; Kitaev, V.; Ozin, G. A. *J. Mater. Chem.* **2004,** *14*, 781-794.
231. Richman, E. K., Hutchison, J.E. *ACS Nano* **2009,** *3*, 2441-2446.
232. Xia, Y.; Xiong, Y.; Lim, B.; Skrabalak, S. E. *Angew. Chem. Int. Ed.* **2009,** *48*, 60-103.
233. Sadik, O. A.; Du, N.; Kariuki, V.; Okello, V.; Bushlyar, V. *ACS Sustain. Chem. Eng.* **2014,** *2*, 1707-1716.
234. Burda, C.; Chen, X.; Narayanan, R.; El-Sayed, M. A. *Chem. Rev.* **2005,** *105*, 1025-1102.
235. Myroshnychenko, V.; Rodriguez-Fernandez, J.; Pastoriza-Santos, I.; Funston, A. M.; Novo, C.; Mulvaney, P.; Liz-Marzan, L. M.; Garcia de Abajo, F. J. *Chem. Soc. Rev.* **2008,** *37*, 1792-1805.
236. Orts-Gil, G.; Natte, K.; Drescher, D.; Bresch, H.; Mantion, A.; Kneipp, J.; Österle, W. *J. Nanopart. Res.* **2011,** *13*, 1593-1604.
237. Oliveri, A. F.; Elliott, E. W.; Carnes, M. E.; Hutchison, J. E.; Johnson, D. W. *ChemPhysChem* **2013,** *14*, 2655-2661.
238. Wuithschick, M.; Paul, B.; Bienert, R.; Sarfraz, A.; Vainio, U.; Sztucki, M.; Kraehnert, R.; Strasser, P.; Rademann, K.; Emmerling, F.; Polte, J. *Chem. Mater.* **2013,** *25*, 4679-4689.
239. Pal, A. K.; Aalaei, I.; Gadde, S.; Gaines, P.; Schmidt, D.; Demokritou, P.; Bello, D. *ACS Nano* **2014,** *8*, 9003-9015.
240. Loubat, A.; Lacroix, L.-M.; Robert, A.; Impéror-Clerc, M.; Poteau, R.; Maron, L.; Arenal, R.; Pansu, B.; Viau, G. *J. Phys. Chem. C* **2015,** *119*, 4422-4430.
241. McKenzie, L. C., Haben, P.M., Kevan, S.D., Hutchison, J.E. *J. Phys. Chem. C* **2010,** *114*, 22055-22063.
242. Murphy, C. J.; Sau, T. K.; Gole, A. M.; Orendorff, C. J.; Gao, J.; Gou, L.; Hunyadi, S. E.; Li, T. *J. Phys. Chem. B* **2005,** *109*, 13857-13870.
243. Wang, Z. L. *J. Phys. Chem. B* **2000,** *104*, 1153-1175.
244. Lofton, C.; Sigmund, W. *Adv. Funct. Mater.* **2005,** *15*, 1197-1208.
245. Elechiguerra, J. L.; Reyes-Gasga, J.; Yacaman, M. J. *J. Mater. Chem.* **2006,** *16*, 3906-3919.
246. Ye, X., Jin, L., Caglayan, H., Chen, J., Xing, G., Zheng, C., Doan-Nguyen, V., Kang, Y., Engheta, N., Kagan, C.R., Murray, C.B. *ACS Nano* **2012,** *6*, 2804-2817.
247. Yadong, Y.; Alivisatos, A. P. *Nature* **2005,** *437*, 664-670.
248. Norris, D. J.; Efros, A. L.; Erwin, S. C. *Science* **2008,** *319*, 1776-1779.
249. Manna, L.; Scher, E. C.; Alivisatos, A. P. *J. Am. Chem. Soc.* **2000,** *122*, 12700-12706.
250. Woehrle, G. H. H., J.E.; Ozkar, S.; Finke, R.G. *Turk. J. Chem.* **2006,** *30*, 1-13.

251. Kaushik, V.; Lahiri, T.; Singha, S.; Dasgupta, A. K.; Mishra, H.; Kumar, U.; Kumar, R. *Bioinformation* **2011,** *7*, 320-323.
252. Rice, K. P.; Saunders, A. E.; Stoykovich, M. P. *Cryst. Growth Des.* **2012,** *12*, 825-831.
253. Lee, Y.-J.; Schade, N. B.; Sun, L.; Fan, J. A.; Bae, D. R.; Mariscal, M. M.; Lee, G.; Capasso, F.; Sacanna, S.; Manoharan, V. N.; Yi, G.-R. *ACS Nano* **2013,** *7*, 11064-11070.
254. Reetz, M. T.; Maase, M.; Schilling, T.; Tesche, B. *J. Phys. Chem. B* **2000,** *104*, 8779-8781.
255. Yeager, M. *Microsc. Res. Tech.* **1995,** *31*, 452-466.
256. Lin, X. M.; Jaeger, H. M.; Sorensen, C. M.; Klabunde, K. J. *J. Phys. Chem. B* **2001,** *105*, 3353-3357.
257. Rolland, J.-P.; Bon, P.; Thomas, D. *Comput. Appl. Biosci.* **1997,** *13*, 563-564.
258. Papari, G.; Petkov, N. *Image Vision Comput.* **2011,** *29*, 79-103.
259. Sonka, M.; Hlavac, V.; Boyle, R., *Image processing, analysis, and machine vision*. Cengage Learning: 2014.
260. Murthy, C. R.; Gao, B.; Tao, A. R.; Arya, G. *Nanoscale* **2015,** *7*, 9793-9805.
261. O'Brien, M. N.; Jones, M. R.; Kohlstedt, K. L.; Schatz, G. C.; Mirkin, C. A. *Nano Lett.* **2015,** *15*, 1012-7.
262. Rodriguez-Fernandez, J., Perez-Juste, Jorge, Mulvaney, Paul, Liz-Marzan, Luis M. *J. Phys. Chem. B* **2005,** *109*, 14257-14261.
263. Xia, Y.; Yang, P.; Sun, Y.; Wu, Y.; Mayers, B.; Gates, B.; Yin, Y.; Kim, F.; Yan, H. *Adv. Mater.* **2003,** *15*, 353-389.
264. Grzelczak, M.; Perez-Juste, J.; Mulvaney, P.; Liz-Marzan, L. M. *Chem. Soc. Rev.* **2008,** *37*, 1783-1791.
265. Lohse, S. E.; Murphy, C. J. *Chem. Mater.* **2013,** *25*, 1250-1261.
266. Jones, M. R.; Mirkin, C. A. *Angew. Chem. Int. Ed.* **2013,** *52*, 2886-91.
267. Near, R. D.; Hayden, S. C.; Hunter, R. E.; Thackston, D.; El-Sayed, M. A. *J. Phys. Chem. C* **2013,** *117*, 23950-23955.
268. Yu, W. W.; Qu, L.; Guo, W.; Peng, X. *Chem. Mater.* **2003,** *15*, 2854-2860.
269. Orendorff, C. J.; Murphy, C. J. *J. Phys. Chem. B* **2006,** *110*, 3990-3994.
270. Ali, M. R. K.; Snyder, B.; El-Sayed, M. A. *Langmuir* **2012,** *28*, 9807-9815.
271. Additional extinction coefficients obtained from the product information provided by Nanopartz, Inc. and Nanoseedz, Inc.
272. Glotzer, S. C.; Solomon, M. J. *Nat. Mater.* **2007,** *6*, 557-562.
273. Jiang, W.; KimBetty, Y. S.; Rutka, J. T.; ChanWarren, C. W. *Nat. Nanotechnol.* **2008,** *3*, 145-150.
274. Jones, M. R.; Osberg, K. D.; Macfarlane, R. J.; Langille, M. R.; Mirkin, C. A. *Chem. Rev.* **2011,** *111*, 3736-3827.
275. Philip, R.; Chantharasupawong, P.; Qian, H.; Jin, R.; Thomas, J. *Nano Lett.* **2012,** *12*, 4661-7.
276. Young, K. L.; Jones, M. R.; Zhang, J.; Macfarlane, R. J.; Esquivel-Sirvent, R.; Nap, R. J.; Wu, J.; Schatz, G. C.; Lee, B.; Mirkin, C. A. *Proc. Natl. Acad. U.S.A.* **2012,** *109*, 2240-5.
277. Nikoobakht, B.; El-Sayed, M. A. *Chem. Mater.* **2003,** *15*, 1957-1962.
278. Extinction coefficient obtained from product information provided by Ted Pella, Inc.
279. O'Brien, M. N.; Jones, M. R.; Kohlstedt, K. L.; Schatz, G. C.; Mirkin, C. A. *Nano Letters* **2015,** *15*, 1012-1017.

280. Personick, M. L.; Langille, M. R.; Wu, J.; Mirkin, C. A. *J. Am. Chem. Soc* **2013,** *135*, 3800-3.
281. Turkevich, J.; Stevenson, P. C.; Hillier, J. *Disc. Faraday Soc.* **1951,** *11*, 55-75.
282. Jana, N. R.; Gearheart, L.; Murphy, C. J. *J. Phys. Chem. B* **2001,** *105*, 4065-4067.
283. Liu; Guyot-Sionnest, P. *J. Phys. Chem. B* **2005,** *109*, 22192-22200.
284. O'Brien, M. N.; Jones, M. R.; Mirkin, C. A. *Proc. Natl. Acad. Sci. U.S.A.* **2016**.
285. Grzelczak, M.; Sánchez-Iglesias, A.; Heidari, H.; Bals, S.; Pastoriza-Santos, I.; Pérez-Juste, J.; Liz-Marzán, L. M. *ACS Omega* **2016,** *1*, 177-181.
286. Grzelczak, M.; Sánchez-Iglesias, A.; Rodríguez-González, B.; Alvarez-Puebla, R.; Pérez-Juste, J.; Liz-Marzán, L. M. *Adv. Funct. Mater.* **2008,** *18*, 3780-3786.
287. Personick, M. L.; Langille, M. R.; Zhang, J.; Harris, N.; Schatz, G. C.; Mirkin, C. A. *J. Am. Chem. Soc.* **2011,** *133*, 6170-6173.
288. Millstone, J. E.; Métraux, G. S.; Mirkin, C. A. *Adv. Funct. Mater.* **2006,** *16*, 1209-1214.
289. Ha, T. H.; Koo, H.-J.; Chung, B. H. *J. Phys. Chem. C* **2007,** *111*, 1123-1130.
290. Jana, N. R.; Gearheart, L.; Murphy, C. J. *Chem. Mater.* **2001,** *13*, 2313-2322.
291. Millstone, J. E.; Hurst, S. J.; Métraux, G. S.; Cutler, J. I.; Mirkin, C. A. *Small* **2009,** *5*, 646-664.
292. Jana, N. R. *Small* **2005,** *1*, 875-882.
293. Straney, P. J.; Andolina, C. M.; Millstone, J. E. *Langmuir* **2013,** *29*, 4396-4403.
294. Chen, L.; Ji, F.; Xu, Y.; He, L.; Mi, Y.; Bao, F.; Sun, B.; Zhang, X.; Zhang, Q. *Nano Lett.* **2014,** *14*, 7201-7206.
295. Hubert, F.; Testard, F.; Rizza, G.; Spalla, O. *Langmuir* **2010,** *26*, 6887-6891.
296. Duff, D. G.; Curtis, A. C.; Edwards, P. P.; Jefferson, D. A.; Johnson, B. F. G.; Kirkland, A. I.; Logan, D. E. *Angew. Chem. Int. Ed.* **1987,** *26*, 676-678.
297. Malikova, N.; Pastoriza-Santos, I.; Schierhorn, M.; Kotov, N. A.; Liz-Marzán, L. M. *Langmuir* **2002,** *18*, 3694-3697.
298. Shankar, S. S.; Rai, A.; Ankamwar, B.; Singh, A.; Ahmad, A.; Sastry, M. *Nat. Mater.* **2004,** *3*, 482-488.
299. Shankar, S. S.; Bhargava, S.; Sastry, M. *J. Nanosci. Nanotechnol.* **2005,** *5*, 1721-1727.
300. Ye, X.; Jones, M. R.; Frechette, L. B.; Chen, Q.; Powers, A. S.; Ercius, P.; Dunn, G.; Rotskoff, G. M.; Nguyen, S. C.; Adiga, V. P.; Zettl, A.; Rabani, E.; Geissler, P. L.; Alivisatos, A. P. *Science* **2016,** *354*, 874-877.
301. Straney, P. J.; Marbella, L. E.; Andolina, C. M.; Nuhfer, N. T.; Millstone, J. E. *J. Am. Chem. Soc.* **2014,** *136*, 7873-7876.
302. Alivisatos, A. P. *J. Phys. Chem.* **1996,** *100*, 13226-13239.
303. Ajayan, P.; Marks, L. *Ph. Transit.* **1990,** *24*, 229-258.
304. Dabbousi, B. O.; Rodriguez-Viejo, J.; Mikulec, F. V.; Heine, J. R.; Mattoussi, H.; Ober, R.; Jensen, K. F.; Bawendi, M. G. *J. Phys. Chem. B* **1997,** *101*, 9463-9475.
305. Mokari, T.; Rothenberg, E.; Popov, I.; Costi, R.; Banin, U. *Science* **2004,** *304*, 1787-1790.
306. Shi, W.; Zeng, H.; Sahoo, Y.; Ohulchanskyy, T. Y.; Ding, Y.; Wang, Z. L.; Swihart, M.; Prasad, P. N. *Nano Lett.* **2006,** *6*, 875-881.
307. Langille, M. R.; Zhang, J.; Personick, M. L.; Li, S.; Mirkin, C. A. *Science* **2012,** *337*, 954-957.

308. Scarabelli, L.; Sánchez-Iglesias, A.; Pérez-Juste, J.; Liz-Marzán, L. M. *J. Phys. Chem. Lett.* **2015,** *6*, 4270-4279.
309. Sibbald, M. S.; Chumanov, G.; Cotton, T. M. *J. Phys. Chem.* **1996,** *100*, 4672-4678.
310. Pérez-Juste, J.; Liz-Marzán, L. M.; Carnie, S.; Chan, D. Y. C.; Mulvaney, P. *Adv. Funct. Mater.* **2004,** *14*, 571-579.
311. Fruton, J. S. *J. Biol. Chem.* **1934,** *105*, 79-85.
312. Gilroy, K. D.; Peng, H.-C.; Yang, X.; Ruditskiy, A.; Xia, Y. *Chem. Commun.* **2017**.
313. Gole, A.; Murphy, C. J. *Chem. Mater.* **2004,** *16*, 3633-3640.
314. Laramy, C. R.; Fong, L.-K.; Jones, M. R.; O'Brien, M. N.; Schatz, G. C.; Mirkin, C. A. *Chem. Phys. Lett.* **2017,** *683*, 389-392.
315. Zhang, Q.; Han, L.; Jing, H.; Blom, D. A.; Lin, Y.; Xin, H. L.; Wang, H. *ACS Nano* **2016,** *10*, 2960-2974.
316. Ye, X.; Zheng, C.; Chen, J.; Gao, Y.; Murray, C. B. *Nano Lett.* **2013,** *13*, 765-771.
317. Macfarlane, R. J.; O'Brien, M. N.; Petrosko, S. H.; Mirkin, C. A. *Angew. Chem. Int. Ed.* **2013,** *52*, 5688-98.
318. Torquato, S.; Jiao, Y. *Nature* **2009,** *460*, 876.
319. Agarwal, U.; Escobedo, F. A. *Nat. Mater.* **2011,** *10*, 230.
320. de Graaf, J.; van Roij, R.; Dijkstra, M. *Phys. Rev. Lett.* **2011,** *107*, 155501.
321. Travesset, A. *ACS Nano* **2017,** *11*, 5375-5382.
322. Auyeung, E.; Macfarlane, R. J.; Choi, C. H.; Cutler, J. I.; Mirkin, C. A. *Adv. Mater.* **2012,** *24*, 5181-6.
323. John, B. S.; Escobedo, F. A. *J. Phys. Chem. B* **2005,** *109*, 23008-23015.
324. Kundu, J.; Rajesh, R. *Phys. Rev. E* **2014,** *89*, 052124.
325. Redl, F. X.; Cho, K. S.; Murray, C. B.; O'Brien, S. *Nature* **2003,** *423*, 968.
326. Anderson, J. A.; Lorenz, C. D.; Travesset, A. *J. Comput. Phys.* **2008,** *227*, 5342-5359.
327. Glaser, J.; Nguyen, T. D.; Anderson, J. A.; Lui, P.; Spiga, F.; Millan, J. A.; Morse, D. C.; Glotzer, S. C. *Comput. Phys. Commun.* **2015,** *192*, 97-107.
328. Sebba, D. S.; Mock, J. J.; Smith, D. R.; LaBean, T. H.; Lazarides, A. A. *Nano Lett.* **2008,** *8*, 1803-1808.
329. Radha, B.; Senesi, A. J.; O'Brien, M. N.; Wang, M. X.; Auyeung, E.; Lee, B.; Mirkin, C. A. *Nano Letters* **2014,** *14*, 2162-2167.
330. Srivastava, S.; Nykypanchuk, D.; Fukuto, M.; Gang, O. *ACS Nano* **2014,** *8*, 9857-9866.
331. Rogers, W. B.; Manoharan, V. N. *Science* **2015,** *347*, 639-642.
332. Seo, S. E.; Wang, M. X.; Shade, C. M.; Rouge, J. L.; Brown, K. A.; Mirkin, C. A. *ACS Nano* **2016,** *10*, 1771-1779.
333. Dickerson, R. E., [5] DNA structure from A to Z. In *Methods in Enzymology*, Academic Press: 1992; Vol. 211, pp 67-111.
334. Potaman, V. N.; Bannikov, Y. A.; Shlyachtenko, L. S. *Nucleic Acids Research* **1980,** *8*, 635-642.
335. Vargason, J. M.; Henderson, K.; Ho, P. S. *Proc. Natl. Acad. Sci. U.S.A.* **2001,** *98*, 7265-7270.
336. Jose, D.; Porschke, D. *Nucleic Acids Research* **2004,** *32*, 2251-2258.
337. Smith, B. D.; Liu, J. *J. Am. Chem. Soc.* **2010,** *132*, 6300-6301.
338. Teif, V. B.; Bohinc, K. *Progress in Biophysics and Molecular Biology* **2011,** *105*, 208-222.

339. Lee, O.-S.; Cho, V. Y.; Schatz, G. C. *J. Phys. Chem. B* **2012,** *116*, 7000-7005.
340. Eickbush, T. H.; Moudrianakis, E. N. *Cell* **1978,** *13*, 295-306.
341. Senesi, A. J.; Lee, B. *Journal of Applied Crystallography* **2015,** *48*, 1172-1182.
342. O'Brien, M. N.; Brown, K. A.; Mirkin, C. A. *ACS Nano* **2016,** *10*, 1363-1368.
343. Zwanikken, J. W.; Guo, P.; Mirkin, C. A.; Olvera de la Cruz, M. *J. Phys. Chem. C* **2011,** *115*, 16368-16373.
344. Manning, G. S. *Quarterly Reviews of Biophysics* **1978,** *11*, 179-246.
345. Laura, R.; Dominic, J. L.; Alexei, A. K. *J. Phys. Condens. Matter.* **2007,** *19*, 416103.
346. Livolant, F.; Leforestier, A. *Progress in Polymer Science* **1996,** *21*, 1115-1164.
347. Senesi, A.; Lee, B. *Journal of Applied Crystallography* **2015,** *48*, 565-577.
348. Case, D. B., V.; Berryman, J.; Betz, R.; Cai, Q.; Cerutti, D.; Cheatham III, T.; Darden, T.; Duke, R.; Gohlke, H. *AMBER*, 2014.
349. Wang, J.; Wolf, R. M.; Caldwell, J. W.; Kollman, P. A.; Case, D. A. *Journal of Computational Chemistry* **2004,** *25*, 1157-1174.
350. Maier, J. A.; Martinez, C.; Kasavajhala, K.; Wickstrom, L.; Hauser, K. E.; Simmerling, C. *Journal of chemical theory and computation* **2015,** *11*, 3696-3713.
351. Pérez, A.; Marchán, I.; Svozil, D.; Sponer, J.; Cheatham, T. E.; Laughton, C. A.; Orozco, M. *Biophysical journal* **2007,** *92*, 3817-3829.
352. Iori, F.; Di Felice, R.; Molinari, E.; Corni, S. *Journal of Computational Chemistry* **2009,** *30*, 1465-1476.
353. Dupradeau, F.-Y.; Pigache, A.; Zaffran, T.; Savineau, C.; Lelong, R.; Grivel, N.; Lelong, D.; Rosanski, W.; Cieplak, P. *Physical Chemistry Chemical Physics* **2010,** *12*, 7821-7839.
354. Schmidt, M. W.; Baldridge, K. K.; Boatz, J. A.; Elbert, S. T.; Gordon, M. S.; Jensen, J. H.; Koseki, S.; Matsunaga, N.; Nguyen, K. A.; Su, S.; Windus, T. L.; Dupuis, M.; Montgomery, J. A. *Journal of Computational Chemistry* **1993,** *14*, 1347-1363.
355. Bayly, C. I.; Cieplak, P.; Cornell, W.; Kollman, P. A. *J. Phys. Chem.* **1993,** *97*, 10269-10280.
356. Phillips, J. C.; Braun, R.; Wang, W.; Gumbart, J.; Tajkhorshid, E.; Villa, E.; Chipot, C.; Skeel, R. D.; Kalé, L.; Schulten, K. *Journal of Computational Chemistry* **2005,** *26*, 1781-1802.
357. El Hassan, M. A.; Calladine, C. R. *Philosophical Transactions of the Royal Society of London. Series A: Mathematical, Physical and Engineering Sciences* **1997,** *355*, 43-100.
358. Roe, D. R.; Cheatham, T. E. *Journal of Chemical Theory and Computation* **2013,** *9*, 3084-3095.